

River-tide interaction and cyclone-induced storm surge in the Ganges-Brahmaputra-Meghna delta

Author:

Elahi, Md Wasif E

Publication Date:

2021

DOI:

<https://doi.org/10.26190/unsworks/1626>

License:

<https://creativecommons.org/licenses/by/4.0/>

Link to license to see what you are allowed to do with this resource.

Downloaded from <http://hdl.handle.net/1959.4/100026> in <https://unsworks.unsw.edu.au> on 2024-04-26

1. THESIS TITLE & ABSTRACT

Thesis Title

River-tide interaction and cyclone-induced storm surge in the Ganges-Brahmaputra-Meghna delta

Thesis Abstract

The estuarine circulation is produced by the combination of tide, wave, wind, and river discharge. During a cyclone, the strong wind along with tide-surge interaction and wave-current interactions produces a cyclone-induced storm surge event that may cause damage to life and property. Hence, the understanding of river-tide interactions and other physical processes related to the generation of storm surge height is vital for coastal zone disaster management.

The Ganges-Brahmaputra-Meghna delta (GBMD), in the Bay of Bengal, is a perfect laboratory to study river-tide interaction as well as cyclone-induced storm surge event due to its hydrodynamic and geographical features. A barotropic model (Delft3D) is established for the GBMD that can reproduce the varying river discharge influence on the tides. Model results show that the tide can propagate up to 205 km inland from the estuary mouth in low river discharge periods. The balance between tidal dissipation and generation depends on the residual velocity generated by the river discharge and the velocity of the principal tides. For the first time, a two-fold influence of river discharge on tides is reported in an estuarine system. Critical river discharge thresholds produce optimal dissipation of semidiurnal tides and generation of quarterdiurnal tides through friction at the upper and middle estuary. River discharge above the critical river discharge amount dissipates both semidiurnal and quarterdiurnal tides more rapidly than it generates quarterdiurnal tides from nonlinear interactions.

Next, the model is converted into a wave-coupled model to investigate wave-current interactions (WCI) during the Cyclone Sidr-induced storm surge event. Results show that the wave-current interaction can increase significant wave height by 1 m (59%) at the cyclone landfall location although the WCI has varying influence depending on the amplitudes and directions of the waves and currents. Wave energy dissipation is one of the key factors affecting the wave height variations and white capping dissipation dominates the wave dissipation processes. Finally, the model is used to study inundation scenarios using different mean sea level rise scenarios under cyclonic conditions. Results demonstrate the importance of considering the floodplain area in numerical modelling studies to estimate storm surge height during a cyclonic event.

2. ORIGINALITY OF PUBLICATION STATEMENT

Thesis Title and Abstract

Declarations

Inclusion of Publications Statement

Corrected Thesis and Responses

ORIGINALITY STATEMENT

I hereby declare that this submission is my own work and to the best of my knowledge it contains no materials previously published or written by another person, or substantial proportions of material which have been accepted for the award of any other degree or diploma at UNSW or any other educational institution, except where due acknowledgement is made in the thesis. Any contribution made to the research by others, with whom I have worked at UNSW or elsewhere, is explicitly acknowledged in the thesis. I also declare that the intellectual content of this thesis is the product of my own work, except to the extent that assistance from others in the project's design and conception or in style, presentation and linguistic expression is acknowledged.

COPYRIGHT STATEMENT

I hereby grant the University of New South Wales or its agents a non-exclusive licence to archive and to make available (including to members of the public) my thesis or dissertation in whole or part in the University libraries in all forms of media, now or here after known. I acknowledge that I retain all intellectual property rights which subsist in my thesis or dissertation, such as copyright and patent rights, subject to applicable law. I also retain the right to use all or part of my thesis or dissertation in future works (such as articles or books).

For any substantial portions of copyright material used in this thesis, written permission for use has been obtained, or the copyright material is removed from the final public version of the thesis.

AUTHENTICITY STATEMENT

I certify that the Library deposit digital copy is a direct equivalent of the final officially approved version of my thesis.

3. INCLUSION OF PUBLICATIONS STATEMENT

Thesis Title and Abstract	Declarations	Inclusion of Publications Statement	Corrected Thesis and Responses
---------------------------	--------------	-------------------------------------	--------------------------------

UNSW is supportive of candidates publishing their research results during their candidature as detailed in the UNSW Thesis Examination Procedure.

Publications can be used in the candidate's thesis in lieu of a Chapter provided:

- The candidate contributed greater than 50% of the content in the publication and are the "primary author", i.e. they were responsible primarily for the planning, execution and preparation of the work for publication.
- The candidate has obtained approval to include the publication in their thesis in lieu of a Chapter from their Supervisor and Postgraduate Coordinator.
- The publication is not subject to any obligations or contractual agreements with a third party that would constrain its inclusion in the thesis.

The candidate has declared that their thesis has publications - either published or submitted for publication - incorporated into it in lieu of a Chapter/s. Details of these publications are provided below.

Publication Details #1

Full Title:	Influence of Seasonal River Discharge on Tidal Propagation in the Ganges-Brahmaputra-Meghna Delta, Bangladesh
Authors:	M. W. E. Elahi, I. Jaión-Rojas, X. H. Wang, E. A. Ritchie
Journal or Book Name:	Journal of Geophysical Research Oceans
Volume/Page Numbers:	Volume 125, Issue 11
Date Accepted/Published:	12 October 2020
Status:	published
The Candidate's Contribution to the Work:	More than 80 % of the work is contributed by the candidate; and he was responsible primarily for the planning, execution, and preparation of the work for publication.

Location of the work in the thesis and/or how the work is incorporated in the thesis: The research article is incorporated as a chapter (Chapter-2) in the thesis.

Publication Details #2

Full Title:	Influence of wave-current interaction on a cyclone-induced storm surge event in the Ganges-Brahmaputra-Meghna Delta
Authors:	M. W. E. Elahi, X. H. Wang, J. Salcedo-Castro, E. A. Ritchie
Journal or Book Name:	Journal of Geophysical Research Oceans
Volume/Page Numbers:	
Date Accepted/Published:	
Status:	submitted
The Candidate's Contribution to the Work:	More than 80 % of the work is contributed by the candidate; and he was responsible primarily for the planning, execution, and preparation of the work for publication.

Location of the work in the thesis and/or how the work is incorporated in the thesis: The research article is incorporated as a chapter (Chapter-3) in the thesis.

Candidate's Declaration



I confirm that where I have used a publication in lieu of a chapter, the listed publication(s) above meet(s) the requirements to be included in the thesis. I also declare that I have complied with the Thesis Examination Procedure.



River-tide interaction and cyclone-induced storm surge in the Ganges-Brahmaputra-Meghna delta

Md. Wasif E Elahi

A thesis in fulfilment of the requirements for the degree of Doctor of Philosophy

School of Science

The University of New South Wales, Canberra

August 2021

Abstract

Knowledge of tidal propagation and tidal properties is essential to understand estuarine systems. Understanding of tides in estuaries are challenging due to non-linear interactions and non-stationary tides generated from the balance of bottom friction, channel geometry and river flow. The Ganges-Brahmaputra-Meghna delta (GBMD), located in the head of the Bay of Bengal, is a tide dominated delta with strong seasonal river discharge variations. Moreover, severe tropical cyclones hit the GBMD at regular intervals and cause devastating cyclone-induced storm surge flooding events. The estuarine circulation is produced by the combination of tide, wave, wind, and river discharge. During a cyclone, the strong wind along with tide-surge interaction and wave-current interactions produces a cyclone-induced storm surge event that may cause damage to life and property. Hence, the understanding of river-tide interactions and other physical processes related to the generation of storm surge height is vital for coastal zone disaster management.

The GBMD is a perfect laboratory to study river-tide interaction as well as cyclone-induced storm surge events due to its hydrodynamic and geographical features. A barotropic model (Delft3D) is validated for the GBMD that can reproduce the varying river discharge influence on the tides. Model results show that the tide can propagate up to 205 km inland from the estuary mouth in low river discharge periods. The balance between tidal dissipation and generation depends on the residual velocity generated by the river discharge and the velocity of the principal tides. For the first time, a two-fold influence of river discharge on tides is reported in an estuarine system. Critical river discharge thresholds produce optimal dissipation of semidiurnal tides and generation of quarterdiurnal tides through friction at the upper and middle estuary. River discharge above the critical river discharge amount dissipates both semidiurnal and quarterdiurnal tides more rapidly than it generates quarterdiurnal tides from nonlinear interactions.

Wave-current interactions (WCI) can modulate storm surge height through modifying the wind- and wave-driven water levels during a cyclone. Role of WCI on water level variations depends on the different characteristics of wave and current, including their amplitude and direction. Next, the model is converted into a wave-coupled model to investigate WCI during the Cyclone Sidr-induced storm surge event. Results show that the wave-current interaction increases the significant wave height up to 1 m (59%) at

the cyclone landfall location although the WCI has varying influence depending on the amplitudes and directions of the waves and currents. Effective wind stress (vectorial difference between wind and current velocity) susceptible to the direction between wind and current dictates the wind-driven wave height as well as wave-setup in the coastal area during a cyclonic event. Tides can influence both wind- and wave-setup by modulating water level. Different idealized scenarios considering different model coupling methods with different boundary forcings are examined. Results show that the significant wave heights are affected more by the water depth in the shallow areas (< 15 m) than the currents, whereas the significant wave heights are dominated by the strong currents in the deeper ocean. Wave energy dissipation is one of the key factors affecting the wave height variations, and white capping dissipation dominates the wave dissipation processes.

Cyclone-induced storm surge causes the most devastating flooding event in the GBMD among all fluvial- and tidal-flooding. According to different future climate projection studies, the GBMD is expected to face adverse consequences in terms of flooding conditions. Hence, finally, the model is used to study inundation scenarios using different mean sea level (MSL) rise scenarios, including a MSL rise of 0.5 m, 1 m and 1.5 m under cyclonic conditions. Results show that for the same cyclone intensity, increasing the mean sea level produces higher inundation in the GBMD. Severe cyclones similar to Cyclone Sidr with up to 1.5 m increased MSL can flood up to 33% of the total coastal area of Bangladesh, which is 7.98% of the total area of Bangladesh. The Western and Central GBMD will be affected more by MSL rise compared to the Eastern GBMD due to low land elevations. The area inundated the cyclone increases linearly with the MSL rise except for the greatest MSL rise simulation of 1.5 m because in this case additional floodplain inundation occurs as the embankments are overtopped. Furthermore, the model results show that increasing the intensity of the cyclone has a greater impact on the storm surge height and flooded area than increasing the size of the cyclone through the radius of maximum wind. These findings provide new understandings of the river-tide interaction and cyclone-induced storm surge in the GBMD. The model can be used as an assessment tool for disaster management planning for different flooding scenarios, particularly in embankment height design and identifying vulnerable locations in the GBMD under different climate and mean sea level rise scenarios.

Acknowledgments

I would like to acknowledge and most sincere thanks to my supervisor Professor Xiao Hua Wang, for his continuous support throughout my time here and for believing in my abilities. This thesis would not have been possible without his constant encouragement, guidance, enthusiasm, and wisdom, and I thank him for everything. I would also like to express my gratitude towards my joint supervisor Professor Liz Ritchie-Tyo for her guidance, insightful feedbacks, encouragement, and support.

I would also like to thank Dr. Isabel Jalón Rojas for helping me with different analyses. I would also like to acknowledge the following individuals for their support and help during this research: Dr. Julio Salcedo-Castro, Gang Yang, Yuan Yuan, Emma Cheng. I would also like to thank my secondary supervisor Professor Munsur Rahman for arranging field data from Bangladesh.

I am highly thankful to all of my colleagues and friends for their constant support, motivation and help in completing the journey of this Ph.D. I would like to thank Assaduzzaman Khan, Kamrul Hassan Mojumder, Moshir Farazi, Zannat Tahera Lamia, Rubaiya Kabir, Ahsanul Habib, Mohammad Mohiuddin Khan for making Canberra life enjoyable.

My heartiest thanks to my parents (Md. Eyaqub Ali and Khalada Akter) and my younger brother (Tausif-E-Elahi) for their patience and loving support and for believing in me in this long journey. I am grateful to my wife, Mahinoor Sultana, for her love, encouragement, sacrifices, and unconditional support over all these years of studies. Finally, I would like to thank our loving daughter, Sarah Sabeen, for keeping me awake and giving me reasons to smile during my thesis writing.

Above all, I am highly grateful to the almighty, who empowered me to complete this research work.

Publications during PhD study:

Journal Article

1. Elahi, M. W. E., Jalón-Rojas, I., Wang, X. H., & Ritchie, E. A. (2020). Influence of seasonal river discharge on tidal propagation in the Ganges-Brahmaputra-Meghna Delta, Bangladesh. *Journal of Geophysical Research: Oceans*, 125, e2020JC016417. <https://doi.org/10.1029/2020JC016417>
2. Elahi, M. W. E., Wang, X. H., J. Salcedo-Castro, & Ritchie, E. A. (2021). Influence of wave-current interaction on a cyclone-induced storm surge event in the Ganges-Brahmaputra-Meghna Delta. *Journal of Geophysical Research: Oceans*. (Currently under revision)

Poster presentation

3. Elahi, M. W. E., Ritchie, E. A. & Wang, X. H. (2021). Role of physical parameters in Cyclone-induced storm surges in the Ganges-Brahmaputra-Meghna delta, Poster presentation, 34th Conference on Hurricanes and Tropical Meteorology, American Meteorological Society, 10-14 May, 2021. <https://ams.confex.com/ams/34HURR/meetingapp.cgi/Paper/373055>

Table of Contents

Abstract	iv
Acknowledgments	vi
Table of Contents.....	viii
List of Figures.....	xii
List of Tables.....	xix
List of Abbreviations	xx
Chapter 1 Introduction.....	1
1.1 Background.....	1
1.2 Problem statement.....	8
1.3 Objectives/Aims.....	11
1.4 Significance	11
1.5 Thesis outline.....	12
Chapter 2 Influence of seasonal river discharge on tidal propagation in the Ganges- Brahmaputra-Meghna Delta, Bangladesh	14
2.1 Introduction.....	14
2.2 Study Site.....	17
2.3 Data and Methods	19
2.3.1 In situ observations of water level and river discharge	19
2.3.2 Numerical model setup	20

2.3.3 Tide analysis method.....	21
2.4 Result and Discussion	24
2.4.1 Model validation.....	24
2.4.2 Temporal and spatial variation of tides	30
2.4.3. River-tide interaction in the upper GBMD	38
2.5 Conclusions.....	47
Chapter 3 Influence of wave-current interaction on a cyclone-induced storm surge event in the Ganges-Brahmaputra-Meghna Delta.....	51
3.1 Introduction.....	51
3.2 Field Site and Data	56
3.2.1 Cyclone Sidr.....	56
3.2.2 Study area.....	58
3.2.3 Field data.....	60
3.3 Methodology.....	61
3.3.1 Numerical model Delft3D.....	62
3.3.2 Model setup.....	68
3.3.3 Description of Scenarios	70
3.4 Result and Discussions	73
3.4.1 Model validation.....	73
3.4.2 Surface water elevation variations	80
3.4.3 Role of tide, wind and waves in the storm surge height.....	82
3.4.4 Role of wave-current interaction in wave setup.....	86

3.4.5 Effects of wave-current interaction on wave	91
3.5 Summary and Conclusions	102
Chapter 4 Cyclone-induced storm surge flooding in the Ganges-Brahmaputra-Meghna delta under different mean-sea level rise scenarios	105
4.1 Introduction.....	105
4.2 Background.....	105
4.3 Methodology.....	110
4.4 Result and Discussion	113
4.4.1 Cyclone-induced storm surge flooding during Cyclone Sidr	113
4.4.2 Cyclone-induced flooding under different MSL scenarios.....	115
4.4.3 Water level variations with different MSL rise scenarios during Cyclone Sidr	119
4.4.4 Storm surge height variations with different cyclone strengths.....	123
4.4.5 Influence of cyclone landfall location and river discharge on cyclone-induced storm surge	129
4.5 Conclusion	132
Chapter 5 Conclusion and future scope	134
5.1 Conclusion	134
5.1.1 How do the seasonal river discharge variations modulate tides along the GBMD?	135
5.1.2 How do the wave-current interactions influence a cyclone-induced storm surge event (Cyclone Sidr, 2007) in the GBMD?.....	136

5.1.3 How does a cyclone-induced storm surge event result in flooding in the GBMD and how will the cyclone-induced storm surge flooding be affected by the future mean sea level rise due to climate change?	137
5.2 Implications	141
5.3 Limitations and future research	142
5.3.1 Limitations	142
5.3.2 Future research	146
References	148
Appendices	175
A. River-tide interaction (Chapter 2)	175
A.1 Complex demodulation method	175
A.2 The stationary harmonic analysis result	176
A.3 Further analysis on river-tide interaction.....	176
B. Wave-current interaction (Chapter 3).....	180
B.1 Cyclone wind and pressure field incorporation.....	180
B.2 Uncertainty related to cyclone model	182
B.3 Tidal amplitude and maximum residual water level comparison.....	185
B.4 Supporting model result for different scenarios	187
C. Cyclone-induced storm surge flooding (Chapter 4).....	192

List of Figures

Figure 1.1. (a) A picture of Polder-26 in 2017, Khulna division, Western GBMD, from the Blue Gold Program (<http://www.bluegoldbd.org>) and (b) A schematic diagram of different physical processes in a cyclone-induced storm surge event is reproduced from Khan et al., 2020. The red box denotes the river-tide interaction that is discussed in Chapter 2. The yellow box represents the wave-current interaction that is addressed in Chapter 3. The purple box indicates the inundation during a cyclone-induced storm surge, discussed in Chapter 4..... 5

Figure 1.2. The structure and main topics of this thesis. The red two-way arrow represents interaction between two processes. The black bracket denotes cyclonic conditions. The green arrow denotes different idealized cases of mean sea level rise. 13

Figure 2.1. (a) Location of the study area. E1-E3 are stations located on the exposed coast and R1-R9 are stations located along the river; (b) Model domain with boundary forcings, (c) A zoomed view of the model grid at R6 within the black square area indicated in Fig. 2.1d, (d) Model bathymetry of the complex channel network in the lower Meghna river. 1-3 (yellow) represent split channels and 4-5 (red) denote examples of shallow land; 0 m denotes mean sea level (e) The complex channel network in the lower Meghna River from the Google Earth..... 18

Figure 2.2. A comparison of simulated water levels with observations for the average flood conditions (2000) at: (a) E1; (b) E2; (c) E3; and (d) R3. HWL and LWL denote daily high-water and low-water levels, respectively. 28

Figure 2.3. Tidal and river discharge conditions for the average flood conditions (2000): (a) The model tidal range; (b) D1 amplitude; (c) D2 amplitude; (d) D4 amplitude; and (e) observed river discharge. Dotted and thick dashed lines denote typical spring and neap tide, respectively. 32

Figure 2.4. Tidal constituents (D1, D2, D4 and MSF) as a function of river discharge and tidal range at the estuary mouth (color bar) at: (a) R8; (b) R5; (c) R2; and (d) R1. Note that the Y-axis ranges have different scales. 35

Figure 2.5. Spatial variations of tidal amplitudes: (a) D1; (b) D2; (c) D4; (d) MSF during different river discharge periods; and (e) Width and depth of the river along the GBMD. Q is the river discharge ($\times 1000 \text{ m}^3 \text{ s}^{-1}$). Amplitudes are averaged over the same river discharge period. 36

Figure 2.6. Tidal damping rate and residual water level slope variations with the river discharge (a, b) and tidal range at mouth (c, d) for the study year.	40
Figure 2.7. Simulated influence on the tide at R2 for a variety of idealized river discharges (Total discharge represented in the legend is in $\times 1000 \text{ m}^3 \text{ s}^{-1}$, e.g., Q125 = $125,000 \text{ m}^3 \text{ s}^{-1}$): (a) amplitude of the D2; and (b) D4 tide variation with river discharge; spatial variation of the maximum amplitude of: (c) D2; and (d) D4 tide with distance from the estuary mouth.	42
Figure 2.8. Amplitudes of: (a) D2; and (b) D4 tide variations at R2 for different boundary and tidal forcing.....	43
Figure 2.9. (a) Maximum total friction, (b) maximum friction related to river, (c) maximum friction related to tide and (d) maximum friction related to river-tide interaction according to Equation 1-4. U_i and ϕ_i are calculated from the model simulated river and tidal current components for different idealized scenarios along the GBMD. Note that y-axes are on different scales.....	45
Figure 3.1. Cyclone Sidr track from the JTWC best track archive with the model domain. Black dotted line indicates the location of the Bengal Canyon.....	58
Figure 3.2. (a) The study area along with Cyclone Sidr and discharge boundary; (b)- (d) the model water level comparison with the observed water level at: (b) Hironpoint; (c) Khepupara; and (d) Cittagong for Cyclone Sidr. The different colour boxes represent different regions of the GBMD.	74
Figure 3.3. Comparison of the spatial variation of significant wave height and wind speed with: (a) model; and (b) ERA5 dataset. Time series comparison of modelled and ERA5 at the blue (left of center) and white (right of center) dots: (c) significant wave height and (d) wind speed, (e) statistical analysis. N.B. The green arrow denotes the landfall time 1500 UTC 15 November 2007.	76
Figure 3.4. (a) Spatial variations of model water level at one-hour after the landfall. Black circles represent the surveyed locations by Shibayama et al. (2008). Numbers represent the maximum water level (Model maximum / Survey maximum water level). (b) Field survey locations map and maximum water level observations. At locations near the E point, there are small channels less than 50 m width, which are not included in the model. Hence, the comparison is not possible at that location.....	79

Figure 3.5. Simulated spatial variations of surface water elevation (shading) and the surface wind field during Cyclone Sidr on 15 November 2007 at: (a) 1200 UTC; (b) 1500 UTC; (c) 1800 UTC; and (d) 2100 UTC. The yellow cross and purple line denote the cyclone eye location and track, respectively. In the current study, the surface water elevation is defined as the total water level driven by a combined tide, wind, and wave. 82

Figure 3.6. Simulated tides and residual water level at different stations during the landfall of Cyclone Sidr for the following scenarios: only tide (blue), only wind (green), tide and wind (black; cyclonic wind stress increase along with tide), and the real case (red; cyclonic wind stress along with tide and wave). The residual water level is calculated by subtracting the tidal water level from the simulated total water level. Purple dashed and purple solid lines represents the landfall time and observed maximum residual water level. 83

Figure 3.7. Difference in the water level between the run with waves (Run7) and the run without waves (Run3) at: (a) Low tide at 1200 UTC 15 November; (b) High tide at 1800 UTC 15 November 2007; and (c) Time series of the tidal water level variations (Run2) at Khepupara. The water level difference is calculated as Run7 minus Run3. Positive (negative) water level difference denotes wave setup (setdown). The length of the vector represents wind speed (max=50 m s⁻¹). The red star in panel (c) denotes the landfall time. 87

Figure 3.8. Simulated wave setups (a-d) along with tidal water level variations, and (e-h) radiation stress gradient magnitude variations with wind speed at: (a), (e) Tajumuddin; (b), (f) Khepupara; (c), (g) D1; and (d), (h) D2. The dotted line indicates the landfall time. The wave setup is plotted on different scales to enhance visibility. 91

Figure 3.9. Significant wave height variations for the 'Only wave' and 'Wave-current interaction' scenarios during the landfall of Cyclone Sidr. The purple line denotes the landfall time at 1500 UTC 15 November 2007. 93

Figure 3.10. Direction and amplitude variations of the surface current and wind at (a), (d) Khepupara, (b), (e) D2 and (c), (f) Tajumuddin for different scenarios. The dashed line represents the cyclone landfall time 1500 UTC 15 November 2007. 95

Figure 3.11. Influence of different parameters on significant wave height during Cyclone Sidr at: (a) Khepupara; (b) Tajumuddin; (c) D1; and (d) D2. 98

Figure 3.12. Maximum: (a) significant wave height; and (b) wave energy variations with and without wave-current interaction at Khepupara for Cyclone Sidr for different wave dissipation processes. Maximum amplitudes of SWH and dissipation are observed at different times of the cyclone passage for different scenarios.100

Figure 3.13. Maximum significant wave height variations along the Bay of Bengal for “Only Wave” and “Wave-Current interaction” conditions under: (a) Only depth-induced breaking; (b) Only whitecapping; (c) Only bottom friction; and (d) All wave dissipation processes. Maximum amplitudes of the SWH are observed at different times of the cyclone for different scenarios. A positive distance represents the oceanward direction. Change in % = (WCI-Only Wave)/Only Wave %.....101

Figure 4.1. (a) The Bangladesh coast embankment network with the track of Cyclone Sidr and station locations in the three different parts of the GBMD; and (b) Schematic diagram of polders in the Western (at Khepupara) and Central (at Tajumuddin) GBMD with channel bathymetry and embankment height. Different mean sea levels are indicated by the dashed lines.110

Figure 4.2. Modelled cyclone flood area comparison with the flood area analyzed from MODIS imagery at 0000 UTC 16 November by the Dartmouth Flood Observatory. The blue dashed line indicates the cloud-free area in MODIS imagery. The white solid lines indicate embankment locations. The nearest station to the track of Cyclone Sidr (Khepupara) is denoted by the star. The area of flooding analyzed from MODIS imagery is reproduced from the map prepared by the Dartmouth Flood Observatory: <https://reliefweb.int/map/bangladesh/bangladesh-cyclone-sidr-rapid-response-inundation-map-16-nov-2007>.....114

Figure 4.3. Cyclone-induced storm surge flooding during the landfall of Cyclone Sidr, valid at 2100 UTC 15 November: (a) MSL at 0 m - current conditions, (b) MSL rise by 0.5 m, (c) MSL rise by 1 m, and (d) MSL rise by 1.5 m. The purple line represents the track of Cyclone Sidr.116

Figure 4.4. Flooded area at 2100 UTC 15 November 2007 for different MSL scenarios with- and without-cyclone conditions.117

Figure 4.5. (a) Model flooded area by Cyclone Sidr and tide under the different MSL rise scenarios; and (b) Model flooded area by tides under different MSL rise scenarios. Note that the flooded area in different colours represent flooded area added from the further increment of MSL and, valid at

2100 UTC 15 November. For example, the red area denotes a newly flooded area in the ‘MSL + 1.5 m’ compared to the ‘MSL + 1 m’.	118
Figure 4.6. Model water level variations across the GBMD during Cyclone Sidr under different MSL rise scenarios. The purple line represents the landfall time of 1500 UTC 15 November 2007.	120
Figure 4.7. Residual water level variations under different MSL rise with Cyclone Sidr. The purple line represents the landfall time of 1500 UTC 15 November 2007.	122
Figure 4.8. Model residual water level and tidal water level variations with different MSL rise scenarios at: (a) Khepupara; and (b) Tajumuddin. The landfall time is indicated by the black arrow. Red arrows indicate decrease (downward) and increase (upward) of maximum tidal water level in the ‘MSL + 1.5 m’ compared to the ‘MSL = 0 m’ scenario. The purple arrow indicates the maximum tidal water level at the time of maximum model water level observed at Tajumuddin in Figure 4.6.	123
Figure 4.9. Cyclone-induced storm surge variations across the GBMD with different maximum wind speed during Cyclone Sidr conditions. The JTWC denotes maximum wind velocity for Cyclone Sidr. Scenarios with maximum wind speed increased by 20 %, 30 % and 50 % are presented by x 1.2, x 1.3 and x 1.5, respectively. The residual water level is estimated by subtracting the tidal water level from the total water level. The purple line represents the landfall time: 1500 UTC 15 November 2007.	124
Figure 4.10. Cyclone-induced storm surge variations across the GBMD with different radius of maximum wind speed during Cyclone Sidr conditions. The purple line represents the landfall time of 1500 UTC 15 November 2007.	126
Figure 4.11. Area of flooding at 2100 UTC, 15 November 2007 for: (a) only tide, Cyclone Sidr (Real case (Tide + Cyclone)), Maximum velocity increased by 50% for Cyclone Sidr (Vmax 50% incr.) and Radius of Maximum wind speed increased by 100% (Rmax 100% incr.); and (b) Area of flooding for the control cyclone track and the eastward-shifted cyclone track with a river discharge of 30,000 m ³ s ⁻¹ . The purple and yellow dashed lines represent the original Cyclone Sidr track and the modified Cyclone Sidr track, respectively. The green shaded area denotes the flooded area in both simulations.	128
Figure 4.12. Percentage change in the area of flooding and average residual water level compared to the control Cyclone Sidr simulation with percentage change in maximum wind speed (Vmax) and	

radius of maximum wind (Rmax). The average maximum residual water level for each idealized case is estimated by averaging the maximum residual water levels at all stations across the GBMD.	129
Figure 4.13. Simulated water level variation for different river discharge amounts for both the original (Control track) and shifted landfall location of Cyclone Sidr (Shifted track). Q00, Q30, Q50 represent $0 \text{ m}^3 \text{ s}^{-1}$, $30000 \text{ m}^3 \text{ s}^{-1}$ and $50000 \text{ m}^3 \text{ s}^{-1}$ of river discharge at the Lower Meghna, respectively. The purple line represents the landfall time of 1500 UTC 15 November 2007.	131
Figure 5.1. Influence of river-tide and wave-current interactions during a cyclone-induced storm surge event.	140
Figure A.1. Spatial variations of tidal amplitudes for: (a) 1998; (b) 2000; and (c) 2001 from the stationary harmonic analysis.	176
Figure A.2. Water level variation during: (a) a dry season ($\sim 10,000 \text{ m}^3 \text{ s}^{-1}$) spring tide; (b) a dry season-neap tide; (c) a wet season ($\sim 60,000 \text{ m}^3 \text{ s}^{-1}$) spring tide; and (d) a wet season-neap tide at R1, R2, R5, and R8.	177
Figure A.3. Spring and neap tide: (a) dissipation in amplitude; and (b) dissipation in percentage along the GBMD for the Q60 compared to the Q00 scenario.	178
Figure A.4. Tidal energy flux variations at R7, R8 and R9 for different river discharge scenarios.	179
Figure A.5. Different tidal amplitudes variations at R7 (50 km from the estuary mouth) for the following river discharge scenarios: (a) D1; (b) D2; (c) MSF; and (d) D4.	179
Figure B.1. Locations of the cyclone eye at 3-hour before and 3-hour after the landfall time from the JTWC best track. Cyclones eye movement is assumed constant between the time period, which causes the discrepancies between the model and ERA5 wind field. Consequently, it also affects the significant wave height variations.	183
Figure B.2. Model water level variation during Cyclone Sidr at different locations. Several idealized cases are assessed for different landfall timings compared to the timing of the JTWC best track archive.	184

Figure B.3. Model water level variations at different locations for different radius of maximum wind after 3-hour Cyclone Sidr landfall. Only radius of maximum wind is modified at 1800 15 November 2007 and rest of the other parameters remain unchanged.	185
Figure B.4. Water level variations at: (a) Galachipa; (b) Khepupara; (c) Tajudmuddin; and (d) Sandwip for different bathymetric conditions. the black line denotes results from the only wind driven flow model considering real bathymetry. The red line denotes the scenario with 2 m deeper bathymetry in the whole study area compared to the real bathymetry. The purple dashed line represents the landfall time: 1500 UTC 15 November 2007.	187
Figure B.5. Model wind magnitude and wind direction during Cyclone Sidr across the GBMD. The purple line denotes the landfall time.	188
Figure B.6. SWH (a), (d), water depth (b), (e), and surface current magnitude (c), (f) for the only waves (Run1) and wave-current interaction (Run7) scenarios at 1400 UTC, 15 November 2007.	189
Figure B.7. Direction of current, wave and wind along with wind speed at: (a) Khepupara; and (b) Tajumuddin for the wave-current interaction scenario (Run7).	190
Figure B.8. Maximum: (a) significant wave height; and (b) wave energy variations with and without wave-current interaction at Tajumuddin during Cyclone Sidr for different wave dissipation processes.	190

List of Tables

Table 2.1. Statistical analysis of model water level compared with observations for 2000.....	28
Table 2.2. Comparison of model tidal amplitude and phase with observations: 2000	29
Table 2.3. Mean R2 values of model tidal range for 2000.	29
Table 2.4. Idealistic scenarios with different boundary forcing.	43
Table 2.5. Maximum amplitude of the D2, and D4 tide, nondimensional maximum residual velocity (U0), maximum velocity of diurnal (U1), semi-diurnal (U2) and maximum velocity of quarterdiurnal (U4) tides, frictional coefficient from Godin (1999) and velocity components in the river-tide friction for the river discharge scenarios (Q00-125) at R2.....	46
Table 3.1. Model parameterization	70
Table 3.2. Scenario details	72
Table 3.3. Statistical analysis of model water level compared with observations for Cyclone Sidr.	74
Table 3.4. Comparison of model outcomes with high water levels and maximum significant wave height extracted from recent studies on Cyclone Sidr.	78
Table 4.1. Idealized model scenario details.....	112
Table B.1. Comparison of model tidal amplitudes and phases with observations during Cyclone Sidr.	186
Table B.2. Model residual water level comparison with observations: Cyclone Sidr	186
Table B.3. Significant wave heights at different stations for the 'Only Wave' and 'WCI' scenarios.....	191
Table C.1. Flooded area in the GBMD for different mean sea level rise scenarios	192

List of Abbreviations

BoB – Bay of Bengal

BWDB – Bangladesh Water Development Board

GBMD – Ganges-Brahmaputra-Meghna-Delta

SWH – Significant wave height

WCI – Wave-current interaction

Chapter 1 Introduction

1.1 Background

The estuarine circulation is a combined effect of the tide, wave, wind, and river discharge. Several non-linear processes, including tide-surge interaction and wave-current interaction, modulate water elevation in shallow and deep ocean regions (Yu et al., 2017). Tides play an important role in varying water levels in the shallow ocean, including the upper reaches of estuaries. The non-linear and non-stationary tides from the balance of bottom friction, channel geometry, and river flow make studying tides challenging in the upper estuary (Savenije et al., 2008; Cai et al., 2014; Guo et al., 2015; Cai et al., 2019). Tidal excursion in the estuary is strongly influenced by river discharge, which dampens the tides and transform energy to overtides from the principal tides due to bottom stress. There are seasonal and annual variations in the tidal ranges with river discharge across the globe. Numerous studies (e.g., Mahakam river, Indonesia by Sassi and Hoitink (2013); St. Lawrence estuary, Canada by Matte et al. (2019); Modaomen estuary by Yang et al. (2020)) have been conducted on focusing the influence of varying river discharges on tides. Several studies (e.g., Cai et al., 2019, Guo et al., 2021) suggest that further rise of river discharge beyond a threshold river discharge decreases the tidal damping in the upper Yangtze River. Therefore, river tide properties differ with substantial river discharge variations in tropical monsoon estuaries. However, the processes causing river tides to vary with river discharge are still poorly understood. In particular, the tide-surge interaction, a non-linear interaction, is a well-known factor that reduces the accuracy of model water level variations in numerical models under extreme weather conditions, which limits understanding (Yu et al., 2017).

Several studies (e.g., Brown et al., 2013, Feng et al., 2016) suggest that the discrepancies in water level variations between models and observations result from the influence of waves. Wind waves can indirectly affect the estuarine circulation by modulating sea surface stress and bed friction coefficient (Smith et al., 1992; Janssen, 1992; Mastenbroek et al., 1993; Moon, 2005). Wave heights vary with water levels and currents through distinct physical processes such as refraction, bottom friction, and blocking (Kudryavtsev et al., 1999; Ris et al., 1999; Samiksha et al., 2017). In shallow regions, wave heights are strongly modulated by time-varying water depth (e.g., Pleskachevsky et al., 2009; Bolaños et al., 2014). Furthermore, ocean currents accelerate or decelerate the energy transfer from surface winds to surface waves outside the estuary depending on the current and wave orientations (Gonazález, 1984; Wolf and Prandle, 1999; Hopkins et al., 2016; Yu et al., 2017). Wave-current interactions depend on various factors such as continental shelf geometry, bathymetry, coastal morphology, and the path of cyclones (Yu et al., 2017). Therefore, the wave-current interactions play a significant role on wave heights in coastal oceans. During a cyclone, the combination of wind setup, tide-surge interaction, and wave-current interaction results in a cyclone-induced storm surge event. Hence, it is crucial to understand these physical processes and their interactions related to the generation of cyclone-induced storm surge height variations.

The Ganges-Brahmaputra-Meghna delta (GBMD) encompasses the entire Bangladesh coastline and located at the head of the Bay of Bengal (BoB). The Ganges-Brahmaputra-Meghna basin covers 174.5 million hectares across parts of the four Eastern Himalayan countries of Bangladesh, India, Bhutan, Nepal, and the Tibet Autonomous Region of China (Rasul, 2014). This large catchment area produces a significant amount of freshwater runoff annually, which flushes to the BoB through the

GBMD. Three mighty rivers, the Ganges, Brahmaputra, and Meghna rivers, convey 80% of the total freshwater discharge from the upper catchment area to the BoB through the Lower Meghna river. More than 700 rivers, including numerous channels, make Bangladesh one of the world's largest river networks (Banglapedia, 2015). These rivers exhibit significant seasonal and annual variations of river discharge (5,000 to 140,000 m³ s⁻¹). Therefore, hydrodynamic features such as tide propagation and fluvio-tidal flooding also demonstrate temporal and spatial variation across the GBMD with the varying river discharge.

The major rivers in the western part of the GBMD, including the Bishkhali, Baleswar, Buriswar, and Pasur rivers, are tide-dominated rivers, which convey a small amount of freshwater to the ocean during the monsoon season. In the central part of the GBMD, the Lower Meghna river conveys 1.07×10^6 m³ of freshwater annually along with 1500 million tons of sediment, which is the second-largest freshwater discharge behind only the Amazon. The presence of extensive shoals at the Lower Meghna estuary mouth with varying depths up to 5.5 m including the Meghna flats and estuarine islands makes the hydrodynamic properties of the estuary more complex than other estuaries (Snead, 2010). The GBMD is recognized as a prograding subaqueous delta (active delta), which intersects the nearshore 'Swatch of No Ground' canyon system (Wilson and Goodbred Jr, 2015). The 'Swatch of No Ground' canyon is a submerged oceanic canyon with varying depths of 100-1400 m that is located 30 km from the coastline of Bangladesh. The shallow continental shelf and funnel shaped geometry results in amplification of tidal influence further inland.

The complex geographical shape and low elevation of land from mean sea level (MSL) make it difficult to understand the hydrodynamics of the GBMD. The land elevation varies from 1 to 3 m above MSL across the coastal area except for the hilly

regions of the eastern part of Bangladesh (Dasgupta et al., 2010). The world's largest mangrove forest, Sundarban, is located in the western coastal area of Bangladesh. The dense vegetation and numerous small channels and creeks of the mangrove forest slow down the tidal propagation in the landward direction. In the 1960s and 1970s a total 139 earthen embankments (locally called polder, Figure 1.1a) were built in the region to protect low-lying agricultural lands from saline water and tidal floods. As a result, almost half of the Bangladesh coast (1.2 million ha out of 2.8 million) is protected by embankments. These embankments increase the riverbed siltation and results in higher water levels in rivers and channels. Moreover, the earthen embankments in the coastal area results in complex hydrodynamic processes by prolonging the coastal flood inundation in several areas (Auerbach et al., 2015, Adnan et al., 2019). Embankment heights vary from 3 m to 7 m across the GBMD with an average designed height of 4.75 m (Dasgupta et al., 2010). Although the primary purpose of the embankments is to protect the land from tidal flooding, it also reduces the inundation area during cyclonic events (Adnan et al., 2019). According to several studies (e.g., Islam et al., 2013, Feroz Islam et al., 2019), the current embankments can protect the coastal area from cyclone-induced storm surge events with a return period of 5 to 12 years.

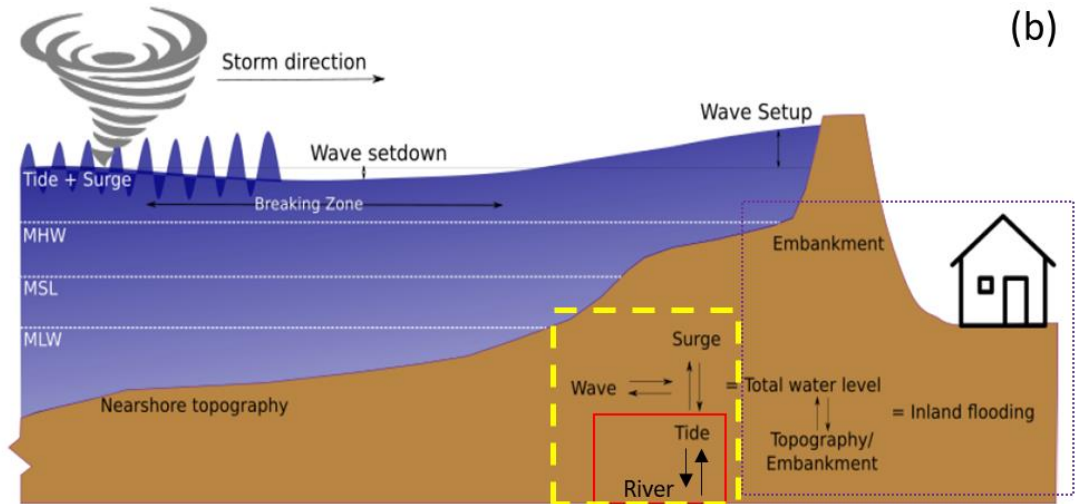


Figure 1.1. (a) A picture of Polder-26 in 2017, Khulna division, Western GBMD, from the Blue Gold Program (<http://www.bluegoldbd.org>) and (b) A schematic diagram of different physical processes in a cyclone-induced storm surge event is reproduced from Khan et al., 2020. The red box denotes the river-tide interaction that is discussed in Chapter 2. The yellow box represents the wave-current interaction that is addressed in Chapter 3. The purple box indicates the inundation during a cyclone-induced storm surge, discussed in Chapter 4.

In the GBMD, tides and river discharge play a vital role in modulating the estuarine circulation and demonstrate the temporal and spatial variation of tidal characteristics across the GBMD. Tides along the GBMD are semidiurnal and average tidal ranges fluctuate between 3 m and 6 m with the maximum tidal range observed just east of the Lower Meghna estuary (Haque and Nicholls, 2018). In addition, the limit of

tidal propagation varies with the river discharge. During low river discharge periods, tides can propagate to the upper part of the GBMD (approximately 150 km from the estuary mouth). The river water salinity shows seasonal variations between 0 to 5 PSU in the lower part of the GBMD during high and low river discharge periods, respectively, (Bricheno and Wolf, 2018) which indicates the strong effect of the river discharge. The influence of the river discharge does vary with less influence in the western and eastern regions of the Bangladesh coast compared with the central region due to the absence of a large river like the Lower Meghna.

The GBMD frequently experiences fluvial floods during the wet season (June-October) as the high volume of water regularly surpasses the water conveyance capacity of the river system. According to the Bangladesh Water Development Board, 60 fluvial flood events occurred in the last 60-year period (1954-2014). Of the 60 events, there were 15 extreme fluvial flood events, which individually flooded more than 24% of the total area of Bangladesh (e.g., 1998). The GBMD is an extremely flood-prone delta because several factors including the seasonal-regional climate and strong monsoon river discharge originating from the Himalayas (Brammer, 1990; Hofer and Messerli, 2006; Brammer, 2014), and heavy local rainfall in monsoon and cyclonic events in the BoB (Haque and Nicholls, 2018). These flooding events can be categorized based on the principal drivers: (i) fluvial flood, (ii) tidal floods, (iii) fluvio-tidal floods, and (iv) storm surge floods (Haque and Nicholls, 2018). Among these floods, the cyclone-induced storm surge floods are well known because of the high level of damage and death toll associated with several cyclonic events, most particularly between 1970-1991 (Alam and Dominey-Howes, 2015; Lumbroso et al., 2017).

Cyclones make landfall on the Bangladesh coast nearly every year, in early summer (April-May) or during the late rainy season (October-November). About 40%

of the impact of total storm surges in the world occurs in Bangladesh making it one of the water bodies in the world that are most prone to cyclone-induced storm surges (Chandrappa et al., 2011). The Bangladesh coast has been exposed to 159 cyclonic events during 1877 – 2009, including 48 severe cyclonic storms, 43 cyclonic storms, and 68 tropical depressions (Dasgupta et al., 2014). Several factors contribute to the high impact of storm surges on the Bangladesh coast including the shallow continental shelf, high tidal range, negligible land elevation above sea-level, coastal protection system, the predominant northward movement of tropical cyclones in the BoB, the triangular shape at the head of the BoB, and high population density (Ali, 1999, Dasgupta et al., 2010). In 2004, UNDP recognized Bangladesh as the most vulnerable country in the world to cyclones (UNDP, 2004). Because the GBMD is one of the most populous deltas globally, with complex hydrodynamic processes, it is essential to study further the impacts of cyclones in the region for the betterment of livelihood and to develop better management plans.

Cyclone-induced storm surge in the Bangladesh coast causes devastation by increasing water levels in rivers and inundation in the coastal area. Although historical records of storm surge heights are limited, published literatures report storm surge heights between 1.5 to 13.6 m during severe cyclones in the region. In 1876, the Great Bakerganj cyclone caused the highest recorded storm surge height of 13.6 m, which made landfall near the Meghna estuary and caused approximately 200,000 fatalities. Approximately half of the casualties were due to the storm surge, and the rest died from the subsequent famine (SMRC, 1998). Another cyclone in 1970, known as the Bhola Cyclone, resulted in 10 m of storm surge height on the Bangladesh coast and caused approximately 500,000 fatalities from the cyclone-induced storm surge inundation.

These examples illustrate the potential extent of devastation due to cyclone-induced storm surge events in the GBMD.

A cyclone-induced storm surge can be more destructive if it makes landfall during high tide aligned with other favourable conditions such as intense wind speed, landfall location at the estuary mouth, and a larger radius of maximum wind (The World Bank, 2010). Furthermore, according to Woodruff et al. (2013), sea-level rise scenarios in the future will increase cyclone-induced flooding. Countries located at lower latitudes including Bangladesh are expected to face adverse impacts due to climate change (Mendelsohn et al., 2006). By applying Regional Climate Model simulations (dynamical models) for current and future climates, several studies reported that the frequency of the highest storm surge will increase in the BoB in the future (e.g., Unnikrishnan et al., 2006, Knutson et al., 2010). This suggests that the Bangladesh coast will be affected more by cyclone-induced storm surge under climate change. Therefore, it further highlights the importance to understand the underlying physical processes that generate cyclone-induced storm surge events in the GBMD.

1.2 Problem statement

Assessing and understanding tides in the upper part of tidal river is a challenging task due to presence of non-linear process such as the balancing relationship between tide and river (Cai et al., 2019). Numerous studies (e.g., Wang et al., 2014, Matte et al., 2017) have been conducted to study the influence of seasonal river discharge on tides in estuaries across the globe. River discharge controls tidal propagation by dissipating tides and energy transformation to overtides from principal tides. Recently, Cai et al. (2019) demonstrate that the tide dissipation in the upper Yangtze river is reduced with the increase of river discharge beyond a threshold value. It indicates the non-linear

interactions between river and tide. River tide characteristics vary estuary to estuary across the globe due to different varying features such as geographical shape and river discharge. Hence, the understanding of river-tide interaction process in an estuarine environment is a challenging task, particularly under strong river discharge. Several numerical studies (e.g., Bricheno et al., 2016, Tazkia et al., 2017) are carried out to study the tides in the GBMD. According to previous studies, the tidal limit is restricted by the river discharge at the confluence of the Ganges and Brahmaputra river. Moreover, Rose and Bhaskaran (2017) reported tidal amplifications in the Meghna estuary compared to the eastern and western GBMD. High river discharge in the Lower Meghna river restricts the tidal propagation limit at the middle of the estuary during the monsoon period, whereas during the dry period, the tides propagate further inland. However, all the previous numerical studies demonstrate discrepancies with the tidal water level observations by the Bangladesh Water Development Board (BWDB), particularly in the upper GBMD likely due to a lack of accurate bathymetry and complex channel network of the estuary in the models (Krien et al., 2016). Since no study has accurately modelled the influence of river discharge on the tide and explained non-linear interactions between river and tides in the GBMD, it is necessary to further study river-tide interactions in the GBMD to better understand water level variations across the GBMD.

As cyclones make landfall in the GBMD, the associated intense wind stress causes high wind setup (wind-driven water level) on the coast and results in cyclone-induced storm surge events. Cyclone-induced storm surge event is associated with different non-linear interactions including surge-tide interaction and wave-current interaction, which dictate the water the water level variations during the storm surge period. Several studies suggest that the coastal ocean current can be affected by the indirect influence of the wind wave through enhanced wind stress (Mastenbroek et al.,

1993) and modified bottom friction (Signell et al., 1990, Davies and Lawrence, 1995). Previous studies (e.g., Samiksha et al., 2017, Prakash and Pant, 2020), which focus on landfalling cyclones on the Indian coast, include the wave effects in the numerical models. These studies demonstrate that a significant portion (up to 20% of the total surge height during cyclone Hudhud) of the storm surge height can result from the wave setup. However, most studies in the GBMD region have ignored the contribution of waves to storm surges in hydrodynamic models, with the notable exception of Deb and Ferreira (2016) and Krien et al. (2017). Although these two studies do include the effect of waves on storm surge, they do not explain the physical processes related to wave-current interactions in the GBMD including different wave dissipations, influence of water depth and current on waves. Thus, the contribution of wave-current interaction to cyclone-induced storm surge heights in the GBMD is yet to be explored.

In this thesis, a 2D hydrodynamic model is developed to study the role of varying river discharge on tides and varying tidal amplitudes across the GBMD (Red box in Figure 1.1b). Stationary and Non-stationary harmonic analyses of model water level along the GBMD are carried out to investigate non-linear interactions between river and tide. Next, a 3D coupled hydrodynamic model is established by considering river, tide, wind, and waves to investigate the role of wave-current interaction in a cyclone-induced storm surge event (Yellow box in Figure 1.1b). Different idealized scenarios by considering different boundary forcings and wave dissipation processes in the model simulation along with cyclonic conditions are investigated to assess the wave setup and wave-current interactions in terms of storm surge height. Finally, the model is applied to study inundation areas during a cyclone-induced storm surge event under different mean sea level rise scenarios (Purple box in Figure 1.1b).

1.3 Objectives/Aims

This thesis aims to understand the physical processes that cause severe cyclone-induced storm surge events in the GBMD.

Specifically, this research will,

- (1) Validate a hydrodynamic model of the GBMD that can reproduce the influence of the temporal and spatial variations of river discharge on the tide and study the river-tide interaction process.
- (2) Establish a 3D wave-current coupled model that includes tide, wind, and wave that can simulate cyclone-induced storm surge events in the GBMD and evaluate the role of wave-current interaction and different wave dissipation processes during storm surge events.
- (3) Assess the variation in inundation area with cyclone-induced storm surge heights under different mean sea level rise scenarios and different cyclonic conditions such as increased maximum wind speed and radius of maximum winds.

1.4 Significance

The influence of varying river discharge on tides, and wave-current interactions on cyclone-induced storm surge height in the GBMD are assessed for the first time. Understanding the influence of river discharge on tides may help in assessing fluvial flooding and tidal propagation along the GBMD. A critical river discharge is identified for the maximal generation of quarterdiurnal tides at the upper part of the GBMD in this

thesis, which can be applied as an indicator for water managers or policymakers to ensure minimum river discharge for restricting the tidal propagation.

The investigation of wave-current interaction during a cyclone-induced storm surge event showed that the storm surge height might increase by 50 % by considering the wave-current interactions. Due to the shallow continental shelf and deep submerged canyon (Swatch of No Ground) near the Bangladesh coast, most previous studies have ignored wave effects by assuming that the wave has negligible influence. In this thesis, the importance of wave effects on cyclone-induced storm surge height is demonstrated and discussed. The effects of future mean sea level conditions and varying cyclonic conditions on inundation patterns in the GBMD are discussed. Understanding these changing conditions into the future in this sensitive region is extremely important to inform policy and to mitigate the risk of increased storm surge. The coastal region is protected from storm surges by an earthen embankment network that was built 50 years ago. Understanding how this embankment affects and moderates the cyclonic storm surge under different realistic future scenarios is crucial for disaster management. The current study will inform the development of a proper disaster management plan for the region. Finally, beyond the specific findings of this thesis, the validated model setup can be used as a tool for investigating risk and hazard related to different flooding conditions in the GBMD.

1.5 Thesis outline

Chapter 1 introduces the background, motivation, aims, and significance of this thesis.

Chapter 2 discusses the hydrodynamic model setup for the GBMD to reproduce varying river discharge influence on tides. The model is applied for three real

hydrological years and twenty idealized scenarios with different boundary forcing. Stationary and non-stationary harmonic analyses are applied to investigate the different tidal components.

Chapter 3 demonstrates the influence of wave-current interactions in cyclone-induced storm surge height in the GBMD. A 3D wave-current coupled model is developed by including tides, winds, and waves. The role of wave-current interactions and different wave dissipation processes are assessed by analyzing twenty-one idealized cases considering different wave dissipation processes and different coupling methods between the hydrodynamic and wave models.

Chapter 4 presents the application of the model in assessing the inundation area variation under different mean sea level rise scenarios and varying cyclonic conditions in the GBMD. Cyclone-induced storm surge height variations and floodplain inundation with mean sea level rise are discussed.

Chapter 5 summarizes the significant findings in this thesis and includes limitations and possibilities for future research in this research area.

The structure and main topics of this thesis are illustrated in Figure 1.2.

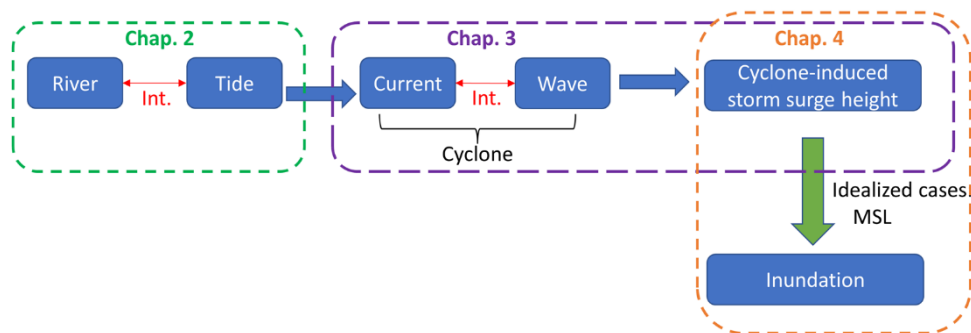


Figure 1.2. The structure and main topics of this thesis. The red two-way arrow represents interaction between two processes. The black bracket denotes cyclonic conditions. The green arrow denotes different idealized cases of mean sea level rise.

Chapter 2 Influence of seasonal river discharge on tidal propagation in the Ganges-Brahmaputra-Meghna Delta, Bangladesh

This chapter has been published as:

Elahi, M. W. E., Jalón-Rojas, I., Wang, X. H., & Ritchie, E. A. (2020). Influence of seasonal river discharge on tidal propagation in the Ganges-Brahmaputra-Meghna Delta, Bangladesh. *Journal of Geophysical Research: Oceans*, 125, e2020JC016417. <https://doi.org/10.1029/2020JC016417>

2.1 Introduction

Knowledge of tidal wave propagation and tidal properties is essential to understand issues such as sediment transport, pollutants dispersion, morphological changes, and nutrient balances in estuarine and deltaic environments (e.g., Dalrymple and Choi, 2007; Ogston et al., 2017). Tides are also an important component in the assessment of flooding and submergence risks in shallow systems. Evaluating and understanding tides in the upper reaches of tidal rivers is particularly challenging, because the balance of bottom friction, channel geometry and river flow results in non-linear and non-stationary tides (Savenije et al., 2008; Cai et al., 2014; Guo et al., 2015; Cai et al., 2019). River flow modulates tidal propagation in the estuary by damping the tidal amplitudes and transforming energy from the principal tides to overtides. For example, the tidal range can be 1.7 and 7.5 times higher during dry periods than wet periods in the upper Yangtze (Guo et al., 2015) and Gironde (Jalón-Rojas et al. 2018)

estuaries, respectively. Influence of seasonal variations of river flow on tides are also found in the Guadalquivir (Wang et al., 2014) and St. Lawrence estuaries (Matte, et al., 2017). Cai et al (2019) shows that the increase of river discharge beyond a critical amount reduces the tidal damping in the upper part of the Yangtze river. River tide properties can thus vary in systems subject to strong fluctuations of river discharge, such as tropical monsoon estuaries. However, river tides in this type of environment are still poorly understood.

The Ganges-Brahmaputra-Meghna Delta (GBMD, Bangladesh) provides an ideal example to investigate river tides dynamics subject to monsoon variability. It contains a large network of rivers, tidal creeks, waterway inlets, which, along with the complex coastline geometry, results in complex hydrodynamic processes. The GBMD is a shallow system, highly susceptible to increased total water level elevations resulting from the combined effects of increased storm surge, wave-induced setup, and astronomical tides that occur during the landfall of severe cyclones (Pethick & Orford, 2013; Tazkia et al. 2017). In recent decades, storm-surges associated with severe cyclones have increased, leading to an increase in the probability of higher and wider spread flooding in the near shore and shallow areas of the GBMD. Importantly, the GBMD also experiences high interannual and seasonal variability of river flow linked with monsoon variability that may affect tidal propagation and properties (Bricheno and Wolf, 2018). Increased understanding of tides in the GBMD delta in connection with river flow is therefore crucial for a proper disaster management plan and maintenance in this complex region.

As with other estuarine systems, previous numerical studies have shown that tidal propagation is controlled by a combination of geometrical shape of channel, bathymetry, bottom friction, and river discharge. Bricheno et al. (2016) showed that tides

cannot travel beyond the confluence of the Ganges and Brahmaputra due to the forcing of river discharge on tide. Rose and Bhaskaran (2017) reported that there is marginal amplification of the diurnal tide and nearly double amplification of the semi-diurnal tides in the Meghna delta compared to the eastern and western coast of the GBMD. All of these previous model studies largely disagree with the tidal range observations by the BWDB, particularly in the upper part of the GBMD due to a lack of accurate bathymetry and complex channel network of the estuary in the models (Krien et al. 2016). Although most of these studies note the importance of river discharge on tide, no study has accurately modelled and evaluated the influence of river discharge on tidal propagation in the GBMD. Furthermore, physical processes controlling the seasonal variability of the M2 (semidiurnal) tide and other main tidal constituents in the GBMD are still poorly understood. Lack of hourly tidal water level stations along the GBMD also explain this research gap and the need to implement numerical studies in the system.

A numerical model setup that reproduces the tidal properties of the GBMD is validated and used to investigate the modulation of tides along the GBMD due to seasonal river discharge variations. Numerical simulations are implemented for real and idealized scenarios of river discharge. The model setup is validated for a combination of three stations located in the exposed coast and six stations along the upper estuary. Stationary and non-stationary harmonic analysis methods are used to evaluate the influence of river discharge on tidal constituents. The structure of the chapter is as follows. Section 2.2 describes the main characteristic of the study site. Water level and river flow observations, the model setup and tidal analysis methods are detailed in Section 2.3. Results and discussion are presented in Section 2.4 including the spatial and temporal variations of tidal constituents for different hydrological years and different discharge scenarios. A summary and conclusions are presented in Section 2.5.

2.2 Study Site

Located in the lower part of Bangladesh, the Ganges-Brahmaputra-Meghna Delta has a 710-km coastline and covers 32% of the country's total geographical area of 147,570 square km (Figure 2.1). Numerous rivers, streams, and canals combine to make up 22% of the GBMD area. With an average annual freshwater discharge of $40,000 \text{ m}^3 \text{ s}^{-1}$, the GBMD is the third largest coastal river system discharge worldwide. These waterways are seasonal and reach their maximum capacity during the monsoon season. The Ganges and Brahmaputra rivers merge with the Meghna river in central Bangladesh, conveying 80% of the total river discharge from the upper catchment area through the GBMD towards the Bay of Bengal (BoB).

The river discharge of these three rivers is subject to high seasonal variability (e.g., BWDB, 2012). The Brahmaputra river discharge starts increasing in the early monsoon period (June–July) and reaches its first peak in the third week of July. It then falls and rises again and attains a second peak in the first week of August. The Ganges river has two peaks: one in the third week of July; and one in the second week of September. The first flood peak in the Upper Meghna typically occurs in the second or third week of May. In general, there is a total annual river discharge inflow into the GBMD from India of $1,110.6 \text{ km}^3$ (FAO, 2016). The high river discharge and its seasonal variations also modulate river salinity in the GBMD. During low river discharge periods, the river water salinity increases up to 5 PSU between 30-40 km from the river mouth whereas the river water salinity is zero at the river mouth during high river discharge periods (Bricheno and Wolf, 2018).

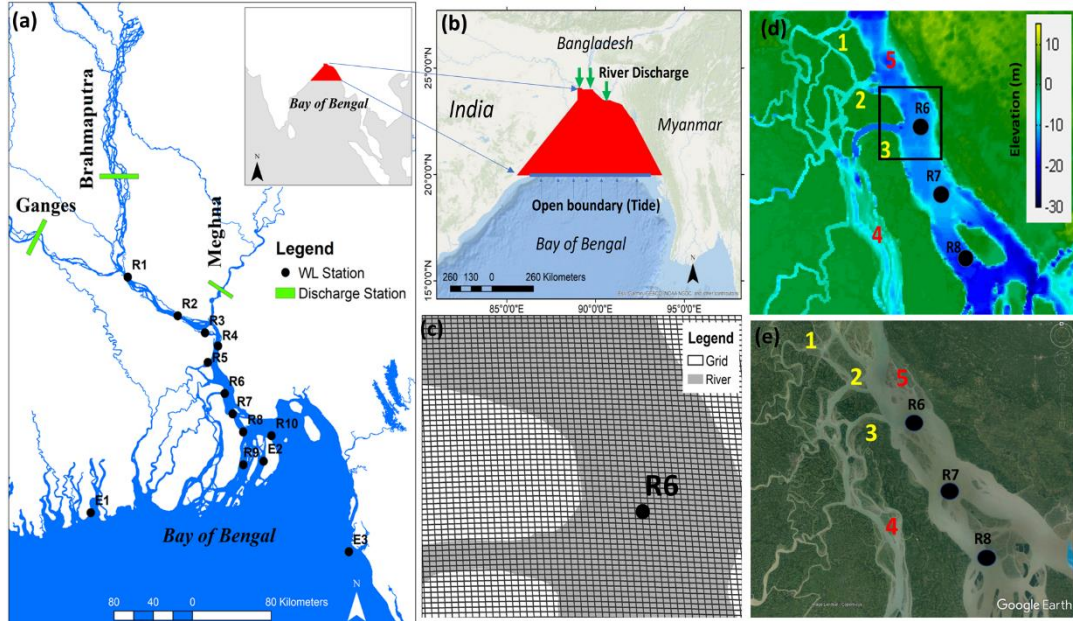


Figure 2.1. (a) Location of the study area. E1-E3 are stations located on the exposed coast and R1-R9 are stations located along the river; (b) Model domain with boundary forcings, (c) A zoomed view of the model grid at R6 within the black square area indicated in Fig. 2.1d, (d) Model bathymetry of the complex channel network in the lower Meghna river. 1-3 (yellow) represent split channels and 4-5 (red) denote examples of shallow land; 0 m denotes mean sea level (e) The complex channel network in the lower Meghna River from the Google Earth.

The Meghna estuary entry into the BoB is divided into a series of extensive shoals including the Meghna flats, mud flats, and estuarine islands (Figure 2.1a, Google, n.d.). The presence of isolated shoals along the GBMD with depths up to 5.5 m makes the hydrodynamic properties of the estuary more complex compared to other estuaries (Snead, 2010). The river morphology of the GBMD is very dynamic as the delta is relatively flat and it is scoured by deep river channels (Bricheno et al., 2016). In particular, the high river flow during the monsoon has a significant influence on the sediment transportation along the GBMD. According to Allison (1998), the cohesive sediments of the GBMD are very mobile, and the position and geometry of the river channels are constantly changing year to year with net gains of 14.8 km² between 1840 and 1972, and of 4.4 km² between 1840 and 1984.

Tides along the GBMD are semi-diurnal. The mean tidal range varies from 3 to 6 m along the Bangladesh coast with the highest tidal range located just east of the Lower

Meghna estuary (Haque and Nicholls, 2018). Coastal flooding from tides is common in the central and western estuaries of the Bangladesh coast. In the 1960s, 123 polders were constructed by the Coastal Embank Project in the southwest coastal region of Bangladesh to protect agricultural land from tidal flooding. This reduced the tidal floodplain area resulting in increased water levels from silted riverbeds and amplified the influence of the tides. The tidal ranges vary from 2-4 m along the GBMD and funnel-shaped estuaries cause local tidal amplification up to 100 km inland of the delta (Rogers and Goodbred 2014).

2.3 Data and Methods

2.3.1 In situ observations of water level and river discharge

This work is based on three sets of data:

- i) Hourly water level data at three stations located on the exposed coast (Figure 2.1a, E1-E3): Hironpoint (E1, 1977-2003), Charchanga (E2, 1980-2000), and Cox's bazar (E3, 1983-2006). These data were provided by the Bangladesh Inland Water Transport Authority (BIWTA).
- ii) Water level data at ten stations along the GBMD (Figure 2.1a, R1-R10). Baruria-transit (R1) and Mawa station (R2) record daily mean water level measurement. The rest of the stations record daily maximum and minimum water level measurement. Data are available from 1983 to 2012. The specific years of data availability are different for each station. These data were supplied by the BWDB.
- iii) Daily river discharge at three stations (Figure 2.1a): Hardinge Bridge (in Brahmaputra river); Bahadurabad (in Ganges river); and Bhairab Bazar (Meghna river).

Discharge data are available from 1996 to 2012. The data contain discontinuities that vary for each station. Records were provided by the BWDB authority.

2.3.2 Numerical model setup

The two-dimensional Delft-3D-Flow numerical model (Delft3D 3.28.50.01) is used to simulate the water level and current velocity in the GBMD. This model calculates non-steady flow and transport phenomena. The Flow module solves the Reynold's equations for an incompressible fluid under shallow water and Boussinesq assumptions. The set of partial differential equations, initial and boundary conditions are solved on a finite difference grid. Detail of the equations and numerical aspects can be found in the Delft 3D flow user manual (Deltares, 2014). The model is applied with a single-layer sigma-coordinate system in vertical and a curvilinear grid for spatial discretization in horizontal. Due to the funnel shape of the Bay of Bengal coastline, the outer boundary of the grid is funnel shaped with varying grid resolution (Figure 2.1b). The grid resolution varies from 1320 m x 956 m in the ocean to 300 m x 200 m in rivers. Figure 2.1c shows a zoom view of the grid resolution at R6 and demonstrates that the grid resolution can accurately represent the complex channel bathymetry of the GBMD. Time series of observed river discharge (Section 2.3.1) are specified as the upstream boundary conditions. Astronomical constituents (including M2, S2, N2, K2, K1, O1, P1, Q1, MF, MM, M4, MS4 and MN4) for the water level at downstream locations (Figure 2.1b) are generated by applying Delft Dashboard, which uses the TPXO 7.2 Global Inverse Tide Model (Egbert and Erofeeva, 2002).

The bathymetry of the rivers and estuaries is specified by using measured cross sections collected during year 2007 to 2014 within the ESPA-delta project of the Bangladesh University of Engineering and Technology (BUET). The inland ground elevation data were collected by the Centre for Environmental and Geographic

Information Services (CEGIS), Bangladesh, which was generated from the FINNMAP (a Finland based private organization) Land Survey 1991, National Digital Elevation Model (DEM) from Floodplain Action Plan-19 (FAP19). The ocean bathymetry is specified using open access data from the General Bathymetric Chart of the Oceans (GEBCO, <http://www.gebco.net/>). The model was calibrated by applying different combinations of Manning's coefficient and then comparing modelled and observed water level at E1, E2, E3 and R3 stations. An increasing roughness parameter from 0.00025 (sea) to 0.05 (upper estuary) provided the best reproduction of observations. A full validation analysis is detailed in Section 2.4.1.

The model is applied to an average flood year and nine idealized scenarios. The average flood year is selected based on BWDB (2012), which categorized historical flood events from 1954 to 2012 according to: wet years (flooded area > 24%); average flood years (flooded area 20-24%); and dry years (flooded area < 20%). The model setup is validated for the average flooding year (2000), which has a large amount of water level data, and then applied to the idealized scenarios covering the typical hydrological conditions of the system, from zero to $125,000 \text{ m}^3 \text{ s}^{-1}$.

2.3.3 Tide analysis method

Water level and current velocities are numerically simulated at R1-R10 (Figure 2.1a) and analysed using four methods: tidal height analysis; stationary harmonic analysis; non-stationary harmonic analysis based on wavelet approach; and computation of the total friction from the subtidal decomposition of current velocities.

2.3.3.1 Tidal height analysis

Water level variations along the Meghna estuary are first plotted together with river discharge to gain insight into the influence of river discharge and tide. The tidal range for each station is calculated as the difference between daily high water and low water level.

2.3.3.2 Stationary harmonic analysis

The stationary harmonic analysis of water level time series at all stations (R1-R10) are performed using T_TIDE (Pawlowicz et al., 2002). This method computes the time average amplitude A and phase Φ of different tidal species. However, T_TIDE cannot provide the time varying amplitude and phase of tidal constituents. Details of the T_TIDE tool can be found in Pawlowicz et al. (2002).

2.3.3.3 Non-stationary harmonic analysis

To assess the seasonal variations of the tidal constituents in the GBMD, a non-stationary harmonic analysis based on the Complex Demodulation method (Bloomfield, 2004) is applied to water level time series. In particular, the temporal variation of the amplitudes and phases of the semidiurnal and quarterdiurnal frequency bands (D2 and D4) are calculated. This method is particularly appropriate to analyse tides in upper estuarine reaches and, unlike other non-stationary tidal analysis methods, it does not require long time series of water level data (Jalón-Rojas et al. 2018). Steps of the complex demodulation method application are briefly discussed in Appendix A.1. Further, detailed information about the method can be also found in Bloomfield (2004) and Jalón-Rojas et al. (2018) .

2.3.3.4 Calculation of the total friction

To investigate the sources of subtidal water level variation, the subtidal friction term is decomposed into contributions from river flow, tidal motion, and interaction between tidal motions and river flow, following Bushman et al. (2009). This method was previously used in several studies (e.g., Guo et al. 2015) to explain the influence of river flow on tidal water level variations. The detected subtidal friction variations are explained based on the total current decomposition by $U = U_0 + U_1 \cos(\omega_1 t + \phi_1) + U_2 \cos(\omega_2 t + \phi_2) + U_4 \cos(\omega_4 t + \phi_4)$ and an approximation of the quadratic friction by $U|U| \approx aU + bU^3$, where U_0 is the non-dimensional residual velocity amplitude, U_1 , U_2 and U_4 are diurnal, semidiurnal and quarterdiurnal nondimensional velocity amplitudes respectively, ω is the angular frequency of the respective tidal component and ϕ_1 , ϕ_2 , ϕ_4 are diurnal, semidiurnal and quarterdiurnal phase lags, respectively and a and b are constants. Velocity components are normalised by dividing by the maximum current velocity. Integration of the friction term over a diurnal tidal cycle leads to three subtidal friction terms (Buschman et al., 2009), as follows:

$$F_r = aU_0 + bU_0^3 \quad (2.1)$$

$$F_{rt} = 1.5bU_0(U_1^2 + U_2^2 + U_4^2) \quad (2.2)$$

$$F_t = 0.75b[U_1^2 U_2 \cos(2\phi_1 - \phi_2) + U_2^2 U_4 \cos(2\phi_2 - \phi_4)] \quad (2.3)$$

$$F_a = F_r + F_t + F_{rt} \quad (2.4)$$

Equations 2.1, 2.2 and 2.3 indicate that the subtidal variations of tidal currents induce variations in the subtidal friction, which result in subtidal water level variations. The values for U_i and ϕ_i are derived from the complex demodulation analysis of the model simulated time series tidal currents. The constants a and b are set to 0.3395 and 0.6791, respectively following Godin (1999).

2.4 Result and Discussion

2.4.1 Model validation

The model setup is validated using an average flood year condition (2000), which has a large amount of water level data available. The modelled water levels and tidal constituents are first compared with the available observations. Figure 2.2a-c shows this comparison for water level at stations E1, E2 and E3. Table 2.1 shows the statistical agreement between the modelled and the observed water level for stations recording continuous water levels (E1-E3). In addition, the stationary harmonic analysis is applied to observed and modelled water level at these stations and the tidal constituents are compared (

Table 2.2).

There is a reasonably good agreement between modelled and observed water levels with correlation coefficient values (R^2) above 0.91 at all three stations (Table 2.1). The highest Mean Squared Error (MSE) occurs at E2 (0.40 m^2), with lower MSE values calculated at E1 (0.22 m^2) and E2 (0.27 m^2). The mean absolute percentage errors (MAPE) are below 25 % at all stations except at E2 (42.75 %). The error values at E2 are likely higher because the model water level is slightly underestimated during the

monsoon period, which might be attributed to less accurate bathymetry in that location. Moreover, the model water level may miss seasonal variations from offshore due to only astronomical tides forcing in the open boundary. It may contribute further error in model result. Figure 2.2a-b shows that the observed water levels gradually increase in May and decrease in November 2000 at the E1 and E2. E2 is located in shallow water between two islands where the river morphology changes rapidly (Figure 2.1a). The comparison of tidal constituents also shows that the model has successfully simulated the tidal forcing (

Table 2.2). This comparison is particularly good at E1 and E3 with very good agreement between model and observed amplitudes of different tidal constituents. Absolute errors (define as the absolute difference between the observed and model data) for the M2 tide are 0.05, 0.08 and 0.02 m at E1, E2 and E3, respectively. The absolute errors for the phase of different tidal constituents also exhibit good agreement. For example, the absolute errors for the M2 tide phases are 14.79, 24.17 and 3.66 degrees at E1, E2 and E3, respectively. The amplitude and phase of the MSF tide (Lunisolar synodic fortnightly constituent, a compound tide with period 355.2 hours) has lower agreement compared to other tidal components at all the three stations (

Table 2.2). Compound tides like the MSF tide are generated from the interaction between principal tides and residual flow velocity. The lower agreement of the MSF tide may be related to the discrepancy between the real and modelled bathymetry, and model residual flow velocity. However, other principal tides demonstrate good agreement with the observed data.

Only daily maximum and minimum water level data are available along Meghna River from R1 to R10, so it is not possible to compare observed and modelled tidal constituents at these stations. However, the modelled and observed tidal ranges are compared from R1 to R10 along the GBMD to validate the model setup (Table 2.3, Figure 2.2d for R3). Most of the stations show overall good agreement with the observed tidal ranges, which provides confidence to apply the model for further analysis (Mean $R^2 > 0.50$ for R3, R6, E1, E2, and E3). However, the mean R^2 is lower at R4, R5, and R8 (0.18, 0.21 and 0.13, respectively). Previous numerical hydrodynamic studies in the GBMD (e.g., Bricheno et al., 2016, Tazkia et al. 2017) also found a lower agreement in the tidal range at these stations. For example, Bricheno et al. (2016) underpredicted tidal range by 1.63 m at R8 (observed and model tidal ranges are 2.63 and 1 m, respectively). These previous studies neglected the varying embankment height on the coast, several channel networks, and the complex bathymetry, and mentioned the importance of using

accurate bathymetry for better model results. In the current study, complex bathymetry (e.g., channel 1, 2 and 3 in Figure 2.1d) has been incorporated. The spatial embankment heights are also considered during bathymetry preparation in the coast based on the BWDB embankment heights. These set-up efforts, together with a new calibration of the roughness coefficient (Section 2.3.2) have improved the prediction of tidal range compared with previous studies (e.g., tidal range of 1.42 m at R8). However, due to a lack of field measurements, it was not possible to include all these channels and shallow lands located in the rivers (e.g., locations 4 and 5 in Figure 2.1e). The presence of such shallow islands may result in a lower agreement with the observed tidal range at some stations. In summary, the lower agreement with the observed tidal range is probably due to the morphological characteristics of the GBMD, which are very dynamic and result in a rapid change of bathymetry in the mouth of the estuary and shallow islands located in the middle of the channels. However, the model is still capable of reproducing reasonable hydrodynamics in most of stations along the delta.

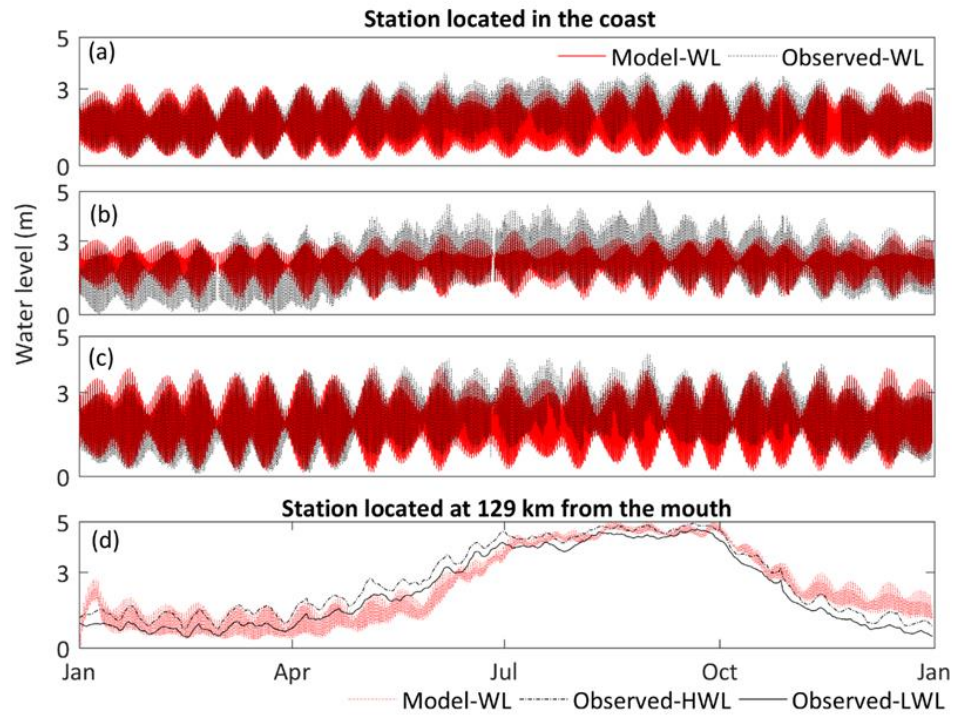


Figure 2.2. A comparison of simulated water levels with observations for the average flood conditions (2000) at: (a) E1; (b) E2; (c) E3; and (d) R3. HWL and LWL denote daily high-water and low-water levels, respectively.

Table 2.1. Statistical analysis of model water level compared with observations for 2000.

Statistical analysis	E1	E2	E3
MSE: Mean Squared Error (m ²)	0.22	0.40	0.27
PSNR: Peak signal-to-noise ratio	54.80	52.10	53.89
R ² :	0.95	0.92	0.94
RMSE: Root-mean-square error (m)	0.46	0.63	0.52
NRMSE: Normalized root-mean-square error	0.12	0.13	0.12
MAPE: Mean Absolute Percentage Error (%)	21.31	42.75	24.80

Table 2.2. Comparison of model tidal amplitude and phase with observations: 2000

Hironpoint (E1)			Charchanga (E2)			Coxsbazar (E3)			
Amplitudes of tidal constituents (m)									
Tide	Model	Observed	Abs Error	Model	Observed	Abs Error	Model	Observed	Abs Error
K1	0.12	0.14	0.03	0.26	0.12	0.14	0.19	0.08	0.11
M2	0.87	0.82	0.05	0.86	0.94	0.08	0.95	0.94	0.02
M4	0.07	0.03	0.03	0.28	0.11	0.17	0.10	0.07	0.04
MSF	0.04	0.02	0.01	0.02	0.12	0.10	0.01	0.11	0.10
N2	0.17	0.16	0.00	0.18	0.18	0.00	0.20	0.17	0.02
O1	0.05	0.05	0.00	0.11	0.08	0.03	0.08	0.08	0.00
S2	0.38	0.35	0.03	0.37	0.32	0.05	0.45	0.38	0.07
Phases of tidal constituents (deg)									
Tide	Model	Observed	Abs Error	Model	Observed	Abs Error	Model	Observed	Abs Error
K1	260.54	269.08	8.54	285.58	278.15	7.43	248.92	282.26	33.34
M2	113.09	127.88	14.79	229.98	205.81	24.17	117.70	121.36	3.66
M4	156.19	142.28	13.91	242.36	288.52	46.16	318.04	163.16	154.88
MSF	40.08	191.33	151.25	219.49	27.72	191.77	216.48	41.10	175.38
N2	108.96	126.43	17.47	211.65	194.34	17.31	109.68	93.05	16.63
O1	254.51	260.55	6.04	264.95	278.00	13.05	234.52	220.47	14.05
S2	147.77	157.54	9.77	249.72	221.39	28.33	145.39	175.02	29.63

Table 2.3. Mean R² values of model tidal range for 2000.

Station name	Notation/ Dist. (km)	Mean R ² value	Station name	Notation/ Dist. (km)	Mean R ² value
Baruria Transit	R1 (205)	No data	Tajumuddin	R8 (32)	0.13
Mawa	R2 (152)	No data	Meghna mouth	R9 (0)	No data
Sureswar	R3 (129)	0.56	Hatiya	R10	0.49
Chandpur	R4 (115)	0.18	Hironpoint	E1	0.90
Nilkamal	R5 (102)	0.21	Charchanga	E2	0.70
Charramdaspur	R6 (69)	0.50	Cox's bazar	E3	0.69
Daulatkhan	R7 (49)	No data			

*All the distances are from R9.

2.4.2 Temporal and spatial variation of tides

The model results show that water level varies seasonally with river discharge along the GBMD. In particular, the water level in the upper estuary is significantly higher during the high river discharge period. It can rise from 2 m at low discharge to 10 m at high discharge in R1 (see Figure A.2 in Appendix A.3). The water level variability with the spring-neap tidal cycles is higher at the stations closer to the mouth, whereas the landward stations show minimal variations during both the high and low river discharge. To evaluate the influence of river discharge on tides, water level time series are decomposed in frequency components. First, stationary harmonic analysis is applied to identify the main harmonic components along the tidal river. Semidiurnal (M2, N2), diurnal (O1, K1), quarterdiurnal (M4) and fortnightly (MSF) components are the main tidal harmonics in the GBMD and their variabilities along the tidal river is presented in Appendix A.2. The diurnal to semidiurnal amplitude ratio $(K1+O1)/(M2+S2)$ is 0.57 at the estuary mouth (R9), which denotes a mixed tidal regime. However, this stationary harmonic analysis does not reproduce time-varying properties such as characteristics of tidal-river dynamics, so these results are not discussed further. Instead, the estimated tidal frequencies are used to apply a non-stationary method based on complex demodulation.

The Complex Demodulation method provides a time series of semidiurnal (D2), quarterdiurnal (D4), diurnal (D1) and fortnightly (MSF) components at each station along the GBMD (see methodological details in Section 2.3.3). Figure 2.3 shows the temporal variation of the total tidal range, the amplitudes of the D1, D2 and D4 components, and the river flow for the study year 2000. Trends can be divided into three groups depending on the location of the station along the longitudinal axis of the GBMD:

- In the lower GBMD (R6-R8, first 70 km from the estuary mouth), the tidal range varies between 2.98 m (at R8) to 3.32 m (at R7). There is an increase in the maximum tidal range by 0.24 m at R7. Amplitudes of D2 shows a steadily decreasing trend from R8 to R6. The maximum amplitude of both the D2 and D4 tides occur at R7: 1.13 m and 0.16 m, respectively, during the spring tide. The amplitude of D1 shows slight decreasing trend from R8 to R6. In general, the tidal ranges and amplitudes at R6-R8 (within 50 km of the estuary mouth) exhibit large spring-neap tide variation, but no significant seasonal variation, which suggests that river discharge has marginal influence in the lower estuary.
- In the upper-middle GBMD (R2-R5, approximately 102-152 km upstream from the estuary mouth), the variability in tidal range and amplitude over the spring-neap cycles is lower, but there is a damping of all tidal components during the monsoon season. During the monsoon (June to October), when the river discharges are over $50,000 \text{ m}^3 \text{ s}^{-1}$, tidal range is significantly reduced (by up to 0.5 m) at R2 to R5 (100 km upstream) and then increased again during the post-monsoon period (October to November). In the middle estuary (R5), the lowest values of the tidal range (0.57 m), D1 (0.01 m), D2 (0.19 m) and D4 (0.009 m) are found in early October during the maximum combined river discharge ($> 63,000 \text{ m}^3 \text{ s}^{-1}$). At R5, D4 is higher than for downstream stations during the neap tide during the dry season. (e.g., R5, the thick dashed line in Figure 2.3c). This phenomenon is due to the balancing act of D4 tide generation and dissipation and will be further examined in the next section. During the monsoon period, the D4 tide at R5 is reduced by 0.02 m but is still higher than for downstream stations such as R8 during the neap tide. In the upper estuary (R2), both the D2 and D4

tides are diminished during the monsoon. The maximum tidal range at R2 ranges from 0.44 m to 0.87 m during neap and spring tides, respectively, during the dry season when the river discharge is below $10,000 \text{ m}^3 \text{ s}^{-1}$.

- R1 (205 km from the mouth) is located near the limit of tidal propagation. Maximum and minimum tidal ranges are 0.38 m (in the dry season) and 0 m (in the monsoon season) for the average flooding year. The amplitudes of the D2 and D4 tides vary between 0 and 0.05 m and between 0 and 0.01 m, respectively. Similarly, D1 tides varies between 0 to 0.03 m during the monsoon to dry season. The seasonal variability of tidal amplitudes is therefore low.

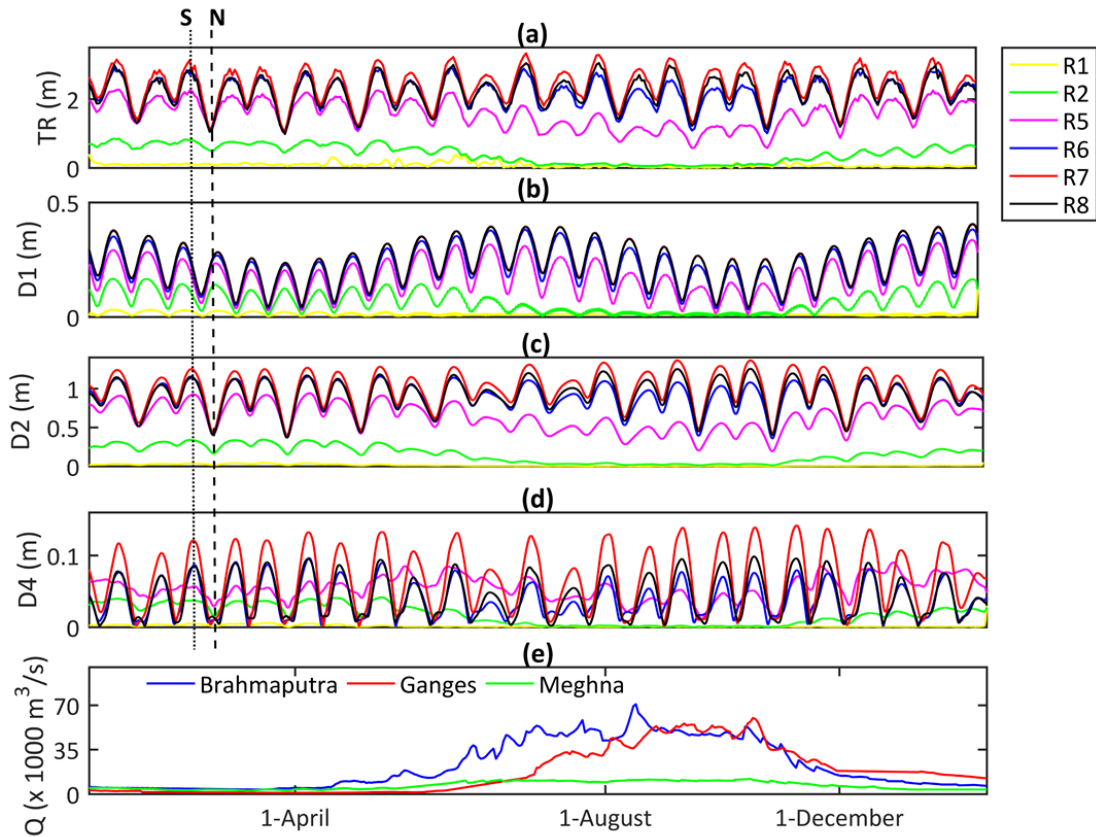


Figure 2.3. Tidal and river discharge conditions for the average flood conditions (2000): (a) The model tidal range; (b) D1 amplitude; (c) D2 amplitude; (d) D4 amplitude; and (e) observed river discharge. Dotted and thick dashed lines denote typical spring and neap tide, respectively.

From Figure 2.3, it is evident that the stations beyond R5 exhibit substantial variations of tides with the river discharge. During the high river discharge period (July-October), both D2 and D4 tides are reduced in both spring and neap tides. For further understanding of the influence of river discharge on the D1, D2, D4 and MSF tides, four stations are plotted as a function of the combined Ganges-Brahmaputra-Meghna river discharge and the tidal range at the estuary mouth in Figure 2.4.

Results show that the amplitude of the D1 tide is approximately 0.60 m less than that of the amplitude of the D2 tide at R8, but 0.30 m higher than that of the amplitude of D4. The D1 tide varies with the spring-neap tides, from 0.04 m to 0.39 m at R8 and from 0.01 m to 0.16 m at R2. The D1 tide does not appear to vary with river discharge along the GBMD, but D1 tide variations in the spring-neap tide are slightly influenced by extremely high river discharges (Figure 2.4a-b). At R1, the D1 tide is zero indicating that it is damped by the weakening of the incoming tidal harmonics (Figure 2.4d).

The D2 tide is dominant at R5 and R8 compared to other tides. At R8, the amplitude of the D2 tide is higher during the spring tide compared to the neap tide period (1 m and 0.4 m, respectively, Figure 2.4a). These differences decrease for the upper stations as the impact of the river flow is more important. While the increase of river discharge does not influence the D2 tide variations at R8, it has a high impact on the other three stations. For a mean tidal range at the mouth, D2 decreases from 0.94 m to 0.19 m at R5 (Figure 2.4b), and from 0.34 m to 0.01 m at R2 (Figure 2.4c) for discharges of 5,000 and 100,000 $\text{m}^3 \text{s}^{-1}$, respectively. The damping of tides was explained by Godin (1999). This study shows that the tidal components contribute to their self-damping along with the mutual damping at a location where tides and river discharge show a strong influence on the water level. The self-damping arises from the velocity component that produces from the tidal harmonic, and the mutual damping is generated

from the velocity components from the river discharge and other tidal harmonics. At R5, both the river discharge and spring-neap tide modulate the D2 tide, and it is therefore influenced by both self-damping and mutual damping. Beyond R5, the spring-neap tides show lower water level variation compared to the river discharge. At R2, D2 is less than 0.5 m even with low river discharge ($5,000 \text{ m}^3 \text{ s}^{-1}$) and is wholly damped for discharges higher than $60,000 \text{ m}^3 \text{ s}^{-1}$ (Figure 2.4c). D2 is completely damped at R1 for all volumes of river discharge (Figure 2.4d).

The D4 tide varies from 0.02 m to 0.16 m with the spring-neap tides at the estuary mouth (R8, Figure 2.4a). The increase of the river discharge significantly influences the D4 tide upstream starting from R5, while there is a lower variability with the spring-neap cycle. At R5, the increase of the river discharge up to approximately $30,000 \text{ m}^3 \text{ s}^{-1}$ increases the D4 tide amplitude to a maximum 0.08 m (Figure 2.4b). Further increase of river discharge ($>30,000 \text{ m}^3 \text{ s}^{-1}$) reduces the D4 tide. A maximum analogue value for the D4 tide is also found at R2 for a river discharge of $10,000 \text{ m}^3 \text{ s}^{-1}$ (Figure 2.4c). This demonstrates the balancing act of generation and dissipation of the D4 tide that occurs with river discharge in a tidal estuary. According to Godin and Martinez (1994), the D4 tide is generated by friction, but also depends on the amplitude of the D2 tide. Higher levels of river discharge results in energy transfer from the D2 to D4 tide and enhances the friction. Up to river discharge amounts of $30,000 \text{ m}^3 \text{ s}^{-1}$, the river-tide interaction may play an active role in the generation of the D4 tide at R5. Further increase of the river discharge makes the river discharge dominant over tides. Therefore, the increase in river discharge beyond an optimum volume dissipates the D4 tide rather than enhancing the generation of the D4 tide. The river-tide interaction mechanism in the generation and dissipation of the D4 tide will be discussed further in the next section.

The MSF tide dominates over the D2 tide at R2 (Figure 2.4c). All the tides are nearly zero (< 0.10 m) at R2 when the total river discharge is above $40,000 \text{ m}^3 \text{ s}^{-1}$ except the MSF tide. The results show that for increasing river discharge, the MSF tide increases with distance from the estuary mouth. According to Godin (1999), as the MSF tide is generated from the friction between double tidal harmonics and a net outflow of river discharge (which is the residual velocity), MSF cannot exist without the presence of the residual velocity component. The increase of river discharge increases the residual velocity component in the up-river direction. Moreover, MSF tide is not affected by self-damping due to the lower velocity produced from the MSF tide. Therefore, the MSF tide increases with increasing river discharge.

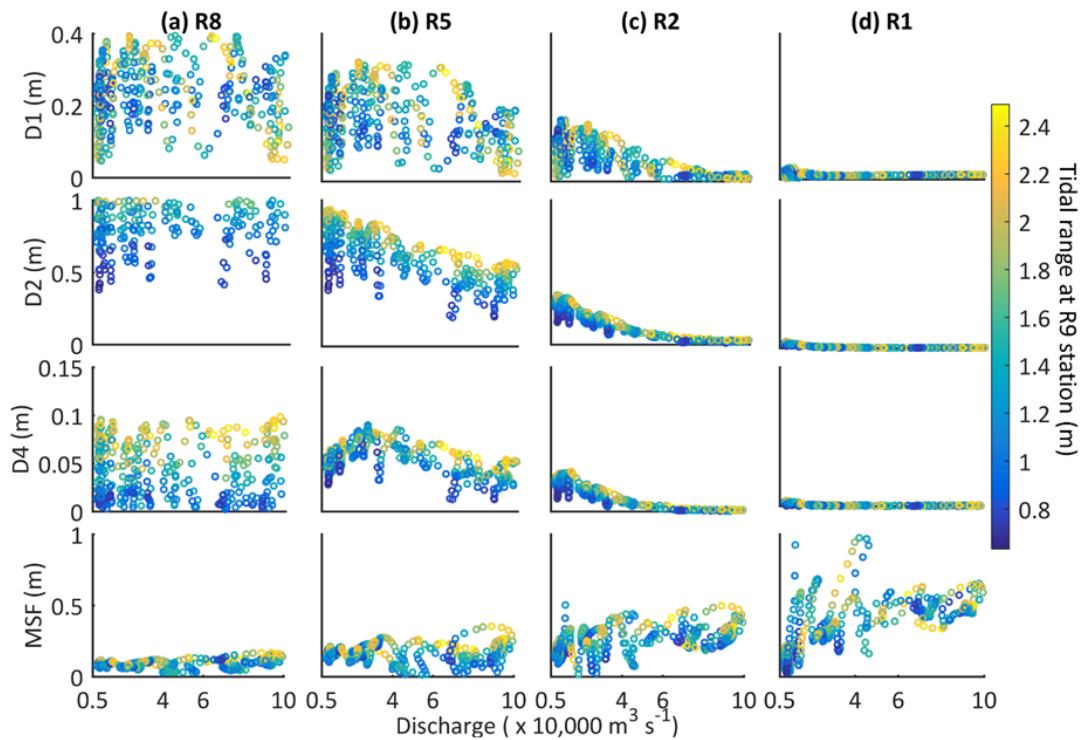


Figure 2.4. Tidal constituents (D1, D2, D4 and MSF) as a function of river discharge and tidal range at the estuary mouth (color bar) at: (a) R8; (b) R5; (c) R2; and (d) R1. Note that the Y-axis ranges have different scales.

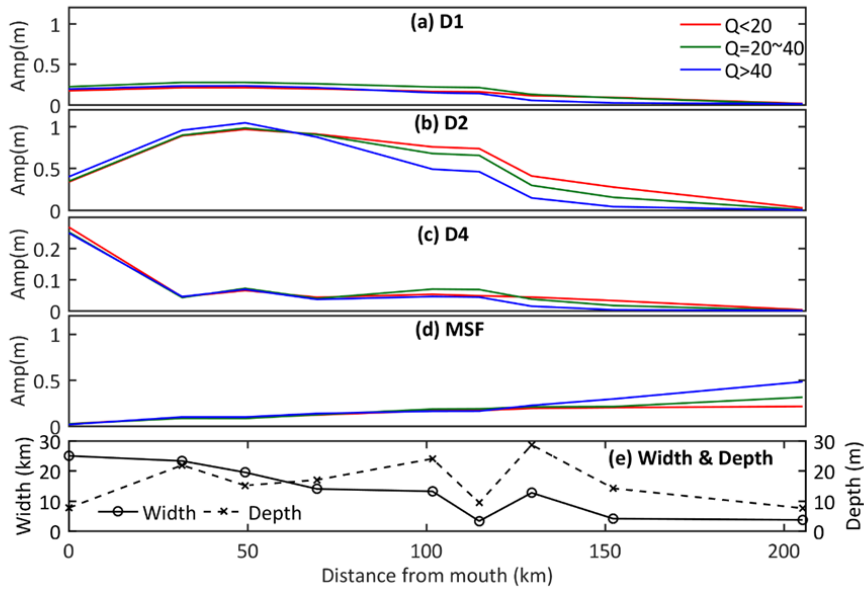


Figure 2.5. Spatial variations of tidal amplitudes: (a) D1; (b) D2; (c) D4; (d) MSF during different river discharge periods; and (e) Width and depth of the river along the GBMD. Q is the river discharge ($\times 1000 \text{ m}^3 \text{ s}^{-1}$). Amplitudes are averaged over the same river discharge period.

The spatial variations of averaged tidal amplitudes for different river discharge periods are illustrated in Figure 2.5. All the tidal components are completely diminished except the MSF tide by 205 km upstream of the estuary mouth regardless of the level of river discharge. The D1 tide shows little spatial variability with the river discharge periods along the GBMD (Figure 2.5a). The D4 tide exhibits maximum amplitude in the lower GBMD for all the river discharges, middle of the GBMD during average river discharge (green), and further upstream during low river discharge periods.

D2 tide exhibits more spatial variability, because of channel geometry (e.g., Bricheno et al., 2016). The Meghna estuary mouth is approximately 25 km wide decreasing to 18 km in the middle of the estuary (50 km upstream, Figure 2.5d). The depth of the Meghna river varies rapidly from approximately 3 m to 30 m between the estuary mouth and R8. The complex geomorphology including shallow shores and islands (e.g., Figure 2.1b) in the estuary along with the narrowing channel upstream

results in amplification of the amplitude of the D2 tide approximately 50 km upstream of the estuary mouth. A slight rise (< 0.1 m) in the D2 tide occurs during the high river discharge period compared to the low river discharge period at the locations close to the estuary mouth (e.g., at 50 km, Figure 2.5b). Although river discharge shows minimal influence on tides at the mouth, it increases water depth at the estuary mouth. Therefore, the incoming tidal energy flux increases at the seaward stations and results in a slight rise of the D2 tidal amplitudes (e.g., Figure 2.7c). Further upstream, the amplitude of the D2 tide decreases regardless of the volume of river discharge. The decrease in D2 amplitude occurs most rapidly about 120 km upstream of the estuary mouth and during high river discharge, the D2 tide is completely damped by about 150 km upstream of the estuary mouth demonstrating the strong D2 tidal dissipation due to river discharge along the GBMD.

The MSF tide demonstrates little variation with river discharge up to 130 km from the estuary mouth. In the upper part of the GBMD, the MSF tide amplitudes are overall higher than the D2 tide and exhibits higher amplitude for higher river discharge. The damping of tidal harmonics is proportionally dependent on tidal frequency and the current produced by river discharge (LeBlond, 1978, Godin, 1999). The MSF tide period (355.2 hours), which is significantly higher than the D1 (24.8 hours), D2 (12.4 hours) and D4 (6.2 hours) tides, is damped less due to its low frequency. A similar increasing trend in the MSF tide is also found in the upper part of the Yangtze and Amazon estuary by Guo et al. (2015) and Gallo and Vinzon (2005), respectively. In Yangtze estuary, the MSF tide increased from 0.02 m to 0.2 m at 220 km from the estuary mouth. The MSF tide amplified to 0.18 m at 600 km in Amazon estuary. Gallo and Vinzon (2005) also show that the influence of river discharge resulted in higher MSF tide in the upper estuary and explained as the upstream propagation of long waves.

2.4.3. River-tide interaction in the upper GBMD

To further evaluate the influence of river discharge on tides, the effect of the residual slope generated from nonlinear friction on the propagation and damping of tides is analyzed, which can be significant in the presence of river discharge (Cai et al., 2014). River discharge affects tidal damping, mainly via a frictional term, and attenuates tidal motion by increasing the quadratic velocity in the numerator, while reducing the effective friction by increasing water depth in the denominator of the momentum equation (Cai et al., 2019). Based on the model tidal amplitudes (η) and residual water level (Z), tidal damping rate (δ) and residual water level slope (S) are estimated over a reach of length by the following equations:

$$\delta = \frac{\eta_2 - \eta_1}{\Delta x} \quad (2.5)$$

$$S = \frac{Z_2 - Z_1}{\Delta x} \quad (2.6)$$

where, η_1 and Z_1 are the tidal amplitude and residual water level on the seaward side, respectively, and η_2 and Z_2 are the corresponding values at a distance of Δx upstream, respectively. Figure 2.6 shows the tidal damping rate and residual water level slope as a function of river discharge and the tidal range at the mouth for the year 2000. Positive tidal damping rate denotes the amplification of tidal amplitudes, so this parameter is referred to as tidal amplification rate. As the D2 tide is dominant over other tides, the tidal damping/amplification rate is calculated based on the D2 tide. Figure 2.6a-b illustrates that river discharge has a marginal influence on tidal damping at the lower study area (e.g., R7-R8, R8-R9), whereas both the tidal damping rate and residual water slope increases with the river discharge beyond the middle of the channel (from R5). The tidal damping rate shows a decreasing trend in the upper study area with the increase of river discharge due to the high dissipation of tide at those stations. For example, the

tidal damping rate is nearly zero at R1-R2 during high river discharge because that tide is almost diminished at the seaward station R2. Residual water level slopes show different trends with river discharge beyond the middle of the channel (Figure 2.6b). High river discharges result in nearly constant residual water level slopes at R1-R2 and R2-R3 from the combined effect of the channel storage capacity limit and the full dissipation of tides. For example, above $40,000 \text{ m}^3 \text{ s}^{-1}$ of river discharge, the channel storage capacity at R1-R2 is over the maximum limit. Therefore, further increase of river discharge only causes increased inundation in the floodplain area rather than an increase of total friction (see Figure 2.9a and b) and thus residual water level slope. However, the residual water level slope at R5-R6 shows a different trend compared with R1-R2 and R2-R3 due to the presence of stronger tides during high river discharge. High river discharges cannot fully diminish the tides at R5-R6 (Figure 2.3c). This result corroborates the influence of river discharge on tide dissipation beyond the middle of the study area. Figure 2.6c shows a higher amplification of tidal amplitudes in the lower estuary (R7-R8 and R8-R9), particularly during spring tides. This amplification is a result of the shoaling effect due to channel convergence between R9 and R7. The damping rate at R5-R6 increases with the tidal range at the mouth due to a combined influence of river discharge and self-damping of the D2 tide. The higher damping is caused by the self-damping (produced from the tidal harmonic) and mutual damping (generated from the influence of river and other tidal harmonics) (Godin, 1999). Moreover, the residual water slope variations do not show any specific trend with the tidal ranges since they are driven by subtidal friction. At the mouth, the residual water slope is nearly constant due to the dominant influence of subtidal friction related to tide and river-tide interaction (Figure 2.9c-d). The role of frictions on the tide modulation is discussed later in this section.

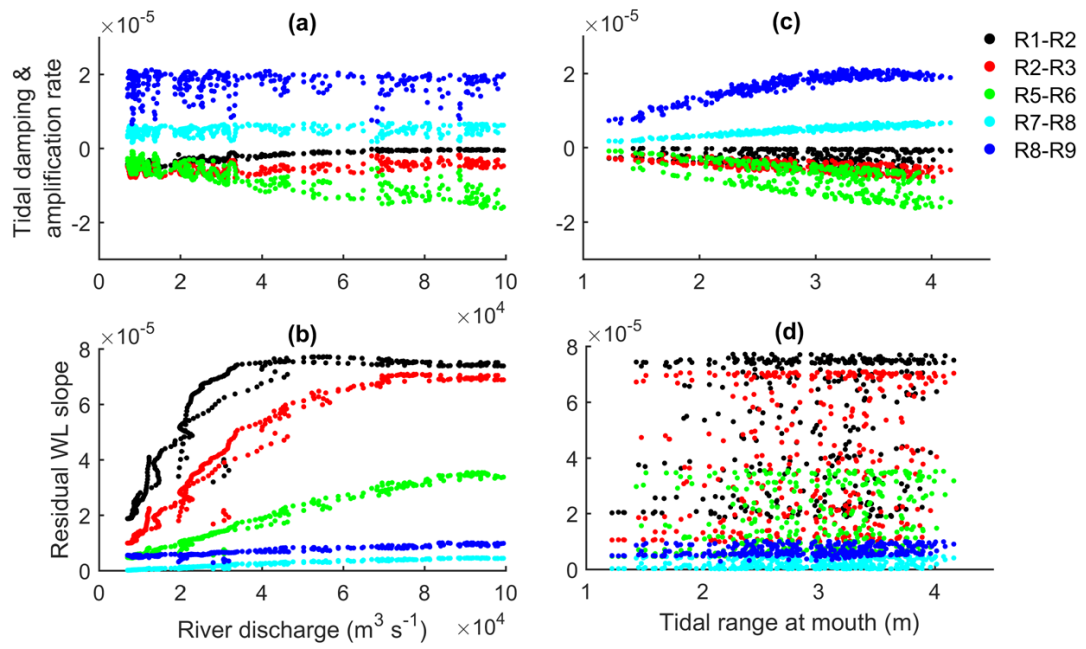


Figure 2.6. Tidal damping rate and residual water level slope variations with the river discharge (a, b) and tidal range at mouth (c, d) for the study year.

To further assess the influence of the river discharge on tides in the GBMD, nine idealized river discharge scenarios are examined. The simulations are run for 31 days and include the spring-neap tide of March 2000. The first and last four days of the simulation are ignored to avoid any error produced by applying the low-pass filter at the boundaries of time series in the complex demodulation method (see formulation in Appendix A.1). Hereafter, the river discharge scenarios are denoted as Q00 (no river discharge), Q05 ($5,000 \text{ m}^3 \text{ s}^{-1}$, multiplying the number by $1,000 \text{ m}^3 \text{ s}^{-1}$ represents river discharge amount), Q10, Q20, Q40, Q60, Q80, Q100 and Q125 ($125,000 \text{ m}^3 \text{ s}^{-1}$). From the observed river discharge in the average flooding year (2000), the Ganges, Brahmaputra, and Meghna rivers are calculated to contribute 32%, 51%, and 17% of the total river discharge, respectively. Therefore, the total river discharge is distributed among the three rivers following these percentages for each idealized scenario. The tidal

forcings from the average year (March 2000) are used for the downstream boundary condition. The current study focuses on the influence of river discharge on tides, and both D1 and MSF tide shows less variability with river discharges compared to D2 tide (Figure 2.4 and Figure 2.5). Therefore, the analysis on the relationship between tides and river discharge focuses on the D2 and D4 tidal constituents.

Figure 2.7 illustrates spatial and temporal variations of D2 and D4 along the GBMD for the idealized scenarios. For better graphical representation and avoiding overlap, the Q05, Q80 and Q100 discharge scenarios are not presented in Figure 2.7. As expected from the earlier results, the amplitude of D2 reaches a minimum value for the highest river discharge scenario (Q125). The no river discharge scenario results in a maximum amplitude of D2 among all idealized scenarios (Q0 in Figure 2.7a). This suggests an inverse relationship between the amount of river discharge and the amplitude of the D2 tide at R2 (152 km from the estuary mouth).

This inverse relationship is also apparent for D4 with one interesting difference. The zero-river discharge scenario has a D4 component (maximum 0.02 m and minimum 0.01 m) with lower amplitude than for Q10 (maximum 0.04 m and minimum 0.01) and Q20 (maximum 0.04 m and minimum 0.01 m) discharge scenarios (Figure 2.7b). This may result from the influence of the river-tide interaction in the friction term, which will be addressed later in this section. The distribution of maximum D2 and D4 amplitudes (Figure 2.7c-d) indicates that the maximum spatial variations of these amplitudes with river discharge occur between 100 to 150 km inland from the estuary mouth.

The tidal limit varies between 205 to 130 km from the estuary mouth for river discharges from Q00 to Q125, respectively. During the monsoon period in the average flood year ($> 60,000 \text{ m}^3 \text{ s}^{-1}$), tides are diminished at 152 km from the estuary mouth.

Regardless of the river discharge, tides become insignificant ($D2 < 0.15$ m, approximate 10% of the amplitudes at the estuary mouth) beyond 190 km from the estuary mouth compared to the estuary mouth. Though the D2 amplitude exhibits a similar rate of change with river discharge along the estuary, the rate of the change for the D4 amplitude shows a different variation with river discharge beyond 100 km from the estuary mouth (Figure 2.7c-d).

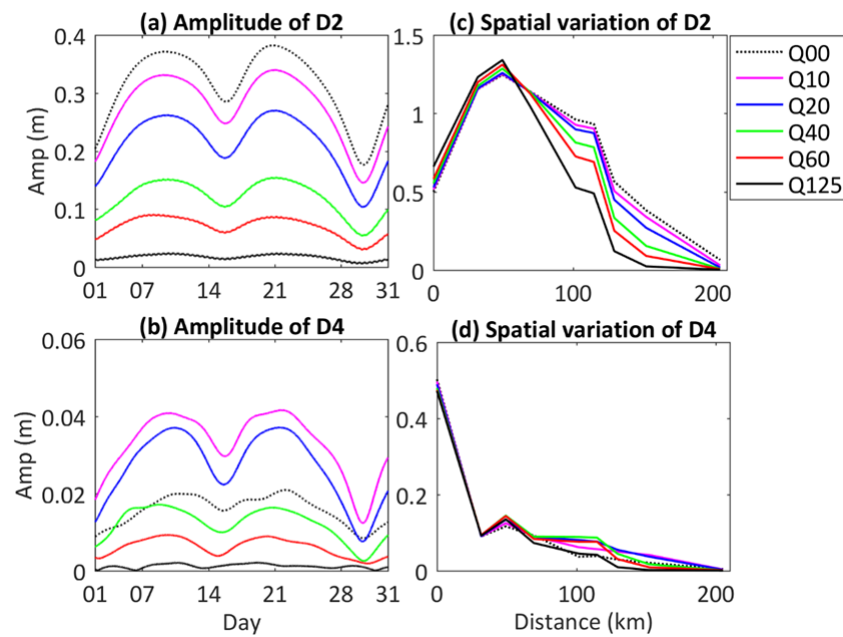


Figure 2.7. Simulated influence on the tide at R2 for a variety of idealized river discharges (Total discharge represented in the legend is in $\times 1000 \text{ m}^3 \text{ s}^{-1}$, e.g., $Q125 = 125,000 \text{ m}^3 \text{ s}^{-1}$): (a) amplitude of the D2; and (b) D4 tide variation with river discharge; spatial variation of the maximum amplitude of: (c) D2; and (d) D4 tide with distance from the estuary mouth.

To identify the mechanism that controls tides in the upper estuary, 10 additional different idealistic scenarios consisting of combinations of river discharge and tidal forcings are simulated (see description in Table 2.4). The simulation period and tide forcing of the idealistic scenarios are kept the same as for the first set of idealized simulations. Figure 2.8 shows the D2 and D4 amplitudes variation at R2 from these simulations. In general, the M2-forced simulations generate both D2 and D4

components, while the corresponding M4-forced simulations generate no D4 component at R2 regardless of the river discharge. This indicates that the D4 component is generated locally from the energy transfer of principal tides (D2 tide) by total friction and non-linear interactions of the tide, including river-tides interactions.

Table 2.4. Idealistic scenarios with different boundary forcing.

Run	River discharge (m ³ /s)	Tide forcing
Q10 M2	10,000	Only M2
Q10 M4	10,000	Only M4
Q10 Tide	10,000	All tidal constituents
Q10 No tide	10,000	No tidal effects
Q00 M2	No discharge	Only M2
Q00 M4	No discharge	Only M4
Q20 M2	20,000	Only M2
Q20 M4	20,000	Only M4
Q40 M2	40,000	Only M2
Q60 M2	60,000	Only M2

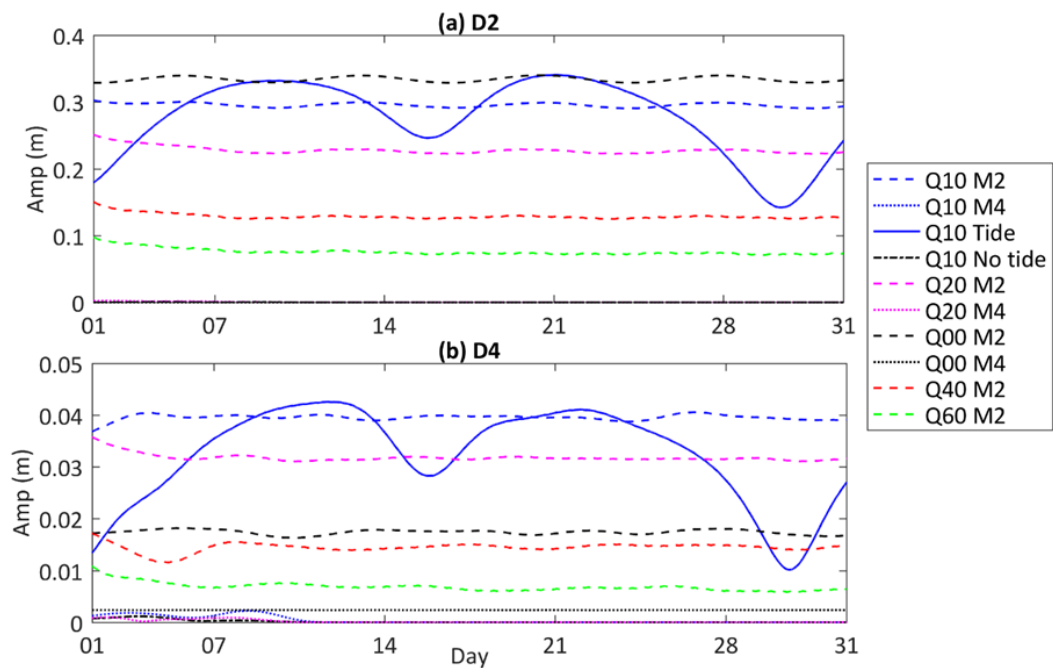


Figure 2.8. Amplitudes of: (a) D2; and (b) D4 tide variations at R2 for different boundary and tidal forcing.

The generation and dissipation of D4 tide are related to its principal companion D2 tide. According to Godin (1999), all tidal components are damped uniformly in the upper regions (where tide is nearing extinction) of a river by the flow velocity due to river discharge. At the same time, frictional nonlinearities also act as a generating mechanism for overtides (e.g., D4), until they reach a point upstream where they are damped more rapidly by friction than they are generated through nonlinear interaction (Matte et al. , 2014). As dissipation of principle tides causes the generation of overtides, the generation of D4 tide has one source: energy transfer from the principal tides to higher frequency tides due to total friction, i.e., dissipation of the D2 tide generates D4 tide. This balancing act between the dissipation and generation of D4 is highlighted in the GBMD.

For a quantitative understanding of the role of friction on tides modulation in the GBMD, the friction term is calculated and decomposed into contributions from river discharge, tide, and river-tide interaction by following Bushman et al. (2009), as shown in Equation 2.1- 2.4. By applying the complex demodulation, U_i and Φ_i are estimated from the modeled river and tidal current components for the different idealized scenarios along the GBMD (Table 2.5). The result of frictional term decomposition along the GBMD (Figure 2.9) shows that the maximum total friction varies 0.2-0.3 N m^{-2} with increasing river discharge between 0-50 km from the estuary mouth. The maximum total friction exhibits significant variation with river discharge beyond 100 km from the mouth. The friction related to tide is higher beyond 100 km from the mouth for low river discharge scenarios compared to high river discharge scenarios. The friction related to river contributes a significant portion of the total friction along the GBMD.

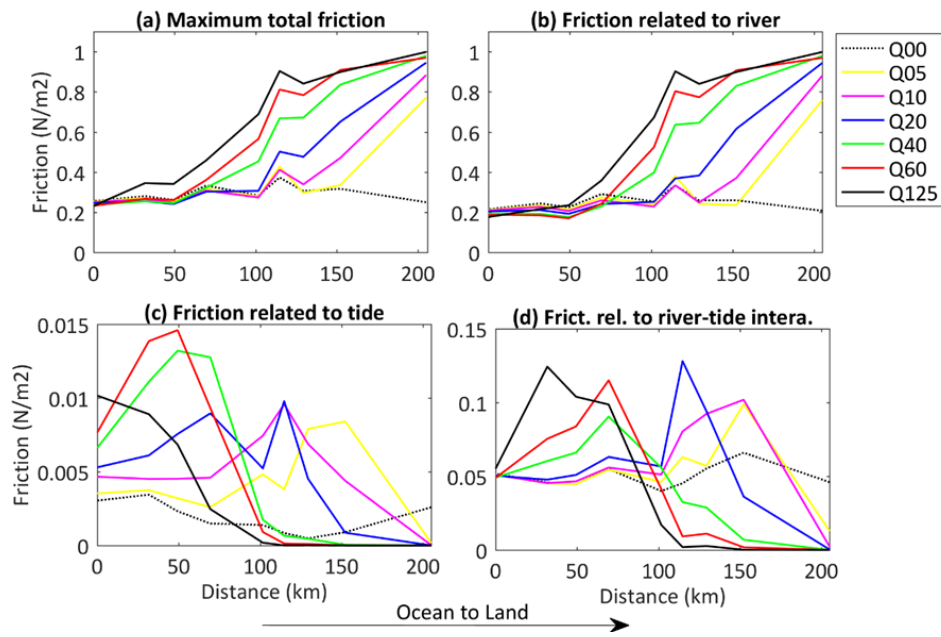


Figure 2.9. (a) Maximum total friction, (b) maximum friction related to river, (c) maximum friction related to tide and (d) maximum friction related to river-tide interaction according to Equation 1-4. U_i and ϕ_i are calculated from the model simulated river and tidal current components for different idealized scenarios along the GBMD. Note that y-axes are on different scales.

As discussed from Figure 2.8, D4 tide is generated locally from energy transfer from the D2 tide through friction. Figure 2.9d shows the variations of friction related to river-tide interaction. Higher river discharges produce lower friction related to river-tide interaction beyond 100 km from the mouth. The residual velocity highly influenced by river discharge reduces the friction related to river-tide interaction beyond this point. The friction related to river-tide interaction varies between 0.05-0.12 N m^{-2} up to 100 km from the mouth. At 152 km (R2), the maximum friction related to river-tide interaction (0.10 N m^{-2}) is found in the Q10 scenario among all the idealized scenarios, whereas the maximum total friction occurs in the Q60 scenario (0.91 N m^{-2}). Figure 2.7d demonstrates that the Q10 scenario generates a higher D4 tide than the Q60 scenario. Therefore, it appears that friction related to river-tide interaction plays a vital role in the generation of D4 though its magnitude is smaller compared to the total friction.

The variations of friction related to river-tide interaction depend on the residual velocity and tidal velocity components. According to Godin (1999), higher frequency tides are generated from the interaction between residual flow and principal tides. The study defined the frictional coefficient as $U_0(U_2^2)$ for D4 tide generation from the development of the quadratic friction term in Newton's equation of motion. Buschman et al. (2009) decomposed the frictional term further into each tidal harmonic constituent (Eq. 2.1-2.4). Table 2.5 shows different non-dimensional velocity components that are affecting the friction related to river-tide interaction at R2.

Table 2.5. Maximum amplitude of the D2, and D4 tide, nondimensional maximum residual velocity (U_0), maximum velocity of diurnal (U_1), semi-diurnal (U_2) and maximum velocity of quarterdiurnal (U_4) tides, frictional coefficient from Godin (1999) and velocity components in the river-tide friction for the river discharge scenarios (Q00-125) at R2.

River discharge (in 10,000 $m^3 s^{-1}$)	Max U_0 (u_0/u_{max})	Max U_1 (u_1/u_{max})	Max U_2 (u_2/u_{max})	Max U_4 (u_4/u_{max})	Max Friction coefficient for D4 from Godin, 1999- $U_0(U_2^2)$	Max Velocity term in Frt in Eq.2 $U_0(U_1^2 + U_2^2 + U_4^2)$	Max D2 (m)	Max D4 (m)
0	0.10	0.10	0.08	0.04	0.00	0.00	0.38	0.02
5	0.14	0.14	0.45	0.09	0.03	0.03	0.36	0.03
10	0.23	0.11	0.40	0.06	0.04	0.04	0.33	0.04
20	0.42	0.07	0.21	0.04	0.02	0.02	0.27	0.03
40	0.70	0.03	0.09	0.01	0.01	0.01	0.15	0.02
60	0.86	0.02	0.04	0.01	0.00	0.00	0.09	0.01
125	0.96	0.01	0.01	0.00	0.00	0.00	0.02	0.00

Increasing river discharge increases the residual velocity and reduces the tidal velocity components (Table 2.5) at R2. Thus, the Q10 scenario generates maximum $U_0(U_1^2 + U_2^2 + U_4^2)$ in Equation 2.2 and the maximum friction coefficient for D4. Table 2.5 shows that there is an optimum balance in the Q10 scenario at R2 between residual velocity and tidal velocity components, which dictates the generation or dissipation of

the D4 tide. Similarly, an optimum balance between residual velocity and tidal velocity components is also found at R3 and R5 for the Q20 and Q40 scenarios, respectively. However, at R4, maximum D4 occurs in the Q40 scenario whereas the Q20 scenario generates maximum $U_0(U_1^2 + U_2^2 + U_4^2)$. This apparent contradiction is caused by rapidly changing geometry of the river (both in width and depth) at that station. According to Godin (1991), the convective term and the continuity term in the equations of motion can also create high-frequency harmonics whenever the river geometry varies rapidly over a short distance. In conclusion, optimal balance between river velocity and velocity of tidal components upstream of the estuary mouth, which is caused by a critical level of river discharge, modulates the generation and dissipation of the D4 tide. For river discharge higher than this critical discharge value, tidal velocity components are negligible compared to the residual velocity ($U_2 \ll U_0$) and dissipates both D2 and D4 tides rapidly.

The rapid dissipation of quarterdiurnal tides due to friction in the upper estuary was also observed in the St. Lawrence estuary by Matte et al. (2014). They found that the M4 tide is damped more rapidly by discharge and the resulting friction than it is generated from the nonlinear interactions between M2 and M4 beyond 186 km from the estuary mouth. Our findings demonstrate that the processes also occur in the complex geometry of the GBMD.

2.5 Conclusions

This study investigates the influence of river discharge on tide variations along the Ganges-Brahmaputra-Meghna Delta, which is fed by a monsoonal catchment. The Delft3d model is configured and applied to the GBMD to reproduce spatial and temporal water level and tidal properties variability for different river discharge conditions. The

model results show good agreement with the observed water levels ($R^2 > 0.92$) and tidal range across the study area for an average flood year condition (2000) in spite of uncertainties associated with the bathymetry and time of data availability. In particular, the modeled tidal ranges have better agreement in the upper estuary compared to previous studies in the GBMD (e.g., Bricheno et al., 2016; and Tazkia et al., 2017).

River discharge plays a key role in water level and tide propagation in the GBMD. The strong monsoon river discharge results in higher water levels in the upper estuary compared to the estuary mouth. Near the upstream limit of tidal propagation at 205 km from the estuary mouth, the mean water level varies seasonally between 2 m (dry season) and 10 m (monsoon season). The tidal ranges also fluctuate with the seasonal river discharge along the estuary; the decrease in tidal range has a close relationship with increasing river discharge beyond 115 km from the estuary mouth. The tidal ranges at the station 30 km from the estuary mouth, are 0.57 m and 0.27 m lower during the wet season ($60,000 \text{ m}^3 \text{ s}^{-1}$) than during the dry season ($10,000 \text{ m}^3 \text{ s}^{-1}$) for neap and spring tides, respectively. The residual water level slope and tidal damping increase with river discharge beyond 100 km from the estuary mouth, which demonstrates the influence of river discharge on tides.

The study shows that the GBMD is a mixed tidal regime where D2 tide is dominant along the delta up to 150 km from the estuary mouth. The D1 tide varies between 0 to 0.4 m along the study area. The D2 tide travels up to 205 km and 130 km from the estuary mouth during the dry and wet season, respectively. The MSF tide travels further into the upper river (beyond 205 km) compared to the D2 tide, because higher frequency tides are dampened faster by river discharge and non-linear interactions. The increase of the river discharge increases the generation and

amplification of the MSF tide beyond 100 km, whereas the other tidal components are reduced to nearly zero.

Results of a non-stationary harmonic analysis of the modelled water levels show the sizeable seasonal variation of D2 and D4 tides with the changing river discharge along the estuary. During the monsoon season D2 is reduced to approximately 0.19 m in the middle of the GBMD (102 km from the estuary mouth) whereas, in the dry season, it increases to 0.94 m. Similar seasonal variation is also found for the D4 tide. Beyond the middle of the GBMD (100 km from the estuary mouth), seasonal variations of the D2 and D4 tides with changing river discharge demonstrate the mechanism of modulating tides through total friction generated from combined effects of river discharge and tides. At R2 where tides are nearly extinct ($D2 < 0.20$ m) in an average year condition, different idealized river discharge scenarios illustrate the presence of a balance between the dissipation of D2 and the generation of D4 tide.

The total friction generated by a specific river discharge scenario ($< 20,000 \text{ m}^3 \text{ s}^{-1}$) results in a higher D4 tide compared to other (lower or higher) river discharge scenarios at the upper GBMD. The decomposition of the frictional term shows that friction related to river-tide interaction plays an essential role in the D4 tide generation with a maximum generated friction producing maximum D4 amplitude in the upper GBMD. The generation of the D4 tide from the river-tide interaction depends on the contribution from the residual and principal tide velocity components. There is an optimum balance between river discharge (the critical discharge) and energy transfer from the D2 tide that controls the local generation or dissipation of the D4 tide in the upper estuary. The optimum balance produces maximum friction related to river-tide interaction that generates maximum amplitude of D4 tide. River discharge beyond the

critical discharge threshold rapidly dissipates both D2 and D4 tides rather than generating the D4 tide.

Finally, the results presented in this study, particularly the influence of strong monsoon river discharge on tides, are important for understanding, modelling, and manage complex estuarine systems like the Ganges-Brahmaputra-Meghna Delta. The established model setup can be further applied to investigate estuarine processes such as flood risk assessment, storm surges, and sediment transport dynamics.

Chapter 3 Influence of wave-current interaction on a cyclone-induced storm surge event in the Ganges-Brahmaputra-Meghna Delta

This chapter has been submitted as a Journal article:

Elahi, M. W. E., Wang, X. H., J. Salcedo-Castro, & Ritchie, E. A. (2021). Influence of wave-current interaction on a cyclone-induced storm surge event in the Ganges-Brahmaputra-Meghna Delta. *Journal of Geophysical Research: Oceans.* (*Currently under revision*)

3.1 Introduction

Wind waves, storm surges and the ocean circulation all play important roles in producing variations in coastal waters. Several non-linear interaction processes including tide-surge interaction and wave-current interaction modulate surface water elevation in both shallow and deep ocean regions. The tide-surge interaction is a well-known factor that limits the ability of numerical models to accurately reproduce observed variations in mean water levels under extreme weather conditions, particularly in shallow areas (Yu et al., 2017). Several studies (Roland et al., 2009, Kim et al., 2010, Dietrich et al., 2011, Brown et al., 2013, Feng et al., 2016) suggest that the discrepancy between model results and observations is due to the influence of wave setup and setdown arising from wave breaking. There are several studies focusing on wave-current interaction (e.g., Tolman, 1990, Zhang et al., 2010, Xie et al., 2001 and 2003). These

studies demonstrate that wind waves can indirectly affect the coastal ocean circulation by enhancing wind stress (Mastenbroek et al., 1993) and by modulating the bed friction coefficient (Signell et al., 1990, Davies and Lawrence, 1995). Xie et al. (2001, 2003) reported that the wave-current interaction significantly influences the overall circulations in coastal regions by modifying surface and bottom stresses. Radiation stress is a source momentum flux between surface waves and underlying ocean currents, and is proportional to the wave energy density (Longuet-Higgins and Stewart, 1964; Smith, 2006). The momentum flux transfer from wind waves to the water column is more evident during wave propagation from deep to shallow water, particularly by the gradient of radiation stress (Longuet-Higgins and Stewart, 1962). Water levels and currents have a complex influence on wave height through distinct physical processes. Significant wave height in shallow regions is strongly modulated by time-varying water depth. Furthermore, ocean currents accelerate or decelerate the energy transfer from surface winds to surface waves outside the estuary based on the orientation of the current and the waves (González, 1984; Wolf and Prandle, 1999; Hopkins et al., 2016). The wave-current interaction depends on various factors such as continental shelf geometry (Resio and Westerink, 2008), bathymetry (Raubenheimer et al., 2001), coastal morphology (Malhadas et al., 2009) and the path of cyclones (Feng et al., 2012).

The GBMD is located at the head of the BoB, a semi-enclosed basin in the north-eastern Indian Ocean, which exhibits unique geographic and hydrographic characteristics. The presence of a wide continental shelf, numerous islands, and the Bengal canyon led to complex hydrodynamics. The BoB receives a large volume of freshwater flux from several rivers, including the Ganges-Brahmaputra-Meghna river system, which is one of the world's largest freshwater outlet into the ocean. This large amount of freshwater also brings tons of sediment annually into the ocean that makes

the world's most largest sediment fan (Prakash and Pant, 2020). The transport of sediments through currents, tidal, and wind waves modulate the local bathymetry in the coastal regions of the bay, particularly during the occurrence of tropical cyclones (TCs). Once every three years, the GBMD is exposed to a severe cyclone including low-lying delta region and large population living in the coast, which make Bangladesh one of the most vulnerable country to TCs (Alam and Collins, 2010).

A large number of TCs form in the BoB during the pre-monsoon (May–June) and post-monsoon (October–December) seasons when favourable meteorological conditions for TC formation prevail (McPhaden et al., 2009). Almost one-sixth of tropical cyclones that develop in the BoB make landfall in the GBMD (Saiful et al., 2011). Due to the low land elevation above mean sea level, the GBMD is vulnerable to frequent coastal and riverine flooding. In addition, the TC-induced storm surge accentuates the flooding conditions in coastal areas, posing a threat to the infrastructure, biodiversity, and the large population living in coastal regions. Storm surge events can be severe in Bangladesh because of the shape and characteristics of the coastline. The tangential wind of the TC drives the seawater towards northward from the south that generates the storm surge. The presence of the wide continental shelf in the eastern part of the Bangladesh coastline amplifies the storm surge when propagating from the deep ocean to shallower water (Rahman et al., 2019; Deb and Ferreira, 2016). Several recent cyclones, including Sidr, Aila, Roanu, and Amphan produced heavy flooding and caused a large extent of devastation to life and property. Therefore, it is vital to understand the mechanisms behind the cyclone-induced storm surge event in the GBMD to improve surge height prediction and provide better quality guidance to coastal disaster management.

Many numerical modelling studies have investigated storm surges in the Bay of Bengal (e.g., Ali, 1979; Rao, 1982; Roy, 1984; Murty, 1984; Murty et al., 1986; Flather, 1994; Das, 1994a, Das, 1994b; Sinha et al., 1996 ; As-Salek, 1998, Dube et al., 1997; Dube et al., 2000; Dube et al., 2004; Dube et al., 2009; Dube, 2012; Lewis et al., 2013; Lewis et al., 2014; Kumar et al., 2015; Krien et al., 2017, Prakash and Pant, 2020). All these studies demonstrate that shallow-water numerical models can reproduce the order of magnitude of maximum observed storm surges. During Cyclone Sidr in 2007, the IIT-D (Indian Institute of Technology - Delhi) storm surge model (Dube et al., 1994) was applied as a part of the early-warning system and showed maximum water level predictive capability with relatively good accuracy that helped to save lives (Krien et al., 2017). Despite these achievements, numerical models struggle to reproduce patterns of coastal flooding both in space and time due to several challenges such as lack of high-quality water level records, uncertainties related to the cyclonic parameter, and lack of high-resolution bathymetric data in the shallow area. The storm surge modelling challenges in the GBMD are discussed in detail in Krien et al. (2017).

One key challenge for storm surge modelling in the delta region is the lack of high-quality verification data. The lack of high-quality water level records during cyclones, bathymetric data in shallow areas, and observations of cyclonic parameters such as the maximum wind speed, and radius of maximum wind speed contribute to errors in model results. Moreover, the contribution of waves in hydrodynamic models has been mostly ignored by researchers in the GBMD, with the notable exception of Deb and Ferreira (2016) and Krien et al. (2017). During TC events, the wind-induced stress at the ocean-atmosphere interface is expected to be the dominant mechanism for storm surge generation over coastal zones bordered by broad and shallow shelves (Flather, 2001; Rego and Li, 2010; Kennedy et al., 2012). Furthermore, currents and waves can

interact each other during a cyclonic event. This interaction depends on the magnitudes of each of the currents and waves. The storm surge, tides, and currents will have a significant effect on the wavefield only if their strengths are sufficient to interact (Samiksha et al., 2017). These wave processes can influence the coastal hydrodynamic conditions in two ways: (i) wave-setup during cyclones that contributes significantly to storm surge and inundation (ii) Wave-current interaction increases the bottom friction (Samiksha et al., 2017). The current can influence the wave by modifying the wave characteristics through refraction, bottom friction, and blocking (Ris et al., 1999). Also, the mean flow will be affected by the addition of momentum and mass fluxes. The depth felt by the waves also changes with variations in water level in the coastal region, thereby modifying the shallow water effects on the waves (Pleskachevsky et al., 2009). Several studies (e.g., Samiksha et al., 2017, Prakash and Pant, 2020) on cyclones making landfall on India's eastern coast include wave effects in the models. These studies demonstrate that a significant portion (0.25 m, 20% of the total surge height during cyclone Hudhud) of the storm surge height can result from the wave setup. However, the contribution of the wave setup and wave-current interactions in the storm surge height in the GBMD is yet to be explored.

The physical environment of the coastal regions is modulated by the mutual interaction between physical processes, such as tides, waves, and currents (Murty et al., 2014). Depending on the tidal phase, wind- and wave-induced currents can reinforce or interfere with tidal currents. Flather (1994) suggests that cyclones and tide conditions can both affect the final surge height. Therefore, this chapter addresses the role of the wave-current interaction in the generation of surge height at the GBMD during cyclonic conditions. A 3-D barotropic online wave-current coupled hydrodynamic model is established using Delft3D and SWAN (The Simulating WAVes Nearshore model). The

model setup is calibrated and validated for Cyclone Sidr. The model is then applied to different idealized scenarios, including different combinations of the physical processes (e.g., only tide scenario, only wave scenario, one-way coupling, two-way coupling) to investigate how different processes and their interactions influence the storm surge height generation in the GBMD.

3.2 Field Site and Data

3.2.1 Cyclone Sidr

Cyclone Sidr has been one of the most devastating cyclones in Bangladesh over the last 20 years. The estimated loss, 1.7 billion USD, resulted from Cyclone Sidr (a 10-year return period) was the highest among all previous cyclones in Bangladesh. The surge height exceeded 7.5 m, and approximately 10,000 fatalities were reported (Hussain and Tajima, 2017). Strong wind and cyclone-induced storm surge flooding caused extensive destruction to coastal and river embankments and road networks. Cyclone Sidr is one of the most well-documented and cyclone events on the Bangladesh coast. As Cyclone Sidr is one of the most documented cyclonic events with the best water level observations and impacted the Bangladesh coast vastly, Cyclone Sidr is an excellent event to investigate further the physical process (Mamnun et al., 2020)

A well-established low-pressure field was identified over the southeast of the Bay of Bengal at 0000 UTC on 11 November 2007. After 9-hour, the low-pressure field transformed into a depression and lay centered at latitude 10.0° N, longitude 92.0° E about 200 km south-southwest of Port Blair, and intensified into a deep depression at 1800 UTC on 11 November 2007. The system rapidly intensified into a severe cyclonic storm at 1200 UTC and into a very severe cyclonic storm (167 km/h) at 1800 UTC on 12 November. The system continued to move northwesterly until 0000 UTC on 13

November. Afterward, the system moved in a northerly direction up to 1200 UTC of 15 November and then moved north- northeastwards. It maintained the same intensity (167 km/h) from 1800 UTC on 12 November to 0000 UTC on 15 November. The system further intensified to 213 km/h at 0300 UTC on the same day. It crossed the west Bangladesh coast around 1500 UTC near latitude 21.7° N, longitude 89.8° E (close to Khepupara in Figure 3.1) with the same intensity (Mamnun et al., 2020). After landfall, the system weakened into a cyclonic storm at 2100 UTC of 15 November. The system further weakened into depression at 0300 UTC and remained depression until 0600 UTC on 16 November. The observed Cyclone Sidr track from the Joint Typhoon Warning Centre (JTWC) is presented in Figure 3.1. The different cyclonic parameters of Cyclone Sidr in the model setup are applied from the best track archives of the JTWC.

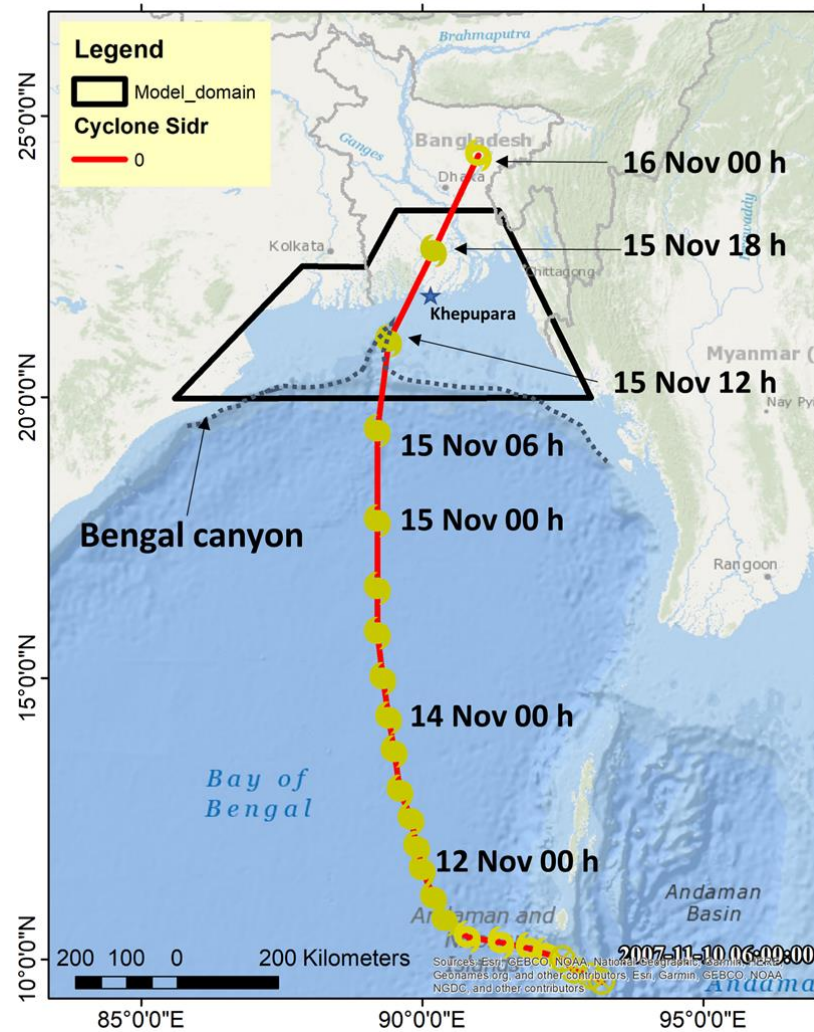


Figure 3.1. Cyclone Sidr track from the JTWC best track archive with the model domain. Black dotted line indicates the location of the Bengal Canyon.

3.2.2 Study area

Bangladesh is one of the world’s disaster-prone countries with 97.7 percent of the total population exposed to multiple hazards, including cyclones (Alam and Collins, 2010). Devastating cyclones that form in the Bay of Bengal cause 80-90 percent of the global loss from cyclones. More than 40 percent of the total population lives in the coastal area making the GBMD vulnerable to cyclone-induced storm surge. The presence of a continental shelf, a deep submerged canyon 100 km from the coast, and

the funnel shaped geography results in amplification of surge height in the GBMD. In addition, the coastal land area lies between 1 to 3 m above mean sea level.

The GBMD is an active delta that conveys a large sediment load from the upper catchment area to the BoB through the Lower Meghna river. Due to dynamic river morphology in the central GBMD, the river bathymetry changes rapidly particularly in the mouth of the Lower Meghna river. The presence of extensive shoals, shallow lands, and islands in the lower Meghna river's estuary mouth cause complex hydrodynamic features compared to other estuary systems (Snead, 2010). The Lower Meghna River has significant seasonal variations in river discharge up to $100,000 \text{ m}^3 \text{ s}^{-1}$. Other rivers located in the western GBMD, including the Bishkhali and Baleswar, are tide-dominated and convey a negligible amount ($< 3000 \text{ m}^3 \text{ s}^{-1}$) of freshwater compared to the central GBMD. There are a few hilly rivers located in the eastern part of the GBMD, which convey freshwater during flash flood events during the monsoon season. Tides in the GBMD are semi-diurnal with a mean tidal range varying from 3 to 6 m along the coast. Tides can propagate over 200 km inland and have strong seasonal variations with the seasonal river discharge variations. Details of variations in river discharge and tides are discussed in Chapter 2 (Elahi et al., 2020). To help mitigate the coastal flooding from storm surge events, 123 earthen embankments were constructed across the GBMD. These structural interventions caused changes of flooding pattern in the coastal area by reducing natural floodplain area, and increasing river-bed siltation (Rogers and Goodbred, 2014).

April to May (early summer) and October to November (late rainy season) are the two main seasons when most of the severe cyclones impact the GBMD. Cyclone Sidr made landfall on the Bangladesh coast on 15 November 2007 during the late rainy season. According to previous studies (e.g., Lewis et al., 2013; Krien et al., 2017), the

river discharge from the Ganges, Brahmaputra and Meghna rivers are $15,000 \text{ m}^3 \text{ s}^{-1}$, $25,000 \text{ m}^3 \text{ s}^{-1}$ and $850 \text{ m}^3 \text{ s}^{-1}$ during Cyclone Sidr, respectively. Case studies have investigated the socio-economic impacts (e.g., Paul, 2009) and physical storm surge processes (e.g., Krien et al., 2017) during Cyclone Sidr. Hence, the current study focusses on wave-current interactions during the Cyclone Sidr surge event. The shallow continental shelf, high tidal range variations, the triangular shape of geography, and low-lying land elevation make the GBMD a perfect laboratory to study the wave-current interactions during a cyclone-induced storm surge event.

3.2.3 Field data

Compromises are often made between parameters in storm surge models used for research (Krien et al., 2017) in order to reproduce the maximum water levels at a single tide gauge. For example, the model may reproduce the maximum water level without considering waves by overestimating wind surge using an artificial increase of maximum wind speed or the radius of maximum wind. Similarly, errors in other factors such as bathymetry, bottom friction, or drag coefficient can offset each other to some extent so that water levels can be correctly reproduced at one location, even when the model does not accurately reproduce the physical processes (Krien et al., 2017). For this study, it is important to ensure that the model properly represents physical processes and accurately represents the water levels during the storm surge event. To do this, the model needs to be validated against a representative set of water level, wind and wave observations at different locations.

Water level observations during cyclonic events in the GBMD are rare. There are several tide gauge stations located in the coastal areas. The float gauges used in these stations are located in remote areas of the coastal zone and the benchmarking and datum checks are not updated regularly. Gaps in the observations and reduced sampling rates

occur in the water level data set because of tidal gauge malfunctions, (Chiu and Small, 2016). There are several limitations regarding water level observations such as the relatively short supply of automatic tide gauges, poor documentation and displacement of tide gauges sometimes by floods or due to maintenance, makes it difficult to validate models consistently in the GBMD (Krien et al., 2017). In addition, tide gauges are often located in rivers which are not resolved by models. Consequently, the validation process in studies often consists of checking that the order of magnitude of the maximum water level is reproduced in the grid wet node that is closest -but sometimes 10 km away or more- from the actual tide location (Krien et al., 2017). Cyclone Sidr made landfall at the mouth of the Bishkhali river, which is a tidal river with a very low freshwater outflow ($< 3000 \text{ m}^3 \text{ s}^{-1}$) compared to the Lower Meghna river ($< 100,000 \text{ m}^3 \text{ s}^{-1}$). The water level variations during Cyclone Sidr are available at Hironpoint, Khepupara and Coxsbazar from the BIWTA (Figure 3.2). In the current study, the model water levels are compared at these three stations.

Finally, to increase the amount of validation data for the model, the significant wave height and atmospheric surface wind data from the European Center for Medium-range Weather Forecasting (ECMWF) ERA5 reanalysis dataset (Dee et al., 2011) is used to validate the model wave heights. The ERA5 dataset is a global atmospheric and ocean surface $0.5^\circ \times 0.5^\circ$ grid resolution dataset available every hour and provides coverage of the deep ocean area of the study region.

3.3 Methodology

A numerical model based on Delft3D with the Delft3D-Wave model is used to simulate the cyclone induced storm surge event in the GBMD. The model is calibrated and validated based on available data during Cyclone Sidr. Several idealized scenarios

are then designed and analyzed to investigate the influence of wave setup and wave-current interaction on the simulated storm surge height. Details of the model setup and processes are discussed in the following sections.

3.3.1 Numerical model Delft3D

The standard Delft3D package (Lesser et al., 2004) has been widely applied for modelling physical processes (e.g., hydrodynamics and sediment transport) in coastal ocean, estuaries and lakes (Deltares, 2013a). In the present study, the standard Delft3D package is applied to simulate the interactions between wave and current in the GBMD. Delft3D-FLOW (referred to as FLOW model for the rest of the paper) solves the unsteady shallow-water equations using a finite difference scheme under Boussinesq and shallow water assumptions. Further details about Delft3D-FLOW can be found in Lesser et al. (2004) and Deltares (2013a). Delft3D-WAVE (referred to WAVE model through the rest of the paper) is a modified version of the third-generation SWAN model (Booij et al., 1999; Ris et al., 1999), which performs well during the evolution of random, short-crested wind-generated waves in coastal environments (Deltares, 2013b). A brief description of the Delft3D-WAVE from Deltares (2013b) is given below.

Wave kinematics

The WAVE model uses the linear wave theory and the conversion of wave crests to estimate wave kinematics. This linear theory for uniform surface gravity waves is valid provided the waves are propagating over slowly varying current and water depth (Phillips, 1966; Whitham, 2011). The WAVE model estimates the wave propagation velocities of wave energy in geographical (c_x , c_y) and spectral space (c_σ , c_θ) from the kinematics of wave trains by following equations (Whitham, 2011):

$$\frac{d\vec{x}}{dt} = (c_x, c_y) = \vec{c}_g + \vec{u} = \frac{1}{2} \left(1 + \frac{2|\vec{k}|d}{\sinh(2|\vec{k}|d)} \right) \frac{\sigma \vec{k}}{|\vec{k}|^2} + \vec{u} \quad (3.1)$$

$$\frac{d\sigma}{dt} = c_\sigma = \frac{\partial \sigma}{\partial d} \left(\frac{\partial d}{\partial t} + \vec{u} \cdot \nabla_{\vec{x}} d \right) - c_g \vec{k} \cdot \frac{\partial \vec{u}}{\partial s} \quad (3.2)$$

$$\frac{d\theta}{dt} = c_\theta = -\frac{1}{k} \left(\frac{\partial \sigma}{\partial d} \frac{\partial d}{\partial m} + \vec{k} \cdot \frac{\partial \vec{u}}{\partial m} \right) \quad (3.3)$$

where \vec{c}_g denotes the group velocity, \vec{k} is the wave number vector, and d is the water depth, s is the space coordinate in the wave propagation direction of θ and m is a coordinate normal to s . Here, \vec{u} represents the current vector and is assumed to be uniform in vertical direction; consequently, depth-averaged current is used in this study.

It is important to point out that the temporal and spatial gradient of the water depth and current can influence the wave propagation velocities (c_x , c_y , c_σ , c_θ). The presence of current flow results in Doppler shifting of the relative radian frequency σ (in a frame of reference moving with current) and becoming absolute radian frequency ω (i.e., the observed frequency, in a frame of reference fixed on ground) based on Equation 3.4 (Song et al., 2020). Thus, the resulting absolute frequency ω modifies the wave number k via the dispersion relation Equation 3.5 (achieved by replacing the relative frequency σ in Equation 3.5 with the absolute frequency ω), leading to a change in wave energy flux (Hopkins et al., 2016). A change of water depth, in contrast, does not modify wave frequency, i.e., absolute frequency ω equals to relative frequency σ .

$$\omega = \sigma + \vec{k} \cdot \vec{u} \quad (3.4)$$

$$\sigma^2 = gk \tanh(kd) \quad (3.5)$$

Spectral action balance equation

The WAVE model considers the action density spectrum $N(\sigma, \theta)$ ($= E(\sigma, \theta)/\sigma$), which may vary in time and space. The evolution of wave spectrum by following the

spectral balance equation for Cartesian co-ordinates is described as (e.g., Hasselmann et al., 1973; Mei, 1989; Komen et al., 1984):

$$\frac{\partial N}{\partial t} + \frac{\partial c_x N}{\partial x} + \frac{\partial c_y N}{\partial y} + \frac{\partial c_\sigma N}{\partial \sigma} + \frac{\partial c_\theta N}{\partial \theta} = \frac{S_{tot}}{\sigma} \quad (3.6)$$

$$S_{tot} = S_{in} + S_{nl3} + S_{nl4} + S_{ds,w} + S_{ds,b} + S_{ds,bk} \quad (3.7)$$

The first term on the left-hand side of Equation 3.6, represents the local change rate of wave action density in time. In the same equation, the second and third terms express the propagation of action in geographical space (x, y) including depth- and current-induced straining, also known as shoaling and mean current advection (or current-induced convergence), respectively. The shifting of relative frequency σ and the refraction during propagation θ in spectral space (σ, θ) are represented by the fourth and fifth terms, respectively, which jointly reflecting the redistribution of energy density over the spectrum (Tolman, 1991; Deltares, 2013b, Song et al., 2020).

The variable S_{tot} on the right hand side of the Equation 3.6, represents the sum of source-sink (see Equation 3.7)) resulting from the interaction of physical process like wind-wave generation S_{in} , non-linear transfer of wave energy through wave-wave interactions (triads S_{nl3} and quadruplets S_{nl4}), and energy dissipation caused by whitecapping $S_{ds,w}$, bottom friction $S_{ds,b}$ and depth-induced breaking $S_{ds,bk}$.

Wave setup

The presence of wave includes radiation stress term in the momentum balance equation. Hence, hydrostatic pressure gradient is modified to balance the wave forcing based on the following vertical integrated momentum balance equation in 1D (cross-shore) case (Longuet-Higgins and Stewart, 1962, 1964). Wave setup is resulted from a

balance between the wave force (gradient of the wave radiation stress) and the hydrodynamic pressure gradient. Note that wave setup is calculated in the FLOW model.

$$\frac{dS_{xx}}{dx} + \rho g H \frac{d\eta}{dx} = 0 \quad (3.8)$$

where $H=d+\eta$ denotes the total water depth and η represents the mean surface elevation including the wave setup; S is the radiation stress tensor:

$$\begin{aligned} S_{xx} &= \rho g \int \left(n \cos^2 \theta + n - \frac{1}{2} \right) E d\sigma d\theta \\ S_{xy} &= S_{yx} = \rho g \int n \sin \theta \cos \theta E d\sigma d\theta \\ S_{yy} &= \rho g \int \left(n \sin^2 \theta + n - \frac{1}{2} \right) E d\sigma d\theta \end{aligned} \quad (3.9)$$

and $n = c_g k / \omega$ is the ratio of group velocity over phase velocity; E is the wave energy.

Depth-induced wave breaking

Sea level determines the maximum wave height beyond which the waves start to break (Viitak et al., 2016). In the WAVE model, the process of energy dissipation caused by depth-induced wave breaking mimics the breaking of a bore applied to random waves (Battjes and Janssen, 1978):

$$S_{ds,bk}(\sigma, \theta) = \frac{D_{tot}}{E_{tot}} E(\sigma, \theta) \quad (3.10)$$

Where $D_{tot} = -\alpha_{BJ} Q_b \sigma_{mean} H_{max}^2 (8\pi)^{-1}$, represents the mean rate of energy dissipation per unit horizontal area due to wave breaking, $\alpha_{BJ} = 1$, σ_{mean} = mean frequency, Q_b = fraction of breaking waves and $H_{max} = \gamma d$ is the maximum wave height that can exist at the given depth d where γ is the breaker parameter (set to 0.73). E_{tot} is the total wave energy integrated over all directions and frequencies.

It is important to note that during a surge event, the water depth increases while the fraction of breaking waves is reduced. This results in moving the breaking zone towards the coast and increasing wave heights in coastal areas (Viitak et al., 2016).

Whitecapping

Energy dissipation due to whitecapping in the WAVE model is represented by the pulse-based model of Hasselmann (1974):

$$S_{ds,w}(\sigma, \theta) = -\mathcal{T} \sigma_{mean} \frac{k}{k_{mean}} E(\sigma, \theta) \quad (3.11)$$

Where, k_{mean} = mean wave number, \mathcal{T} = coefficient depends on the overall wave steepness (The SWAN team, 2014). When currents and waves are in opposite directions, the waves experience enhanced whitecapping because wave number and wave steepness increase with the opposing current.

Bottom friction

The energy dissipation due to bottom friction in the WAVE model is expressed by means of JONSWAP empirical model (Hasselmann et al., 1973),

$$S_{ds,b}(\sigma, \theta) = -C_b \frac{\sigma^2}{g^2 \sinh^2(kd)} E(\sigma, \theta) \quad (3.12)$$

where $C_b = 0.038 \text{ m}^2 \text{ s}^{-3}$ is the bottom friction coefficient (The SWAN team, 2014).

As the surface currents affect the spectral wave energy, the bottom friction will also change. Bottom friction will increase with increasing wave energy for example in the case of an opposing current (Viitak et al., 2016).

Wave-Current Interactions and Coupling procedures

Delft3d considers five physical processes in computations of wave-current interactions, which represent the effects of waves on the Eulerian flow (Mulligan et al., 2008). These are (1) radiation stress gradients (Longuet-Higgins and Stewart, 1964) are considered in the flow momentum equations, (2) enhance bed shear stress (Jørgen, 1984), (3) vertical mixing and turbulence are induced (Lesser et al., 2004), (4) Stokes drifts is accounted for via a Generalised Lagrangian Mean (GLM) approach (Groeneweg and Battjes, 2003) and Mean current advection and refraction of wave energy (Fredse and Deigaard, 1992). Waves result in excess flows of momentum through radiation stress. Wave energy dissipation can transfer momentum to the Eulerian flow via radiation stress gradient. The wave energy dissipation rate in SWAN is estimated internally as the sum of energy dissipation related to depth induced breaking, whitecapping and bottom friction per unit time. The energy dissipation related to wave breaking is estimated by the formulation of Battjes & Janssen (1978). Detail method of the wave-current interactions in Delft3d can be found in the Flow User Manual Delft3D (See section 9.7, Page 220 in Deltares, 2021).

Delft3d module offer different types of wave computations such as a standalone wave computation using SWAN, an offline coupling of WAVE with Delft3d-FLOW and an online coupling of WAVE with Delft3d-FLOW. In case the offline coupling or the online coupling between the FLOW and WAVE module of Delft3d, data is exchanged using a communication file (com-file), which contains the most recent data of the flow and wave computations.

Coupling between the WAVE and FLOW models can be one-way or two-way, which means the interactions (i.e., information transfer) between the two models occur unidirectionally and bidirectionally, respectively. In one-way coupling for the flow to wave condition, the WAVE model takes the water level and current velocity information from a transfer communication file from the FLOW model and calculates their impacts on waves but does not pass the wave information back to the FLOW model. Similarly, in one-way coupling for the wave to flow condition, the flow model uses the wave information from a transfer communication file from the WAVE model and estimates the wave influence on water level and current velocity. Two-way coupling allows the waves to feed into the flow and vice versa and is more realistic. During the two-way coupling, the flow model passes water level and current velocity to the wave model, which calculates their impacts on wave kinematics, and then passes the wave height, wave direction and mass fluxes, back to the next round of flow computation.

3.3.2 Model setup

The model is setup to simulate storm surge events in the GBMD. In this study, a three-dimensional version of Delft3D is used to set up the barotropic model for the GBMD. A two-way coupling of the FLOW and WAVE model is applied to the establishment of the model setup. The model setup is computed on a boundary-fitted curvilinear grid of 200 – 1320 m resolution with ten sigma layers in a vertical direction. The combined time-varying river discharge of the Ganges-Brahmaputra-Meghna river is applied at the upstream boundary condition following Krien et al., (2017). Astronomical constituents (including K1, O1, P1, Q1, M2, S2, N2, K2, M4, MS4, MN4, MSF) for the water level at downstream locations are generated by applying the TPXO 7.2 Global Inverse Tide Model (Egbert and Erofeeva, 2002). The model simulation time

covers 10-16 November 2007. To avoid initial computational errors from model spinup, the first 24-hours of simulation are ignored in the analysis.

The cyclonic wind and pressure field are generated from the JTWC cyclone best track for Cyclone Sidr (2007) on the computational grid by using the Delft-Dashboard module (DDB) (Ormond et al., 2020). The DDB calculates wind and pressure field by following the methodology of Holland et al. (2010). The Holland profile is a smooth analytic profile of wind and pressure extending from the cyclone center to outer radius and is shaped by cyclone parameters including maximum wind intensity, the radius of maximum wind, and minimum pressure from the JTWC best track archive. The profiles can be calculated at regular time intervals by using the 6-hourly JTWC estimates to produce time-varying wind and pressure fields that serve as the input to the hydrodynamic model. The wave model is applied with 36 directions and 24 frequency bins, with the cut-off frequencies being 0.04 and 1 Hz. The details of cyclonic wind and pressure fields incorporation and related uncertainty are described in the Appendix B.1 and B.2.

The model river and estuary bathymetry are prepared by using measured cross-sections collected during 2007 to 2014 within the ESPA-delta (Assessing health, livelihoods, ecosystem services and poverty alleviation in populous deltas) project of the Bangladesh University of Engineering and Technology (BUET). The inland ground elevation data is specified from the FINNMAP (a Finland based private organization) Land Survey 1991, National Digital Elevation Model (DEM) from Floodplain Action Plan-19 (FAP19), which were collected through aerial photographic surveys and field measurements by the Centre for Environmental and Geographic Information Services (CEGIS), Bangladesh. The ocean bathymetry is specified using open-access data from the General Bathymetric Chart of the Oceans (GEBCO, <http://www.gebco.net/>). The

model was calibrated by applying different combinations of Manning's coefficient and then comparing modelled and observed water level at Hironpoint, Khepupara, and Chittagong stations for Cyclone Sidr (2007). An increasing roughness parameter from 0.00025 (sea) to 0.05 (upper estuary) provided the best reproduction of observations. Other parametrisations are specified in Table 3.1. A full validation analysis is detailed in Section 3.4.1. The variation of the different tidal components in the GBMD for different hydrodynamic years were already discussed in Chapter 2 and the same tidal forcings are applied in this chapter.

Table 3.1. Model parameterization

Delft3d FLOW		
Parameters	Model	Coefficients
Bottom roughness	Manning	0.00025 – 0.05 (sea to land)
Stress formulation	Fredsoe, 1984	
Background horizontal viscosity / diffusivity	-	1 m ² s ⁻¹
Background vertical viscosity / diffusivity		0.1 m ² s ⁻¹
Model for 3D turbulence	k-Epsilon	
Wind drag coefficients		0.001 for U ₁₀ = 0 m s ⁻¹ 0.003 for U ₁₀ = 30 m s ⁻¹
Time step		0.5 min
SWAN		
Generation mode for physics	3-rd generation	
Depth-induced breaking	B&J model (Battjes and Janssen, 1978)	Alpha = 1, Gamma = 0.73
Non-linear triad interaction	-	Alpha = 0.1, Beta = 2.2
Bottom friction	JONSWAP	Coef. = 0.08 m ² s ⁻³
Diffraction	-	Smoothing coef. = 0.2 Smoothing steps = 5 Adapt propagation = Yes
Other processes activated in SWAN		
Wind growth	Yes	
Whitecapping	Yes (following Komen et al., 1984)	
Wave propagation in spectral space	Refraction and Frequency shift are activated	

3.3.3 Description of Scenarios

Eighteen sensitivity scenarios are designed to investigate the role of different factors including wave-current interactions in the generation of storm surge height

during a cyclonic event (Table 3.2). To reduce the computational time, the sensitivity simulations were run for just the last four days of the Cyclone Sidr period (13-16 November 2007). The simulation period covers the time from two days prior to landfall time. The influence of depth and current on waves can be computed individually by passing the corresponding information from the FLOW model to the WAVE model.

One wave-only model (Run1) is conducted to examine the wind-wave generation under cyclonic conditions in the GBMD. One tide-only model (Run2) and one tide and wind model (Run3) are applied by using only the FLOW model to evaluate the cyclonic wind influence on surge height generation. Three one-way coupled (FLOW to WAVE: Run4, Run4_wl, Run4_cu) simulations are used to distinguish the influence of water level and current on wave height variations. A one-way coupled (WAVE to FLOW: Run5) is conducted without the tide and wind forcing to estimate the wave-driven current and water level variations. A similar approach is also applied using two-way coupling to study the wave-current interaction influence (Run7, Run7_wl and Run7_cu). To investigate significant wave height (SWH) variations, six additional model simulations are run by ignoring different dissipation processes in the WAVE model using two-way coupling (Run7a-c) and only-wave conditions (Run8a-c). Furthermore, to understand the influence of tide on the SWH variations, one two-way coupled model (Run7d) is applied while considering all the dissipation terms in the WAVE and ignoring the tide forcing in the FLOW model. The details of each model scenario are specified in Table 3.2. Similar modelling approaches have also been applied in the Bohai Bay, China, to study wave-current interactions during extreme weather conditions by Song et al. (2020).

Table 3.2. Scenario details

Run name	FLOW (hydrodynamic model)	Coupling method			WAVE (SWAN model)	Remarks
		Water level	curr ent	Meth		
Run1					Base wave run = Wind forcing: Sidr wind field. Processes: all on	→ one way (Flow result influence wave) ← one way (Wave result influence flow) ↔ two way (both flow and wave receive feedback) 'OW': 'Only wave'
Run2	Only tide forced flow model					Influence of tide: 'Only tide'
Run3	Base Flow run = Tide + Wind (Cyclone Sidr)					Influence of tide along with cyclonic wind-pressure field
Run4	Base flow run (Run3)	✓	✓	→	Run1	Influence of (water level + Current) on wave
Run4_wl	Run3	✓		→	Run1	Influence of water level on wave
Run4_cu	Run3		✓	→	Run1	Influence of current level on wave
Run5	Run3 without tide and wind	✓	✓	←	Run1	'OWC': wave driven current and water level variations
Run6	Run3	✓	✓	←	Run1	Wave influence on current and water level: 'Wave to flow'
Run7	Run3	✓	✓	↔	Run1	Wave-current interactions (WCD, Real case).
Run7_wl	Run3	✓		↔	Run1	Influence of depth on Wave-current interactions
Run7_cu	Run3		✓	↔	Run1	Influence of Current on Wave-current interactions
Experiments designed to study the wave dissipation						
Run7a	Run3	✓	✓	↔	Run1	Only depth induced breaking considered in WAVE
Run7b	Run3	✓	✓	↔	Run1	Only whitecapping considered in WAVE
Run7c	Run3	✓	✓	↔	Run1	Only bottom friction considered in WAVE
Run7d	Run3 without tide	✓	✓	↔	Run1	All process on.
Run8a	-				Run1	Only depth induced breaking considered in WAVE
Run8b	-				Run1	Only whitecapping considered in WAVE
Run8c	-				Run1	Only bottom friction considered in WAVE

'meth.' represents coupling method.

'-' indicates the corresponding model and the coupling is not considered, e.g., Run1a is a wave-only model run and Run1b is a current-only model run.

'→' is the way and the direction of coupling, e.g., 'FLOW←WAVE' denotes wave model is one-way coupled to flow model.

3.4 Result and Discussions

3.4.1 Model validation

The model simulated water level variations during Cyclone Sidr are compared with observations at Hironpoint (Figure 3.2b), Khepupara (Figure 3.2c) and Chittagong (Figure 3.2d) (Table 3.3). The model reproduces the storm surge signals at all these three-stations reasonably well with better performance at Hironpoint ($R^2 = 0.84$) and Chittagong ($R^2 = 0.71$) compared to Khepupara ($R^2 = 0.44$), perhaps because Khepupara stopped working during the landfall period. After the cyclone made landfall, the gauge stations stopped working, and the peak water levels at Hironpoint and Khepupara were missed (Ikeuchi et al., 2017). At Chittagong, the model water level was consistently underestimated by approximately 1.5 m for the preceding four days prior to landfall. This error could be contributed by errors in the bathymetry since the Chittagong estuary lacks field measurements and the bathymetry is based on the GEBCO dataset. In contrast, the maximum model high water level during the cyclone event matches the observations at Chittagong, indicating that the model successfully captures the storm surge peak signal. The model results demonstrate that it can capture the phase of maximum and minimum water level observations along with the storm surge peak. Further comparison of model tidal amplitudes and maximum residual water level are presented in Appendix B.3.

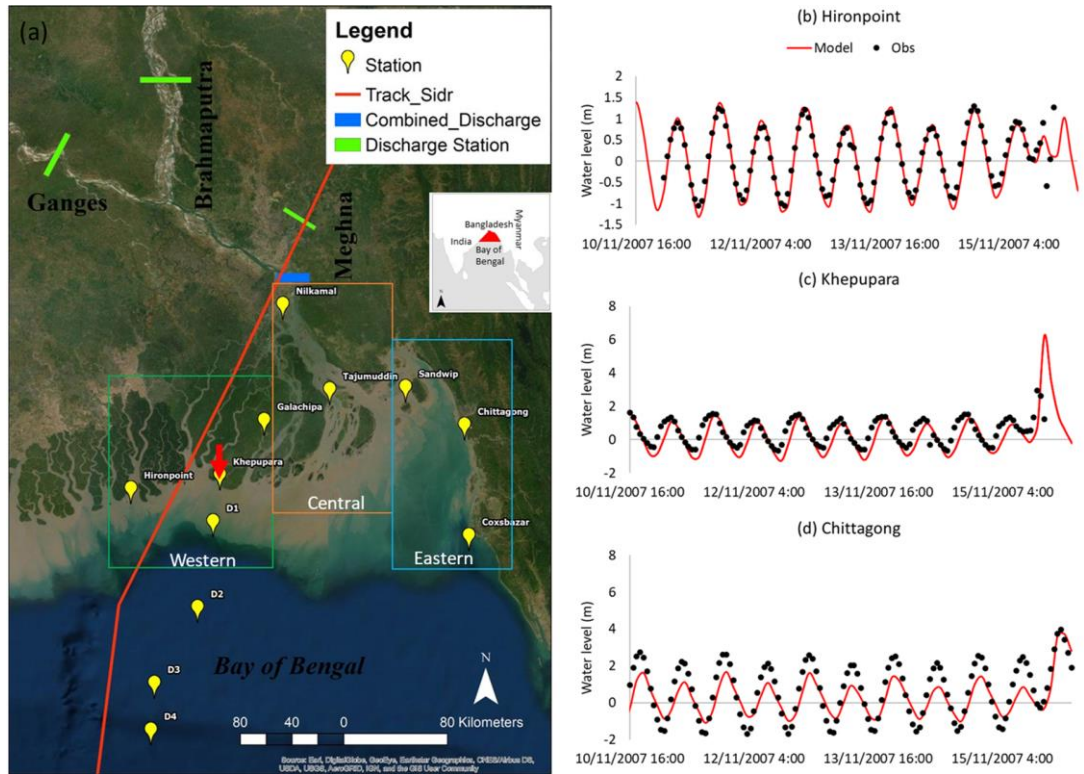


Figure 3.2. (a) The study area along with Cyclone Sidr and discharge boundary; (b)- (d) the model water level comparison with the observed water level at: (b) Hironpoint; (c) Khepupara; and (d) Chittagong for Cyclone Sidr. The different colour boxes represent different regions of the GBMD.

Table 3.3. Statistical analysis of model water level compared with observations for Cyclone Sidr.

(Water level)	Hironpoint	Khepupara	Chittagong
MSE: Mean squared error (m ²)	0.08	0.46	0.74
PSNR: Peak signal to noise ratio	59.37	51.50	49.41
R sq. value:	0.84	0.44	0.71
RMSE: Root mean square deviation (m):	0.27	0.68	0.86
NRMSE: Normalized Root-mean-square error (%)	0.12	0.19	0.15

There are few available observations of wind speed and wave height in the GBMD delta and so, the model results are compared with the ERA5 reanalysis dataset (Hersbach et al., 2020). The ERA5 ocean data does not resolve the estuary mouth regions of the GBMD and a point-by-point comparison of model significant wave height (SWH)

and model wind speed with the ERA5 data is not possible because of the very different model grid resolutions. Therefore, the model data are compared with the ERA5 data at two locations, one on the right side and one on the left side of the cyclone's eye near the radius of maximum winds. Figure 3.3a-b show the model and the ERA5 SWH at 1200 UTC 15 November 2007, three hours earlier than Cyclone Sidr's landfall time. The results show that the model can reproduce the spatial variations of SWH variations due to cyclonic conditions in the study area. The time series of wind speed and SWH are compared at two points: one is on the right side (90.94° E 20.76° N) and the other on the left side (88.56° E 20.80° N) of the cyclone eye, and presented in Figure 3.3c-d. Figure 3.3c-e shows that the model can reproduce the trend of temporal variations of SWH ($R^2 = 0.89$) and wind speed ($R^2 = 0.95$) of the ERA5. The peak values are similar although there are finer temporal variations in the model SWH (RMSE = 1.12 m) and wind speed (RMSE = 3.94 m s^{-1}) compared with the ERA5 likely due to the better resolved spatial features in the wind and SWH near the radius of maximum winds in the much finer model grid. The statistical analysis at these two points (Figure 3.3e) demonstrates that the model can reasonably reproduce SWH and wind speed in the BoB during the cyclone event.

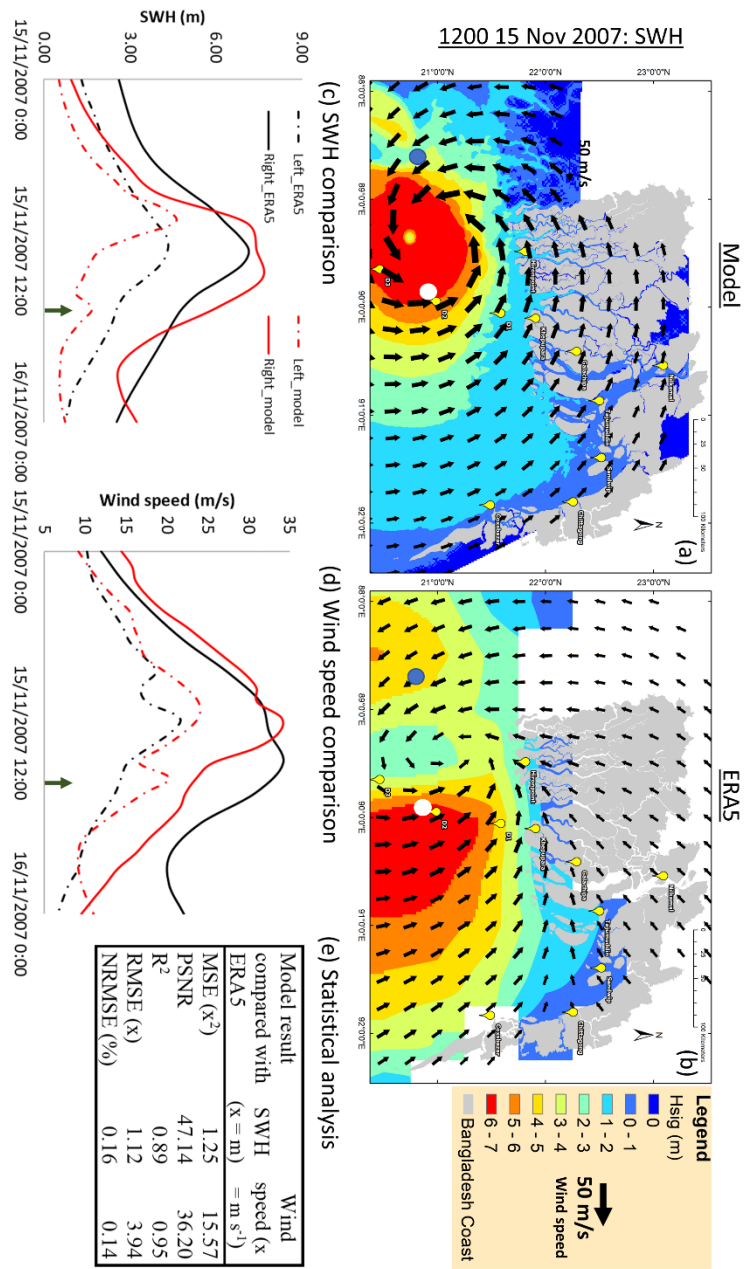


Figure 3.3. Comparison of the spatial variation of significant wave height and wind speed with: (a) model; and (b) ERA5 dataset. Time series comparison of modelled and ERA5 at the blue (left of center) and white (right of center) dots: (c) significant wave height and (d) wind speed, (e) statistical analysis. N.B. The green arrow denotes the landfall time 1500 UTC 15 November 2007.

Many studies have investigated the storm surge event during Cyclone Sidr. Among them, Deb and Ferreira (2016) and Krien et al. (2017) consider the wave-current interaction in their study, whereas, other studies neglect the wave-current interaction

(e.g., Lewis et al., 2013). Deb and Ferreira (2016) focus on storm surge height variations in the Bangladesh coastal area for the first time by considering wave influence and demonstrate that waves can influence surge height. However, the study is restricted to the exposed coastal area due to a lack of good bathymetry and a relatively coarse grid resolution (e.g., 900 m). Moreover, Deb and Ferreira (2016) do not discuss how the wave-current interaction influences wave height. A comparison of these model results with Deb and Ferreira (2016) and Lewis et al. (2013) is provided in Table 3.4 and demonstrates that the model can reproduce reasonable high-water level and maximum SWH during Cyclone Sidr compared with other published modelling studies. The water level has a higher RMSE for the Lewis et al. (2013) study compared with the Deb and Ferreira (2016) study. Since Lewis et al. (2013) does not consider the wave-current interaction, this is reasonable. The evolution of the high-water level ($R^2 = 0.92$) and maximum significant wave height ($R^2 = 0.87$) demonstrate good agreement with Deb and Ferreira (2016). While the model maximum SWH is underestimated by 1.5 m and 1.4 m compared to Deb and Ferreira (2016) at Chittagong and Galachipa, respectively, Galachipa is located between two earthen embankments and is further inland compared to other stations. Since Deb and Ferreira (2016) do not consider embankment heights in their study, the difference in the maximum SWH likely has resulted from the improved bathymetry and finer grid resolution in this current study.

Table 3.4. Comparison of model outcomes with high water levels and maximum significant wave height extracted from recent studies on Cyclone Sidr.

Locations	Chittagong	Coxsazar	Sandwip	Khepupara	Galachipa	Hironpoint	R²	RMSE (m)
Lat	22.19	21.46	22.48	21.88	22.03	21.81		
Long	91.81	91.92	91.55	90.10	90.34	89.49		
High water level during cyclone Sidr (m)								
This study	4.8	2.4	6.1	6.5	5.4	1.2		
Deb and Ferreira, 2016	3	2.0	4.5	5.9	6.5	2.5	0.92	1.23
Lewis et al., 2013	3.2	2.0	3.4	5.5	6.1	2.5	0.87	1.48
Maximum significant wave height during cyclone Sidr (m)								
This study	1.7	1.6	2.2	2.9	1.6	3.1		
Deb and Ferreira, 2016	3.2	1.8	3.1	2.1	3	3	0.87	0.97

To gain further confidence, the model water levels are compared with the field survey report, which was conducted by Shibayama et al. (2008). The comparison demonstrate that the model is successfully reproduced the spatial variations of water level during Cyclone Sidr in Figure 3.4. Overall, the model in this study reproduces the storm surge event in the GBMD reasonably well.

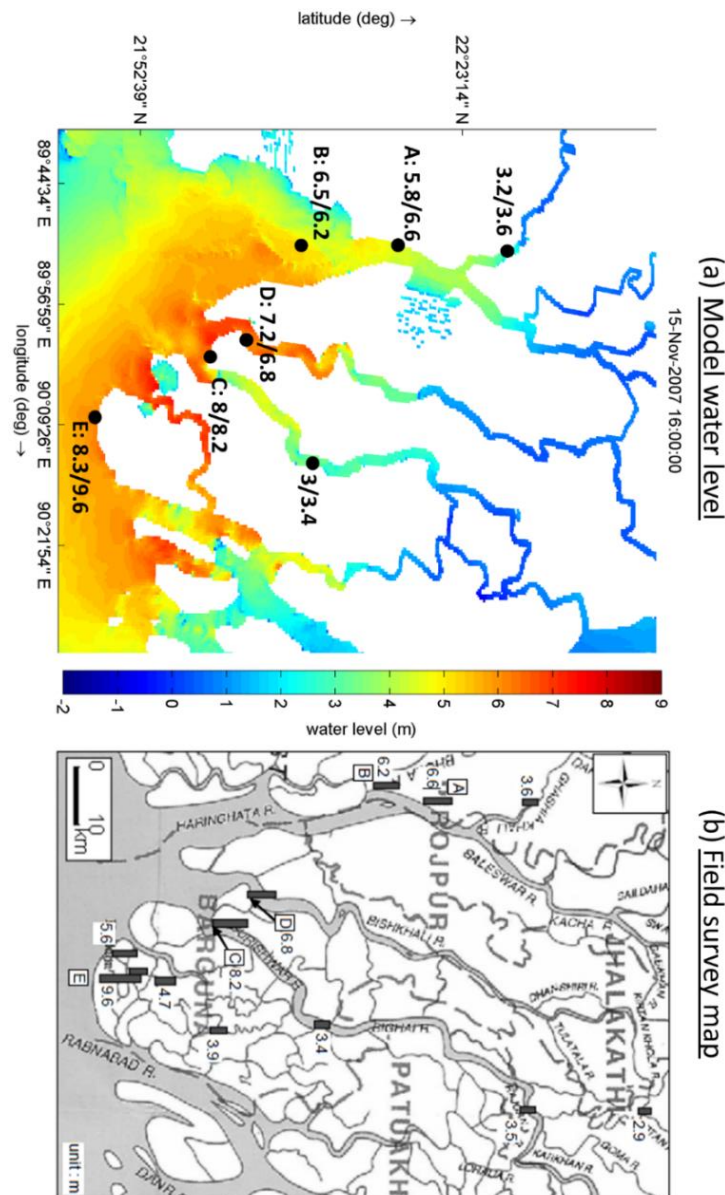


Figure 3.4. (a) Spatial variations of model water level at one-hour after the landfall. Black circles represent the surveyed locations by Shibayama et al. (2008). Numbers represent the maximum water level (Model maximum / Survey maximum water level). (b) Field survey locations map and maximum water level observations. At locations near the E point, there are small channels less than 50 m width, which are not included in the model. Hence, the comparison is not possible at that location.

3.4.2 Surface water elevation variations

Cyclone Sidr made landfall at Khepupara on the Bangladesh coast in the western GBMD at 1500 UTC 15 November 2007. The cyclone tracked slightly north-northeastward and passed close to several stations including Khepupara, Galachipa, D1 and Hironpoint (Figure 3.2a), which recorded maximum winds of $\sim 50 \text{ m s}^{-1}$.

As the cyclone approached the coast it produced storm surges across the GBMD with the central GBMD (Figure 3.2a) observing a high-water level of up to 7 m during the landfall event (Deb and Ferreira, 2016). Figure 3.5 shows the evolution of the model surface water elevation for the real case control simulation (Run7 in Table 3.2) at 3-hourly intervals during 15 November 2007. At 1200 UTC, while the centre of Cyclone Sidr was still well offshore (Figure 3.5a), the western (green box in Figure 3.2a) and central (orange box in Figure 3.2a) GBMD coastline was under the influence of the outer easterly wind field north of the cyclone centre. The eastern GBMD (blue box in Figure 3.2a) was located east of the cyclone centre and the outer-core winds extending onto this coastline were southerly. Because of the funnel shaped geometry of the GBMD coastline, the water elevation initially increased on the eastern edge of the estuary mouth in the eastern GBMD driven by the southerly outer-core wind field east of the cyclone centre.

By 1500 UTC as the cyclone approached land, the strong inner-core wind field began to directly affect the coast in the western and central GBMD (Figure 3.5b). The strong inner-core southerlies north and east of the cyclone centre drove increased water elevations in the western GBMD with a maximum of 7.2 m observed at Khepupara (red arrow in Figure 3.2a). As the cyclone continued to move inland over the course of the next few hours (Figure 3.5c, d), the strong wind field moved inland over the central GBMD, and the high water levels were driven inland along the numerous rivers and

narrow channels in the delta region with anomalous water levels of more than 4 m (Figure 3.5c, 3d). By 2100 UTC the high-water levels had spread inland up the Meghna River and east to the eastern GBMD.

Throughout the period as the cyclone approached, made landfall and then continued to move inland, the main storm surge shifted across the delta region with initial high-water levels in the eastern GBMD while Cyclone Sidr was still well offshore and then shifting to the landfall region in the western GBMD as Cyclone Sidr made landfall and then extending east to the central, and finally back to the eastern GBMD. The main driving force for the increased water levels were the cyclonic winds that were directed perpendicular to the coast (e.g., Figure 3.5b-d). Thus, the eastern GBMD was affected earlier than the other regions because the outer core winds ahead of the cyclone centre were directed perpendicular to that coastline ahead of the arrival of the cyclone inner core. Even after the most intense inner-core winds had moved inland and dissipated, the strong outer-core storm-force winds ($\sim 24 \text{ m s}^{-1}$) still continued to force storm surge into the central and eastern GBMD (Figure 3.5d). However, in the regions where the winds were directed parallel to the coast there appeared to be little forcing for storm surge.

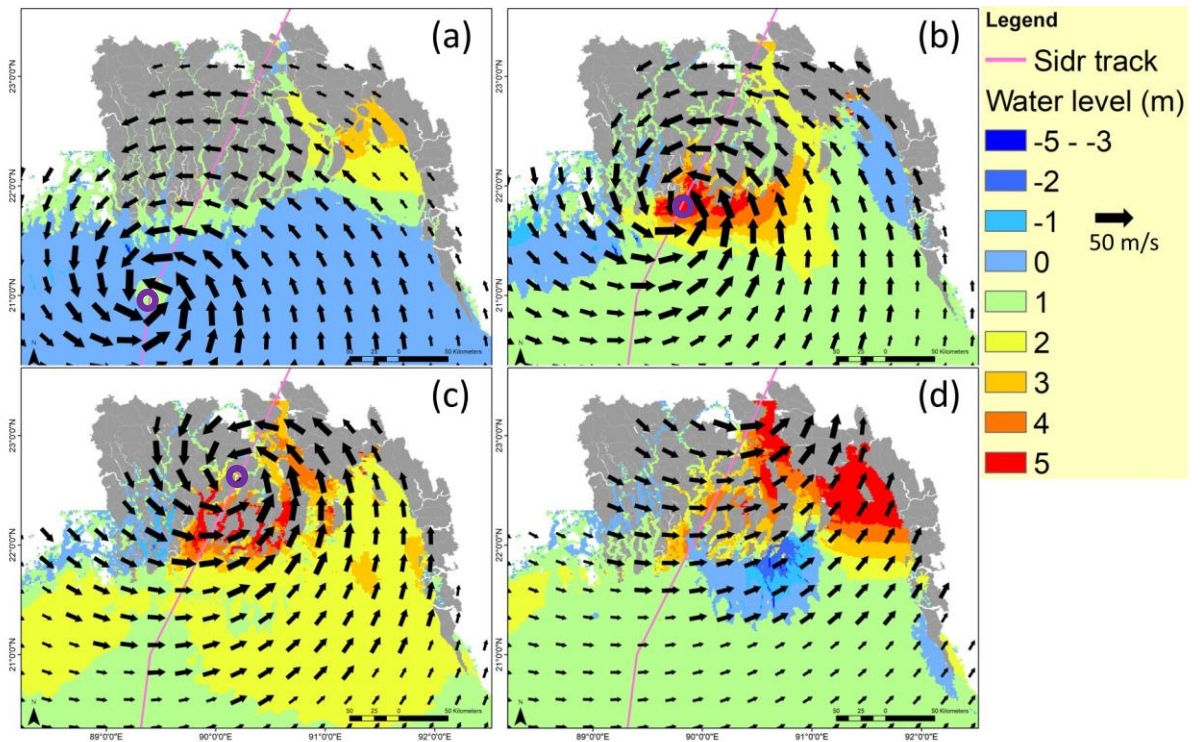


Figure 3.5. Simulated spatial variations of surface water elevation (shading) and the surface wind field during Cyclone Sidr on 15 November 2007 at: (a) 1200 UTC; (b) 1500 UTC; (c) 1800 UTC; and (d) 2100 UTC. The yellow cross and purple line denote the cyclone eye location and track, respectively. In the current study, the surface water elevation is defined as the total water level driven by a combined tide, wind, and wave.

3.4.3 Role of tide, wind and waves in the storm surge height

The magnitude variations of the surface elevation depend not only on the wind but also on the tides and wind-driven waves. Although the strong surface wind is the dominant factor in generating the cyclone-induced storm surge height, other factors including the tidal phase and wave-current interactions can also contribute further to the surge height. To study the influence of the tide, cyclonic wind, and wave on the storm surge height, the model is applied to three different experiments: (a) only tide (Run2 in Table 3.2), (b) tide and wind (Run3), and (c) considering tide, wind and wave together using two-way coupling (Run7). The time series of residual water level variations at different stations across the GBMD are presented in Figure 3.6. Residual water level is computed by subtracting tidal water level from the total water level.

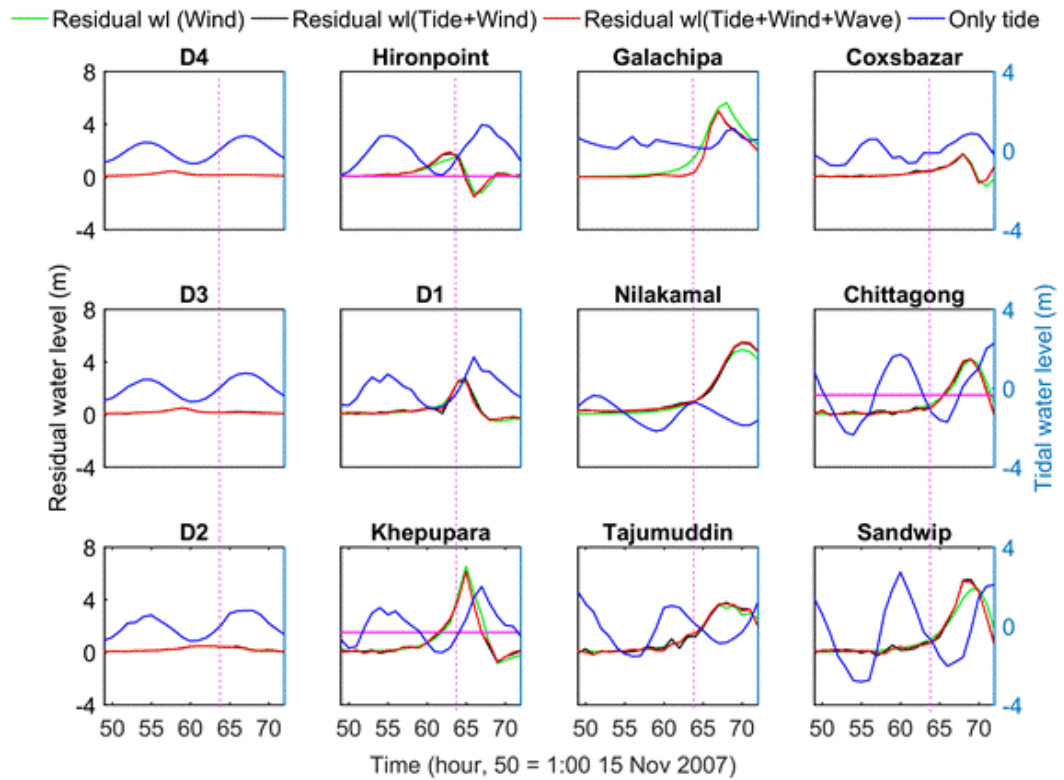


Figure 3.6. Simulated tides and residual water level at different stations during the landfall of Cyclone Sidr for the following scenarios: only tide (blue), only wind (green), tide and wind (black; cyclonic wind stress increase along with tide), and the real case (red; cyclonic wind stress along with tide and wave). The residual water level is calculated by subtracting the tidal water level from the simulated total water level. Purple dashed and purple solid lines represents the landfall time and observed maximum residual water level.

The total water level of the storm surge height is a combined result of tide, wind and pressure, and wave influence on the water level. By analysing the sensitivity of the water level to changes in cyclone pressure, we found that the contribution related to the pressure in the total water level (isostatic response) is negligible compared to the wind setup (< 10 % of the wind setup). Therefore, the contribution of the isostatic response of the sea level to surface elevation variation is ignored in the rest of the discussion. Figure 3.6 demonstrates that the landfall time (64 hours in Figure 3.6) occurs during different tidal phases across the GBMD. Hussain and Tajima (2017) discussed the tidal characteristics in the eastern part of the GBMD. They observed an approximately 2-h

tidal phase difference between the incoming tides at the western end and incoming tides at the eastern end. As a result, the tide propagates in a northeast direction toward the Bangladesh coast in an oblique manner and simultaneously reaches the coast of Hironpoint (station located on the left side of the cyclone track in Figure 3.2a) and Coxsbazar (Figure 3.2a), which is also mentioned by Carvajal et al. (2011). Thus, during the landfall time, the tidal phases are in flood tide at the western GBMD (Khepupara) and ebb tide in the central GBMD (Tajumuddin). Due to the lower water level during the ebb tide phase in the central GBMD, Tajumuddin and Sandwip stations show relatively lower surge heights compared to the stations in the flood tide phase (e.g., Khepupara).

During a cyclone-induced storm surge event, the wind is typically the dominant factor producing the storm surge. By comparing the “only wind” scenario with the “wind + tide” and the “wind + tide + wave” scenarios, it can be seen that the wind setup (described as wind driven water level) explains the total water level at all stations except Khepupara, Galachipa, Nilkamal and Sandwip (Figure 3.6). The inconsistencies in residual water levels among the “only wind” scenario and other scenarios at these stations demonstrate that the wind setup is inversely proportional to total water depth, which is affected by tides (see Figure B.4 in Appendix B). For example, the residual water level differences among the “only wind” and “wind + tide” are resulted from the wind-tide interaction, which cause the wind setup to be decreased at high tide (e.g., 0.05-0.04 m Galachipa) and increased at low tide (e.g., 0.72-0.53 m at Sandwip). Furthermore, the stations located offshore are less affected by wind setup. This is why D2-D4 (> 100 m) have a lower maximum storm surge height compared to the station located closer to the coast (e.g., D1 < 15 m) even though all these stations are close to the cyclone path.

During a cyclonic event, the water level variability at a location relative to the cyclone centre is affected by the speed and direction of the winds at the station, as well as how the cyclone changes over time as it passes by. Hence, the timing of the peak water level due to the wind also varies station to station (See Figure B.5 in Appendix B). For example, Chittagong and Coxsbazar are located approximately 300 km from the landfall location. Though these two stations are relatively less affected by the strong cyclonic wind, they exhibit peaks in the water levels 4 hours after the landfall time (Figure 3.6). Results show that the peak water levels at Chittagong and Coxsbazar are 4 m and 1.8 m higher, respectively, when compared to the “only tide” scenario. Khepupara and Galachipa experience higher residual water levels compared to other stations. Both these two stations are located in the right side and close to the cyclone track in the strongest wind region. Hironpoint is also located close to the cyclone track, but on the left side of the cyclone track (Figure 3.2a). The wind direction on the right side of the cyclone eye is southerly, and the left side of the cyclone eye is northerly during the approach of, and at landfall. Therefore, wind setdown reduces the water level by up to 1.5 m at Hironpoint compared with the tidal water level during landfall regardless of whether waves are included in the simulation or not. All the other stations are located on the right of track and are embedded in the generally southerly cyclonic flow. For these stations, there is significantly higher residual water levels compared with the only tide driven experiment because of the wind setup.

When waves are also considered (Run7), there is no clear difference in the water levels compared to the wind and tide scenario (Run3), and this demonstrates the dominant role of wind setup in the cyclone-induced storm surge height. The tidal phase and amplitude also play a supporting role by modifying the combined influence of wind and tide on the storm surge height.

3.4.4 Role of wave-current interaction in wave setup

Although the wind-driven wave contribution to the total water level is much less compared to the wind-driven water level there is an increment of over 0.25 m in the water level near Khepupara due to the wave coupling (Figure 3.7). During low tide at 1200 UTC 15 November, the wind is easterly, and the wind-driven waves produce a positive increment of up to 0.15 m of water level in the estuary and a maximum decrease of 0.10 m in the area close to the cyclone eye (Figure 3.7a). During high tide at 1800 UTC, which is 3 hours after landfall, the wind has switched to westerly (Figure 3.7b). Furthermore, the higher surface elevations due to the high tide contribute further to the setup from the waves (e.g., Figure 3.7c). Hence, the wave coupling produces higher surface elevations near Khepupara compared with there being no wave coupling. Wave setdown also occurs in the mouth of the estuaries. This is because after landfall, the wind blows from the land to the ocean near Khepupara. Therefore, the radiation stress generated from the strong wind-driven wave moves water volume from the land toward the ocean, which causes wave setdown at the estuary mouth. Thus, waves have the potential to increase (decrease) the storm surge height up to 0.3 m through wave setup (setdown) near the landfall area in the GBMD during a cyclone-induced storm surge event. Figure 3.7 demonstrates that the wave influence on the water level varies with the cyclonic wind direction and tidal phase.

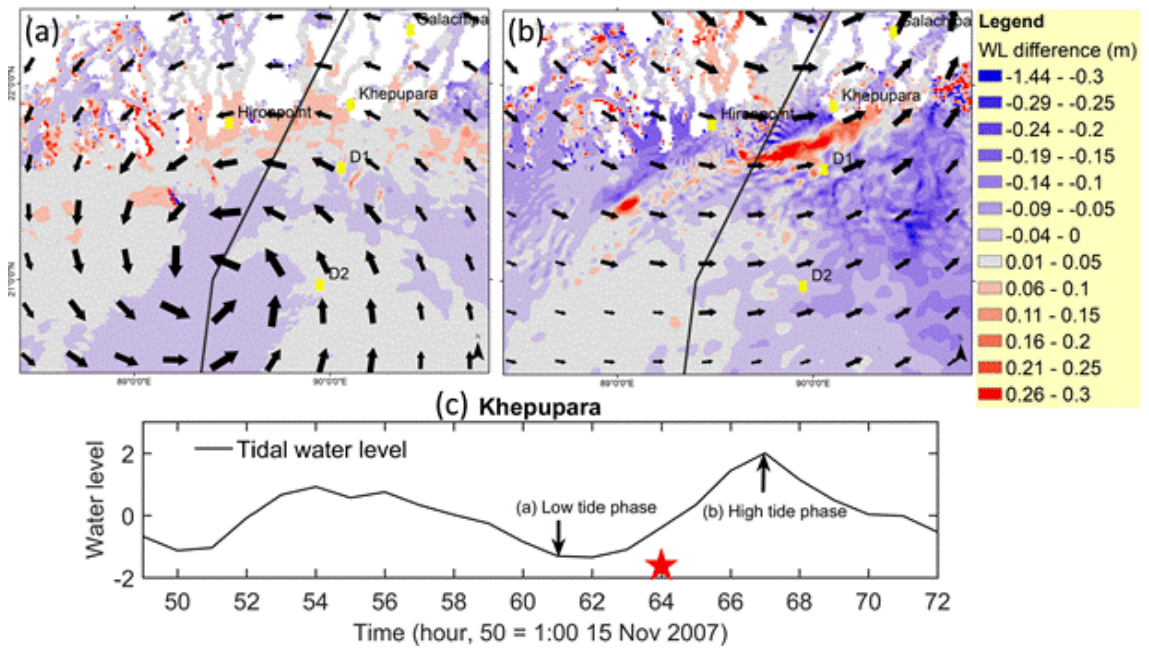


Figure 3.7. Difference in the water level between the run with waves (Run7) and the run without waves (Run3) at: (a) Low tide at 1200 UTC 15 November; (b) High tide at 1800 UTC 15 November 2007; and (c) Time series of the tidal water level variations (Run2) at Khepupara. The water level difference is calculated as Run7 minus Run3. Positive (negative) water level difference denotes wave setup (setdown). The length of the vector represents wind speed ($\text{max}=50 \text{ m s}^{-1}$). The red star in panel (c) denotes the landfall time.

Figure 3.8 shows the wave setup variations at four stations located either on, or just off the GBMD coast and represents the different bathymetric features and tidal phases. The depths of Khepupara and D1 are less than 15 m, whereas Tajumuddin and D2 are less than 25 m and 100 m, respectively. D1 and D2 are located in the open ocean and Khepupara is located on the coast. Tajumuddin is located at the estuary mouth and is surrounded by shallow lands and islands. All these stations are in the flood tide phase during the cyclone landfall except Tajumuddin, which is in the ebb tide phase.

The setups due to wave for ‘OWC’ (Run5 in Table 3.2), ‘Wave to flow’ (Run6) and ‘WCI’ (Run7) scenarios are estimated by comparing the water level with the base flow model (without wave, Run3) result. Figure 3.8 illustrates that during high tide wave-current interactions produce a higher wave setup at Khepupara relative to no wave-

current interactions after landfall has occurred. In the ‘Wave to flow’ scenario, the radiation stress gradient is independent to the variation of currents and water levels in Equation 3.8. In the ‘OWC’ scenario, the water level and current are only varied due to the radiation stress gradient as tides and winds are ignored in the FLOW model. It should be noted that the radiation stress gradients are the same in both ‘Wave to flow’ and ‘OWC’ scenarios. Hence, the differences between wave setups in both ‘Wave to flow’ and ‘OWC’ scenarios result from the influence of tides and winds in the total water depths and mean surface elevations in Equation 3.8.

The ‘WCI’ scenario produces a maximum wave setup of 0.3 m at Khepupara, four hours after the landfall time (Figure 3.8b). The maximum wave setup of 0.07 m in the ‘OWC’ scenario is observed during the landfall time and the maximum wave setdown by 0.07 m four hours after landfall at Khepupara. In the ‘WCI’, the combined influence of tides, winds and waves results 7.5 m higher water depth (see Figure B.6 in Appendix B) at Khepupara during landfall compared to the ‘Only Wave’ scenario. According to Equation 3.8, if the radiation stress gradient is independent to the variation of water levels (in one-way coupling method, e.g., Wave to flow), then it is the high/low tide, causing larger/smaller water depth that will produce a smaller/larger increase in wave setup. Therefore, the ‘Wave to flow’ scenario produces higher wave setup (0.05 m) at 1200 UTC 15 November compared to the ‘OWC’ scenario (low tide phase in Khepupara). At the landfall time, 1500 UTC 15 November, the increased water depth along with the unchanged radiation stress gradient causes 0.04 m lower wave-setup in the ‘Wave to flow’ compared to the ‘OWC’ scenario.

Interestingly, the ‘WCI’ scenario changes from wave setdown to wave setup at 1900 UTC 15 November compared to the ‘OWC’ scenario at Khepupara. The ‘Wave to flow’ scenario also generates a wave setup of 0.07 m at 1900 UTC 15 November. This

indicates that the interaction between waves and currents can change the wave setdown to wave setup. As the radiation stress gradients are the same in both the ‘Wave to flow’ and the ‘OWC’ scenarios, the transformation of wave setdown to setup in ‘Wave to flow’ must result from the increased water depth and mean surface elevations. In the ‘WCI’ scenario, the radiation stress gradient is increased by approximately two times higher than the other scenarios due to the increased wave energy dissipation (Figure 3.8f). Therefore, the ‘WCI’ scenario generates three times higher wave setup than the ‘Wave to flow’ scenario. The reason behind increased wave energy dissipation at Khepupara will be discussed further in a later section.

The maximum wave setup (0.8 m) and setdown (0.4 m) among all the scenarios are observed at Tajumuddin in the ‘Wave to flow’ scenario (Figure 3.8a). The maximum wave setup and maximum wave setdown are observed two hours (1300 UTC) and one hour (1400 UTC 15 November) earlier than the landfall time during the flood tide phase at Tajumuddin, respectively. The wave setup and setdown follow a similar trend over the period of the storm surge event with different magnitudes at Tajumuddin for both the ‘WCI’ and ‘Wave to flow’ scenarios. After the landfall time, the wave setups vary between -0.1 m (setdown) to 0.1 m at Tajumuddin for the ‘WCI’ scenario, whereas the wave setups vary between -0.3 m (setdown) to 0.17 m for the ‘Wave to flow’ scenario. Due to its location at the estuary mouth, strong current variations occur at Tajumuddin with the flood and ebb tides (Figure 3.10f). Figure 3.8e shows that the magnitude of the radiation stress gradient is negligible ($< 0.1 \text{ kg m}^{-1} \text{ s}^{-2}$) at Tajumuddin prior to the landfall time. The ‘OWC’ scenario shows negligible variation in wave setup (0.08 m setdown) at Tajumuddin compared to other scenarios, which indicates there is only a weak influence of waves in the wave setup. Considering the current and water level variation (from the FLOW model) in the other two scenarios, a greater change is observed in the

wave setup at Tajumuddin due to the increased water depth. Therefore, it is evident that the wave setup variations at Tajumuddin prior to the landfall time result from the tidal influence on the total water depth and mean water level according to Equation 3.8.

The ‘Wave to flow’ scenario produces the highest setup at D1 and D2 stations. Both the stations are located in the open ocean, and the cyclone eye crosses these stations three hours earlier than the landfall time. The WCI at both D1 and D2 produces slightly lower setup (0.01 m) and higher setdown (0.01 m) during the surge event than the ‘Wave to flow’. The wave setup varies between -0.02 to 0.09 m at D2 for all the scenarios. These lower setups are associated with the less wave breaking due to the deep ocean (< 100 m). Due to the location in a relatively shallow ocean, D1 experiences higher wave setup and setdown than D2 due to the increased wave breaking, which is also reflected in the radiation stress gradient magnitude variations in Figure 3.8g-h.

Finally, the dynamic characteristics of water level elevation and wave-induced setup and setdown along with the coastal areas, particularly during a storm surge event, have cumulative effects that depend on the mutual interaction between waves, currents, and tides (Bhaskaran et al., 2020). Waves are modified by the presence of currents generated by tide and surge. Breaking waves in the shallow region contribute to radiation stresses that affect resultant water level and circulation through wave-induced setup. Figure 3.8 demonstrates that ignoring the wave-current interaction in the computation can cause approximately 0.3 m lower wave setup in the coastal area (Khepupara). Moreover, this may produce spurious wave setdown in the region (strongly influenced by current, e.g., Tajumuddin), when there is really wave setup occurring. This type of error can result in incorrect assumptions in the management plan for cyclones. The wave setup and setdown are directly related to the generation and dissipation of wave energy. During the propagation of waves into shallower regions from the deep ocean, the wave

heights are modified through breaking resulted from different wave dissipation process. Therefore, the wave height variations and wave dissipations during Cyclone Sidr are further investigated in the next section.

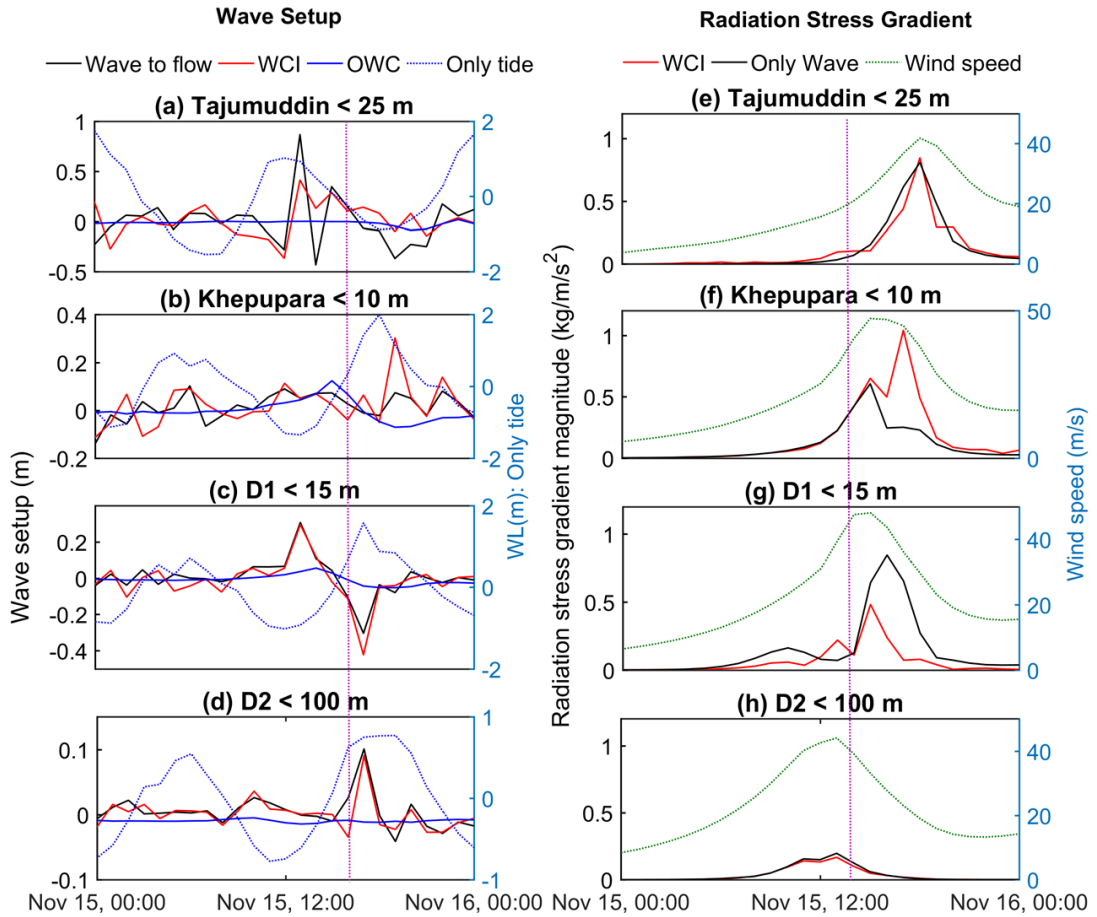


Figure 3.8. Simulated wave setups (a-d) along with tidal water level variations, and (e-h) radiation stress gradient magnitude variations with wind speed at: (a), (e) Tajumuddin; (b), (f) Khepupara; (c), (g) D1; and (d), (h) D2. The dotted line indicates the landfall time. The wave setup is plotted on different scales to enhance visibility.

3.4.5 Effects of wave-current interaction on wave

3.4.5.1 Effects on significant wave height

During cyclonic events, waves create significant impacts over the whole continental shelf and Bangladesh coast (As-Salek, 1998). Cyclonic events generate higher wave height variations in the shallow compared with deep ocean regions due to

the strong wind field. During the propagation of the wind-driven waves from the deep ocean to shallower areas, the magnitude of the wave height is modified through wave-current interactions, wave dissipation by bottom friction, whitecapping, and depth-induced breaking. The results of the ‘Only Wave’ (Run1) and ‘WCI’ (Run7) scenarios at stations across the GBMD are presented in Figure 3.9 to investigate the effects of the wave-current interactions on the waves. Including the effect of wave-current interactions on waves produces a comparatively higher SWH than including only wind-driven waves at all the stations except Tajumuddin. The highest increase of SWH (1.19 m) is observed at D1, and the highest decrease of SWH is observed at Tajumuddin (-0.36 m) due to the wave-current interaction. Near to the landfall location (Khepupara), the SWH is increased by 59 % (1.07 m) due to the wave-current interaction. The stations located on the right side of track within the highest winds in the inner core at landfall (Khepupara, Galachipa and D1) have the highest percentages of change (more than 40 %) in SWH from the wave-current interaction. More details of the SWH change can be found in Table B.3 in Appendix B. Neglecting the mutual influence of waves and current on each other can cause an under-estimation of the SWH by 1.2 m during a Sidr-like storm-surge event in the GBMD.

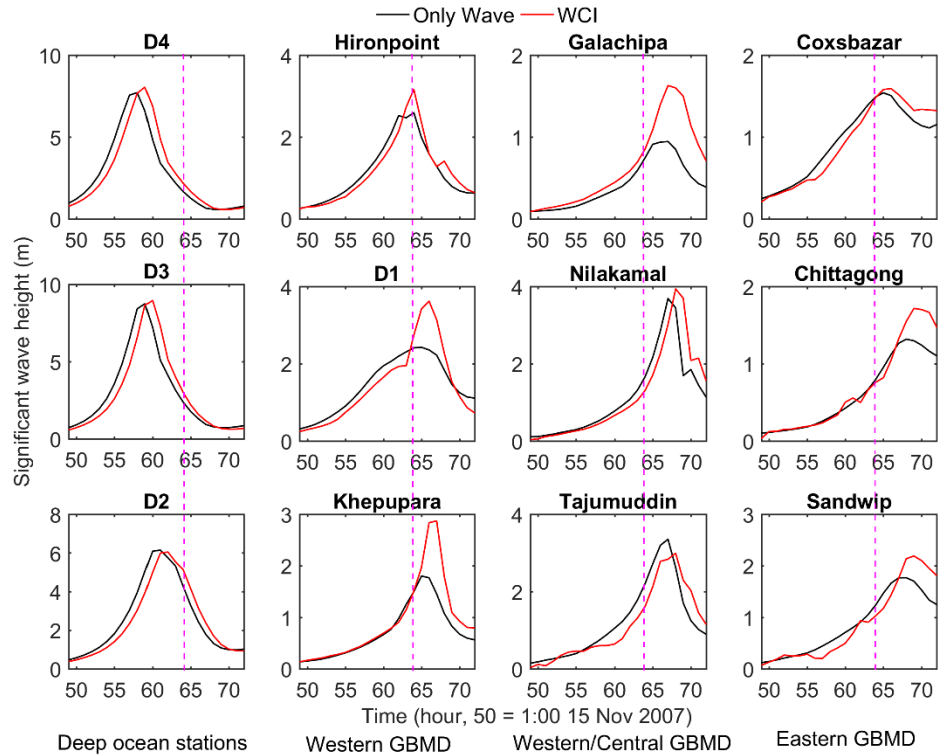


Figure 3.9. Significant wave height variations for the 'Only wave' and 'Wave-current interaction' scenarios during the landfall of Cyclone Sidr. The purple line denotes the landfall time at 1500 UTC 15 November 2007.

3.4.5.2 Influence of effective wind stress on SWH

The 'WCI' scenario produces higher SWH compared to the 'Only Wave' scenario. Both the scenarios are conducted by applying the same wind field and considered all the wave dissipation processes. The only difference is about the influence of the current and water level variations in the 'WCI' scenario. The results show that the generation of the wind-wave is increased in the 'WCI' scenario for the most of stations. The effective wind determines the wind-wave growth, i.e., the relative wind effect (defined as the vectorial difference between wind vector and current vector (Deltares, 2013b)). To investigate the increase in SWH in the 'WCI' scenario further, the amplitude and direction of the current and wind are examined at three different stations: Khepupara, D2, and Tajumuddin (Figure 3.10). The wave-driven current is computed

from the ‘OWC (Only Wave-driven)’ scenario (Run5 in Table 3.2). The same wind field as the ‘WCI’ scenario is used to produce the wind-wave. Figure 3.10a shows that the current-direction is in the opposite direction to the wind-direction in the ‘WCI’ scenario at Khepupara, whereas both the current and wind are in the same direction in the ‘OWC’ scenario. At Khepupara, the current is dominated by a channel steered flood tidal current resulting its direction in opposite to that of the wind in the ‘WCI’ scenario. The ‘WCI’ scenario produces a 1.6 m s^{-1} higher magnitude of surface current than the ‘OWC’ scenario (Figure 3.10d) with a correspondingly higher effective wind stress at Khepupara. This higher effective wind stress produced by the wind-current interaction produces a higher SWH than the ‘Only Wave’ in Figure 3.9. Conversely, the ‘WCI’ scenario generates a higher magnitude of surface current at D2, but both the current and wind direction are almost in the same direction (Figure 3.10b and e). The current and wind direction are also in the same direction at Tajumuddin for both the scenarios during the strong wind period ($> 20 \text{ m s}^{-1}$). Similar directions of the current and the wind reduce the effective wind stress magnitude, which causes a lower generation of wind-driven waves (Deltares, 2013b). When the current and winds are in opposite directions it produces a higher effective wind stress, which increases wind-wave generation (S_{in} in Equation 3.7). This illustrates that the WCI can generate higher amplitude waves by modifying the effective wind stress by changing the current direction with respect to the wind direction. Therefore, the WCI scenario generates higher SWH than the Only Wave scenario at Khepupara. Further influence of current and wave direction on SWH is discussed in the next section.

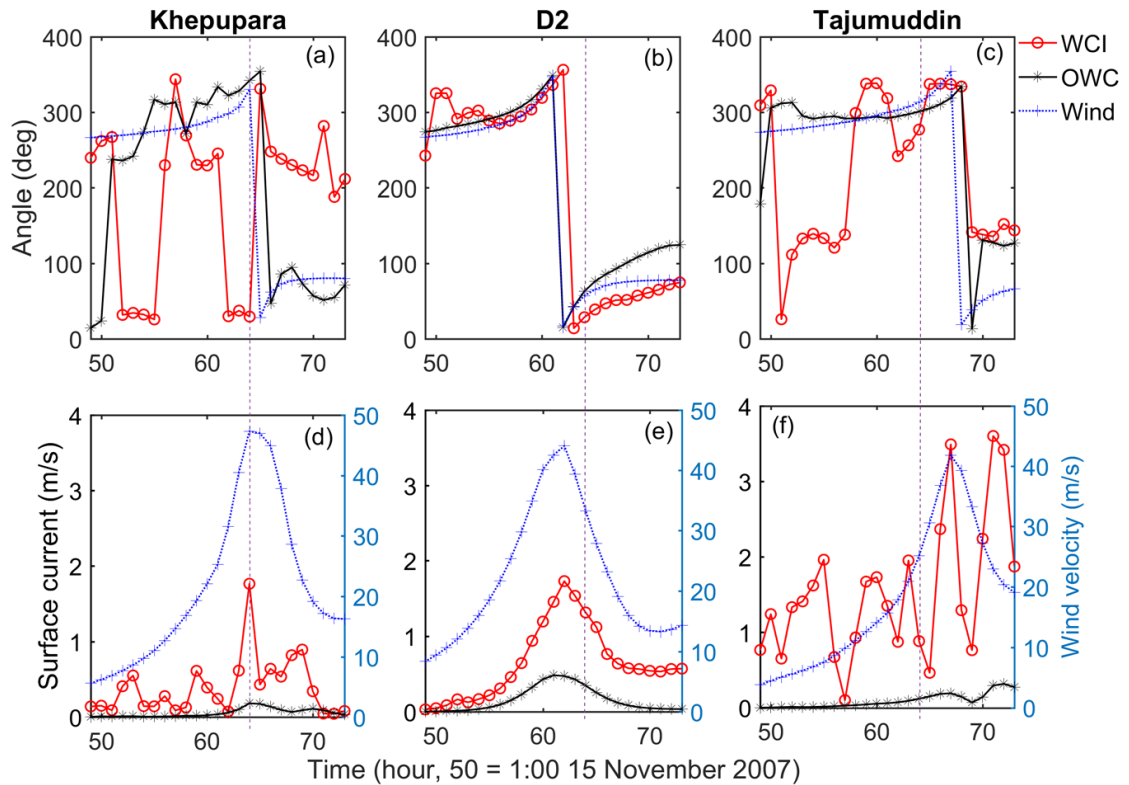


Figure 3.10. Direction and amplitude variations of the surface current and wind at (a), (d) Khepupara, (b), (e) D2 and (c), (f) Tajumuddin for different scenarios. The dashed line represents the cyclone landfall time 1500 UTC 15 November 2007.

3.4.5.3 Influence of water level, current and wave direction on SWH

Three additional one-way model experiments are conducted to investigate the sensitivity of the SWH variations with the water level and current variations. To study the combined influence of water level and current variations, Run4 (WL+Cu to Wv) is conducted, where the water level and current variations can influence waves using one-way coupling. Similarly, the individual influence of the water level and the current is investigated by running Run4_wl and Run4_cu, respectively. Details of the experiments are described in Table 3.2. The variations of SWH under different forcings are presented in Figure 3.11. The ‘WCI’ (Run7) scenario generates the highest amplitude of SWH at Khepupara, whereas the highest SWH at Tajumuddin is observed in the Run4_wl (WL to Wv). Minimum amplitudes of SWH at all stations are observed in Run4_cu (Cu to Wv).

Wv). In Run4_cu (Cu to Wv), the cyclone-induced storm surge height and tidal water level variations are ignored. Therefore, the wave dissipation in Run4_cu (Cu to Wv) should be more affected by depth-induced breaking and bottom friction compared to the other experiments due to water depth changes. When the depth is the greatest (at D2), Run4_cu (Cu to Wv) produces approximately the same magnitude of SWH compared to all other experiments. Thus, depth-induced breaking and bed friction do not affect the waves at D2. Stations that are located in shallow waters (Khepupara (< 10 m), Tajumuddin (< 25 m) and D1 (< 15 m)) compared to D2, have a higher SWH produced by the Run4_wl (WL to Wv) compared with the Run1 (Only wind driven wave (OW)) because the effect of bed friction and depth-induced breaking on the wave is reduced.

However, there are other differences among these three stations. At Tajumuddin, Run4 (WL + Cu to Wv), Run4_cu (Cu to Wv) and Run7 (WCI) generate the same maximum SWH with Run4 and Run4_cu almost exactly the same. This indicates that the current plays a dominant role over the water level in the modulation of SWH at Tajumuddin if the wave-current interaction is included. Conversely, Run4_wl (WL to Wv) produces a similar SWH variation with Run4 (WL + Cu to Wv) at Khepupara, suggests that water level plays a dominant role in the wave-current interaction.

The high and low magnitudes of SWH are found in the WCI scenario compared to other scenarios at Khepupara and Tajumuddin, respectively. As discussed in the previous section, the increased/decreased effective wind stress from the opposite/same direction of wind and current causes these high and low magnitudes of SWH at Khepupara and Tajumuddin, respectively. Moreover, from the kinematics in spatial and spectral space (Equation 3.1-3.3), it is evident that the second and third left-side terms will be smaller in Equation 3.6 when waves and currents are propagating in opposite directions. This will result in an increase in the wave energy and, therefore, also in the

wave height. With waves and currents propagating in the same direction, the effect is reversed (Viitak et al., 2016). At Khepupara, the wave and current are in opposite directions in the WCI, whereas both are in the same directions at Tajumuddin. Thus, the wave-current interaction at Khepupara generates higher SWH than the other scenarios. As the current and the wave are propagating more or less in the same direction (Figure 3.10c), this results in a decrease of SWH (0.4 m) at Tajumuddin in the wave-current interaction scenario compared to the only wave scenario. The similar variations of SWH are also observed at D2. The order of influence of the current, water level, and wave-current interaction on the SWH modulation is the same at Khepupara and D1. Finally, the results illustrate that the current plays a dominant role in the modulation of SWH over the water level in the deep ocean and deeper areas like Tajumuddin (< 25 m). The water level becomes the dominant factor when the propagates in the shallower region from the deeper ocean. The influence of the wave-current interaction on the SWH modulation depends not only on the current and wind direction but also on the wave and current direction and water level.

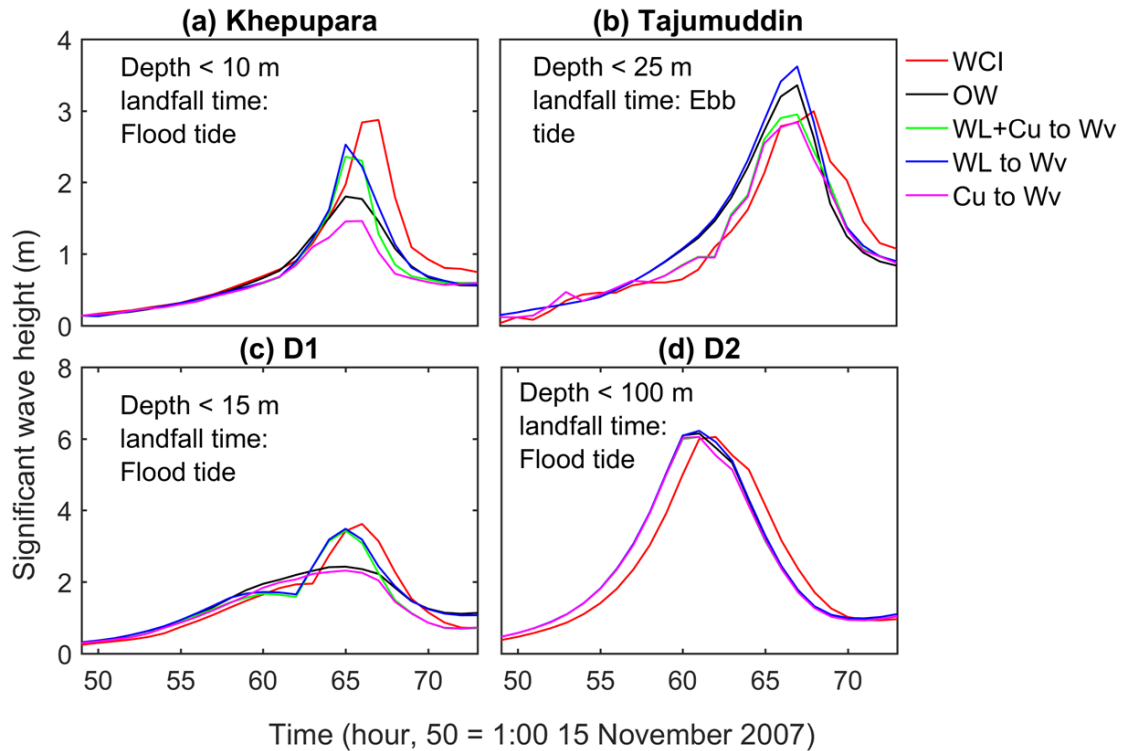


Figure 3.11. Influence of different parameters on significant wave height during Cyclone Sidr at: (a) Khepupara; (b) Tajumuddin; (c) D1; and (d) D2.

3.4.5.4 Wave dissipation

The presence of a shallow continental shelf and the ‘Swatch of no ground’ (a submerged canyon < 1500 m) causes wave energy dissipation 60-80 km from the coastline. The strong dissipation of the wave energy results in a lower magnitude of wave height (< 2 m) at the coast. The tidal water level variations will also modulate the wave height in the shallow region near the coast. To study the wave dissipation processes with and without the wave-current interaction conditions, six additional model experiments (Run7a-c and Run8a-c) are conducted by considering the individual dissipation term of Equation 3.7 in the WAVE model. The experiment details are described in Table 3.2. The maximum amplitudes of SWH and wave energy dissipation at Khepupara are presented in Figure 3.12 without wave-current interaction (‘Only wave’ in Figure 3.12) and with wave-current interaction (‘WCI’ in Figure 3.12). The

timing of maximum amplitudes of SWH varies based on factors such as the timing of the maximum wind and current direction, and total water level. Results show that the whitecapping process is dominant among all the wave dissipation terms for both conditions at Khepupara. The whitecapping term is represented by the pulse-based model of Hasselmann (1974) in the WAVE model, which is directly proportional to the wave steepness (The SWAN team, 2014). During the opposing current, there is increased whitecapping of the waves because the wave number and wave steepness increase due to the opposing current. Consequently, the opposite directions of current and wave increase the wave height by increasing the wave energy as discussed in section 3.4.5.3. In the 'WCI' simulation, the current and the wind are in opposite directions at Khepupara. As the wind-wave follows the wind direction, the wave propagates in the opposite direction to the current at Khepupara. Therefore, the maximum wave dissipation related to whitecapping is more than doubled when wave-current interaction is included. The dissipation due to bottom friction is small for both scenarios because with higher water levels bottom friction is reduced resulting in the highest SWH when only this term is considered.

Thus, the higher amplitudes of maximum SWH and wave energy dissipation at Khepupara result from increased effective wind stress and increased wave steepness, respectively. The opposite directions of current and wind increase the effective wind stress, which results in higher generation of wind-driven waves. Conversely, the opposite directions of waves and current increase the wave energy and also result in increased wave steepness. Higher wave energy causes a higher magnitude of wave energy dissipation (due to the wave energy term in all the dissipation equations, Equation 3.10-3.12). Finally, the dissipation related to the whitecapping term in Equation 3.7 is more sensitive than the dissipations related to the depth-induced breaking and the bottom

friction during a cyclone-induced storm surge event at Khepupara. The wave-current interaction plays a significant role in estimating wave energy dissipation and significant wave height.

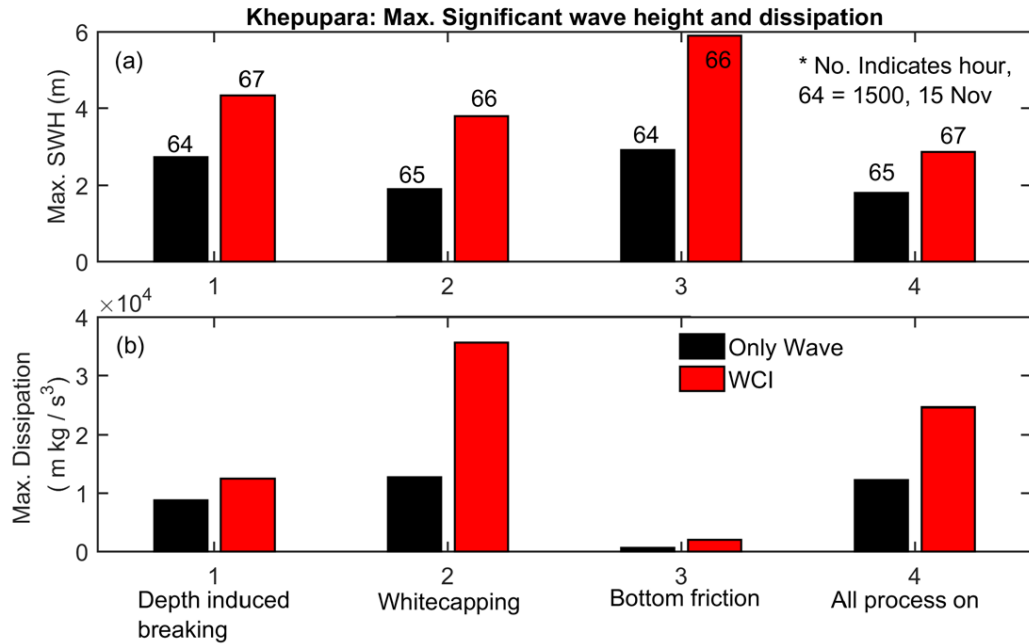


Figure 3.12. Maximum: (a) significant wave height; and (b) wave energy variations with and without wave-current interaction at Khepupara for Cyclone Sidr for different wave dissipation processes. Maximum amplitudes of SWH and dissipation are observed at different times of the cyclone passage for different scenarios.

To further quantify WCI influence on the SWH modulation, maximum SWH variations along the GBMD are plotted for different wave dissipation conditions for “only wave” and WCI scenarios in Figure 3.13. Results demonstrate that the WCI increases the SWH magnitude at all stations. When only depth-induced breaking is included, the SWH magnitudes are increased up to 50% in shallow regions in the WCI condition compared to the “only wave” condition (Figure 3.13a). This suggests that the depth-induced wave breaking in shallow regions is reduced due to the higher water level and variations in currents relative to “only wave”. When only whitecapping dissipation is allowed, then WCI causes maximum change in SWH in shallow regions where the

current and wind are in opposite directions (Figure 3.13b). When only bottom friction dissipation is allowed, then WCI also produces a higher change in SWH in shallow regions compared to the “only wave” condition (Figure 3.13c). The ‘whitecapping’ dissipation produces the closest maximum SWH variations to the realistic case (Figure 3.13d). This suggests that dissipation related to whitecapping plays a dominant role among the three dissipation terms during the cyclone-induced storm surge event. Furthermore, wave-current interaction causes higher SWH modulation in shallow regions (-50 to 50 km from Khepupara) compared with in the deep ocean (beyond 50 km from the coast) and the wave energy dissipation is one of the key factors affecting the SWH variations in those deep-ocean regions.

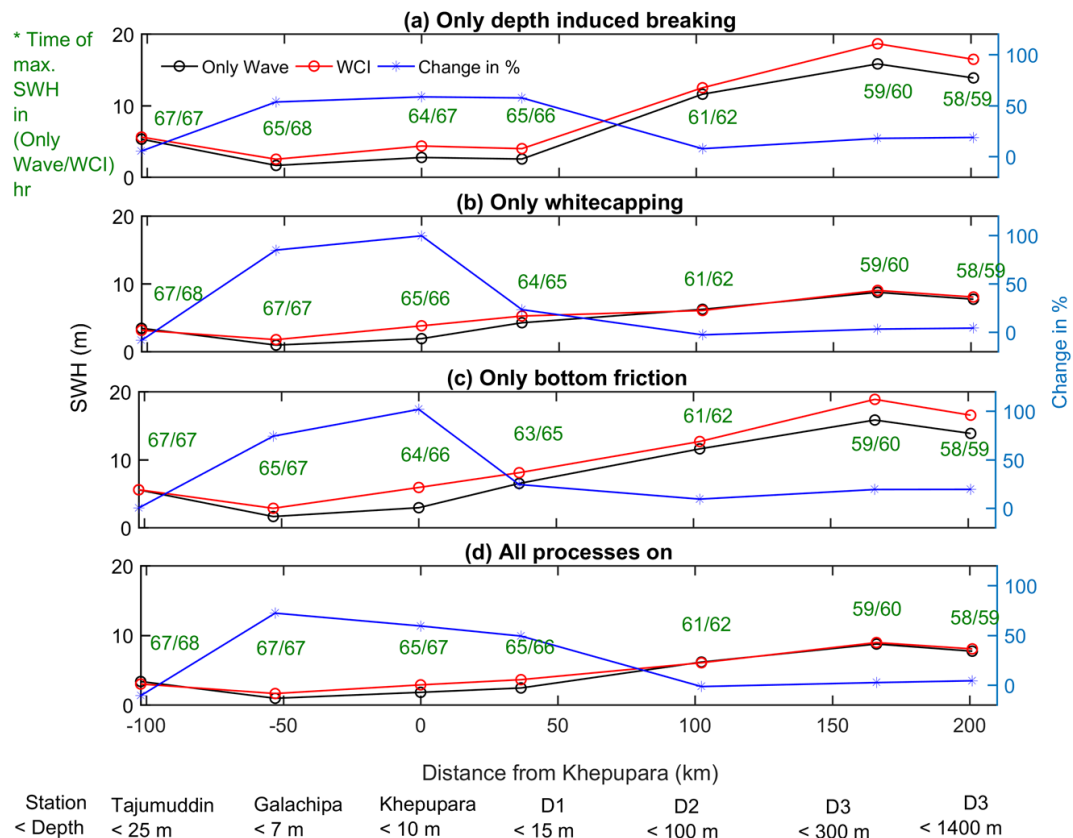


Figure 3.13. Maximum significant wave height variations along the Bay of Bengal for “Only Wave” and “Wave-Current interaction” conditions under: (a) Only depth-induced breaking; (b) Only whitecapping; (c) Only bottom friction; and (d) All wave dissipation processes. Maximum amplitudes of the SWH are observed at different times of the cyclone for different scenarios. A positive distance represents the oceanward direction. Change in % = (WCI-Only Wave)/Only Wave %.

3.5 Summary and Conclusions

Cyclone-induced storm surge events cause significant devastation in the GBMD. Due to the funnel's geographical shape and the shallow coastal area (1-3 m above the mean-sea level), storm surge heights are amplified and result in inundation in the GBMD. Although the GBMD is a tide-dominated delta, the strong winds during a cyclone event can produce substantial wave heights (e.g., approximate 3 m at Khepupara during Cyclone Sidr) at the coast. Several studies (e.g., Lewis et al., 2013) have studied the cyclone-induced storm surge events in the GBMD, but the majority of studies neglected the wind-wave effects on the storm surge height except Deb and Ferreira (2016), and Krien et al (2017). Major challenges to developing a numerical model for the region is the lack of wave-buoy data in the coastal area of the GBMD for calibration and validation. Continuous observed water level data are also scarce during cyclonic events because of the hazardous conditions that can cause damage to instruments. Therefore, most of the studies are based on the assumption that the wind-wave has negligible impact on the storm surge height as the major portion of the wave dissipates far from the coastline due to the presence of a deep submerged canyon 80 km offshore that causes dissipation of wind-driven waves far from the coast. The findings in this chapter suggests that that wind-driven waves and wave-current interactions are important considerations when reproducing cyclone-forced storm surge in the GBMD.

Including wind-wave interactions can increase the surface water level up to 0.3 m near the landfall location due to wave setup. In addition, the wave-current interaction results in higher significant wave heights (1.1 m higher at the Cyclone Sidr landfall location of Khepupara) compared with only wind-driven wave model results. During Cyclone Sidr landfall, all stations except those located in the central GBMD were in

flood phase. Therefore, the varying wind speed and direction during Cyclone Sidr with different tidal characteristics result in different WCI effects on the wave height variations across the GBMD. Considering the WCI in the model simulation shows increase (e.g., 1.07 m at Khepupara) and decrease (e.g., 0.36 at Tajumuddin) of wave heights compared to the without WCI model simulation. The increase/decrease of wave heights are resulted from the opposite/same directions of current and wave. In addition, the effective wind stress (vectorial difference between wind and current magnitude) is influenced by the WCI, which also causes the varying wind setup across the GBMD. The total storm surge height is generated from the combined influence of wind, tide, and wave. Although wind setup is the dominant factor among tide and waves, interactions between each component can modify the total storm surge height. Tidal features can influence both wind- and wave setup by modulating water level and effective wind stress. In addition, different current directions, and magnitudes with tidal phase variations along with wind also influence wave height variation. This chapter clearly demonstrates the importance of considering the wave-current interactions in the study of cyclone-induced storm surge events in the GBMD.

Results illustrate that the current plays a dominant role in the modulation of SWH compared with the water level in both the deep ocean and deeper coastal waters (e.g., Tajumuddin < 25 m). However, the water level becomes the dominant factor when the waves propagate into shallower regions (e.g., Khepupara < 10 m) from the deeper ocean. The SWH variations are strongly influenced by wave-current interactions in the shallower region between 50 km landward to 50 km offshore. Whitecapping dissipation dominates the wave dissipation processes.

Finally, the results presented in this chapter, particularly the influence of wave-current interaction on waves, are essential for understanding, modelling, and managing

a vulnerable estuarine system like the Ganges-Brahmaputra-Meghna Delta that is impacted by cyclones. The established model setup can be further applied to improve disaster management plans particularly in hazard and risk mapping, embankment height design, and further investigating the cyclone-induced storm surge events in the GBMD.

Chapter 4 Cyclone-induced storm surge flooding in the Ganges-Brahmaputra-Meghna delta under different mean-sea level rise scenarios

4.1 Introduction

During a cyclonic event, both river-tide interaction and wave-current interaction modulate the cyclone-induced storm surge height that causes inundation in the cyclone-affected area. The influence of river discharge on tides and wave-current interactions during cyclone-induced storm surge events were discussed in Chapters Two and Three. Here, cyclone-induced flooding in the GBMD is investigated using a case study of Cyclone Sidr perturbed with different mean sea level rise scenarios to understand processes related to the inundation area. Furthermore, the influence of different cyclone intensity, river discharge, and landfall location is also investigated by applying the model for different idealized cases.

4.2 Background

Cyclone-induced storm surge flooding affects many regions globally and can cause significant economic loss and loss of life (Needham et al., 2015). Numerous studies (e.g., You, 2019; Wang et al., 2020; Ramos-Valle et al., 2020) have investigated cyclone-induced storm surge flooding around the world. Cyclone-induced storm surge flooding properties vary with geographical location (e.g., Ferreira et al., 2014; Hu et al., 2015) and cyclone characteristics (e.g., Rego and Li, 2009 ; Berg, 2013; Li et al., 2013). A significant amount of research effort has been devoted to cyclone-induced storm surge

height prediction in the Bay of Bengal (e.g., Dube, 2012; Lewis et al., 2013; Lewis et al., 2014; Kumar et al., 2015; Krien et al., 2017, Prakash and Pant, 2020; Khan et al., 2020). However, most of the studies focused on storm surge heights in the open ocean and at the river mouth. These studies ignore the inundation processes in the GBMD floodplain.

Coastal inundation in the GBMD can be broadly classified into monsoon flood and cyclone-induced storm surge flood (Haque and Nicholls, 2018). Monsoon floods result from increased river discharge in the major rivers (including the Ganges, the Brahmaputra and the Meghna river) from July to September, which is the peak monsoon season. The high river discharge interacts with the tides in the GBMD and can produce extensive flooding in the coastal area. Cyclone-induced storm surge flooding typically occurs during pre-and post-monsoon periods (April, May, and November) because these are the most active periods for cyclone formation in the BoB (Haque and Nicholls, 2018). Monsoon floods and cyclone-induced storm-surge floods rarely coincide in the GBMD (Haque and Nicholls, 2018). The processes associated with monsoon floods were specifically addressed in Chapter two. This chapter is focuses on cyclone-induced storm surge flooding in the GBMD.

On average a severe cyclone affects the Bangladesh coast every three years and causes loss of life and substantial economic loss (World Bank, 2010). For example, Cyclone Sidr (2007) affected 8.9 million people and caused a total US\$70.7 million of damage (Government of the People's Republic of Bangladesh, 2009) and Cyclone Aila (2009) affected 3.9 million people with estimated damages of US\$270 million (EMDAT, cited in Feroz Islam et al., 2019). In addition, the frequency of very severe cyclonic storms in the BoB has increased by 0.86 per decade in the post-monsoon period (October-December) from 2000 to 2018 (Danda, 2020). During this period (2000-2018),

15 very severe cyclonic storms occurred in the BoB. Mendelsohn et al. (2006) predicts that low-latitude countries, including Bangladesh, will be most economically affected due to climate change (World Bank, 2015). Much of this increased economic loss is expected to be related to cyclone impacts in the GBMD under future climate change scenarios.

In addition to the changes in cyclone climatology and resulting impacts that is expected in the future, cyclone-induced flooding is also expected to increase due only to sea-level rise (Woodruff et al., 2013). Future climate projections under the RCP8.5 scenario predict that the sea level in the GBMD will rise by 0.18 m to 0.33 m and 0.49 m to 1 m by 2050 and 2100, respectively, compared to the sea level in 2000 (Kebede et al., 2018). The RCP8.5 scenario of the Intergovernmental Panel on Climate Change (IPCC) is defined as a worst possible scenario (90th percentile emissions scenario) and is considered a likely outcome if no measures are taken to cut greenhouse gas emissions. The Bangladesh Delta Plan 2100 (100 years planning by Bangladesh Government) considers 0.2 m to 1 m sea level rise for low to high emission scenario in 2100 for the Bay of Bengal according to IPCC (2013). Many studies recognize that climate-change-induced sea-level rise may increase the intensity of storm-surges associated with tropical cyclones (Frazier et al., 2010; Mousavi et al., 2011; Saxena et al., 2013; Fang et al., 2016;). Hoque et al. (2018) integrated the local sea-level rise scenarios with a geographic information system (GIS) based surge model to assess the hazard, vulnerability and risk in the coastal region of Bangladesh under future climate change scenarios. They found that a mean sea-level rise of 0.34 m would amplify cyclone-induced storm surges in this region and increase the inundation area by 5–10% by 2050. Another recent study by Hasan et al. (2020) focused on the Bangladesh coast by downscaling 28 global climate models and predicted sea-level rise for future scenarios.

The study predicts 0.77 m to 1.15 m of MSL rise in the Bangladesh coast by the year 2100 for the RCP4.5 and RCP8.5 scenarios, respectively. The inundation area is also projected to increase to 2098 sq. km due to a 1 m MSL rise by Hasan et al. (2020). Several studies (e.g., Hoque et al., 2018; Mehvar et al., 2019) applying different global climate models to predict MSL rise and by comparing the digital elevation model data of the Bangladesh coast also find that there will be significant increased inundation area because of an increase in MSL. An increased inundation area has potential to raise the overall disaster risk in the Bangladesh coastal regions because of increased erosion, reduced soil productivity due to saline water intrusion, destruction of infrastructure, and disruption of transport networks and other utility services (Nicholls et al., 2007). Murshed et al. (2021) discussed the importance of considering the MSL along with other climatic factors including tropical cyclones, storm surge and shoreline change for accurate prediction of coastal risks.

Given the potential for increasing impacts in Bangladesh, it is important to study the impacts of different sea-level rise scenarios on cyclone-induced flooding in the GBMD to understand future flooding conditions. While several studies (e.g., Murty and Flather, 1994; Ali, 1999; Karim and Mimura, 2008; Jisan et al., 2018; Alam et al., 2018; Hoque et al., 2018; Rahman et al., 2019) have been conducted to assess cyclone-induced storm surge flooding under different sea-level rise scenarios, they ignore several important processes including wave-current interaction and the role of floodplain and embankment height in storm surge height estimation. This chapter overcomes these limitations by using a wave-current coupled hydrodynamic 3D model and applying a finer model bathymetry by considering the total floodplain area and embankment heights in the GBMD.

The Bangladesh coast is protected by a network of coastal embankments, enclosing low-lying land with earthen embankments, which are known locally as polders. Polders were built in coastal areas beginning in the 1960s to protect farmland from tidal flooding and saline water intrusion. At present, there are a total of 139 polders in the coastal areas of Bangladesh with 103 polders located in the study area (Figure 4.1a). The polders play an important role in the extent and pattern of inundation in the GBMD. A schematic diagram of embankments in the Western and Central GBMD is presented in Figure 4.1b. Embankment heights vary from 3 m to 7 m across the GBMD (Dasgupta et al., 2010). Embankment locations and heights from the database of the Water Resources Planning Organization, Bangladesh are applied to the model bathymetry. If there are missing embankment height data then an average embankment design height of 4.75 m is applied in the model bathymetry (BWDB, 2013). The existing embankments heights are considered adequate to protect the coastal area from cyclone-induced storm surge with 5 to 12 year return periods (Islam et al., 2013). Land protected by embankments can be flooded in two ways during a cyclonic event: (1) by embankment overtopping and (2) by embankment breaching through scouring and landslide (Feroz Islam et al., 2019). In the present study, only flooding by embankment overtopping is considered in the model setup.

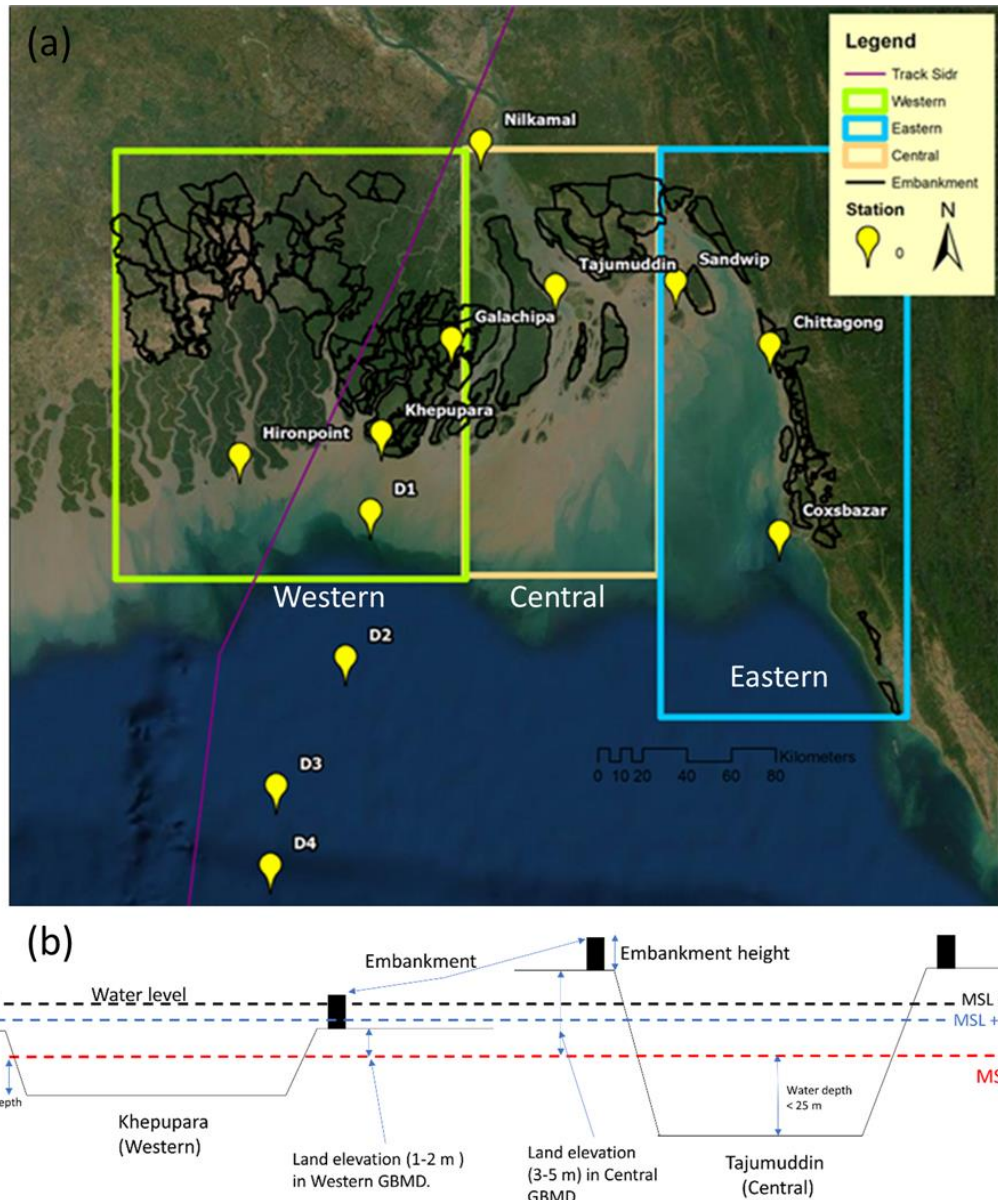


Figure 4.1. (a) The Bangladesh coast embankment network with the track of Cyclone Sidr and station locations in the three different parts of the GBMD; and (b) Schematic diagram of polders in the Western (at Khepupara) and Central (at Tajumuddin) GBMD with channel bathymetry and embankment height. Different mean sea levels are indicated by the dashed lines.

4.3 Methodology

A wave-current coupled 3D numerical model is used to simulate cyclone-induced storm surge events in the GBMD. Model results, including storm surge height, wave height and wind speed were calibrated and validated for Cyclone Sidr (2007). The

model results, including storm surge height, wave height and wind speed during Cyclone Sidr are compared with observations and published literature in Chapter 3. The model is applied to cyclone-induced flooding in the GBMD during Cyclone Sidr. The control simulation uses the MSL in 2000 as the MSL condition. Three different MSL rise scenarios: 0.5 m, 1 m, and 1.5 m, which cover the projected sea level rise scenarios in the BoB from the fifth assessment report of the IPCC for low to highest emission scenarios (IPCC, 2014), are used to assess the impacts of projected MSL rise on inundation areas in the GBMD (Table 4.1). To apply these MSL changes, the model bathymetry is everywhere reduced relative to the MSL by 0.5, 1.0, and 1.5 m, for each of the three MSL rise scenarios. For example, for a MSL rise of 0.5 m, this means the channel bathymetry at Khepupara deepens to 8.2 m from 7.7 m, and the floodplain elevations near Khepupara decrease from 2.2 m above MSL to 1.7 m above MSL. Similarly, the polder heights relative to MSL are also reduced in the model bathymetry according to the MSL rise scenarios. All other boundary forcings including tides, wind, and river discharge are unchanged so that the impact due only to MSL rise on cyclone-induced flooding can be assessed. A similar approach to incorporate the MSL rise in a numerical modelling study of cyclone-induced storm surge flooding was applied in Jisan et al., (2018). The model is also applied with only tide forcing to understand the flooding scenarios in the three MSL rise scenarios with- and without the cyclone forcing (Table 4.1). The model inundation area is estimated from the model water level results. The inundation area is calculated by removing the area of water bodies (e.g., rivers, channel and ocean) from the total area covered by water by applying the ArcGIS spatial tool.

Table 4.1. Idealized model scenario details

Run	MSL (m)	Bathymetry	Cyclone characteristics	Tide and River	Remarks
MSL rise scenarios					
With Cyclone (Wind + Tide + Wave)	MSL = 0 m	Real case bathymetry	Cyclone Sidr, best track from JTWC	Realistic river discharge and tides are same as year 2000	The base model setup
	MSL + 0.5 m	Real case + 0.5 m	Same as above	“	
	MSL + 1 m	Real case + 1 m	Same as above	“	
	MSL + 1.5 m	Real case + 1.5 m	Same as above	“	
Without Cyclone (Only Tide)	MSL = 0 m	Real case bathymetry		“	
	MSL + 0.5 m	Real case + 0.5 m		“	
	MSL + 1 m	Real case + 1 m		“	
	MSL + 1.5 m	Real case + 1.5 m		“	
Cyclonic scenarios					
Max. wind velocity	MSL = 0 m	Real case bathymetry	Max. wind velocity of JTWC increased by 20 %	Same as above	Only max. wind velocity is modified during the cyclone period. Other parameters are kept same.
	“	“	Increased by 30%	“	
	“	“	Increased by 50%	“	
Radius of Max. wind	MSL = 0 m	Real case bathymetry	Max. wind radius of JTWC increased by 20 %	“	Only radius of max. wind is modified during the cyclone period. Other parameters are kept same.
	“	“	Increased by 50%	“	
	“	“	Increased by 100%	“	
Landfall location & River discharge	MSL = 0 m	Real case bathymetry	Cyclone Sidr, best track from JTWC	Constant 50,000 m ³ s ⁻¹ and tide are same as above.	
	“	“	Cyclone Sidr, makes landfall at the Lower Meghna estuary	No river discharge and tide same as above	
	“	“	“	Constant 30,000 m ³ s ⁻¹ and tide are same as above.	

Three other sets of idealised simulations are designed to investigate the role of cyclone intensity, cyclone size (specifically the radius of maximum wind), and the influence of river discharge on the cyclone-induced storm surge event in the GBMD (Table 4.1). To investigate the effects of changing the cyclone intensity and size, the maximum wind speed and radius of maximum wind are altered by the amounts shown in Table 4.1. To investigate the influence of river discharge, the track of Cyclone Sidr is shifted so that the landfall location is at the Lower Meghna estuary mouth during a high river discharge period. All the idealized scenarios are described in detail in Table 4.1.

4.4 Result and Discussion

4.4.1 Cyclone-induced storm surge flooding during Cyclone Sidr

Cyclone Sidr made landfall near Khepupara on 1500 UTC, 15 November 2007 and caused extensive flooding in the coastal area. A cyclone event is typically accompanied by a large region of clouds, which affects whether satellite images can be used to observe ground flooding. Furthermore, the flooding that occurs may be due to a combination of storm surge inundation and intense cyclone-related rainfall. It is difficult to separate these two effects using only satellite imagery. The Dartmouth Flood Observatory prepared an inundation map for Cyclone Sidr at 0000 UTC, 16 November. However, the available cloud-free area (in dashed blue line Figure 4.2) covers only the Lower Meghna estuary and does not capture the full extent of the inundation area. Figure 4.2 shows a comparison of the inundation area between the model result and the satellite image analysis. The results demonstrate that the embankments in the Lower Meghna estuary (in the Central GBMD) protect the land from cyclone-induced storm surge flooding during Cyclone Sidr. Within the cloud-free area, the modelled cyclone-induced storm surge flooding matches the satellite analysis reasonably well. Within this

overlapping area, the modelled flood area is 157 sq. km higher than the satellite-based analysis (Figure 4.2). Several factors may result in this difference including bathymetric error, embankment breaching and rainfall during Cyclone Sidr. The detailed model results from this control simulation, including cyclone-induced storm surge height, wind speed, and wave height, were compared with the observations, and discussed in detail in Chapter 3.

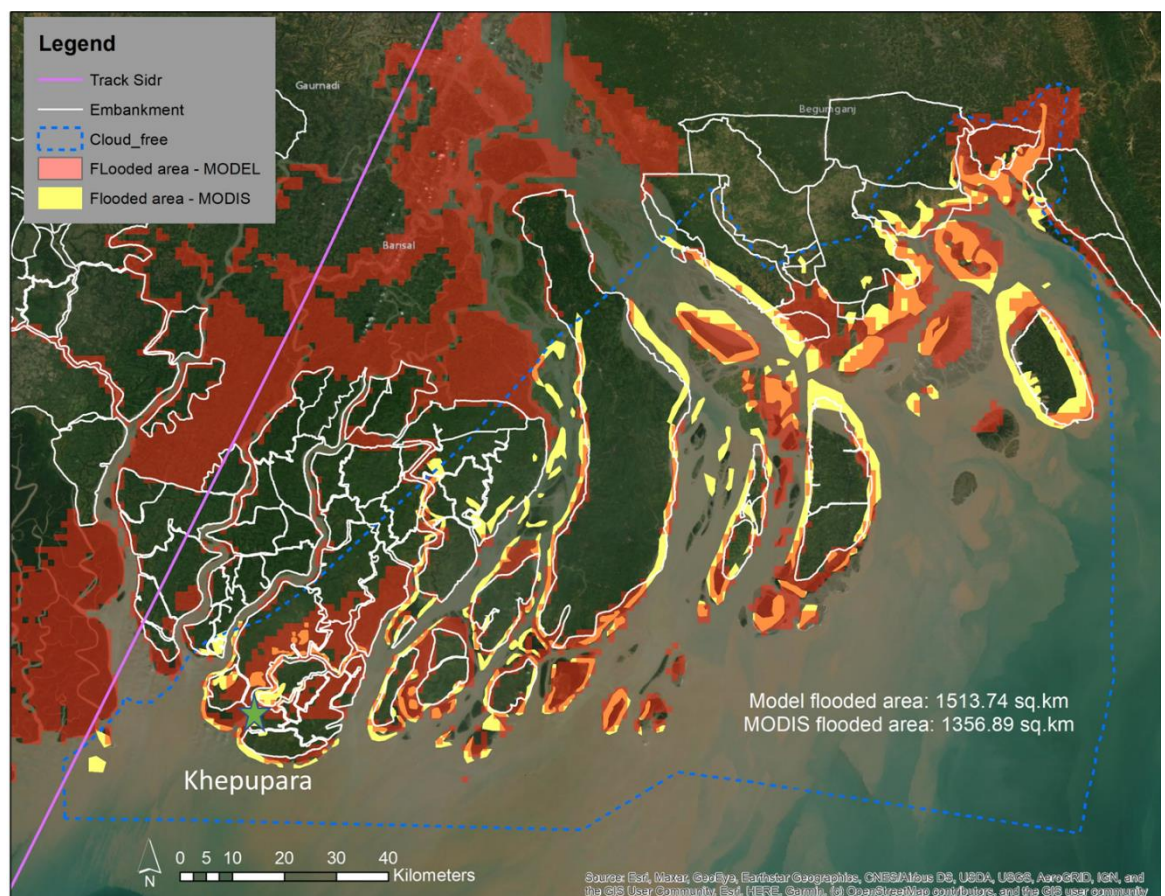


Figure 4.2. Modelled cyclone flood area comparison with the flood area analyzed from MODIS imagery at 0000 UTC 16 November by the Dartmouth Flood Observatory. The blue dashed line indicates the cloud-free area in MODIS imagery. The white solid lines indicate embankment locations. The nearest station to the track of Cyclone Sidr (Khepupara) is denoted by the star. The area of flooding analyzed from MODIS imagery is reproduced from the map prepared by the Dartmouth Flood Observatory: <https://reliefweb.int/map/bangladesh/bangladesh-cyclone-sidr-rapid-response-inundation-map-16-nov-2007>.

4.4.2 Cyclone-induced flooding under different MSL scenarios

The model is applied to the three idealized MSL rise scenarios in Table 4.1. The results are shown in Figure 4.3. The cyclone-induced flooded area is calculated at 2100 UTC, 15 November 2007, which is 6 hours after landfall, to capture the full impact of the cyclone-induced storm surge over the GBMD. Results show that the cyclone-induced flooded area increases with increasing MSL by 1209 sq. km, 3487 sq. km and 7564 sq. km for ‘MSL + 0.5 m’, ‘MSL + 1 m’ and ‘MSL + 1.5 m’ compared to the ‘MSL = 0’, respectively (Figure 4.4). In comparison, when the cyclone effect is removed and only tidal forcing is considered, the flooding increases by 802 sq. km, 2444 sq. km and 6515 sq. km for the ‘MSL + 0.5 m’, ‘MSL + 1 m’ and ‘MSL + 1.5 m’ compared to the ‘MSL = 0’, respectively (see Table C.1 in Appendix C). The results demonstrate that the MSL rise will increase the flooding area regardless of whether a cyclone is present. There is also a higher amount of flooding in the Western and Central GBMD than the Eastern GBMD for both conditions (Figure 4.3). This is a result of the lower land elevations in the Western and Central GBMD, which are less than 3 m above MSL, whereas the overall land elevations are higher than 3 m in the Eastern GBMD (World Bank, 2010).

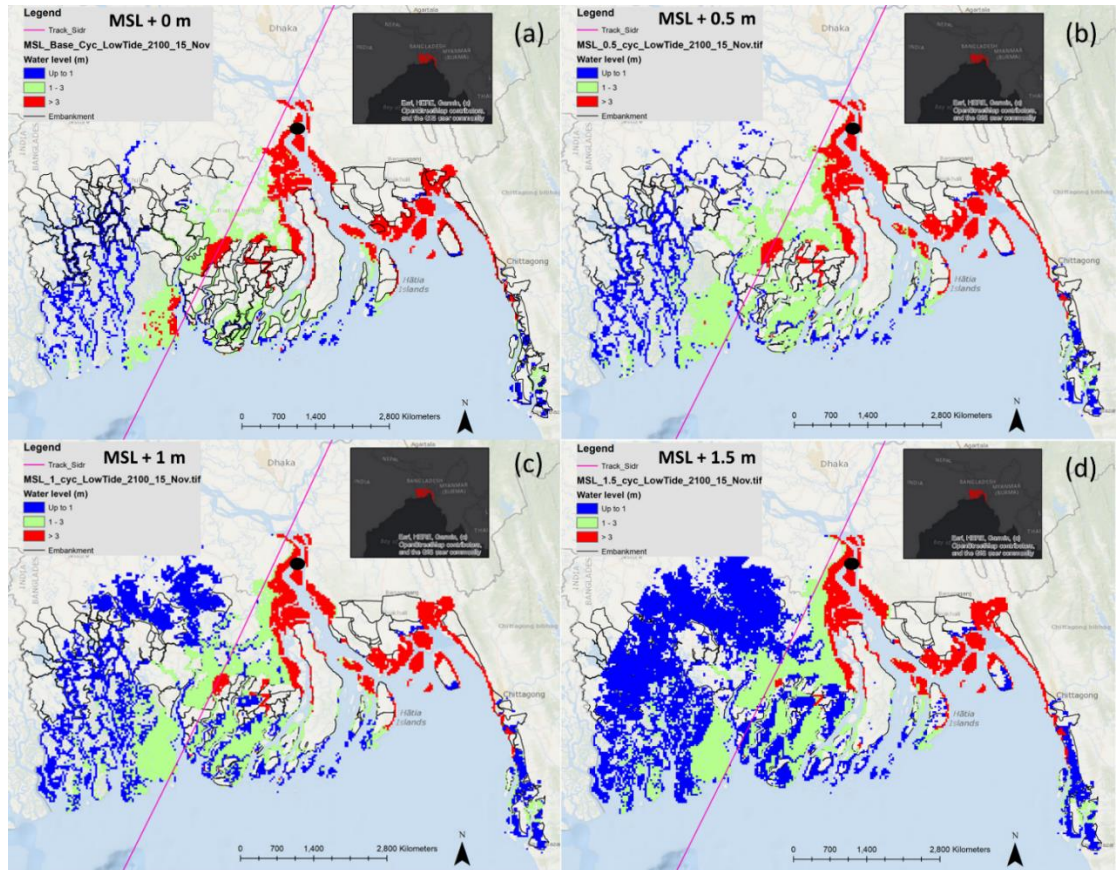


Figure 4.3. Cyclone-induced storm surge flooding during the landfall of Cyclone Sidr, valid at 2100 UTC 15 November: (a) MSL at 0 m - current conditions, (b) MSL rise by 0.5 m, (c) MSL rise by 1 m, and (d) MSL rise by 1.5 m. The purple line represents the track of Cyclone Sidr.

Figure 4.4 shows that each increment of 0.5 m in MSL rise results in a linearly increase of flooded area regardless of whether a cyclone is present. The flooding due to just the cyclone without tide is estimated by subtracting the flooding due just to tide from the flooding due to combination of cyclone and tide. The cyclone areal flooding increases linearly with MSL rise up to the highest (+ 1.5 m) MSL (Figure 4.4 and Figure 4.5a). In this scenario, more than 70 % of the Western GBMD and 45 % of Central GBMD are already flooded due to tides with increased mean sea level (Figure 4.5b). Hence, the cyclone-induced storm surge does not increase the flooded area as much as it does for the more conservative MSL rise scenarios (see Table C.1 in Appendix C). The results illustrate that a Sidr-like cyclone will cause higher inundation in the GBMD

due to MSL rise alone given no change in the embankment structure. The inundation area increases up to 33 % from 12 % of the total coastal area for a 1.5 m MSL rise compared to the current MSL for Cyclone Sidr. The total projected flooded area due to Cyclone Sidr in a ‘MSL + 1.5 m’ scenario is 8 % of the area of Bangladesh. This is 2.5 % higher than that suggested by Rahman et al. (2019). The higher inundation area in this study is probably due to the non-linear interaction between waves and currents, which is ignored by Rahman et al. (2019).

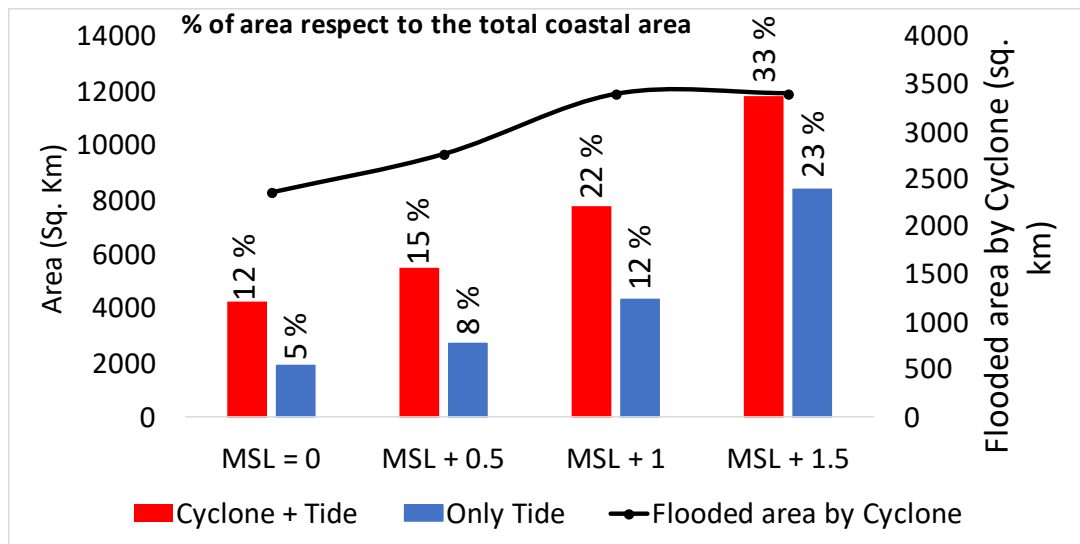


Figure 4.4. Flooded area at 2100 UTC 15 November 2007 for different MSL scenarios with- and without-cyclone conditions.

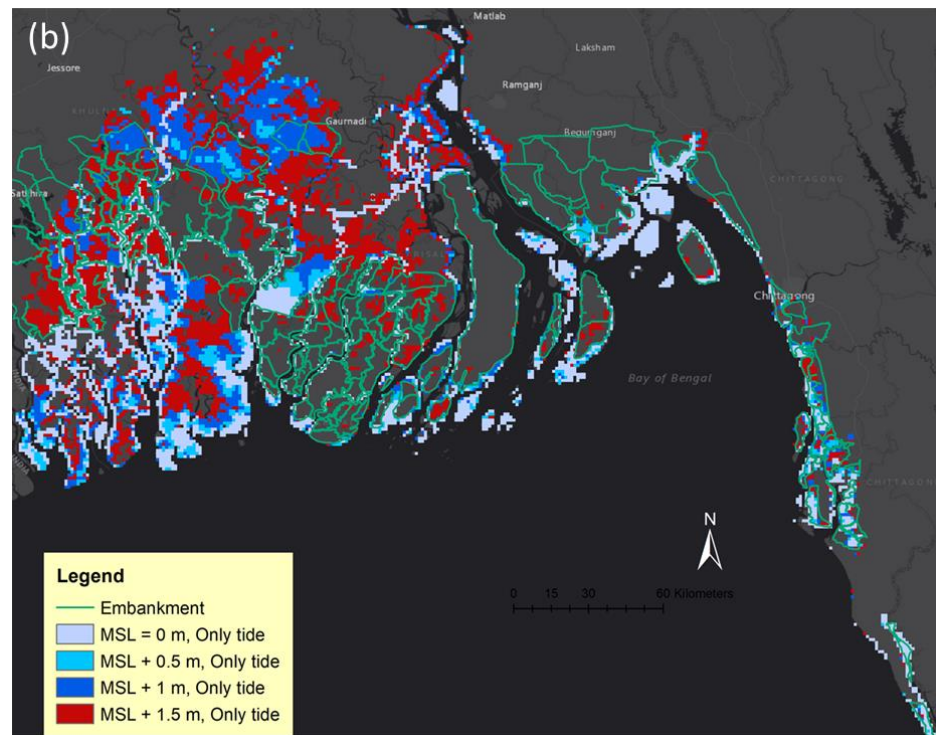
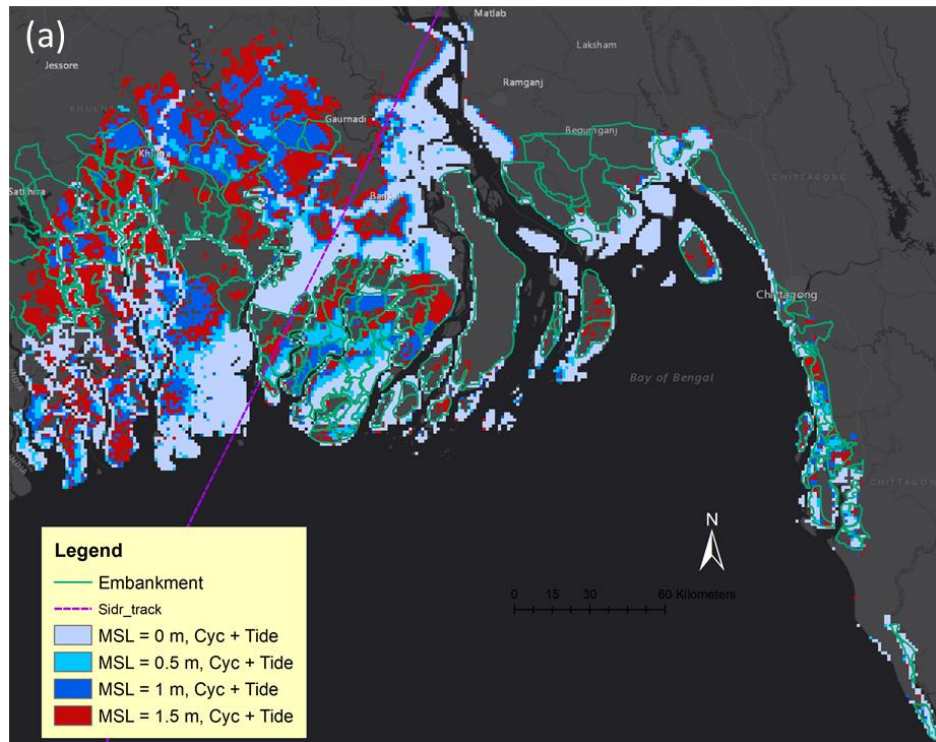


Figure 4.5. (a) Model flooded area by Cyclone Sidr and tide under the different MSL rise scenarios; and (b) Model flooded area by tides under different MSL rise scenarios. Note that the flooded area in different colours represent flooded area added from the further increment of MSL and, valid at 2100 UTC 15 November. For example, the red area denotes a newly flooded area in the 'MSL + 1.5 m' compared to the 'MSL + 1 m'.

4.4.3 Water level variations with different MSL rise scenarios during Cyclone Sidr

Water level variations across the GBMD under the different MSL rise scenarios are presented in Figure 4.6. Results show spatially varying influences of MSL rise on water level variations. The water levels at the deep ocean stations (> 50 m depth) exhibit small variations (< 0.2 m) with MSL rise, which are insignificant compared to the existing water depths. For example, the water depth at D2 in the ‘MSL at 0 m’ is 97 m. The ‘MSL + 1.5 m’ increases water depth by 1.5 m, which is a 1.5 % increase of the existing water depth.

Cyclone-induced storm surge water level decreases with rising MSL in the Western and Eastern GBMD but not in the Central GBMD. There are two processes that reduce the water levels in these two regions: (1) reduced wind setup due to increased channel depth with increasing MSL; and (2) embankment overtopping from reduced embankment height due to MSL rise. In Chapter 3 (Section 3.4.3) it was found that the wind setup is inversely proportional to total water depth, which is affected by increased MSL (also see equation (4.1)). At Khepupara, a MSL increase of 1.5 m increases the channel water depth from 7.7 m to 9.2 m and the modelled maximum water level decreases from 6.8 m to 5.4 m. Decreases in maximum water levels are also observed at other stations located in shallow regions (water depth less than 15 m) such as Galachipa, Nilkamal, Chittagong, Coxsbazar, and Sandwip. In contrast, the cyclone-induced storm-surge maximum water level at Tajumuddin (located in the estuary mouth of the Central GBMD) increases with increasing MSL (denoted by a green arrow in Figure 4.6). Reasons for reduced and increased maximum water levels at shallow stations (e.g., Khepupara and Tajumuddin, respectively), are discussed later in this section.

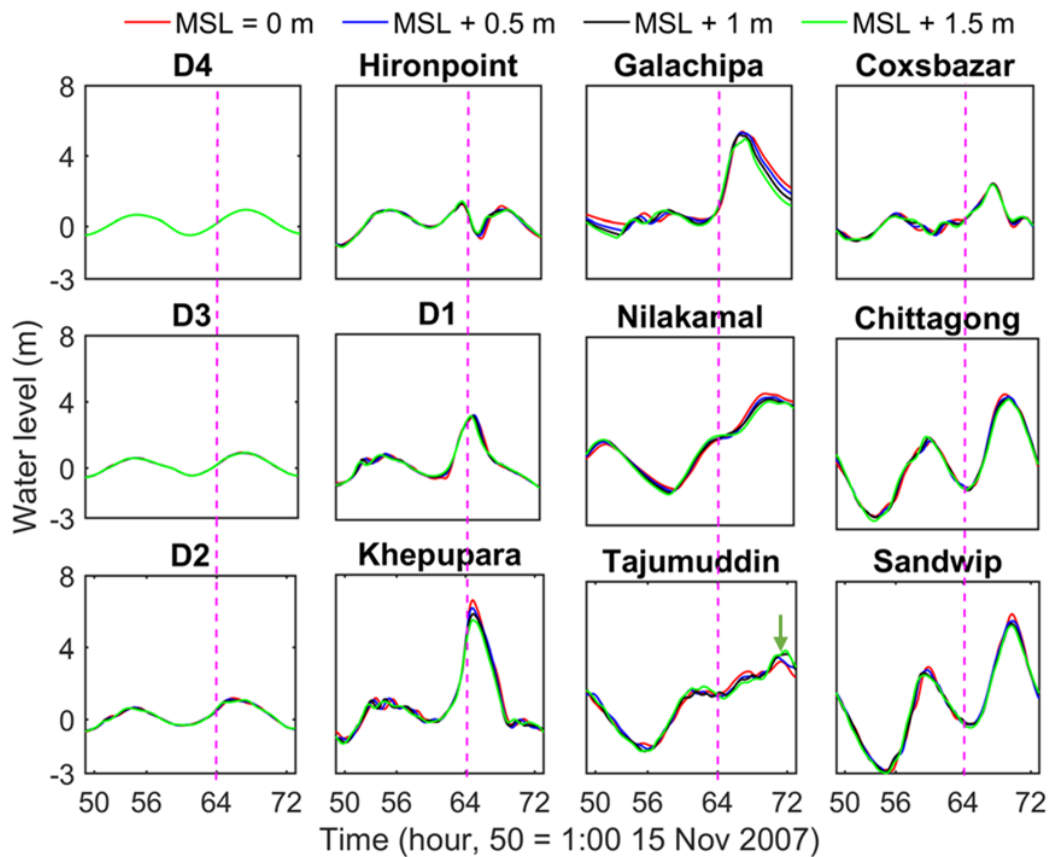


Figure 4.6. Model water level variations across the GBMD during Cyclone Sidr under different MSL rise scenarios. The purple line represents the landfall time of 1500 UTC 15 November 2007.

To investigate the reason behind the increase and decrease of maximum water level at shallow stations, model residual water levels are plotted for different MSL scenarios in Figure 4.7. Residual water levels across the GBMD are estimated by subtracting tidal water levels from the water levels for different MSL rise scenarios. Note that the residual water level is a combination of the wind- and wave-setup that is defined as the storm surge height (see Chapter 3 and equation (4.1)). Results demonstrate that residual water level decreases with the MSL rise at all stations except the deep stations (e.g., D2-D4). Although the total water level (water surface elevation) increases with increasing MSL at Tajumuddin, the residual water level decreases by 0.05 m for a 1.5 m increase in MSL. The decrease in residual water level is because of a reduced wind setup (wind-driven water level) due to increasing water depth as MSL increases.

However, the maximum total water level at Tajumuddin increases by 0.30 m for a 1.5 m increase in MSL (at 2250 UTC, 15 November 2007, 7 hours after the landfall, 71-hour in Figure 4.6).

The model results with tidal forcing only (no cyclonic forcing) for different MSL scenarios demonstrate that the MSL rise increases the tidal water level variations at Tajumuddin higher than at other stations such as Khepupara (Figure 4.8). This indicates that the increase of incoming tidal flux energy with MSL rise at Tajumuddin results in a rise of tidal water level. Therefore, the total water level variations at Tajumuddin increase with MSL rise during cyclonic conditions (Figure 4.6). The tidal energy flux is proportional to water depth and velocity vector (Song et al., 2013). Tajumuddin is located in the estuary mouth of the Lower Meghna with a water depth of 24 m and is exposed to strong current variations. MSL rise from 0 m to 1.5 m increases the current magnitude from 0.6 m s^{-1} to 2.2 m s^{-1} at Tajumuddin, whereas at Khepupara, which is located in a shallower region (water depth 7.7 m), the current magnitude increases to 0.5 m s^{-1} from 0.25 m s^{-1} , respectively. Therefore, increasing MSL results in higher incoming tidal energy flux at Tajumuddin compared to Khepupara. The increased tidal energy flux raises the tidal water level at both Tajumuddin and Khepupara. Due to low land elevations near Khepupara, the embankments are overtopped as the MSL increases and resulted in reduced maximum water level. However, the land elevations near Tajumuddin are relatively higher than in other regions. Hence, the water levels do not overtop the embankments near Tajumuddin in the MSL rise scenarios. Due to the increase of MSL, the incoming tidal flux increases and results in a higher volume of water at Tajumuddin. Consequently, the maximum water level during a cyclone-induced storm surge event increases at Tajumuddin with an increase of MSL. Finally, the model results under different MSL rise scenarios illustrate the importance of considering the

floodplain and embankment height in modelling studies of cyclone-induced storm surge events.

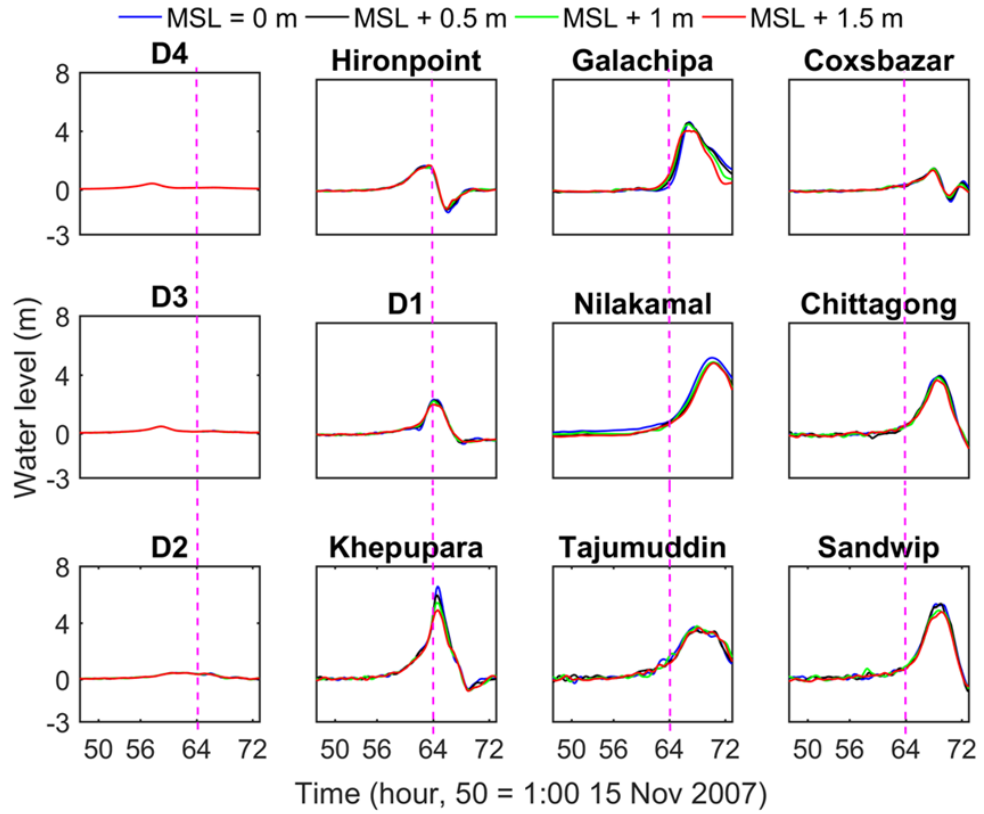


Figure 4.7. Residual water level variations under different MSL rise with Cyclone Sidr. The purple line represents the landfall time of 1500 UTC 15 November 2007.

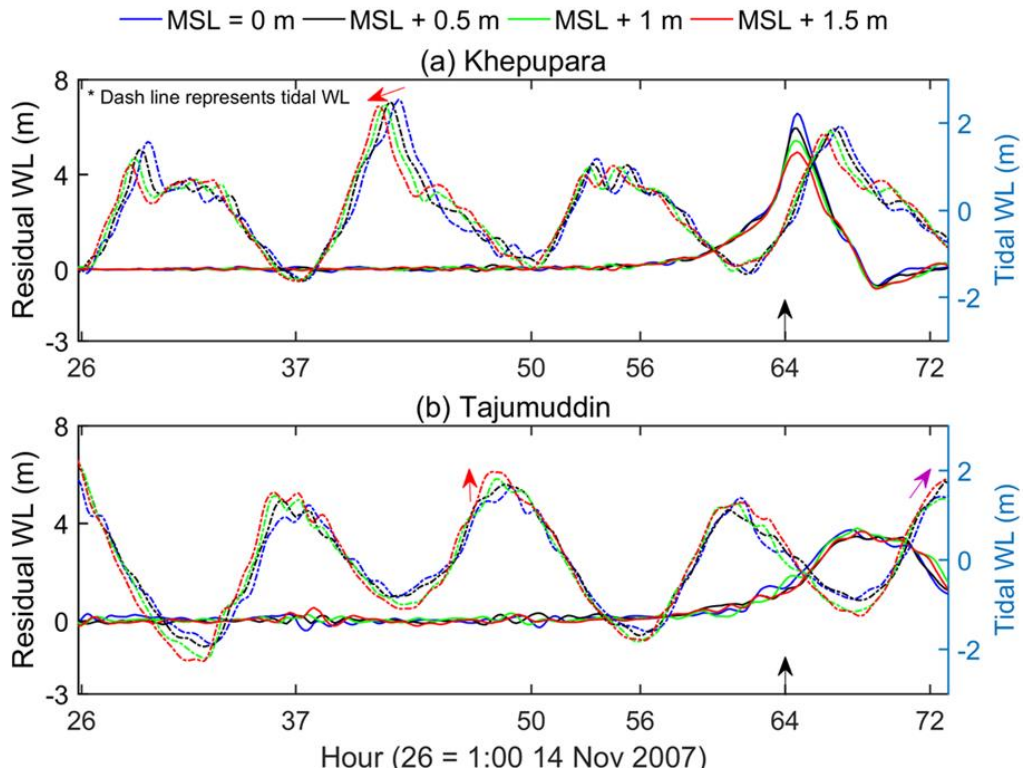


Figure 4.8. Model residual water level and tidal water level variations with different MSL rise scenarios at: (a) Khepupara; and (b) Tajumuddin. The landfall time is indicated by the black arrow. Red arrows indicate decrease (downward) and increase (upward) of maximum tidal water level in the 'MSL + 1.5 m' compared to the 'MSL = 0 m' scenario. The purple arrow indicates the maximum tidal water level at the time of maximum model water level observed at Tajumuddin in Figure 4.6.

4.4.4 Storm surge height variations with different cyclone strengths

The focus thus far, has been on the impacts of a Cyclone Sidr-like cyclone. In this section, the intensity and size of the cyclone is modified to test how the inundation changes for different types of cyclones. It is important to assess this in the GBMD since cyclone frequency, intensity and structure are expected to change under future climate scenarios. To do this, the maximum wind velocity and the radius of maximum wind for Cyclone Sidr is modified in the model to test the sensitivity of the storm-surge flooding to changes in cyclone structure (Figure 4.9 and Figure 4.10). All other cyclone parameters including the track and landfall time are unaltered.

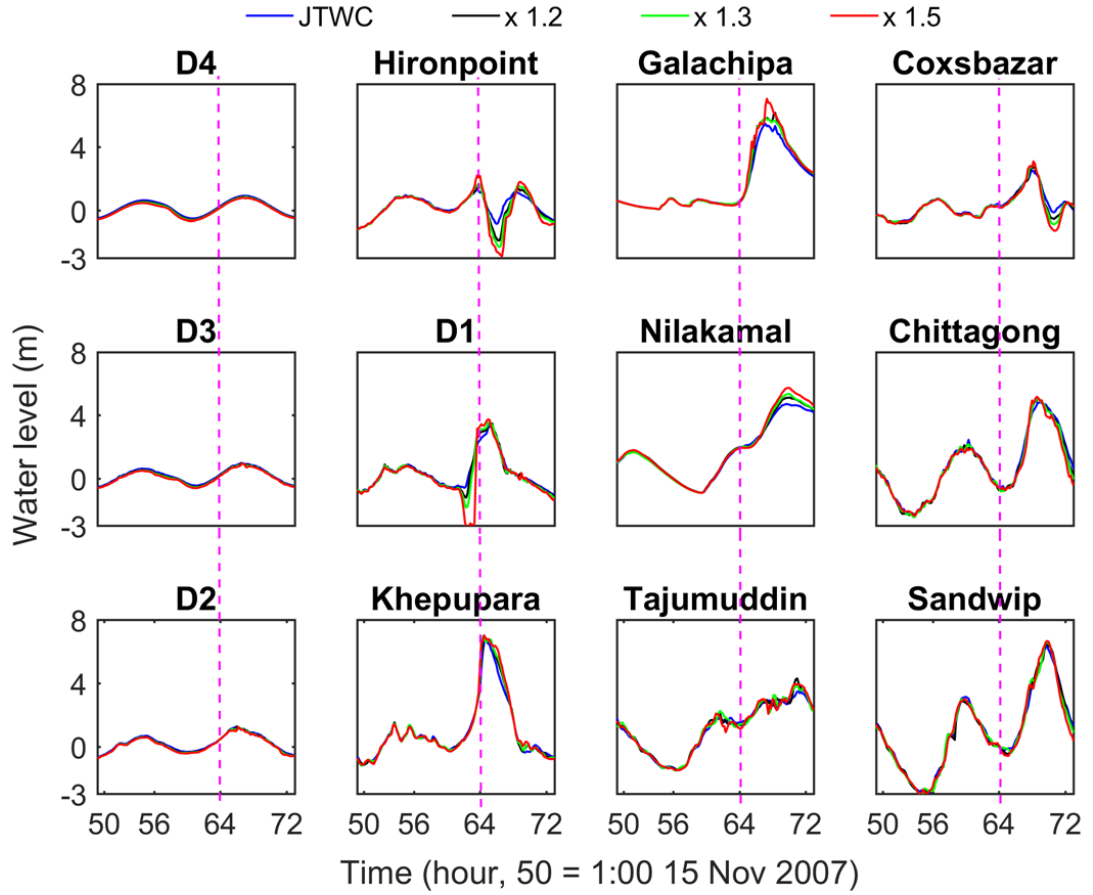


Figure 4.9. Cyclone-induced storm surge variations across the GBMD with different maximum wind speed during Cyclone Sidr conditions. The JTWC denotes maximum wind velocity for Cyclone Sidr. Scenarios with maximum wind speed increased by 20 %, 30 % and 50 % are presented by x 1.2, x 1.3 and x 1.5, respectively. The residual water level is estimated by subtracting the tidal water level from the total water level. The purple line represents the landfall time: 1500 UTC 15 November 2007.

Changing the cyclone intensity affects the storm surge heights variably across the GBMD (Figure 4.9). The cyclone-induced storm surge results from non-linear processes including wave-current interactions and effective wind stress, which will be affected by the changes in cyclone intensity. By neglecting bottom friction and other external forces and applying a momentum conservation argument, the wind-driven surge can be expressed in terms of wind setup as follows (Resio and Westerink, 2008; Woodruff et al., 2013):

$$\text{wind setup} = \frac{\tau_{sy}}{\rho_{\text{water}} g(h+\eta)} \quad (4.1)$$

$$\tau_{sy} = -\rho C_D |\boldsymbol{v}| v \quad (4.2)$$

Here, η is mean surface elevation, h is water depth, ρ_{water} is water density, τ_{sy} is wind stress (north-south component), ρ is air density, C_D is wind drag coefficient, $|\boldsymbol{v}|$ (bolded) is the magnitude of the wind velocity vector and v is the wind velocity (north-south component). At deeper stations, the influence of increased maximum wind velocity on the storm surge heights is negligible (< 0.02 m) because of the depth of the water (> 50 m). At Hironpoint and D1, there is a decrease in the cyclone-induced storm surge height, which results from the change of wind direction as the cyclone eye crosses these locations. Both these stations are located at near shore and on the left side of Cyclone Sidr track. At Khepupara, the storm surge height only slightly increases (0.2 m) with a 50 % increase in the maximum wind speed. This is likely due to overtopping embankments that results in extensive flooding (Figure 4.11a) in the floodplain area near Khepupara. The maximum increase in storm surge height (1.75 m), compared to the control Cyclone Sidr simulation is observed at Galachipa, which is in a shallow region with 6.1 m depth, and occurs when the intensity is increased by 50 %. Other stations also have increased storm surge height with increased wind intensity. However, the magnitude of the storm surge increase is dependent on channel water depths and embankment overtopping. In general, an increase of cyclone intensity results in a higher percentage of flooded area rather than an increase in storm surge height at stations located in rivers (Figure 4.12) because of a tendency for embankments to overtop.

The influence of cyclone size on storm surge is also investigated by increasing the radius of maximum winds, which shifts the maximum wind out from the centre of the cyclone and increases the overall size of the cyclonic wind field (Table 4.1). Increasing the radius of maximum winds impacts stations located far from the cyclone

track more than stations closer to the cyclone track. For example, a 100 % increase of radius of maximum wind compared to Cyclone Sidr increases the maximum storm surge height by 0.5 m at Khepupara, which is located 27 km from the track, compared with 1.2 m for Tajumuddin, which is located 70 km from the track (Figure 4.10). Figure 4.11a (yellow coloured area) shows that a 100 % increase in the radius of maximum wind results in a higher flooded area and water levels after 6 hours of landfall in the Eastern GBMD compared to other regions.

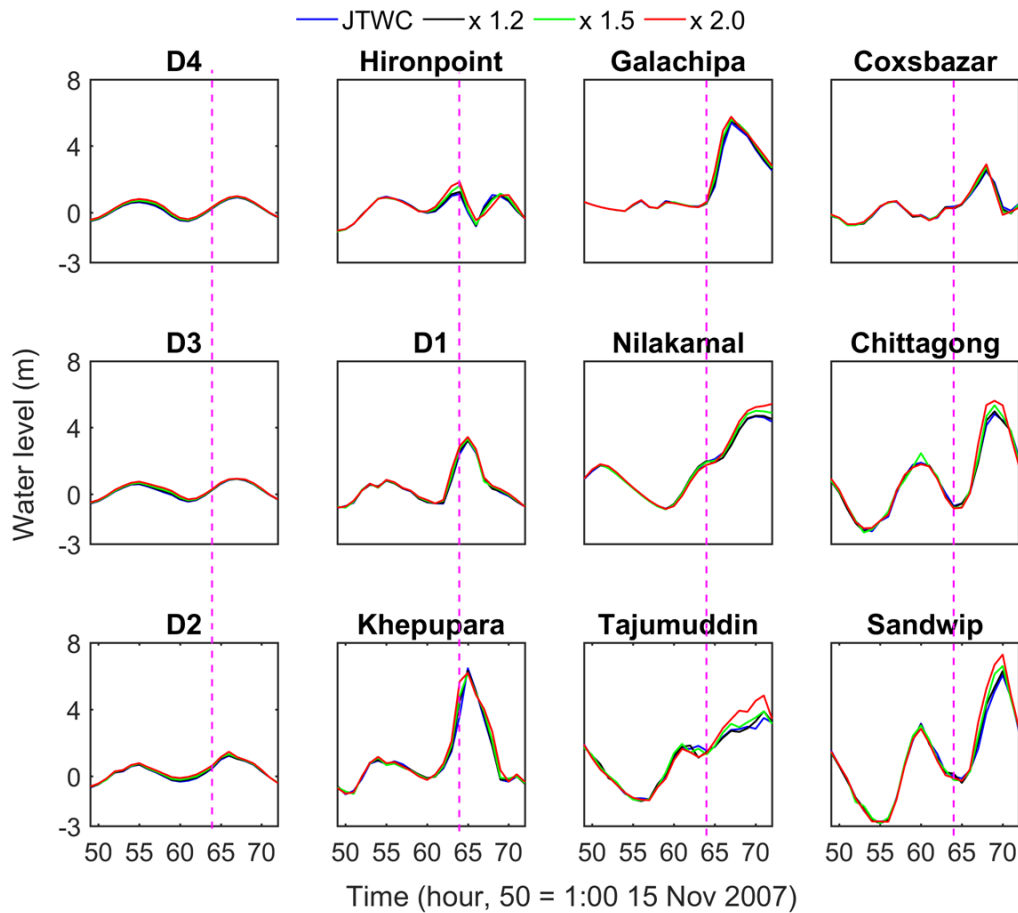


Figure 4.10. Cyclone-induced storm surge variations across the GBMD with different radius of maximum wind speed during Cyclone Sidr conditions. The purple line represents the landfall time of 1500 UTC 15 November 2007.

The changes in the area of flooding and average of maximum residual water level across the GBMD with increasing maximum wind velocity and radius of maximum wind are shown in Figure 4.12. The average maximum residual water level for each idealized case is estimated by averaging the maximum residual water levels at all stations across the GBMD. Results show that the area of flooding and storm surge height is more sensitive to changes the maximum wind speed than the radius of maximum wind. Although a 50 % increase in maximum wind speed causes a 21 % increase in the storm surge height, the flooded area increases by 45 % compared to the original (control) Cyclone Sidr simulation. This demonstrates that increasing the maximum wind speed increases the storm surge height, but because of the complex arrangement of embankments, actually results in higher flooding because the capacity of the embankments is exceeded. Figure 4.11a also shows the expanded flooding in the Central and Eastern GBMD.

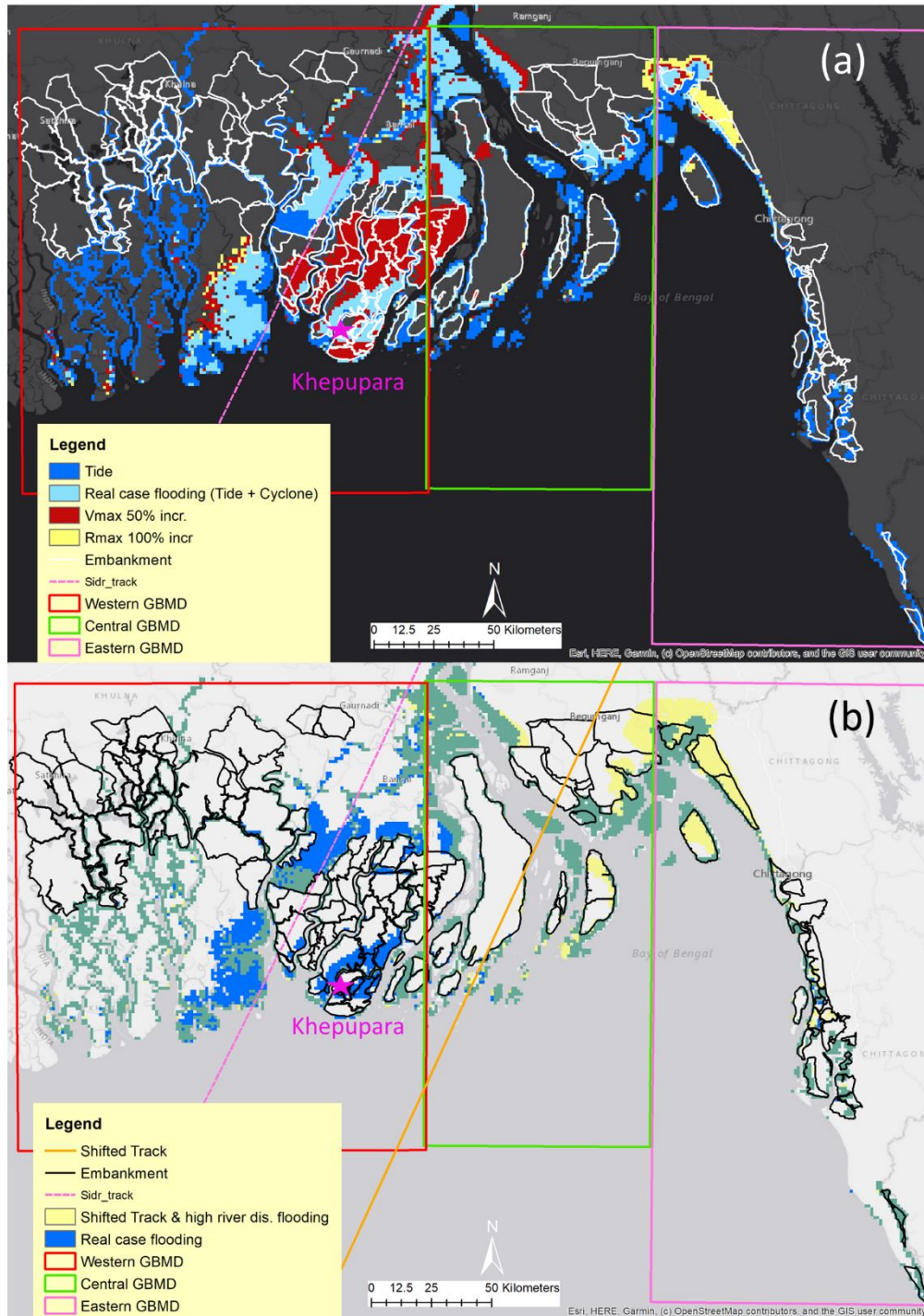


Figure 4.11. Area of flooding at 2100 UTC, 15 November 2007 for: (a) only tide, Cyclone Sidr (Real case (Tide + Cyclone)), Maximum velocity increased by 50% for Cyclone Sidr (V_{max} 50% incr.) and Radius of Maximum wind speed increased by 100% (R_{max} 100% incr.); and (b) Area of flooding for the control cyclone track and the eastward-shifted cyclone track with a river discharge of $30,000 \text{ m}^3 \text{ s}^{-1}$. The purple and yellow dashed lines represent the original Cyclone Sidr track and the modified Cyclone Sidr track, respectively. The green shaded area denotes the flooded area in both simulations.

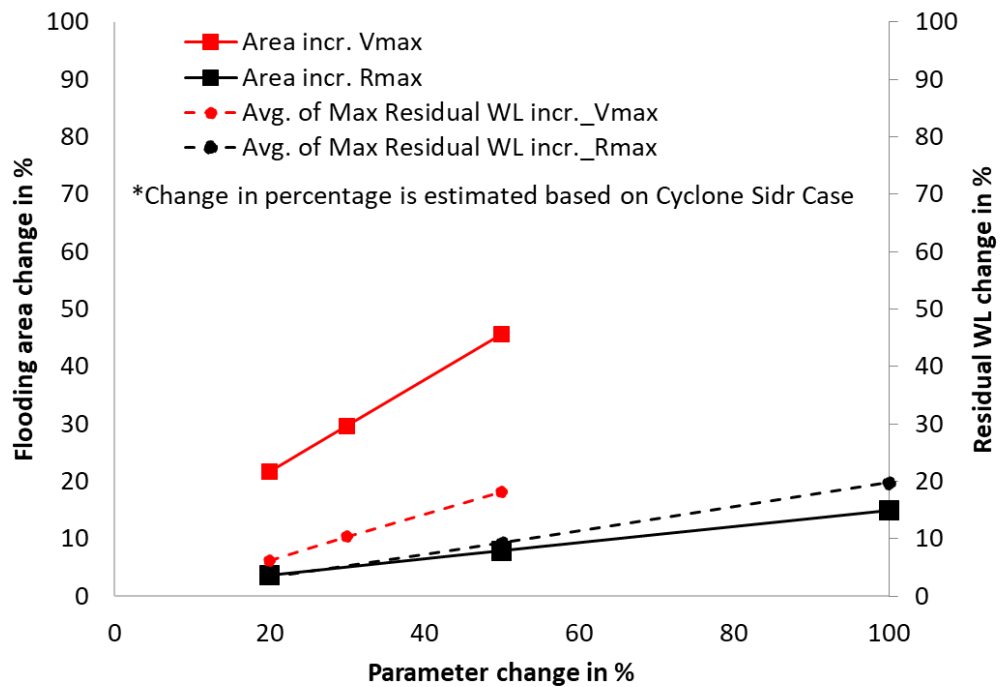


Figure 4.12. Percentage change in the area of flooding and average residual water level compared to the control Cyclone Sidr simulation with percentage change in maximum wind speed (V_{max}) and radius of maximum wind (R_{max}). The average maximum residual water level for each idealized case is estimated by averaging the maximum residual water levels at all stations across the GBMD.

4.4.5 Influence of cyclone landfall location and river discharge on cyclone-induced storm surge

The landfall location of a cyclone also affects the amount of area that is affected by floods due to cyclone-induced storm surge because of the complex geomorphology of the region. Moreover, a cyclone-induced storm surge event during a high river discharge period should result in a higher amount of flooding than a low river discharge period. To understand how the river discharge affects the GBMD, different river discharge ($10,000 \text{ m}^3 \text{ s}^{-1}$ to $50,000 \text{ m}^3 \text{ s}^{-1}$) scenarios are considered with the original Cyclone Sidr track. A separate simulation to assess a change in landfall location and different river discharge ($0 \text{ m}^3 \text{ s}^{-1}$ to $30,000 \text{ m}^3 \text{ s}^{-1}$) scenarios is also run by shifting the landfall location of Cyclone Sidr eastward to the Lower Meghna estuary (Figure 4.11b).

The model water level variations for these different scenarios are presented in Figure 4.13. Results show that increased river discharge results in increased water levels at the stations located in the Central GBMD regardless of the different landfall locations. For the original Cyclone Sidr track (Control track in Figure 4.13), the water levels increase by 1.3 m at Nilkamal due to increase of river discharge from $10,000 \text{ m}^3 \text{ s}^{-1}$ to $50,000 \text{ m}^3 \text{ s}^{-1}$ before landfall. During the passage of the cyclone eye at Nilkamal (67-hour, 1800 UTC 15 November 2007), the water level is increased by 0.5 m due to the increased river discharge. At Tajumuddin, the increased of river discharge does not show any influence on water levels except a 0.5 m rise at 69-hour, 2000 UTC, 15 Nov 2007. Other stations in the Western and Eastern GBMD do not show any water level variations with increase of river discharge for the control track. Similarly, for the shifted track, the increase of river discharge results in higher water level only in the Central GBMD. Results demonstrate that higher river discharge only affects the water level variations in the more northern areas of Central GBMD. Stations in the other regions do not show any fluctuation with the different river discharges.

When the landfall location is shifted to the Lower Meghna estuary, the maximum water level increases at all stations located in the Central and Eastern GBMD (Figure 4.13). In contrast, no variations in the water level are observed in the Western GBMD (Figure 4.13). The shifting of the track and landfall location to the east generally shifts the location of the flooding east (Figure 4.11b). In addition, there is no flooding in the Western GBMD when the river discharge is also increased to $30,000 \text{ m}^3 \text{ s}^{-1}$ (Figure 4.11b). In Figure 4.11b, the green shading represents the flooding common to both the control cyclone track and the eastward shifted track, the blue (yellow) shading is the flooding due only to the control (eastward-shifted with $30,000 \text{ m}^3 \text{ s}^{-1}$ river discharge) Cyclone Sidr simulation. The common green shaded flooding area in Figure 4.11b is a

result of tidal flooding rather than directly due to the cyclonic influence (compare with the blue-shaded tidal flood area in Figure 4.11a). The results suggest that river discharge only influences cyclone-induced storm surge events if the cyclone makes landfall near the Lower Meghna estuary in the Central GBMD. This highlights the importance of the landfall location in this region and the importance of capturing the interaction between the Meghna river discharge, the tidal components, and the cyclonic storm surge to properly predict the spatial distribution of the flooding in the GBMD. Furthermore, though the coastal area of Bangladesh is protected by embankments, the landfall location is an essential factor in the generation of cyclone-induced storm surge height and flooded area in the GBMD.

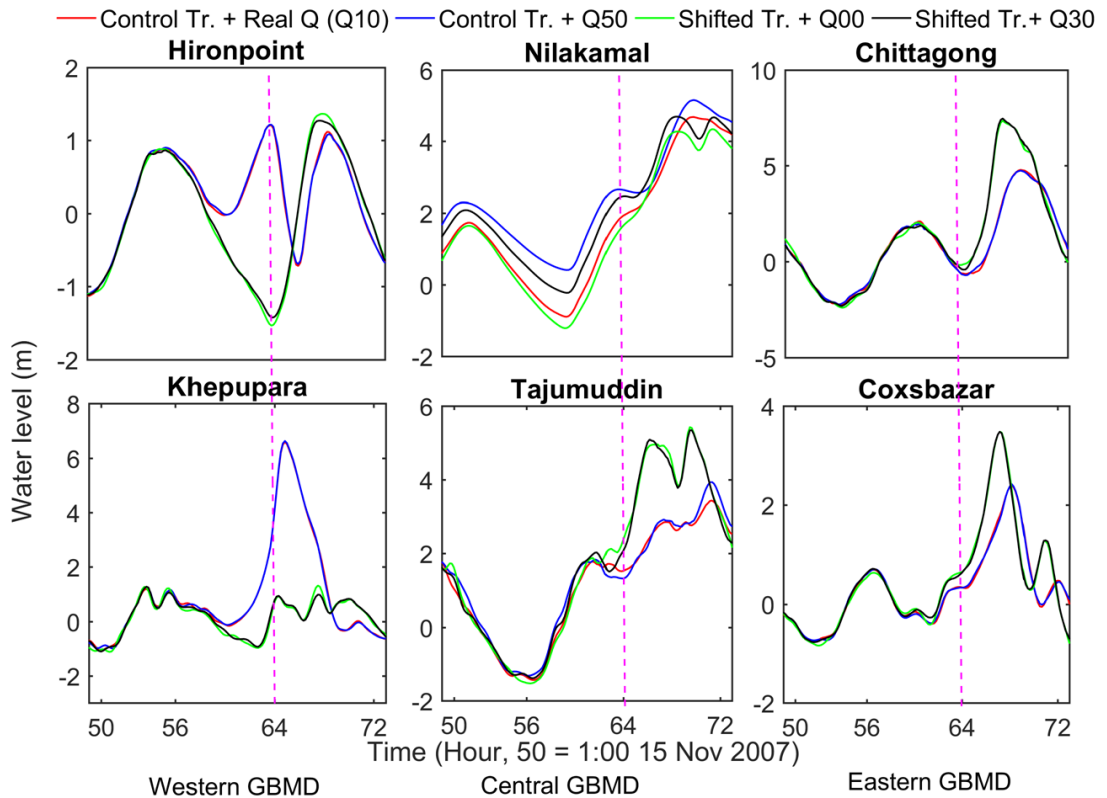


Figure 4.13. Simulated water level variation for different river discharge amounts for both the original (Control track) and shifted landfall location of Cyclone Sidr (Shifted track). Q_{00} , Q_{30} , Q_{50} represent $0 \text{ m}^3 \text{ s}^{-1}$, $30000 \text{ m}^3 \text{ s}^{-1}$ and $50000 \text{ m}^3 \text{ s}^{-1}$ of river discharge at the Lower Meghna, respectively. The purple line represents the landfall time of 1500 UTC 15 November 2007.

4.5 Conclusion

The GBMD delta is exposed to cyclone-induced storm surge flooding approximately every three years, which causes significant economic loss and death toll in the Bangladesh coast. It is projected that the Bangladesh coast will face worse consequences from severe cyclones in the future due to climate change (e.g., Hoque et al., 2018; Mehvar et al., 2019). In this chapter, a wave-current coupled hydrodynamic 3D model has been used to investigate the processes associated with storm surge and associated flooding in the GBMD during Cyclone Sidr. The sensitivity of the cyclone-induced storm surge height and associated flooding to MSL rise, the intensity and size of cyclone, river discharges and a shift in the track of Cyclone Sidr are all investigated.

Results show that a 1.5 increase in MSL with Cyclone Sidr, will cause flooding of up to 33 % of the total coastal area of Bangladesh, which is 8 % of the total area of Bangladesh. Depending on the amount of MSL rise, storm surge height may actually decrease with MSL rise at some locations (e.g., Khepupara) because embankments are overtopped releasing the waters into the floodplain. The Western and Central GBMD are affected more by MSL rise compared to the Eastern GBMD because the land elevations are generally lower (< 3 m above current MSL). The amount of area inundated by the cyclone increases linearly with MSL rise except for the 1.5 m rise of MSL because this triggers extensive tidal flooding in the Western and Central GBMD. This suggests that current cyclones will cause more flooding in the GBMD in the future because of MSL rise alone.

An increase in the cyclone maximum wind speed is more likely to increase the area that is inundated rather than increase storm surge height at river stations in the GBMD because the protective embankments are overtopped releasing the waters into

the floodplain. An increase in the radius of maximum wind produces larger changes at stations located further from the cyclone track compared to the stations located near the cyclone track likely because the strongest winds have been shifted further away from the centre of the cyclone. Finally, the influence of river discharge on cyclone-induced storm surge events in the GBMD is dependent on the cyclone landfall location with more impacts if the landfall location is closer to the estuary mouth, and only affects the stations located in the Central GBMD.

The area that is vulnerable to coastal flooding in the GBMD can be identified by analysing model inundation results for different hydrodynamic and cyclonic conditions. In this chapter only a few sensitivity scenarios have been explored. However, the model can be used as an assessment tool for disaster management planning for different flooding scenarios, particularly in embankment height design and identifying vulnerable locations in the GBMD under different cyclone and mean sea level rise scenarios.

Chapter 5 Conclusion and future scope

5.1 Conclusion

The Ganges-Brahmaputra-Meghna delta (GBMD), located in the lower part of the Bangladesh coast, is exposed to strong seasonal river discharge variations and tropical cyclones at regular intervals. The Lower Meghna river is the second largest freshwater outlet to the ocean after the Amazon river. Several factors including the presence of a shallow coastal shelf, low land elevations above the mean sea level, geographical locations, varying high river discharge from the upper catchment area, strong semi-diurnal tides at river mouths, and regular cyclonic events make the GBMD a perfect laboratory to study river-tide interactions and cyclone-induced storm surge events. The main topics of the thesis, illustrated in Figure 1.2, are summarized below in response to three questions:

- How do the seasonal river discharge variations modulate tides along the GBMD?
- How do the wave-current interactions influence a cyclone-induced storm surge event (Cyclone Sidr, 2007) in the GBMD?
- How does a cyclone-induced storm surge event result in flooding in the GBMD, and how will the cyclone-induced storm surge flooding be affected by future mean sea level rise due to climate change?

5.1.1 How do the seasonal river discharge variations modulate tides along the GBMD?

A hydrodynamic model is validated by using Delft3D to investigate tidal variations with varying river discharge in the GBMD. The model is validated and calibrated for an average hydrological flood year (2000) and then applied to two different hydrological years, with nine idealized river discharge scenarios covering the typical hydrological conditions of the GBMD. The model water level results are analyzed using stationary harmonic analysis (T_TIDE) and a non-stationary harmonic analysis method (Complex demodulation Method).

Results demonstrate that the upper limit of tidal excursion shifts 75 km upstream during the dry season. The residual water level slope and tidal damping rate increase with river discharge beyond 100 km from the estuary mouth. Longer tidal periods including the MSF (14.6 days) can be amplified by high river discharges. The balance between dissipation and generation of tides depends on the residual velocity generated by river discharge and the velocity of principal tides. The decomposition analysis of the total friction shows that the maximal generation of the quarterdiurnal tides in the upper GBMD depends on the friction generated from the river-tide interaction. For the first time, the two-fold role of river discharge on tides: (1) tide dissipation; and (2) tide generation, are explained. A critical river discharge threshold produces an optimal dissipation of semidiurnal tides and the generation of quarterdiurnal tides via friction at the upper and middle part of the GBMD (Figure 5.1). River discharge above the critical river discharge dissipates both semidiurnal and quarterdiurnal tides rather than generating quarterdiurnal tides from nonlinear interactions (Elahi et al., 2020). A recent study by Guo et al. (2021) shows that these findings are also applicable in other estuaries having strong river discharge across the world.

5.1.2 How do the wave-current interactions influence a cyclone-induced storm surge event (Cyclone Sidr, 2007) in the GBMD?

Severe cyclones make landfall in the GBMD at regular intervals and cause cyclone-induced storm surge events in the Bangladesh coast. Although the GBMD is a tide-dominated delta, wind-driven waves during a cyclonic event can contribute to the cyclone-induced storm surge height. Most of the previous studies (e.g., Hussain and Tajima, 2017) assessed cyclone-induced storm surge events in the GBMD by assuming that the wave has negligible influence on the storm surge height. A barotropic 3D (ten sigma layers) online wave-current coupled model is used to study the role of wave-current interactions during a cyclone-induced storm surge event. The model is calibrated and validated for Cyclone Sidr (2007). Twenty-one idealized cyclonic scenarios are designed by considering different model coupling methods and different boundary forcing to evaluate the influence of wave and wave-current interactions in a cyclone-induced storm surge event.

Results reveal that the wave-current interaction can increase the surge height up to 0.3 m along the coastline due to the wave setup during Cyclone Sidr. Including wave-current interactions in the simulation results in an increase of 1.1 m in significant wave height at Khepupara, near the landfall location. All other stations also have higher significant wave heights when the wave-current interactions are included compared to no wave-current interactions except Tajumuddin. The significant wave height increase in the wave-current scenario occurs because the waves and currents are in opposite directions. In addition, the effective wind stress (vectorial difference between current and wind speed) is influenced by the wave-current interaction and results in varying wind setup across the GBMD. The varying effective wind stress and different

magnitudes and directions of wave and current are causing the varying wave heights (Figure 5.1).

Different idealized scenario cases that consider different coupling methods between the hydrodynamic model and the wave model with different parameters including water levels and currents demonstrate that in regions of deep water (e.g., deep ocean and deeper coastal regions such as Tajumuddin ~ 25 m), the current dominates the significant wave height. As the waves propagate into shallower regions (e.g., Khepupara < 10 m) from the deeper ocean, the water level becomes dominant in modulating the significant wave height. The wave-current interactions cause higher modulation in the region between 50 km landward to 50 km offshore. Furthermore, whitecapping dissipation is dominant among all other wave dissipation processes, such as depth-induced breaking and bottom friction during the cyclone-induced storm surge event.

The present study illustrates the important role of wave-current interactions in cyclone-induced storm surge in the GBMD, and that not including this process in numerical simulations will contribute to errors in the magnitude and timing of the maximum surge height.

5.1.3 How does a cyclone-induced storm surge event result in flooding in the GBMD and how will the cyclone-induced storm surge flooding be affected by the future mean sea level rise due to climate change?

Cyclone-induced storm surge flooding is significant in the GBMD. The presence of a protective earthen embankment network and low land elevations relative to the mean sea level complicate the flooding. Moreover, many future projection studies (e.g., World Bank, 2015; Danda, 2020) suggest that the GBMD will be vulnerable to impacts

from rising mean sea levels from climate change and that it may exacerbate the effects of cyclone-induced flooding. Therefore, numerous studies have been carried out to study cyclone-induced storm surge events in the GBMD. However, all these studies neglect several important processes including wave-current interactions, the floodplain area in model bathymetry, and embankment heights. Here, all these limitations have been overcome by applying a wave-current coupled hydrodynamic 3d model with a finer model bathymetry that includes the floodplain area and embankment height in the GBMD.

A case study of Cyclone Sidr under different idealized mean sea rise scenarios, including mean sea level increases of 0.5 m, 1 m, and 1.5 m is simulated using the model. The results show that as the mean sea level increases, there is a higher cyclone-induced storm surge flooded area for Cyclone Sidr. For example, a mean sea level rise of 1.5 m with Cyclone Sidr results in 33 % of the total coastal area being flooded, which is 8 % of the total area of Bangladesh. In contrast, Cyclone Sidr, with no mean sea level rise, causes flooding in 12 % of the coastal area. The Western and Central GBMD are more affected by mean sea level rise than the Eastern GBMD because of low land elevations (< 3 m above mean sea level). The maximum water levels at various stations show an increasing trend with rising mean sea level except for the maximum 1.5 m increase scenario. At a 1.5 m mean sea level rise, the protective embankments are overtopped in the Western and Central GBMD causing extensive tidal flooding and as a result, the maximum water levels are slightly reduced at stations located in these two regions.

The sensitivity to cyclonic forcing on inundation is investigated by increasing the maximum wind speed and the radius of maximum wind. Results demonstrate that increasing the maximum wind speed of Cyclone Sidr increases the size of the flooding in the floodplain rather increasing the storm surge height at river stations because the

protective embankments are overtopped. Stations located close to the cyclone track are less affected by an increase in the radius of maximum wind than stations located far from the cyclone track. Finally, the influence of river discharge on cyclone-induced storm surge events in the GBMD depends on the cyclone landfall location because of the complex morphology of the region and dominance of the Meghna river in draining the GBMD to the ocean and only affects the stations located in the Eastern GBMD.

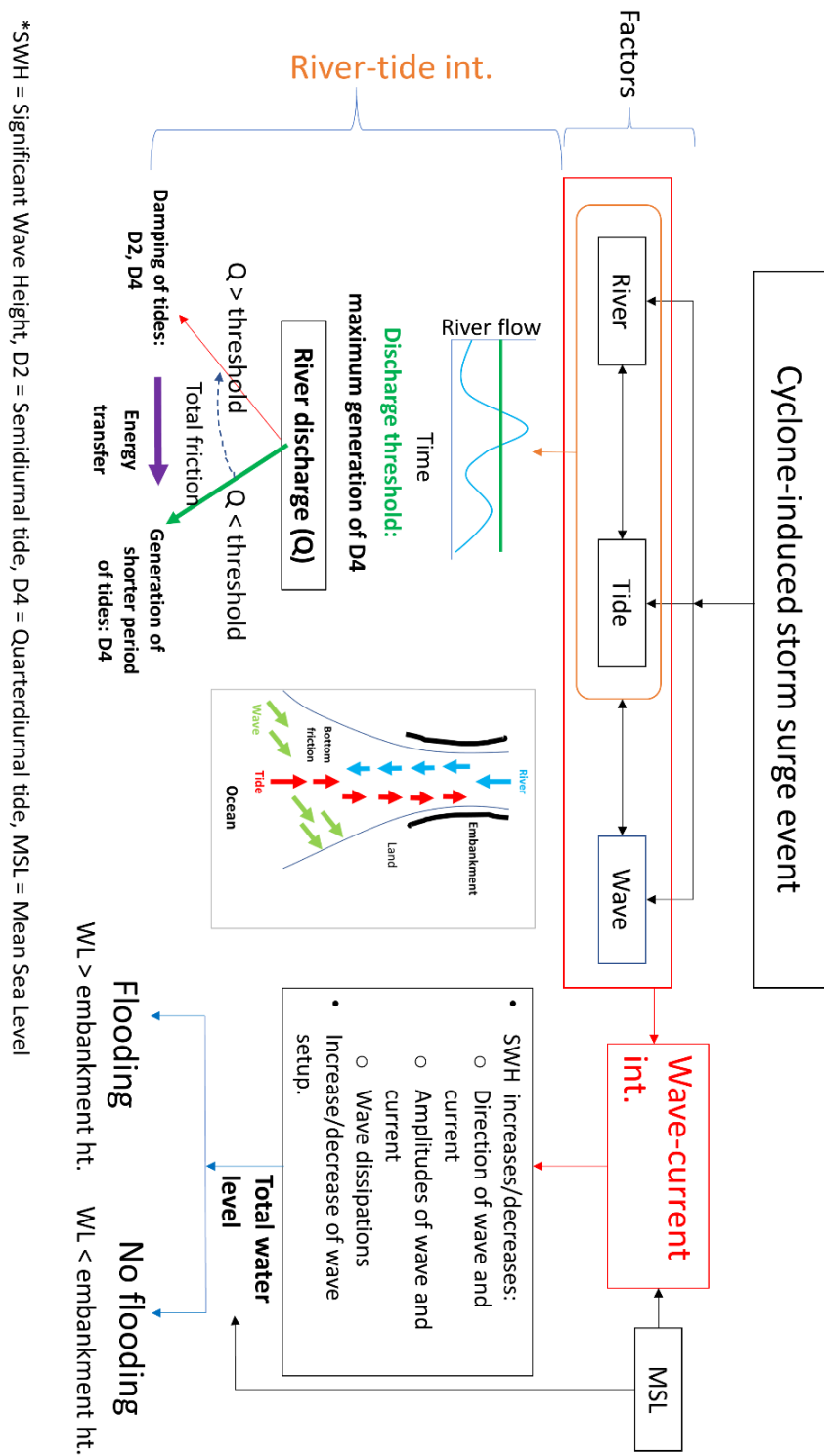


Figure 5.1. Influence of river-tide and wave-current interactions during a cyclone-induced storm surge event.

Figure 5.1 summarizes the important processes that take part in a cyclone-induced storm surge event. The threshold river discharge dictates the generation and dissipation of tides at the upper middle of the estuary. At the mouth, the tide is dominant over river

discharge and dictates the current magnitude and direction. During a cyclonic period, strong cyclonic wind fields result in cyclone-induced storm surge heights across the coast, which is influenced by a combination of river-tide interaction and wave-current interaction. MSL rise can also increase the magnitudes of the storm surge heights by modifying wind setup and wave-current interaction. Most of the Bangladesh coast is protected by an earthen embankment network that strongly influences the flooding pattern for all flooding events including fluvio-tidal flooding and cyclone-induced storm surge flooding.

5.2 Implications

This thesis will help explain tidal water level variations with substantial seasonal river discharge variations along an estuary with a high river discharge. The nonlinear tide generation and dissipation analysis with varying river discharge complement the understanding of tidal excursion in a complex estuary like the GBMD. The applied methodology for identifying the critical river discharge for tide dissipation and generation is also applicable for other estuaries. Estimating critical river discharge can be helpful to control the upstream river discharge for restricting tidal propagation along an estuary.

Wave-current interaction is an essential process during a cyclone-induced storm surge event, even in a tide-dominated shallow delta region like the GBMD. The findings illustrate that considering wave-current interaction in the numerical model results in higher wave-setup and significant wave height along the GBMD. Results demonstrate that wave-current interaction can result in up to 1.5 m higher significant wave height at the cyclone landfall location compared with a no wave-current interaction simulation result. Furthermore, the results suggest that the increased radiation stress along the

GBMD results in stronger currents when including wave-current interaction. The findings complement the understanding of the role of wave-current interactions in the GBMD.

Cyclone-induced flooding results demonstrate that for the same cyclone intensity, more floodplain area may be inundated as the mean sea level rises. The model developed for this research can be a tool for evaluating different flooding events, including fluvial flooding and cyclone-induced flooding in the GBMD. Moreover, the model will be useful for designing embankment heights, risk mapping, and disaster management planning. Finally, the thesis outcomes will help to better identification of hotspot for cyclone-induced storm surge height for the policymakers. They can assess usefulness of placing of cyclone shelters by analysing inundation area from the model result. The model can be used as a resource for emergency managers, researchers, and policymakers to understand the different hydrodynamic processes in the GBMD.

5.3 Limitations and future research

5.3.1 Limitations

5.3.1.1 Tide analysis

The tidal water levels at different locations across the GBMD are analysed by applying two statistical approaches: (1) Stationary harmonic analysis (T_TIDE) and (2) non-stationary harmonic analysis (Complex demodulation method). The results demonstrate that the Stationary harmonic analysis fails to capture the influence of varying river discharge on tides, whereas the non-stationary harmonic analysis successfully capture the variation of tidal amplitudes with varying river discharges.

Although, the longer period tides including MSF tide (period 14.6 days) shows an increasing trend with river discharge, the detailed analysis in this thesis is limited to the semidiurnal and quarterdiurnal tides. Rose and Bhaskaran (2016) also observe seasonal variations in compound tides in the GBMD. Hence, further analysis of longer and shorter period of tides could provide insight in extreme tidal flooding events in the GBMD.

5.3.1.2 Wave-current interaction study

Due to a lack of field data, the model predicted wave field is compared with the ERA5 reanalysis dataset (Hersbach et al., 2020). The ERA5 ocean data does not resolve the estuary mouth regions of the GBMD and a point-by-point comparison of model significant wave height (SWH) and model wind speed with the ERA5 data is not possible because of the very different model grid resolutions. Although, the model is calibrated and validated by comparing the model water level with the available observations, it was not possible to compare the model predicted current with observations for with- and without-cyclone conditions due to lack of current observations. Discrepancies in current magnitude and direction between the model result and the observations may contribute error in the model results including wave heights, wave setup and time of maximum surge height.

In the present study, the wave-current interaction is investigated in terms of change in water level and significant wave height. The wave-current interaction also affects currents through increased radiation stress and enhanced bottom friction. According to Hashemi et al. (2015), the wave-current interaction can reduce the tidal energy by up to 20 % during extreme wave scenarios in the Irish Sea. Therefore, the wave-current interaction can also be studied by analyzing velocity profile, and tidal- and wave-energy. Due to a lack of observation of current velocity, the present study does not include this kind of analysis.

5.3.1.3 Inundation during cyclone

Heavy rainfall accompanying the passage of a cyclone can generate extensive fresh-water inundation in the cyclone affected area (e.g., Uddin et al., 2019; Li et al., 2020). However, the present study ignores precipitation during Cyclone Sidr and investigates only inundation produced from cyclone-induced storm surge height through embankment overtopping. Moreover, the inundation associated with embankment breaching is not considered in the model setup. Finally, because of cyclone-related cloud coverage, satellite-based estimation of the inundation area in the GBMD during Cyclone Sidr is limited and this limits the validation of the model results.

5.3.1.4 Grid resolution

The model grid resolution varies from 1320 m x 956 m in the ocean to 300 m x 200 m in rivers. The existing grid resolution can represent all the major rivers and channels across the GBMD. However, there are numerous channels with less than 200 m width located in the Western GBMD. These channels are part of the mangrove forest and play an important role in flooding in the Western GBMD. Therefore, finer grid resolution will improve the model water level and flooding in the Western GBMD.

5.3.1.5 Bathymetry measurement

Due to a lack of bathymetric measurements, several rivers including the Kobodak river (in the Western GBMD), Gorai river (in the Central GBMD) and Feni river (in the Eastern GBMD) are not included in the model setup. The bathymetry of the Lower Meghna river mouth changes rapidly due to strong tidal current and the sediment load from the upper catchment area. Hence, the bathymetry continuously changes at the estuary mouth. In the present study, the model bathymetry is prepared based on field measurements over the period 2009-2013 and the model results are validated for 2000

and Cyclone Sidr (2007). Having regularly updated measurements for the same period as any model simulations will likely improve the model results further.

5.3.1.6 Model domain, baroclinic effects and remote signals

The current model domain covers whole Bangladesh coast (730 km long) including 200 km towards offshore and 200 km towards inland area. The approximate area covered by the model grid in land including river network is 47,222 square km. The total grid point is 676,488 with 10 sigma layers. As the spatial resolution of the computational grid requires fine grid resolution to satisfactorily the wave-induced setup in the surf zone (especially for embankments) (Krien et al., 2017), the grid size varies between 200 m to 300 m in rivers and lands. Simulation time for the current model setup for a 7-day cyclone event is 3 days in a high performance computing system. Hence, we did not consider a larger domain that will take longer time to simulate one single event. As a result, the model setup may miss remotely generated surge and swell signal, which may affect the coastal region of Bangladesh. To our best knowledge, the current model setup contains finest model grid covering the whole Bangladesh coast considering wave-current interaction process with cyclonic conditions.

Several studies (e.g., Deb and Ferreira, 2016, Krien et al., 2017, Mammun et al., 2020) considered large domains covering the Bay of Bengal and specified wave spectral boundary as an open boundary conditions also did not find any remotely generated surge setup and swell along the Bangladesh coast. It may be resulted due to the presence of the ‘Swatch of no ground’, which is also known as the Bengal Canyon (newly added Figure 3.1). The head of Bengal Canyon is located 30 km offshore from the coast and bathymetry vary between 1000 m to 1400 m. The combined effect of shallow continental shelf (< 50 m) and the Bengal canyon might diminish the remotely generated surge setup

and swell. It would be an interesting research scope to assess the influence of the Bengal Canyon on the Bangladesh coast.

The present model setup ignores different baroclinic processes including sea temperature, salinity, sediment concentration. These baroclinic processes play important role in deep ocean to modulate current velocity profile. Considering these processes may improve the results of wave-current interactions by improving current velocity profile.

5.3.2 Future research

The thesis work including the numerical modelling has some limitations as mentioned in the previous section, leading to potential further progress in the future.

A barotropic model is used to simulate hydrodynamics of the GBMD by considering tide, river discharge and wind. The model could be improved by considering baroclinic effects such as salinity, sediment, and temperature. Due to a lack of field data, it is not possible to calibrate the model current velocity and wave height, and direction with the observed time series.

Due to a lack of observed river discharge and bathymetry, several rivers including the Kobodak river (in the Western GBMD), Gorai river (in the Central GBMD) and Feni river (in the Eastern GBMD) are not included in the model setup. Including these rivers in the study could further improve the model tidal water levels.

The GBMD is a tide-dominated active delta. Therefore, the bathymetry of the GBMD is changing rapidly through riverbank erosion and a large sediment load (annually 1 billion tons of sediment) transport from the upper catchment area. By transforming the established model into a baroclinic model, the sediment transport and

floodplain sedimentation processes in the GBMD could be studied further. This would make it possible to study the change of the coastal line of the GBMD under different climate change scenarios by considering the sediment process in the model setup.

River salinity in the GBMD shows seasonal variations with river discharge (Bricheno et al., 2016). By considering salinity in the existing model setup, the salinity intrusion in the GBMD could be studied for different hydrological conditions under different sea level rise scenarios. Finally, a detailed investigation of risk and vulnerability related to cyclone-induced storm surge flooding in the GBMD could be undertaken to develop a detailed disaster management plan under present and future climate scenarios.

References

- Adnan, M.S.G., Haque, A., Hall, J.W., 2019. Have coastal embankments reduced flooding in Bangladesh? *Sci. Total Environ.* 682, 405–416. <https://doi.org/https://doi.org/10.1016/j.scitotenv.2019.05.048>
- Alam, E., Collins, A.E., 2010. Cyclone disaster vulnerability and response experiences in coastal Bangladesh. *Disasters* 34, 931–954. <https://doi.org/10.1111/j.1467-7717.2010.01176.x>
- Alam, E., Dominey-Howes, D., 2015. A new catalogue of tropical cyclones of the northern Bay of Bengal and the distribution and effects of selected landfalling events in Bangladesh. *Int. J. Climatol.* 35, 801–835. <https://doi.org/https://doi.org/10.1002/joc.4035>
- Alam, E., Momtaz, S., Bhuiyan, H.U., Baby, S.N., 2018. Climate Change Impacts on the Coastal Zones of Bangladesh: Perspectives on Tropical Cyclones, Sea Level Rise, and Social Vulnerability BT - Bangladesh I: Climate Change Impacts, Mitigation and Adaptation in Developing Countries, in: Islam, M.N., van Amstel, A. (Eds.), . Springer International Publishing, Cham, pp. 145–166. https://doi.org/10.1007/978-3-319-26357-1_6
- Ali, A., 1999. Climate change impacts and adaptation assessment in Bangladesh. *Clim. Res.* 12, 109–116.
- Ali, A., 1979. Storm Surges in the Bay of Bengal and Some Related Problems. University of Reading.
- Allison, M. a, 1998. Geologic framework and environmental status of the Ganges-Brahmaputra delta. *J. Coast. Res.* 14, 826–836.

<https://doi.org/10.1017/CBO9781107415324.004>

As-Salek, J.A., 1998. Coastal Trapping and Funneling Effects on Storm Surges in the Meghna Estuary in Relation to Cyclones Hitting Noakhali–Cox’s Bazar Coast of Bangladesh. *J. Phys. Oceanogr.* 28, 227–249. [https://doi.org/10.1175/1520-0485\(1998\)028<0227:CTAFEO>2.0.CO;2](https://doi.org/10.1175/1520-0485(1998)028<0227:CTAFEO>2.0.CO;2)

Auerbach, L.W., Goodbred Jr, S.L., Mondal, D.R., Wilson, C. a., Ahmed, K.R., Roy, K., Steckler, M.S., Small, C., Gilligan, J.M., Ackerly, B. a., 2015. Flood risk of natural and embanked landscapes on the Ganges–Brahmaputra tidal delta plain. *Nat. Clim. Chang.* 5, 153–157. <https://doi.org/10.1038/nclimate2472>

Banglapedia, 2015. River [WWW Document]. URL <http://en.banglapedia.org/index.php/River> (accessed 6.2.21).

Battjes, J.A., Janssen, J.P.F.M., 1978. Energy Loss and Set-Up Due to Breaking of Random Waves, in: *Coastal Engineering 1978*. pp. 569–587. <https://doi.org/10.1061/9780872621909.034>

Berg, N.J., 2013. On the influence of storm parameters on extreme surge events at the Dutch coast. University of Twente.

Bhaskaran, P.K., Rao, A.D., Murty, T., 2020. Tropical Cyclone–Induced Storm Surges and Wind Waves in the Bay of Bengal, *Techniques for Disaster Risk Management and Mitigation*. <https://doi.org/10.1002/9781119359203.ch17>

Bloomfield, P., 2004. *Fourier Analysis of Time Series: An Introduction*, Wiley Series in Probability and Statistics. Wiley.

Bolaños, R., Brown, J.M., Souza, A.J., 2014. Wave–current interactions in a tide dominated estuary. *Cont. Shelf Res.* 87, 109–123.

<https://doi.org/https://doi.org/10.1016/j.csr.2014.05.009>

- Booij, N., Ris, R.C., Holthuijsen, L.H., 1999. A third-generation wave model for coastal regions 1. Model description and validation. *J. Geophys. Res. Ocean.* 104, 7649–7666. <https://doi.org/10.1029/98JC02622>
- Brammer, H., 2014. Bangladesh's dynamic coastal regions and sea-level rise. *Clim. Risk Manag.* 1, 51–62. <https://doi.org/10.1016/j.crm.2013.10.001>
- Brammer, H., 1990. Floods in Bangladesh: Geographical Background to the 1987 and 1988 Floods. *Geogr. J.* 156, 12–22. <https://doi.org/10.2307/635431>
- Bricheno, L., Wolf, J., 2018. Modelling Tidal River Salinity in Coastal Bangladesh, in: Nicholls, R.J., Hutton, C.W., Adger, W.N., Hanson, S.E., Rahman, M.M., Salehin, M. (Eds.), *Ecosystem Services for Well-Being in Deltas: Integrated Assessment for Policy Analysis*. Springer International Publishing, Cham, pp. 315–332. https://doi.org/10.1007/978-3-319-71093-8_17
- Bricheno, L.M., Wolf, J., Islam, S., 2016. Tidal intrusion within a mega delta: An unstructured grid modelling approach. *Estuar. Coast. Shelf Sci.* 182, 12–26. <https://doi.org/10.1016/j.ecss.2016.09.014>
- Brown, J.M., Bolaños, R., Wolf, J., 2013. The depth-varying response of coastal circulation and water levels to 2D radiation stress when applied in a coupled wave–tide–surge modelling system during an extreme storm. *Coast. Eng.* 82, 102–113. <https://doi.org/https://doi.org/10.1016/j.coastaleng.2013.08.009>
- Buschman, F.A., Hoitink, A.J.F., Van Der Vegt, M., Hoekstra, P., 2009. Subtidal water level variation controlled by river flow and tides. *Water Resour. Res.* 45, 1–12. <https://doi.org/10.1029/2009WR008167>

- BWDB, 2013. Technical Feasibility Studies and Detailed Design for Coastal Embankment Improvement Programme (CEIP) (Main Report). Dhaka, Bangladesh.
- BWDB, 2012. Annual Report: Flood Forecasting and Warning Centre, Processing and Flood Forecasting Circle. Dhaka, Bangladesh.
- Cai, H., Savenije, H., Garel, E., Zhang, X., Guo, L., Zhang, M., Liu, F., Yang, Q., 2019a. Seasonal behaviour of tidal damping and residual water level slope in the Yangtze River estuary: identifying the critical position and river discharge for maximum tidal damping. *Hydrol. Earth Syst. Sci.* 23, 2779–2794. <https://doi.org/10.5194/hess-23-2779-2019>
- Cai, H., Savenije, H.H.G., Toffolon, M., 2014. Linking the river to the estuary: Influence of river discharge on tidal damping. *Hydrol. Earth Syst. Sci.* 18, 287–304. <https://doi.org/10.5194/hess-18-287-2014>
- Cai, H, Savenije, H.H.G., Toffolon, M., 2014. Linking the river to the estuary: influence of river discharge on tidal damping. *Hydrol. Earth Syst. Sci.* 18, 287–304. <https://doi.org/10.5194/hess-18-287-2014>
- Cai, H., Savenije, H.H.G.G., Garel, E., Zhang, X., Guo, L., Zhang, M., Liu, F., Yang, Q., 2019b. Seasonal behaviour of tidal damping and residual water level slope in the Yangtze River estuary: identifying the critical position and river discharge for maximum tidal damping. *Hydrol. Earth Syst. Sci.* 23, 2779–2794. <https://doi.org/10.5194/hess-23-2779-2019>
- Chandrappa, R., Gupta, S., Kulshrestha Chandra, U., 2011. Coping with Climate Change, *Mining Magazine*. Springer, Berlin, Heidelberg.

<https://doi.org/10.1007/978-3-642-19674-4>

Chiu, S., Small, C., 2016. Observations of Cyclone-Induced Storm Surge in Coastal Bangladesh. *J. Coast. Res.* 321, 1149–1161. <https://doi.org/10.2112/JCOASTRES-D-15-00030.1>

Dalrymple, R.W., Choi, K., 2007. Morphologic and facies trends through the fluvial-marine transition in tide-dominated depositional systems: A schematic framework for environmental and sequence-stratigraphic interpretation. *Earth-Science Rev.* 81, 135–174. <https://doi.org/10.1016/j.earscirev.2006.10.002>

Danda, A.A., 2020. Climate Change and Sea-Level Rise in the BIMSTEC Region : Towards a Suitable Response.

Das, P.K., 1994a. Prediction of storm surges in the Bay of Bengal. *Proc Indian Natl Sci Acad* 60, 513–533.

Das, P.K., 1994b. Prediction of storm surges in the Bay of Bengal. *Proc Indian Natl Sci Acad* 60, 583–595. <https://doi.org/10.1007/BF02835641>

Dasgupta, Susmita, Huq, M., Khan, Z., Ahmed, M., Mukherjee, N., Khan, M., Pandey, K., 2010. Vulnerability of Bangladesh to Cyclones in a Changing Climate: Potential Damages and Adaptation Cost. *World Bank Policy Res. Work. Pap.*

Dasgupta, S., Huq, M., Khan, Z.H., Ahmed, M.M.Z., Mukherjee, N., Khan, M.F., Pandey, K., 2014. Cyclones in a changing climate: the case of Bangladesh. *Clim. Dev.* 6, 96–110. <https://doi.org/10.1080/17565529.2013.868335>

Dasgupta, S, Huq, M., Khan, Z.H., Ahmed, M.M.Z., Mukherjee, N., Khan, M.F., Pandey, K., 2010. Vulnerability of Bangladesh to Cyclones in a Changing Climate Potential Damages and Adaptation Cost. *World* 16, 54.

<https://doi.org/10.1111/j.1467-7717.1992.tb00400.x>

Davies, A.M., Lawrence, J., 1995. Modeling the Effect of Wave-Current Interaction on the Three-Dimensional Wind-Driven Circulation of the Eastern Irish Sea. *J. Phys. Oceanogr.* 25, 29–45. [https://doi.org/10.1175/1520-0485\(1995\)025<0029:MTEOWI>2.0.CO;2](https://doi.org/10.1175/1520-0485(1995)025<0029:MTEOWI>2.0.CO;2)

Deb, M., Ferreira, C.M., 2016. Simulation of cyclone-induced storm surges in the low-lying delta of Bangladesh using coupled hydrodynamic and wave model (SWAN + ADCIRC). *J. Flood Risk Manag.* <https://doi.org/10.1111/jfr3.12254>

Dee, D.P., Uppala, S.M., Simmons, A.J., Berrisford, P., Poli, P., Kobayashi, S., Andrae, U., Balmaseda, M.A., Balsamo, G., Bauer, P., Bechtold, P., Beljaars, A.C.M., van de Berg, L., Bidlot, J., Bormann, N., Delsol, C., Dragani, R., Fuentes, M., Geer, A.J., Haimberger, L., Healy, S.B., Hersbach, H., Hólm, E. V, Isaksen, L., Kållberg, P., Köhler, M., Matricardi, M., McNally, A.P., Monge-Sanz, B.M., Morcrette, J.-J., Park, B.-K., Peubey, C., de Rosnay, P., Tavolato, C., Thépaut, J.-N., Vitart, F., 2011. The ERA-Interim reanalysis: configuration and performance of the data assimilation system. *Q. J. R. Meteorol. Soc.* 137, 553–597. <https://doi.org/https://doi.org/10.1002/qj.828>

Deltares, 2021a. Delft3d-FLOW: Simulation of multi-dimensional hydrodynamic flows and transport phenomena, including sediments. MH Delft.

Deltares, 2021b. Wind Enhance Scheme for cyclone modelling. MH Delft.

Deltares, 2021c. 3D/2D modelling suite for integral water solutions: Hydro-Morphodynamics.

Deltares, 2013a. Delft3D-FLOW User Manual. Delft3D-FLOW User Man. 3.15, 30808.

- Deltares, 2013b. Delft3D-WAVE User Manual. Delft3D-WAVE User Man. 3.05, 30013.
- Deltares, D., 2014. Delft3D-FLOW Simulation of Multi-Dimensional Hydrodynamic Flows and Transport Phenomena Including Sediments, User Manual.
- Dietrich, J.C., Zijlema, M., Westerink, J.J., Holthuijsen, L.H., Dawson, C., Luettich, R.A., Jensen, R.E., Smith, J.M., Stelling, G.S., Stone, G.W., 2011. Modeling hurricane waves and storm surge using integrally-coupled, scalable computations. *Coast. Eng.* 58, 45–65. <https://doi.org/https://doi.org/10.1016/j.coastaleng.2010.08.001>
- Dube, S.K., 2012. Prediction of Storm Surges in the Bay of Bengal. *Trop. Cyclone Res. Rev.* 1, 67–74. <https://doi.org/https://doi.org/10.6057/2012TCRR01.08>
- Dube, S.K., Chittibabu, P., Sinha, P.C., Rao, A.D., Murty, T.S., 2004. Numerical Modelling of Storm Surge in the Head Bay of Bengal Using Location Specific Model. *Nat. Hazards* 31, 437–453. <https://doi.org/10.1023/B:NHAZ.0000023361.94609.4a>
- Dube, S.K., Jain, I., Rao, A.D., Murty, T.S., 2009. Storm surge modelling for the Bay of Bengal and Arabian Sea. *Nat. Hazards* 51, 3–27. <https://doi.org/10.1007/s11069-009-9397-9>
- Dube, S.K., Rao, A.D., Sinha, P.C., Chittibabu, P., 1994. A Real Time Storm Surge Prediction System: An Application to East Coast of India. *Proc. Indian Natl. Sci. Acad.* 60, 157–170.
- Dube, S.K., Rao, A.D., Sinha, P.C., Murty, T.S., Bahulayan, N., 1997. Storm surge in the Bay of Bengal and Arabian Sea the problem and its prediction. *Mausam* 48,

283–304.

- Egbert, G.D., Erofeeva, S.Y., 2002. Efficient Inverse Modeling of Barotropic Ocean Tides. *J. Atmos. Ocean. Technol.* 19, 183–204. [https://doi.org/10.1175/1520-0426\(2002\)019<0183:EIMOBO>2.0.CO;2](https://doi.org/10.1175/1520-0426(2002)019<0183:EIMOBO>2.0.CO;2)
- Elahi, M.W.E., Jalón-Rojas, I., Wang, X.H., Ritchie, E.A., 2020. Influence of Seasonal River Discharge on Tidal Propagation in the Ganges-Brahmaputra-Meghna Delta, Bangladesh. *J. Geophys. Res. Ocean.* 125, e2020JC016417. <https://doi.org/https://doi.org/10.1029/2020JC016417>
- Fang, Y., Yin, J., Wu, B., 2016. Flooding risk assessment of coastal tourist attractions affected by sea level rise and storm surge: a case study in Zhejiang Province, China. *Nat. Hazards* 84, 611–624. <https://doi.org/10.1007/s11069-016-2444-4>
- FAO, 2016. AQUASTAT - FAO's Information System on Water and Agriculture [WWW Document]. URL http://www.fao.org/nr/water/aquastat/countries_regions/profile_segments/gbm-WR_eng.stm (accessed 5.4.18).
- Feng, X., Yin, B., Yang, D., 2016. Development of an unstructured-grid wave-current coupled model and its application. *Ocean Model.* 104, 213–225. <https://doi.org/https://doi.org/10.1016/j.ocemod.2016.06.007>
- Feng, X., Yin, B., Yang, D., 2012. Effect of hurricane paths on storm surge response at Tianjin, China. *Estuar. Coast. Shelf Sci.* 106, 58–68. <https://doi.org/https://doi.org/10.1016/j.ecss.2012.04.032>
- Feroz Islam, M., Bhattacharya, B., Popescu, I., 2019. Flood risk assessment due to cyclone-induced dike breaching in coastal areas of Bangladesh. *Nat. Hazards Earth*

Syst. Sci. 19, 353–368. <https://doi.org/10.5194/nhess-19-353-2019>

Ferreira, C.M., Irish, J.L., Olivera, F., 2014. Quantifying the potential impact of land cover changes due to sea-level rise on storm surge on lower Texas coast bays. *Coast. Eng.* 94, 102–111. <https://doi.org/https://doi.org/10.1016/j.coastaleng.2014.08.011>

Flather, R.A., 2001. Storm Surges, in: *The Cytokine Factsbook*. San Diego, pp. 2882–2892. <https://doi.org/10.1006/rwos.2001.0124>

Flather, R.A., 1994. A Storm Surge Prediction Model for the Northern Bay of Bengal with Application to the Cyclone Disaster in April 1991. *J. Phys. Oceanogr.* 24, 172–190. [https://doi.org/10.1175/1520-0485\(1994\)024<0172:ASSPMF>2.0.CO;2](https://doi.org/10.1175/1520-0485(1994)024<0172:ASSPMF>2.0.CO;2)

Frazier, T.G., Wood, N., Yarnal, B., Bauer, D.H., 2010. Influence of potential sea level rise on societal vulnerability to hurricane storm-surge hazards, Sarasota County, Florida. *Appl. Geogr.* 30, 490–505. <https://doi.org/https://doi.org/10.1016/j.apgeog.2010.05.005>

Fredsøe, J., Deigaard, R., 1992. *Mechanics of Coastal Sediment Transport*. WORLD SCIENTIFIC. <https://doi.org/10.1142/1546>

Gallo, M., Vinzon, S., 2005. Generation of overtides and compound tides in Amazon estuary. *Ocean Dyn.* 55, 441–448. <https://doi.org/10.1007/s10236-005-0003-8>

Godin, G., 1999. The Propagation of Tides up Rivers With Special Considerations on the Upper Saint Lawrence River. *Estuar. Coast. Shelf Sci.* 48, 307–324. <https://doi.org/https://doi.org/10.1006/ecss.1998.0422>

Godin, G., 1991. Compact approximations to the bottom friction term, for the study of tides propagating in channels. *Cont. Shelf Res.* 11, 579–589.

[https://doi.org/10.1016/0278-4343\(91\)90013-V](https://doi.org/10.1016/0278-4343(91)90013-V)

Godin, G., Martinez, A., 1994. Numerical experiments to investigate the effects of quadratic friction on the propagation of tides in a channel. *Cont. Shelf Res.* 14, 723–748. [https://doi.org/https://doi.org/10.1016/0278-4343\(94\)90070-1](https://doi.org/https://doi.org/10.1016/0278-4343(94)90070-1)

González, F.I., 1984. A Case Study of Wave–Current–Bathymetry Interactions at the Columbia River Entrance. *J. Phys. Oceanogr.* 14, 1065–1078. [https://doi.org/10.1175/1520-0485\(1984\)014<1065:ACSOWI>2.0.CO;2](https://doi.org/10.1175/1520-0485(1984)014<1065:ACSOWI>2.0.CO;2)

Google, n.d. No Title [WWW Document]. URL <https://www.google.com/maps/@22.70103,90.80391,185671m/data=!3m1!1e3> (accessed 4.3.20).

Government of the People’s Republic of Bangladesh, 2009. Bangladesh Climate Change Strategy and Action Plan. Dhaka, Bangladesh.

Groeneweg, J., Battjes, J.A., 2003. Three-dimensional wave effects on a steady current. *J. Fluid Mech.* 478, 325–343.

Guo, L., Wegen, M. van der, Jay, D.A., Matte, P., Wang, Z.B., Roelvink, D., He, Q., 2015. River-tide dynamics: Exploration of nonstationary and nonlinear tidal behavior in the Yangtze River estuary. *J. Geophys. Res. C Ocean.* 120, 3499–3521. <https://doi.org/10.1002/2014JC010491>.Received

Guo, L., Zhu, C., Cai, H., Wang, Z.B., Townend, I., He, Q., 2021. River-enhanced non-linear overtide variations in river estuaries. *Hydrol. Earth Syst. Sci. Discuss.* 2021, 1–31. <https://doi.org/10.5194/hess-2021-75>

Haque, A., Nicholls, R.J., 2018. Floods and the Ganges-Brahmaputra-Meghna Delta, in: *Ecosystem Services for Well-Being in Deltas*. Springer International Publishing,

Cham, pp. 147–159. https://doi.org/10.1007/978-3-319-71093-8_8

Hasan, M.K., Kumar, L., Gopalakrishnan, T., 2020. Inundation modelling for Bangladeshi coasts using downscaled and bias-corrected temperature. *Clim. Risk Manag.* 27, 100207. <https://doi.org/https://doi.org/10.1016/j.crm.2019.100207>

Hashemi, M.R., Neill, S.P., Robins, P.E., Davies, A.G., Lewis, M.J., 2015. Effect of waves on the tidal energy resource at a planned tidal stream array. *Renew. Energy* 75, 626–639. <https://doi.org/https://doi.org/10.1016/j.renene.2014.10.029>

Hasselmann, K., 1974. On the spectral dissipation of ocean waves due to white capping. *Boundary-Layer Meteorol.* 6, 107–127. <https://doi.org/10.1007/BF00232479>

Hasselmann, K., Barnett, T.P., Bouws, E., Carlson, H., Cartwright, D.E., Enke, K., Ewing, J.A., Gienapp, H., Hasselmann, D.E., Kruseman, P., Meerburg, A., Mueller, P., Olbers, D.J., Richter, K., Sell, W., Walden, H., 1973. Measurements of wind-wave growth and swell decay during the Joint North Sea Wave Project (JONSWAP) 95.

Hersbach, H., Bell, B., Berrisford, P., Hirahara, S., Horányi, A., Muñoz-Sabater, J., Nicolas, J., Peubey, C., Radu, R., Schepers, D., Simmons, A., Soci, C., Abdalla, S., Abellan, X., Balsamo, G., Bechtold, P., Biavati, G., Bidlot, J., Bonavita, M., De Chiara, G., Dahlgren, P., Dee, D., Diamantakis, M., Dragani, R., Flemming, J., Forbes, R., Fuentes, M., Geer, A., Haimberger, L., Healy, S., Hogan, R.J., Hólm, E., Janisková, M., Keeley, S., Laloyaux, P., Lopez, P., Lupu, C., Radnoti, G., de Rosnay, P., Rozum, I., Vamborg, F., Villaume, S., Thépaut, J.-N., 2020. The ERA5 global reanalysis. *Q. J. R. Meteorol. Soc.* 146, 1999–2049. <https://doi.org/https://doi.org/10.1002/qj.3803>

- Hofer, T., Messerli, B., 2006. Floods in Bangladesh: History, dynamics and rethinking the role of the Himalayas, *Appropriate Technology*. United Nations University Press, Paris.
- Holland, G.J., Belanger, J.I., Fritz, A., 2010. A revised model for radial profiles of hurricane winds. *Mon. Weather Rev.* 138, 4393–4401.
<https://doi.org/10.1175/2010MWR3317.1>
- Hopkins, J., Elgar, S., Raubenheimer, B., 2016. Observations and model simulations of wave-current interaction on the inner shelf. *J. Geophys. Res. Ocean.* 121, 198–208.
<https://doi.org/10.1002/2015JC010788>
- Hoque, M.A.A., Phinn, S., Roelfsema, C., Childs, I., 2018. Modelling tropical cyclone risks for present and future climate change scenarios using geospatial techniques. *Int. J. Digit. Earth* 11, 246–263. <https://doi.org/10.1080/17538947.2017.1320595>
- Hu, K., Chen, Q., Wang, H., 2015. A numerical study of vegetation impact on reducing storm surge by wetlands in a semi-enclosed estuary. *Coast. Eng.* 95, 66–76.
<https://doi.org/https://doi.org/10.1016/j.coastaleng.2014.09.008>
- Hussain, M.A., Tajima, Y., 2017. Numerical investigation of surge–tide interactions in the Bay of Bengal along the Bangladesh coast. *Nat. Hazards* 86, 669–694.
<https://doi.org/10.1007/s11069-016-2711-4>
- Ikeuchi, H., Hirabayashi, Y., Yamazaki, D., Muis, S., Ward, P.J., Winsemius, H.C., Verlaan, M., Kanae, S., 2017. Compound simulation of fluvial floods and storm surges in a global coupled river-coast flood model: Model development and its application to 2007 Cyclone Sidr in Bangladesh. *J. Adv. Model. Earth Syst.* 9, 1847–1862. <https://doi.org/10.1002/2017MS000943>

- IPCC, 2014. Climate Change 2013 – The Physical Science Basis: Working Group I Contribution to the Fifth Assessment Report of the Intergovernmental Panel on Climate Change. Cambridge University Press, Cambridge. [https://doi.org/DOI: 10.1017/CBO9781107415324](https://doi.org/DOI:10.1017/CBO9781107415324)
- IPCC, 2013. Climate Change 2013: The Physical Science Basis. Contribution of Working Group I to the Fifth Assessment Report of the Intergovernmental Panel on Climate Change. NY, USA.
- Islam, S., Khan, Z., Alam, R., Nur-A-Jahan, I., 2013. Adequacy Check of Existing Crest Level of Sea Facing Coastal Polders by the Extreme Value Analysis Method. IOSR J. Mech. Civ. Eng. 8, 89–96. <https://doi.org/10.9790/1684-0818996>
- Jalón-Rojas, I., Sottolichio, A., Hanquiez, V., Fort, A., Schmidt, S., 2018. To What Extent Multidecadal Changes in Morphology and Fluvial Discharge Impact Tide in a Convergent (Turbid) Tidal River. J. Geophys. Res. Ocean. 3241–3258. <https://doi.org/10.1002/2017JC013466>
- Janssen, P.A.E.M., 1992. Experimental Evidence of the Effect of Surface Waves on the Airflow. J. Phys. Oceanogr. 22, 1600–1604. [https://doi.org/10.1175/1520-0485\(1992\)022<1600:EEOTEO>2.0.CO;2](https://doi.org/10.1175/1520-0485(1992)022<1600:EEOTEO>2.0.CO;2)
- Jisan, M.A., Bao, S., Pietrafesa, L.J., 2018. Ensemble projection of the sea level rise impact on storm surge and inundation at the coast of Bangladesh. Nat. Hazards Earth Syst. Sci. 18, 351–364. <https://doi.org/10.5194/nhess-18-351-2018>
- Jørgen, F., 1984. Turbulent Boundary Layer in Wave-current Motion. J. Hydraul. Eng. 110, 1103–1120. [https://doi.org/10.1061/\(ASCE\)0733-9429\(1984\)110:8\(1103\)](https://doi.org/10.1061/(ASCE)0733-9429(1984)110:8(1103))
- Karim, M.F., Mimura, N., 2008. Impacts of climate change and sea-level rise on

cyclonic storm surge floods in Bangladesh. *Glob. Environ. Chang.* 18, 490–500.
<https://doi.org/10.1016/J.GLOENVCHA.2008.05.002>

Kebede, A.S., Nicholls, R.J., Allan, A., Arto, I., Cazcarro, I., Fernandes, J.A., Hill, C.T., Hutton, C.W., Kay, S., Lázár, A.N., Macadam, I., Palmer, M., Suckall, N., Tompkins, E.L., Vincent, K., Whitehead, P.W., 2018. Applying the global RCP–SSP–SPA scenario framework at sub-national scale: A multi-scale and participatory scenario approach. *Sci. Total Environ.* 635, 659–672.
<https://doi.org/https://doi.org/10.1016/j.scitotenv.2018.03.368>

Kennedy, A.B., Westerink, J.J., Smith, J.M., Hope, M.E., Hartman, M., Taflanidis, A.A., Tanaka, S., Westerink, H., Cheung, K.F., Smith, T., Hamann, M., Minamide, M., Ota, A., Dawson, C., 2012. Tropical cyclone inundation potential on the Hawaiian Islands of Oahu and Kauai. *Ocean Model.* 52–53, 54–68.
<https://doi.org/https://doi.org/10.1016/j.ocemod.2012.04.009>

Khan, M.J.U., Durand, F., Bertin, X., Testut, L., Krien, Y., Islam, A.K.M.S., Pezerat, M., Hossain, S., 2020. Towards an efficient storm surge and inundation forecasting system over the Bengal delta: Chasing the super-cyclone Amphan. *Nat. Hazards Earth Syst. Sci.* 1–29. <https://doi.org/10.5194/nhess-2020-340>

Kim, S.Y., Yasuda, T., Mase, H., 2010. Wave set-up in the storm surge along open coasts during Typhoon Anita. *Coast. Eng.* 57, 631–642.
<https://doi.org/https://doi.org/10.1016/j.coastaleng.2010.02.004>

Knutson, T.R., McBride, J.L., Chan, J., Emanuel, K., Holland, G., Landsea, C., Held, I., Kossin, J.P., Srivastava, A.K., Sugi, M., 2010. Tropical cyclones and climate change. *Nat. Geosci.* 3, 157–163. <https://doi.org/10.1038/ngeo779>

- Komen, G.J., Hasselmann, S., Hasselmann, K., 1984. On the existence of a fully developed wind-sea spectrum. *J. PHYS. Ocean.* 14, 1271–1285. [https://doi.org/10.1175/1520-0485\(1984\)014<1271:oteoaf>2.0.co;2](https://doi.org/10.1175/1520-0485(1984)014<1271:oteoaf>2.0.co;2)
- Krien, Y., Mayet, C., Testut, L., Durand, F., Tazkia, A.R., Islam, A.K.M.S., Gopalakrishna, V. V, Becker, M., Calmant, S., Shum, C.K., Khan, Z.H., Papa, F., Ballu, V., 2016. Improved Bathymetric Dataset and Tidal Model for the Northern Bay of Bengal. *Mar. Geod.* 39, 422–438. <https://doi.org/10.1080/01490419.2016.1227405>
- Krien, Y., Testut, L., Islam, A.K.M.S.K.M.S., Bertin, X., Durand, F., Mayet, C., Tazkia, A.R., Becker, M., Calmant, S., Papa, F., Ballu, V., Shum, C.K., Khan, Z.H., 2017. Towards improved storm surge models in the northern Bay of Bengal. *Cont. Shelf Res.* 135, 58–73. <https://doi.org/https://doi.org/10.1016/j.csr.2017.01.014>
- Kudryavtsev, V.N., Makin, V.K., Chapron, B., 1999. Coupled sea surface-atmosphere model: 2. Spectrum of short wind waves. *J. Geophys. Res. Ocean.* 104, 7625–7639. <https://doi.org/https://doi.org/10.1029/1999JC900005>
- Kumar, T.S., Murty, P.L.N., Kumar, M.P., Kumar, M.K., Padmanabham, J., Kumar, N.K., Shenoi, S.C., Mohapatra, M., Nayak, S., Mohanty, P., 2015. Modeling Storm Surge and its Associated Inland Inundation Extent Due to Very Severe Cyclonic Storm Phailin. *Mar. Geod.* 38, 345–360. <https://doi.org/10.1080/01490419.2015.1053640>
- LeBlond, P.H., 1978. On tidal propagation in shallow rivers. *J. Geophys. Res. Ocean.* 83, 4717–4721. <https://doi.org/10.1029/JC083iC09p04717>
- Lesser, G.R., Roelvink, J.A., van Kester, J.A.T.M., Stelling, G.S., 2004. Development

and validation of a three-dimensional morphological model. *Coast. Eng.* 51, 883–915. <https://doi.org/10.1016/j.coastaleng.2004.07.014>

Lewis, M., Bates, P., Horsburgh, K., Neal, J., Schumann, G., 2013. A storm surge inundation model of the northern Bay of Bengal using publicly available data. *Q. J. R. Meteorol. Soc.* 139, 358–369. <https://doi.org/10.1002/qj.2040>

Lewis, M., Horsburgh, K., Bates, P., 2014. Bay of Bengal cyclone extreme water level estimate uncertainty. *Nat. Hazards* 72, 983–996. <https://doi.org/10.1007/s11069-014-1046-2>

Li, R., Xie, L., Liu, B., Guan, C., 2013. On the sensitivity of hurricane storm surge simulation to domain size. *Ocean Model.* 67, 1–12. <https://doi.org/https://doi.org/10.1016/j.ocemod.2013.03.005>

Li, X., Zhao, G., Nielsen-Gammon, J., Salazar, J., Wigmosta, M., Sun, N., Judi, D., Gao, H., 2020. Impacts of urbanization, antecedent rainfall event, and cyclone tracks on extreme floods at Houston reservoirs during Hurricane Harvey. *Environ. Res. Lett.* 15, 124012. <https://doi.org/10.1088/1748-9326/abc4ff>

Longuet-Higgins, M.S., Stewart, R. w., 1964. Radiation stresses in water waves; a physical discussion, with applications. *Deep Sea Res. Oceanogr. Abstr.* 11, 529–562. [https://doi.org/https://doi.org/10.1016/0011-7471\(64\)90001-4](https://doi.org/https://doi.org/10.1016/0011-7471(64)90001-4)

Longuet-Higgins, M.S., Stewart, R.W., 1962. Radiation stress and mass transport in gravity waves, with application to ‘surf beats.’ *J. Fluid Mech.* 13, 481–504. <https://doi.org/10.1017/S0022112062000877>

Lumbroso, D.M., Suckall, N.R., Nicholls, R.J., White, K.D., 2017. Enhancing resilience to coastal flooding from severe storms in the USA: international lessons. *Nat.*

- Hazards Earth Syst. Sci. 17, 1357–1373. <https://doi.org/10.5194/nhess-17-1357-2017>
- Malhadas, M.S., Leitão, P.C., Silva, A., Neves, R., 2009. Effect of coastal waves on sea level in Óbidos Lagoon, Portugal. *Cont. Shelf Res.* 29, 1240–1250. <https://doi.org/https://doi.org/10.1016/j.csr.2009.02.007>
- Mamnun, N., Bricheno, L.M., Rashed-Un-Nabi, M., 2020. Forcing ocean model with atmospheric model outputs to simulate storm surge in the Bangladesh coast. *Trop. Cyclone Res. Rev.* 9, 117–134. <https://doi.org/https://doi.org/10.1016/j.tcr.2020.04.002>
- Mastenbroek, C., Burgers, G., Janssen, P.A.E.M., 1993. The Dynamical Coupling of a Wave Model and a Storm Surge Model through the Atmospheric Boundary Layer. *J. Phys. Oceanogr.* 23, 1856–1866. [https://doi.org/10.1175/1520-0485\(1993\)023<1856:TDCOAW>2.0.CO;2](https://doi.org/10.1175/1520-0485(1993)023<1856:TDCOAW>2.0.CO;2)
- Matte, P., Secretan, Y., Morin, J., 2019. Drivers of residual and tidal flow variability in the St. Lawrence fluvial estuary: Influence on tidal wave propagation. *Cont. Shelf Res.* 174, 158–173. <https://doi.org/https://doi.org/10.1016/j.csr.2018.12.008>
- Matte, P., Secretan, Y., Morin, J., 2017. Hydrodynamic modeling of the St. Lawrence fluvial estuary. II: Reproduction of spatial and temporal patterns. *J. Waterw. Port, Coast. Ocean Eng.* 143, <xocs:firstpage xmlns:xocs=""/>. [https://doi.org/10.1061/\(ASCE\)WW.1943-5460.0000394](https://doi.org/10.1061/(ASCE)WW.1943-5460.0000394)
- Matte, P., Secretan, Y., Morin, J., 2014. Temporal and spatial variability of tidal-fluvial dynamics in the St. Lawrence fluvial estuary: An application of nonstationary tidal harmonic analysis. *J. Geophys. Res. Ocean.* 119, 5724–5744.

<https://doi.org/10.1002/2014JC009791>

McPhaden, M.J., Foltz, G.R., Lee, T., Murty, V.S.N., Ravichandran, M., Vecchi, G.A., Vialard, J., Wiggert, J.D., Yu, L., 2009. Ocean-Atmosphere Interactions During Cyclone Nargis. *Eos, Trans. Am. Geophys. Union* 90, 53–54. <https://doi.org/https://doi.org/10.1029/2009EO070001>

Mehvar, S., Filatova, T., Sarker, M.H., Dastgheib, A., Ranasinghe, R., 2019. Climate change-driven losses in ecosystem services of coastal wetlands: A case study in the West coast of Bangladesh. *Ocean Coast. Manag.* 169, 273–283. <https://doi.org/https://doi.org/10.1016/j.ocecoaman.2018.12.009>

Mei, C.C., 1989. *The applied dynamics of ocean surface waves*. World scientific.

MENDELSON, R., DINAR, A., WILLIAMS, L., 2006. The distributional impact of climate change on rich and poor countries. *Environ. Dev. Econ.* 11, 159–178. <https://doi.org/10.1017/S1355770X05002755>

Moon, I.J., 2005. Impact of a coupled ocean wave-tide-circulation system on coastal modeling. *Ocean Model.* 8, 203–236. <https://doi.org/10.1016/j.ocemod.2004.02.001>

Mousavi, M.E., Irish, J.L., Frey, A.E., Olivera, F., Edge, B.L., 2011. Global warming and hurricanes: the potential impact of hurricane intensification and sea level rise on coastal flooding. *Clim. Change* 104, 575–597. <https://doi.org/10.1007/s10584-009-9790-0>

Murshed, S., Paull, D.J., Griffin, A.L., Islam, M.A., 2021. A parsimonious approach to mapping climate-change-related composite disaster risk at the local scale in coastal Bangladesh. *Int. J. Disaster Risk Reduct.* 55, 102049.

<https://doi.org/https://doi.org/10.1016/j.ijdr.2021.102049>

- Murty, P.L.N.N., Sandhya, K.G., Bhaskaran, P.K., Jose, F., Gayathri, R., Balakrishnan Nair, T.M., Srinivasa Kumar, T., Sheno, S.S.C., 2014. A coupled hydrodynamic modeling system for PHAILIN cyclone in the Bay of Bengal. *Coast. Eng.* 93, 71–81. <https://doi.org/https://doi.org/10.1016/j.coastaleng.2014.08.006>
- Murty, T.S., 1984. Storm surges-meteorological ocean tides. *Can. Bull. Fish. Aquat. Sci.* Can. Dep. Fish. Ocean. 212, 897.
- Murty, T.S., Flather, R.A., 1994. Impact of Storm Surges in the Bay of Bengal. *J. Coast. Res.* 149–161.
- Murty, T.S., Flather, R.A., Henry, R.F., 1986. The storm surge problem in the bay of Bengal. *Prog. Oceanogr.* 16, 195–233. [https://doi.org/https://doi.org/10.1016/0079-6611\(86\)90039-X](https://doi.org/https://doi.org/10.1016/0079-6611(86)90039-X)
- Needham, H.F., Keim, B.D., Sathiaraj, D., 2015. A review of tropical cyclone-generated storm surges: Global data sources, observations, and impacts. *Rev. Geophys.* 53, 545–591. <https://doi.org/https://doi.org/10.1002/2014RG000477>
- Nicholls, R.J., Wong, P.P., Burkett, V., Codignotto, J., Hay, J., McLean, R., Ragoonaden, S., Woodroffe, C.D., Abuodha, P.A.O., Arblaster, J., others, 2007. Coastal systems and low-lying areas, *Climate Change 2007: Impacts, Adaptation and Vulnerability*.
- Ogston, A.S., Allison, M.A., Mclachlan, R.L., Nowacki, D.J., Stephens, J.D., 2017. How tidal processes impact the transfer of sediment from source to sink: Mekong River collaborative studies. *Oceanography*. <https://doi.org/10.5670/oceanog.2017.311>
- Ormond, M., Nederhoff, K., van Dongeren, A., 2020. Delft dashboard: a quick set-up

tool for hydrodynamic models. *J. Hydroinformatics*.
<https://doi.org/10.2166/hydro.2020.092>

Paul, B.K., 2009. Why relatively fewer people died? The case of Bangladesh's Cyclone Sidr. *Nat. Hazards* 50, 289–304.

Pawlowicz, R., Beardsley, B., Lentz, S., 2002. Classical tidal harmonic analysis including error estimates in MATLAB using TDE. *Comput. Geosci.* 28, 929–937.
[https://doi.org/10.1016/S0098-3004\(02\)00013-4](https://doi.org/10.1016/S0098-3004(02)00013-4)

Pethick, J., Orford, J.D., 2013. Rapid rise in effective sea-level in southwest Bangladesh: Its causes and contemporary rates. *Glob. Planet. Change* 111, 237–245.
<https://doi.org/10.1016/J.GLOPLACHA.2013.09.019>

Phillips, O.M., 1966. The dynamics of the upper ocean. CUP Archive.

Pleskachevsky, A., Eppel, D.P., Kapitza, H., 2009. Interaction of waves, currents and tides, and wave-energy impact on the beach area of Sylt Island. *Ocean Dyn.* 59, 451–461. <https://doi.org/10.1007/s10236-008-0174-1>

Prakash, K.R., Pant, V., 2020. On the wave-current interaction during the passage of a tropical cyclone in the Bay of Bengal. *Deep. Res. Part II Top. Stud. Oceanogr.* 172, 104658. <https://doi.org/10.1016/j.dsr2.2019.104658>

Rahman, S., Islam, A.K.M.S., Saha, P., Tazkia, A.R., Krien, Y., Durand, F., Testut, L., Islam, G.M.T., Bala, S.K., 2019a. Projected changes of inundation of cyclonic storms in the Ganges–Brahmaputra–Meghna delta of Bangladesh due to SLR by 2100. *J. Earth Syst. Sci.* 128, 1–11. <https://doi.org/10.1007/s12040-019-1184-8>

Rahman, S., Islam, A.K.M.S.M.S., Saha, P., Tazkia, A.R., Krien, Y., Durand, F., Testut, L., Islam, G.M.T.T., Bala, S.K., 2019b. Projected changes of inundation of cyclonic

- storms in the Ganges--Brahmaputra--Meghna delta of Bangladesh due to SLR by 2100. *J. Earth Syst. Sci.* 128, 145. <https://doi.org/10.1007/s12040-019-1184-8>
- Ramos-Valle, A.N., Curchitser, E.N., Bruyère, C.L., 2020. Impact of Tropical Cyclone Landfall Angle on Storm Surge Along the Mid-Atlantic Bight. *J. Geophys. Res. Atmos.* 125, e2019JD031796. <https://doi.org/https://doi.org/10.1029/2019JD031796>
- Rao, A.D., 1982. Numerical storm surge prediction in India.
- Rasul, G., 2014. Why eastern himalayan countries should cooperate in transboundary water resource management. *Water Policy* 16, 19–38. <https://doi.org/10.2166/wp.2013.190>
- Raubenheimer, B., Guza, R.T., Elgar, S., 2001. Field observations of wave-driven setdown and setup. *J. Geophys. Res. Ocean.* 106, 4629–4638.
- Rego, J.L., Li, C., 2010. Nonlinear terms in storm surge predictions: Effect of tide and shelf geometry with case study from Hurricane Rita. *J. Geophys. Res. Ocean.* 115. <https://doi.org/10.1029/2009JC005285>
- Rego, J.L., Li, C., 2009. On the importance of the forward speed of hurricanes in storm surge forecasting: A numerical study. *Geophys. Res. Lett.* 36. <https://doi.org/10.1029/2008GL036953>
- Resio, D.T., Westerink, J.J., 2008. Modeling the physics of storm surges. *Phys. Today* 61, 33–38. <https://doi.org/10.1063/1.2982120>
- Ris, R.C., Holthuijsen, L.H., Booij, N., 1999. A third-generation wave model for coastal regions: 2. Verification. *J. Geophys. Res. Ocean.* 104, 7667–7681. <https://doi.org/https://doi.org/10.1029/1998JC900123>

- Rogers, K.G., Goodbred, S.L., 2014. The Sundarbans and Bengal Delta: The World's Largest Tidal Mangrove and Delta System, in: V. S. Kale (Ed.), *Landscapes and Landforms of India*. Springer, pp. 181–187. https://doi.org/10.1007/978-94-017-8029-2_18
- Roland, A., Cucco, A., Ferrarin, C., Hsu, T.-W.W., Liao, J.-M.M., Ou, S.-H.H., Umgiesser, G., Zanke, U., 2009. On the development and verification of a 2-D coupled wave-current model on unstructured meshes. *J. Mar. Syst.* 78, S244–S254. <https://doi.org/https://doi.org/10.1016/j.jmarsys.2009.01.026>
- Rose, L., Bhaskaran, P.K., 2017. Tidal propagation and its non-linear characteristics in the Head Bay of Bengal. *Estuar. Coast. Shelf Sci.* 188, 181–198. <https://doi.org/10.1016/J.ECSS.2017.02.024>
- Rose, L., Bhaskaran, P.K., 2016. The role of environmental forcing on tidal dynamics along complex near-shore waters off Bangladesh. *Ocean Eng.* 116, 68–81. <https://doi.org/10.1016/J.OCEANENG.2016.02.031>
- Roy, G.D., 1984. Numerical storm surge prediction in Bangladesh. IIT Delhi.
- S. K. Dube P. Chittibabu, A.D.R.P.C.S.T.S.M., Dube, S.K., Chittibabu, P., Rao, A.D., Sinha, P.C., Murty, T.S., 2000. Extreme Sea Levels Associated With Severe Tropical Cyclones Hitting Orissa Coast of India. *Mar. Geod.* 23, 75–90. <https://doi.org/10.1080/01490410050030652>
- Saiful, I.A., Kumar, B.S., Asad, H.M., Abed, H.M., Mafizur, R.M., 2011. Performance of Coastal Structures during Cyclone Sidr. *Nat. Hazards Rev.* 12, 111–116. [https://doi.org/10.1061/\(ASCE\)NH.1527-6996.0000031](https://doi.org/10.1061/(ASCE)NH.1527-6996.0000031)
- Samiksha, V., Vethamony, P., Antony, C., Bhaskaran, P., Nair, B., 2017. Wave-current

- interaction during Hudhud cyclone in the Bay of Bengal. *Nat. Hazards Earth Syst. Sci.* 17, 2059–2074. <https://doi.org/10.5194/nhess-17-2059-2017>
- Sassi, M.G., Hoitink, A.J.F.F., 2013. River flow controls on tides and tide-mean water level profiles in a tidal freshwater river. *J. Geophys. Res. Ocean.* 118, 4139–4151. <https://doi.org/10.1002/jgrc.20297>
- Savenije, H.H.G., Toffolon, M., Haas, J., Veling, E.J.M., 2008. Analytical description of tidal dynamics in convergent estuaries. *J. Geophys. Res. Ocean.* 113, n/a-n/a. <https://doi.org/10.1029/2007JC004408>
- Saxena, S., Purvaja, R., Mary Divya Suganya, G., Ramesh, R., 2013. Coastal hazard mapping in the Cuddalore region, South India. *Nat. Hazards* 66, 1519–1536. <https://doi.org/10.1007/s11069-012-0362-7>
- SHIBAYAMA, T., TAJIMA, Y., KAKINUMA, T., NOBUOKA, H., YASUDA, T., AHSAN, R., RAHMAN, M., ISLAM, M.S., 2008. Field Survey of Storm Surge Disaster due to Cyclone Sidr in Bangladesh. *Proc. Coast. Eng. Jsce* 55, 1396–1400. <https://doi.org/10.2208/proce1989.55.1396>
- Signell, R.P., Beardsley, R.C., Graber, H.C., Capotondi, A., 1990. Effect of wave-current interaction on wind-driven circulation in narrow, shallow embayments. *J. Geophys. Res. Ocean.* 95, 9671–9678. <https://doi.org/https://doi.org/10.1029/JC095iC06p09671>
- Sinha, P.C., Rao, Y.R., Dube, S.K., Rao, A.D., Chatterjee, A.K., 1996. Numerical investigation of tide-surge interaction in hooghly estuary, india. *Mar. Geod.* 19, 235–255. <https://doi.org/10.1080/01490419609388082>
- Smith, J.A., 2006. Wave-current interactions in finite depth. *J. Phys. Oceanogr.* 36,

1403–1419. <https://doi.org/10.1175/JPO2911.1>

Smith, S.D., Anderson, R.J., Oost, W.A., Kraan, C., Maat, N., De Cosmo, J., Katsaros, K.B., Davidson, K.L., Bumke, K., Hasse, L., Chadwick, H.M., 1992. Sea surface wind stress and drag coefficients: The hexos results. *Boundary-Layer Meteorol.* 60, 109–142. <https://doi.org/10.1007/BF00122064>

SMRC, 1998. The impact of tropical cyclones on the coastal regions of SAARC countries and their influence in the region. Dhaka, Bangladesh.

Snead, R.E., 2010. Bangladesh, in: Bird, E.C.F. (Ed.), *Encyclopedia of the World's Coastal Landforms*. Springer Netherlands, Dordrecht, pp. 1077–1080. https://doi.org/10.1007/978-1-4020-8639-7_201

Song, D., Wang, X.H., Zhu, X., Bao, X., 2013. Modeling studies of the far-field effects of tidal flat reclamation on tidal dynamics in the East China Seas. *Estuar. Coast. Shelf Sci.* 133, 147–160. <https://doi.org/https://doi.org/10.1016/j.ecss.2013.08.023>

Song, H., Kuang, C., Hua, X., Ma, Z., 2020. Wave-current interactions during extreme weather conditions in southwest of Bohai Bay , China. *Ocean Eng.* 216, 108068. <https://doi.org/10.1016/j.oceaneng.2020.108068>

Tazkia, A.R., Krien, Y., Durand, F., Testut, L., Islam, A.S., Papa, F., Bertin, X., 2017. Seasonal modulation of M2 tide in the Northern Bay of Bengal. *Cont. Shelf Res.* 137, 154–162. <https://doi.org/10.1016/J.CSR.2016.12.008>

Team, S., 2014. SWAN user manual. SWAN Cycle III version 40.91. Delft Univ. Technol. Tech. Doc. 123.

The World Bank, 2010. Bangladesh - Economic of adaptation to climate change 1–130.

Tolman, H.L., 1991. A Third-Generation Model for Wind Waves on Slowly Varying,

- Unsteady, and Inhomogeneous Depths and Currents. *J. Phys. Oceanogr.* 21, 782–797. [https://doi.org/10.1175/1520-0485\(1991\)021<0782:ATGMFW>2.0.CO;2](https://doi.org/10.1175/1520-0485(1991)021<0782:ATGMFW>2.0.CO;2)
- Tolman, H.L., 1990. *Wind wave propagation in tidal seas*. Delft: Technische Universiteit Delft.
- Uddin, M.J., Li, Y., Cheung, K.K., Nasrin, Z.M., Wang, H., Wang, L., Gao, Z., 2019. Rainfall Contribution of Tropical Cyclones in the Bay of Bengal between 1998 and 2016 using TRMM Satellite Data. *Atmosphere* (Basel). 10. <https://doi.org/10.3390/atmos10110699>
- UNDP, 2004. *Reducing Disaster Risk: a Challenge for Development-a Global Report, Disaster and Crisis Management*.
- Viitak, M., Maljutenko, I., Alari, V., Suursaar, Ü., Rikka, S., Lagemaa, P., 2016. The impact of surface currents and sea level on the wave field evolution during St. Jude storm in the eastern Baltic Sea. *Oceanologia* 58, 176–186. <https://doi.org/https://doi.org/10.1016/j.oceano.2016.01.004>
- Wang, X., Xu, L.-L., Cui, S.-H., Wang, C.-H., 2020. Reflections on coastal inundation, climate change impact, and adaptation in built environment: progresses and constraints. *Adv. Clim. Chang. Res.* 11, 317–331. <https://doi.org/https://doi.org/10.1016/j.accre.2020.11.010>
- Wang, Z., Winterwerp, J., He, Q., 2014. Interaction between suspended sediment and tidal amplification in the Guadalquivir Estuary. *Theor. Comput. Obs. Oceanogr.* 64, 1487–1498. <https://doi.org/10.1007/s10236-014-0758-x>
- Whitham, G.B., 2011. *Linear and nonlinear waves*. John Wiley & Sons.
- Wilson, C.A., Goodbred Jr, S.L., 2015. *Construction and Maintenance of the Ganges-*

- Brahmaputra-Meghna Delta: Linking Process, Morphology, and Stratigraphy. *Ann. Rev. Mar. Sci.* 7, 67–88. <https://doi.org/10.1146/annurev-marine-010213-135032>
- Wolf, J., Prandle, D., 1999. Some observations of wave–current interaction. *Coast. Eng.* 37, 471–485. [https://doi.org/https://doi.org/10.1016/S0378-3839\(99\)00039-3](https://doi.org/https://doi.org/10.1016/S0378-3839(99)00039-3)
- Woodruff, J.D., Irish, J.L., Camargo, S.J., 2013. Coastal flooding by tropical cyclones and sea-level rise. *Nature* 504, 44–52. <https://doi.org/10.1038/nature12855>
- World Bank, 2015. “Vulnerable Twenty” Ministers Call for More Action and Investment in Climate Resiliency and Low-Emissions Development [WWW Document]. URL <https://www.worldbank.org/en/news/feature/2015/10/08/vulnerable-twenty-ministers-more-action-investment-climate-resilience-low-emissions-development> (accessed 6.9.21).
- Xie, L., Pietrafesa, L.J., Wu, K., 2003. A numerical study of wave-current interaction through surface and bottom stresses: Coastal ocean response to Hurricane Fran of 1996. *J. Geophys. Res. Ocean.* 108, 1–18. <https://doi.org/https://doi.org/10.1029/2001JC001078>
- Xie, L., Wu, K., Pietrafesa, L., Zhang, C., 2001. A numerical study of wave-current interaction through surface and bottom stresses: Wind-driven circulation in the South Atlantic Bight under uniform winds. *J. Geophys. Res. Ocean.* 106, 16841–16855. <https://doi.org/https://doi.org/10.1029/2000JC000292>
- Yang, H., Zhang, X., Cai, H., Hu, Q., Liu, F., Yang, Q., 2020. Seasonal changes in river-tide dynamics in a highly human-modified estuary: Modaomen Estuary case study. *Mar. Geol.* 427, 106273.

<https://doi.org/https://doi.org/10.1016/j.margeo.2020.106273>

You, Z.-J.J., 2019. Tropical Cyclone-Induced Hazards Caused by Storm Surges and Large Waves on the Coast of China. *Geosciences* 9.

<https://doi.org/10.3390/geosciences9030131>

Yu, X., Pan, W., Zheng, X., Zhou, S., Tao, X., 2017. Effects of wave-current interaction on storm surge in the Taiwan Strait: Insights from Typhoon Morakot. *Cont. Shelf Res.* 146, 47–57.

<https://doi.org/https://doi.org/10.1016/j.csr.2017.08.009>

Zhang, W.-Z., Shi, F., Hong, H.-S., Shang, S.-P., Kirby, J.T., 2010. Tide-surge interaction intensified by the Taiwan Strait. *J. Geophys. Res. Ocean.* 115, 5762.

<https://doi.org/10.1029/2009JC005762>

Appendices

A. River-tide interaction (Chapter 2)

A.1 Complex demodulation method

The complex demodulation method can be used to compute time varying tidal constituents. Details of the method are described by Jalón-Rojas et al. (2018) as below:

Complex Demodulation theory assumes that the time series $X(t)$ is composed of a nearly periodic signal with frequency σ and a non-periodic signal $Z(t)$ given by:

$$X(t) = A(t) \cos(\sigma t + \phi(t)) + Z(t). \quad (\text{A.1})$$

Here, A and ϕ denote tidal amplitude and phase, respectively. Tidal component of frequency influences the nearly periodic signal.

The nearly periodic signal is influenced by the tidal component of frequency σ ($2\pi/12.48 \text{ h}^{-1}$ for D_2 or $2\pi/6.24 \text{ h}^{-1}$ for D_4) with amplitude A and phase ϕ . The amplitude and phase are allowed to vary with time but slowly compared to the frequency σ . These parameters are estimated in three steps:

The original time series is multiplied by $e^{-i\sigma t}$ in order to shift the frequency of interest to zero:

$$Y(t) = X(t)e^{-i\sigma t} = \frac{A(t)}{2} e^{-i\phi(t)} + \frac{A(t)}{2} e^{-i(2\sigma t + \phi(t))} + Z(t)e^{-i\sigma t} \quad (\text{A.2})$$

$Y(t)$ is then low-pass filtered to remove frequencies at or above σ , i.e. the terms $\frac{A(t)}{2} e^{-i(2\sigma t + \phi(t))} + Z(t)e^{-i\sigma t}$ are removed to give

$$Y'(t) = \frac{A'(t)}{2} e^{-i\phi'(t)} \quad (\text{A.3})$$

The corresponding $A'(t)$ and $\phi'(t)$ are calculated from the Inverse Fourier Transform of the filtered spectrum $Y'(t)$:

$$A'(t) = 2|Y'| = 2(\text{Re}(Y')^2 + \text{Im}(Y')^2)^{1/2} \quad (\text{A.4})$$

$$\phi'(t) = \text{specific} \left(\frac{\text{Re}(Y')}{\text{Im}(Y')} \right) \quad (\text{A.5})$$

The estimated $A'(t)$ and $\phi'(t)$ are used as the amplitude and phase in this study.

A.2 The stationary harmonic analysis result

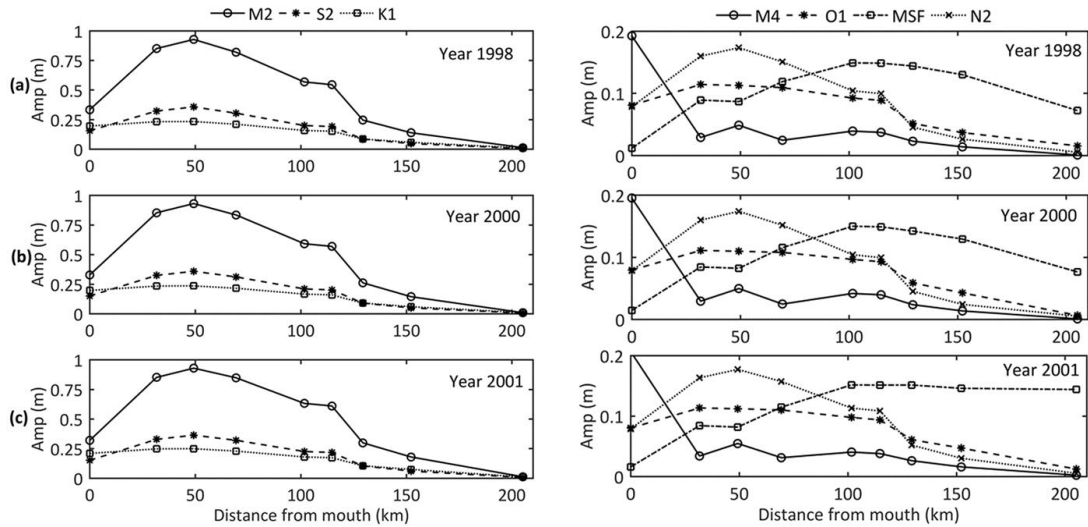


Figure A.1. Spatial variations of tidal amplitudes for: (a) 1998; (b) 2000; and (c) 2001 from the stationary harmonic analysis.

A.3 Further analysis on river-tide interaction

The seasonal river discharge influences the tidal propagation along the Ganges-Brahmaputra-Meghna Delta (GBMD). In the Chapter 2, we did not include the result of seasonal water level variation during the spring-neap tide with the wet-dry season along the GBMD (Figure A.1). We did a deeper analysis of the dissipation of the spring-neap tide along the

channel to illustrate the influence of the river discharge along the GBMD (Figure A.2). To investigate further the influence of river discharge at the lower reaches, we estimated the tidal energy variations (by following Song et al., 2013) for the different idealized scenarios (Table 2.4). Afterward, we showed the variations of tidal amplitude at R7 station, where we observed a slight increase of tidal amplitude with the increase of river discharge from the increase of tidal energy through the increase of water depth (Figure A.5).

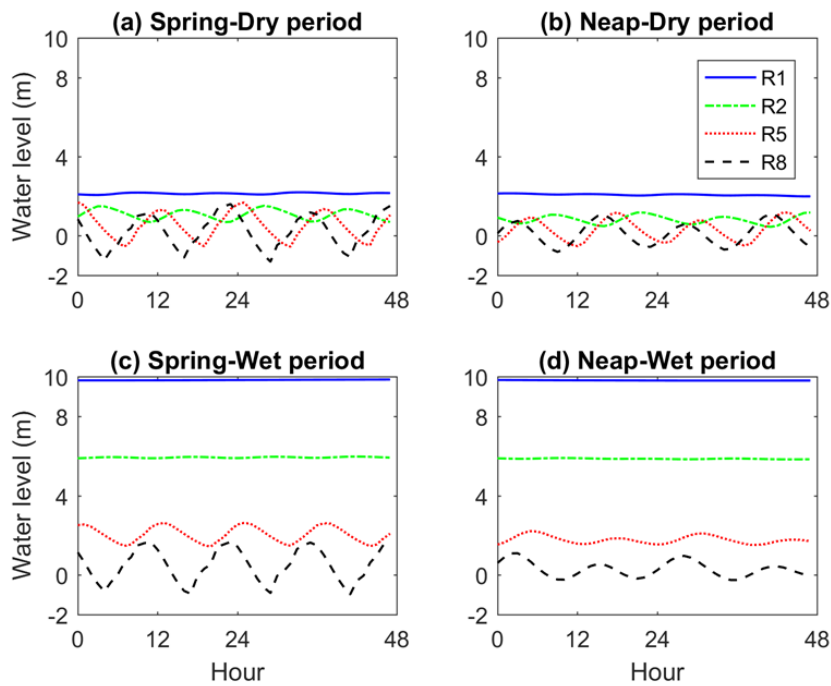


Figure A.2. Water level variation during: (a) a dry season ($\sim 10,000 \text{ m}^3 \text{ s}^{-1}$) spring tide; (b) a dry season-neap tide; (c) a wet season ($\sim 60,000 \text{ m}^3 \text{ s}^{-1}$) spring tide; and (d) a wet season-neap tide at R1, R2, R5, and R8.

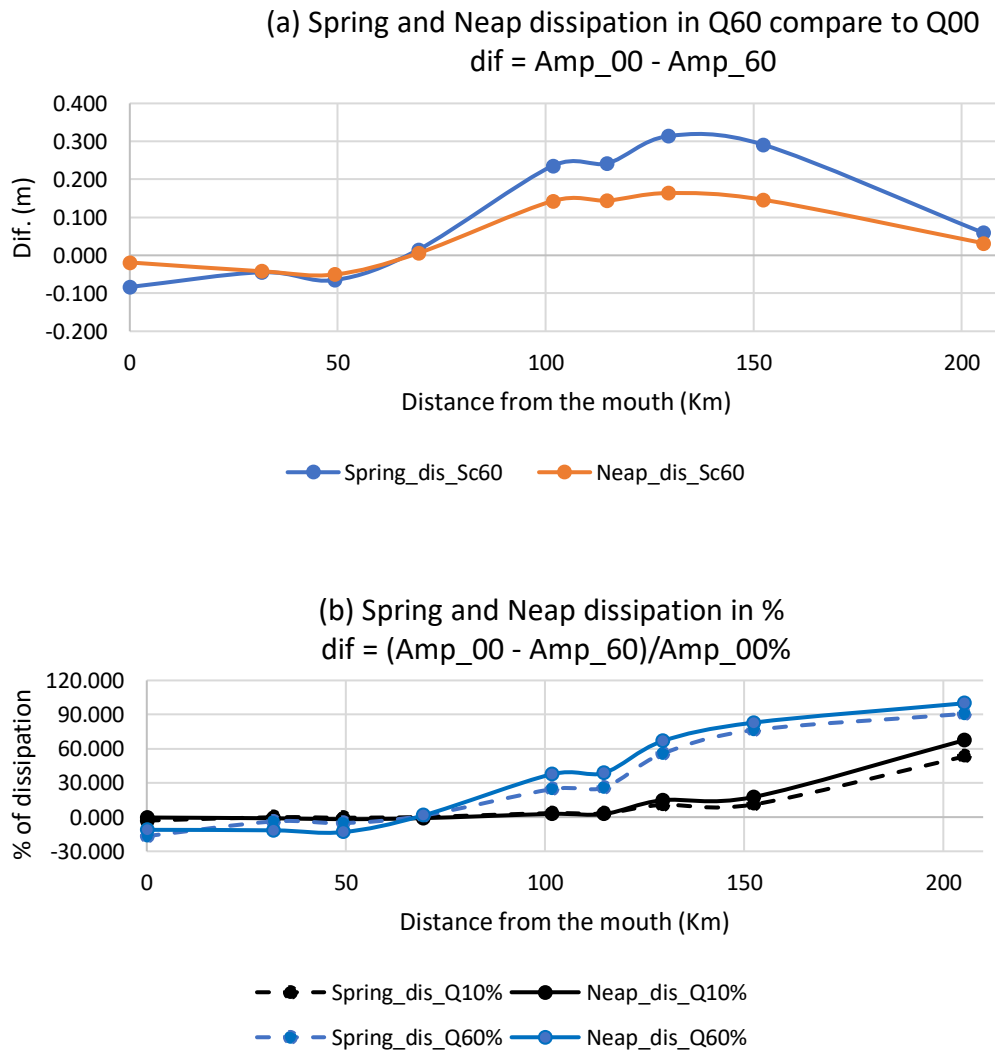


Figure A.3. Spring and neap tide: (a) dissipation in amplitude; and (b) dissipation in percentage along the GBMD for the Q60 compared to the Q00 scenario.

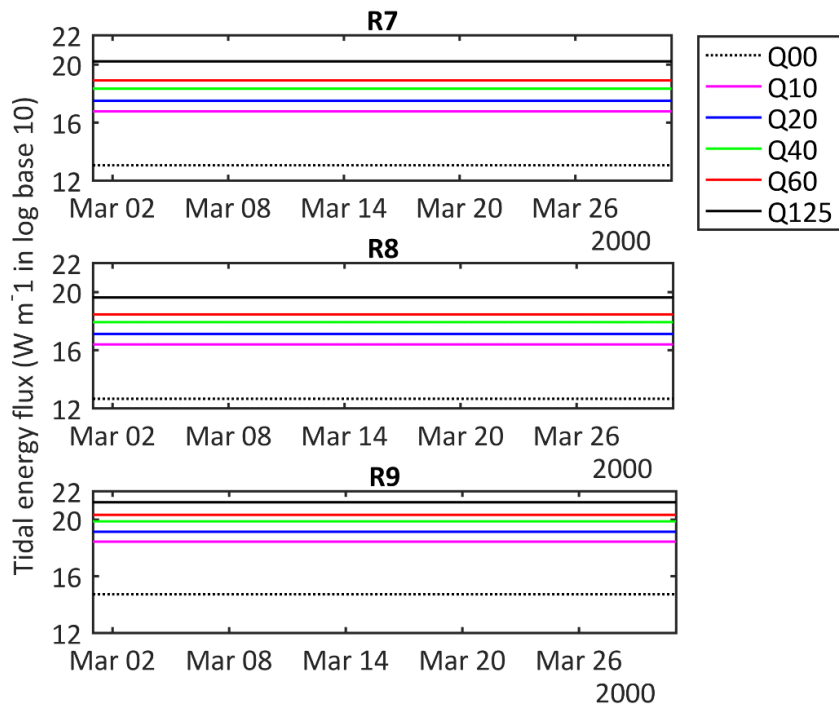


Figure A.4. Tidal energy flux variations at R7, R8 and R9 for different river discharge scenarios.

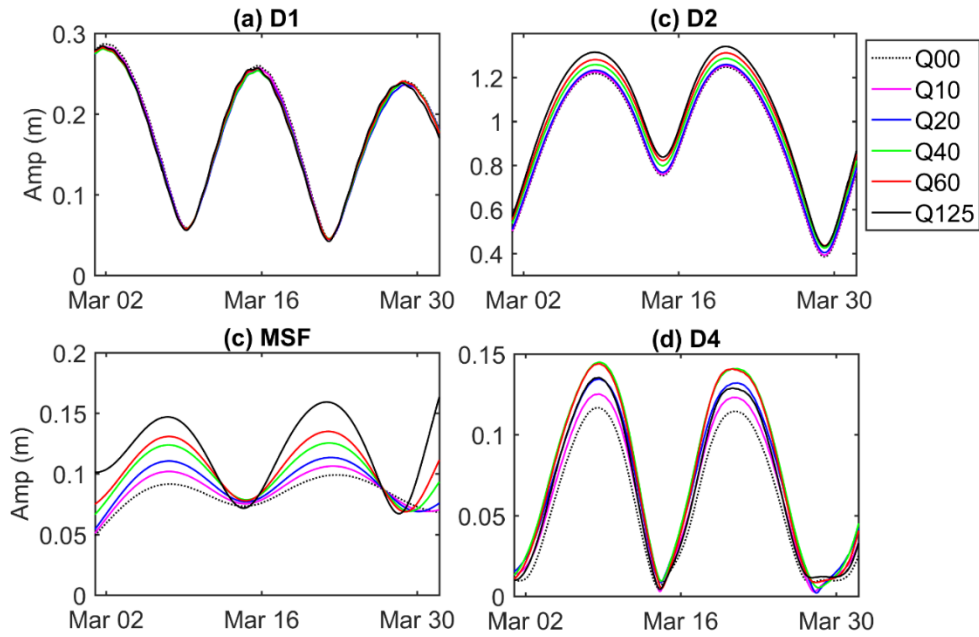


Figure A.5. Different tidal amplitudes variations at R7 (50 km from the estuary mouth) for the following river discharge scenarios: (a) D1; (b) D2; (c) MSF; and (d) D4.

B. Wave-current interaction (Chapter 3)

B.1 Cyclone wind and pressure field incorporation

The JTWC best track archive provides following data at each point along a cyclone track: time, position (latitude and longitude in degrees), maximum sustained wind speed V_{\max} (in knots), radius of maximum wind R_{\max} (in NM) and central pressure P_c (in Pa). Additionally, the wind speed radii of 35, 50, 65 and 100 knots (R_{35} , R_{50} , R_{65} and R_{100} in NM) may be provided for the four quadrants (NE, SE, SW and NW) by the JTWC best track based on data availability. Following the Holland wind model, the geostrophic wind speed V_g of a cyclone can be expressed as:

$$V_g(r) = \sqrt{\frac{AB\rho_{drop}\exp\left(-\frac{A}{rB}\right)}{\rho r^B} + \frac{r^2 f^2}{4} - \frac{rf}{2}} \quad (\text{B.1})$$

Where, r = distance from the center of the cyclone, f = Coriolis parameter, ρ = density of air (assumed to be constant, 1.10 kg m^{-3}), $\rho_{drop} = \rho_n - \rho_c$, ρ_n – ambient pressure (theoretically at infinite radius, however in this model the average pressure over the model domain is used), ρ_c = central pressure of the eye, A and B = empirical parameters.

Physically parameter A determines the relation of the pressure or wind profile relative to the origin, and parameter B defines the shape of the profile. In the region of maximum winds, the Coriolis force is small in comparison to the pressure gradient and centrifugal forces, and therefore the air is in cyclostrophic balance. The cyclostrophic wind V_c at a distance r in this region is given by:

$$V_c(r) = \sqrt{\frac{AB\rho_{drop}\exp\left(-\frac{A}{rB}\right)}{\rho r^B}} \quad (\text{B.2})$$

By setting $d V_c/dr = 0$, the radius of maximum winds (R_w) can be obtained and given as follows:

$$R_w = A^{1/B} \quad (\text{B.3})$$

Where, the R_w is independent of the relative values of ambient and central pressure, and it is defined entirely by the scaling parameters A and B. Substituting Equation B.3 back into Equation B.2 yields an expression for the maximum wind speed as follows:

$$V_{max} = \sqrt{\frac{B \rho_{drop}}{\rho e}} \quad (\text{B.4})$$

Where e is the base of the natural logarithm (= 2.71..).

Parameters A and B can now be expressed as functions of measurable quantities as follows:

$$A = R_w^B \quad (\text{B.5})$$

$$B = \frac{\rho e V_{max}^2}{\rho_{drop}} \quad (\text{B.6})$$

And the central pressure drop is given by

$$\rho_{drop} = \frac{\rho e V_{max}^2}{B} \quad (\text{B.7})$$

By substituting equations B.6 and B.7 into equation B.1, the geostrophic wind V_g can be presented as a function of R_w :

$$V_g(r) = \sqrt{(R_w/r)^B V_{max}^2 \exp(1 - (R_w/r)^B + \frac{r^2 f^2}{4} - \frac{r f}{2})} \quad (\text{B.8})$$

After determining the values of parameters, A and B, the cyclone winds as a function of distance r and direction θ on a spiderweb like grid can be computed by using equation B.8. Further details of wind and pressure drop calculation can be found in the

Deltares (Deltares, 2021b). The profiles can be calculated at regular time intervals by using the 6-hourly JTWC estimates to produce time-varying wind and pressure fields that serve as the surface boundary condition of the hydrodynamic model. At the free surface boundary conditions for the momentum equations are considered in the Delft3d FLOW as:

$$\frac{v_V}{H} \frac{\partial u}{\partial \sigma} = \frac{1}{\rho_0} \left| \vec{\tau}_s \right| \cos(\theta) \quad (\text{B.9})$$

$$\frac{v_V}{H} \frac{\partial v}{\partial \sigma} = \frac{1}{\rho_0} \left| \vec{\tau}_s \right| \sin(\theta) \quad (\text{B.10})$$

where θ is the angle between the wind stress vector, u and v are flow velocities in x and y direction, H is water depth and v_V is vertical eddy viscosity. Without wind, the stress at the free surface is zero. The magnitude of the wind shear-stress is defined by following quadratic expression:

$$\left| \vec{\tau}_s \right| = \rho_a C_d U_{10}^2 \quad (\text{B.11})$$

where, ρ_a is the density of air, U_{10} is the wind speed 10 meter above the free surface (time and space dependent) and C_d is the wind drag coefficient, dependent on U_{10} . The generated wind fields also applied as a surface boundary forcing in the SWAN model. For a full description of the cyclonic wind and pressure field generation and incorporation in the hydrodynamic model, the reader is referred to the Deltares (Deltares, 2021b) and the flow manual of Delft3d (Deltares, 2021c).

B.2 Uncertainty related to cyclone model

Maximum wind speed and area of maximum wind speed at the radius of maximum of the cyclone eye are not captured well in the ERA5 dataset due to its coarser

grid resolution. Moreover, it is difficult to identify accurate maximum wind speed and location of cyclone eye during a cyclone event. The location of cyclone eye is an important factor that is resulting in discrepancies between the model and the ERA5 wind field. The JTWC best track provides 6-hourly values for the cyclone eye location, maximum wind speed, radius of maximum wind and pressure drop.

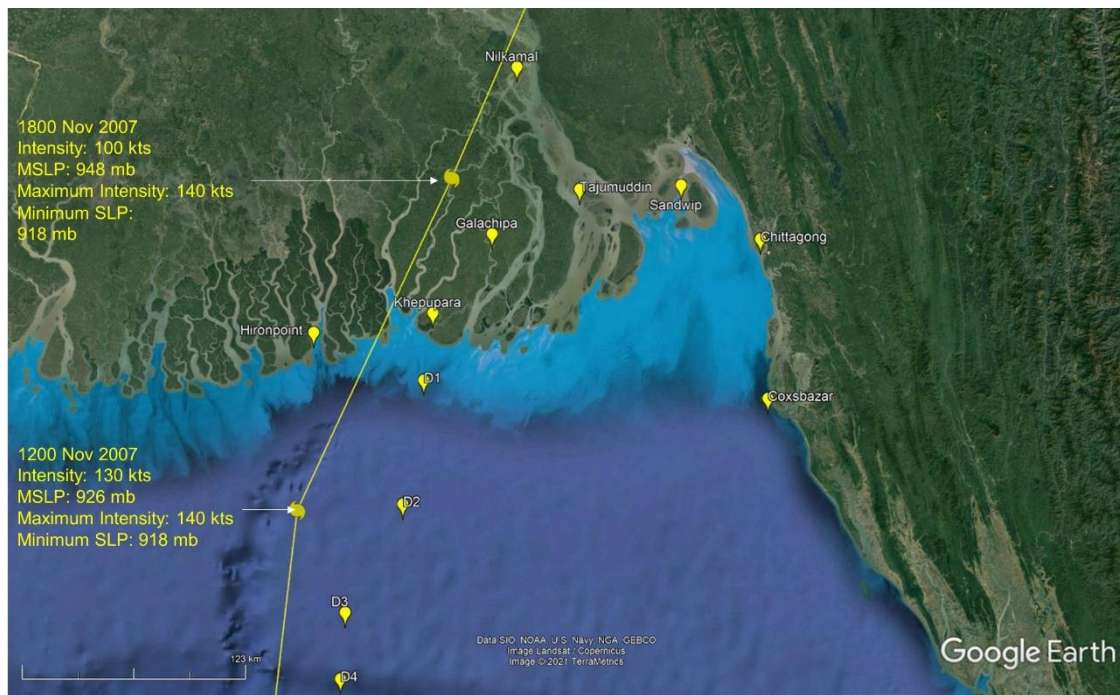


Figure B.1. Locations of the cyclone eye at 3-hour before and 3-hour after the landfall time from the JTWC best track. Cyclones eye movement is assumed constant between the time period, which causes the discrepancies between the model and ERA5 wind field. Consequently, it also affects the significant wave height variations.

The JTWC best track (<https://www.metoc.navy.mil/jtwc/jtwc.html?north-indian-ocean>) provides specific parameters of cyclonic wind structure such as radius of maximum wind, wind speed at specified distances from the cyclone eye. As the JTWC best track provides 6-hourly parameters, it missed the parameters for the landfall timing of Cyclone Sidr. From the track information, the cyclone eye is located approximate 100 km toward offshore at 1200 15 November 2007, and the cyclone eye already in land at 1800 15 November 2007. Therefore, Cyclone Sidr makes landfall at a time between 1200-1800 15 Novmeber. Most of the studies related to Cyclone Sidr reported that the

landfall time is 1500, 15 November 2007. In the present study, the landfall time is 1500 15 November 2007 by assuming that the cyclone eye forward speed remains constant between 1200-1800 15 Novmeber. Rest of the other parameters are kept unchaged according to the JTWC best track. It may result in discprenciens between the timing of storm surge height peaks with the observations and the real event (Figure B.2). Moreover, there is a sudden rise of Rmax (= 30 Nautical mile) at 1800 15 November from 10 Nautical mile at 1200 15 November 2007, which also affect the timing and magnitude of model cyclone-induced storm surge height peak (Figure B.3). Hence, we also investigated the sensitivity of the landfall timing (Figure B.2) and radius of maximum wind (Figure B.3). Results demonstrate that the time of landfall is highly sensitive with the tidal phase in generation of torm surge peaks (Figure B.2). The increase in radius of maximum wind affects the stations located further from the cyclone track such as Tajumuddin, Nilkamal, Sandwipin Figure B.3.

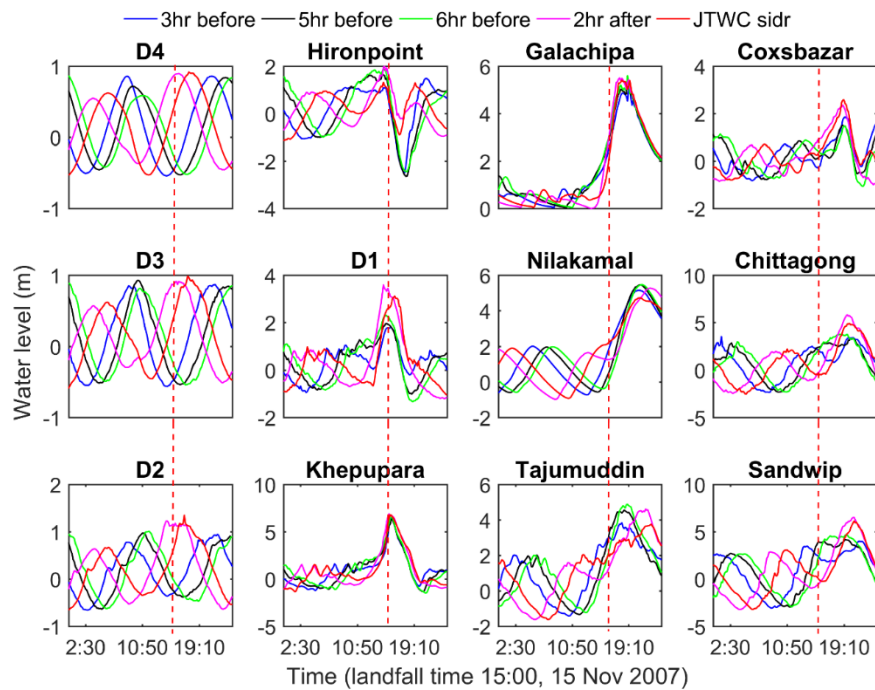


Figure B.2. Model water level variation during Cyclone Sidr at different locations. Several idelized cases are assessed for differnt landfall timings compared to the timing of the JTWC best track archive.

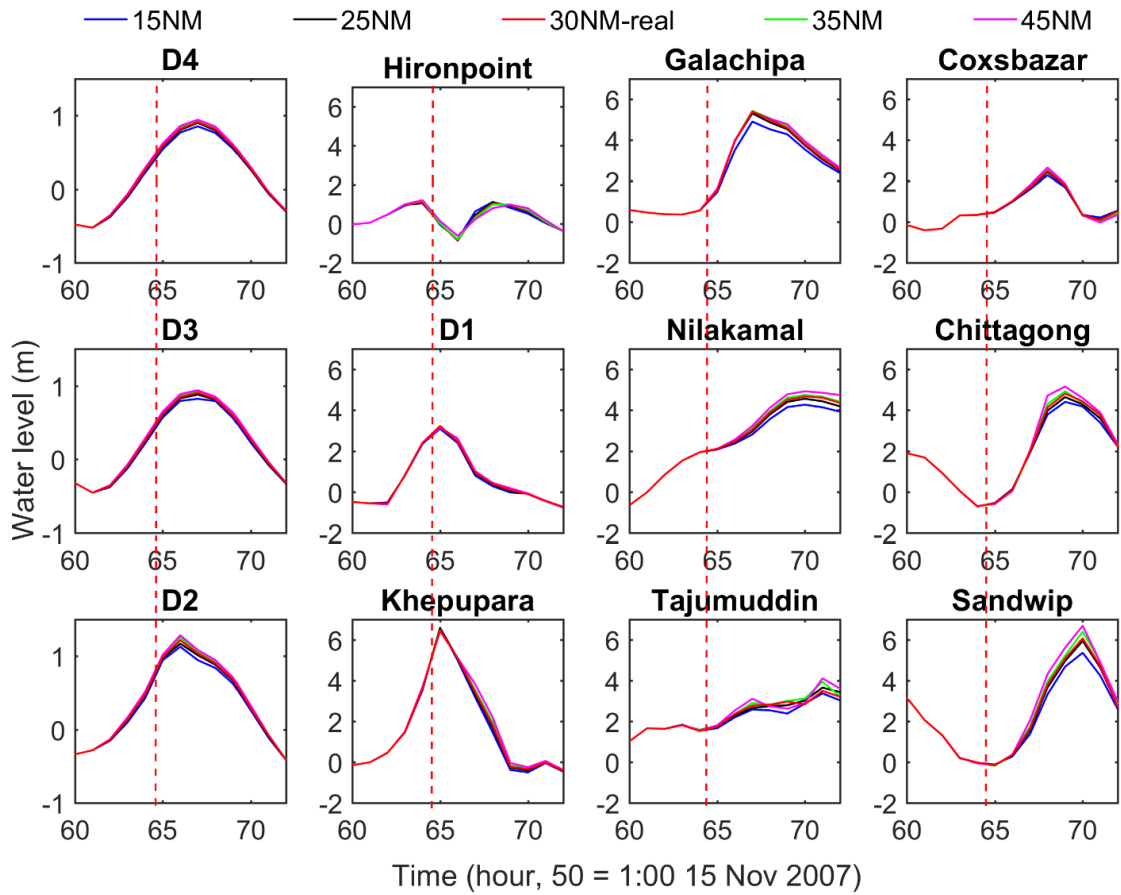


Figure B.3. Model water level variations at different locations for different radius of maximum wind after 3-hour Cyclone Sidr landfall. Only radius of maximum wind is modified at 1800 15 November 2007 and rest of the other parameters remain unchanged.

B.3 Tidal amplitude and maximum residual water level comparison

The stationary harmonic analysis of water level time series at three stations (Hironpoint, Khepupara and Chittagong) are performed using T_Tide (Pawlowicz et al., 2002) for the model and the observed water levels during Cyclone Sidr. Table B.1 shows that the model can reproduce similar tidal amplitudes and phases to the observations during Cyclone Sidr event.

Table B.1. Comparison of model tidal amplitudes and phases with observations during Cyclone Sidr

Amplitudes of tidal components (m)									
Tide	Hironpoint			Khepupara			Chittagong		
	Model	Obs	Abs error (m)	Model	Obs	Abs error (m)	Model	Obs	Abs error (m)
K1	0.16	0.19	0.03	0.16	0.19	0.03	0.46	0.30	0.16
M2	1.03	0.91	0.13	1.03	0.91	0.13	1.06	1.94	0.88
M3	0.09	0.03	0.05	0.09	0.03	0.05	0.07	0.08	0.00
M4	0.05	0.04	0.01	0.05	0.04	0.01	0.13	0.08	0.06
2MK5	0.02	0.03	0.01	0.02	0.03	0.01	0.01	0.02	0.01
M6	0.03	0.02	0.01	0.03	0.02	0.01	0.02	0.03	0.01
3MK7	0.01	0.01	0.01	0.01	0.01	0.01	0.01	0.01	0.00
M8	0.01	0.02	0.01	0.01	0.02	0.01	0.02	0.00	0.01
Total	1.39	1.24		1.74	1.43		1.79	2.49	
Phases of tidal components (degree)									
Tide	Hironpoint			Khepupara			Chittagong		
	Model	Obs	Abs error (deg)	Model	Obs	Abs error (deg)	Model	Obs	Abs error (deg)
K1	222.14	226.35	4.21	222.14	226.35	4.21	286.63	244.86	41.77
M2	85.94	77.44	8.50	85.94	77.44	8.50	186.31	173.10	13.21
M3	196.30	173.59	22.71	196.30	173.59	22.71	230.42	132.85	97.57
M4	116.05	131.50	15.45	116.05	131.50	15.45	290.82	209.64	81.18
2MK5	126.42	338.22	211.80	126.42	338.22	211.80	317.05	305.47	11.58
M6	304.60	36.96	267.64	304.60	36.96	267.64	249.01	249.13	0.12
3MK7	331.64	262.74	68.90	331.64	262.74	68.90	194.32	307.09	112.77
M8	123.05	46.25	76.80	123.05	46.25	76.80	151.21	236.25	85.04

Table B.2. Model residual water level comparison with observations: Cyclone Sidr

	<u>Max. WL (m)</u>		<u>Tidal amp (m)</u>		<u>Residual WL (m)</u>		Abs error (m)
	Model	Obs	Model	Obs	Model	Obs	
Hironpoint	1.39	1.30	1.39	1.24	0	0.06	0.06
Khepupara	6.25	2.94	1.74	1.43	4.51	1.51	3
Chittagong	4.11	3.97	1.79	2.49	2.32	1.48	0.84

As mentioned earlier in Section 3.4.1 that the observations missed storm surge peaks. Therefore, there are discrepancies in residual water levels between the model and observations. Though the observation at Khepupara is showing the maximum water level, 2.94 m, it is not correct. All the field surveys and published studies reported that the maximum water level at Khepupara varied between 5 to 7 m, which is not captured in the water level observations.

B.4 Supporting model result for different scenarios

A barotropic numerical 3D model is used to investigate the cyclone-induced storm surge event during Cyclone Sidr. The established model setup is applied for different idealized cyclonic scenarios to study the role of wave-current interactions on the storm surge height.

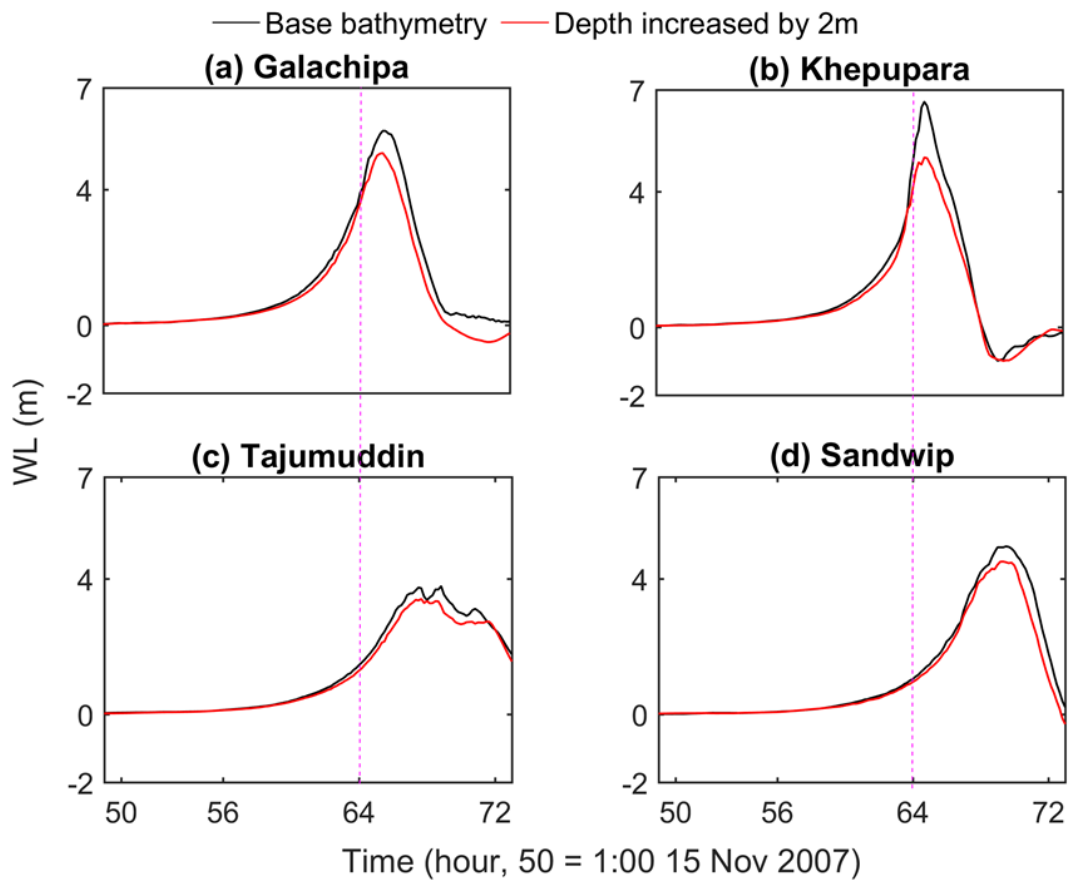


Figure B.4. Water level variations at: (a) Galachipa; (b) Khepupara; (c) Tajudmuddin; and (d) Sandwip for different bathymetric conditions. the black line denotes results from the only wind driven flow model considering real bathymetry. The red line denotes the scenario with 2 m deeper bathymetry in the whole study area compared to the real bathymetry. The purple dashed line represents the landfall time: 1500 UTC 15 November 2007.

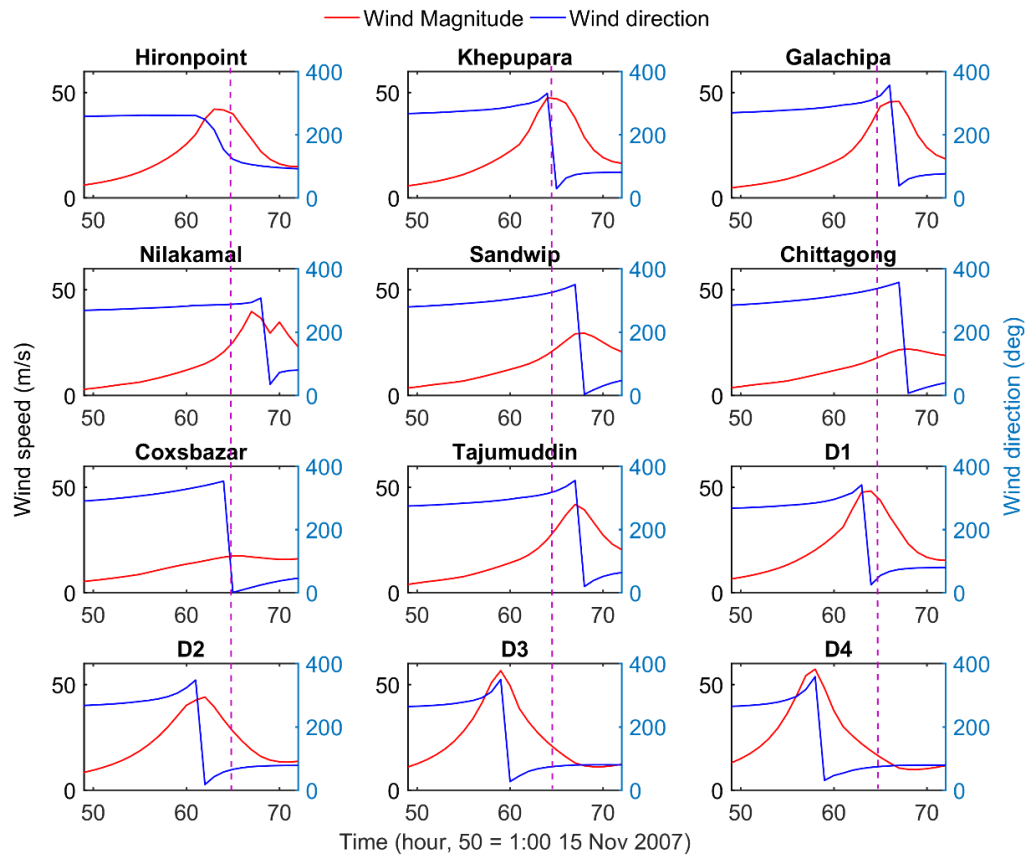


Figure B.5. Model wind magnitude and wind direction during Cyclone Sidr across the GBMD. The purple line denotes the landfall time.

Wave current int. 1400 15 November 2007 Only Wave

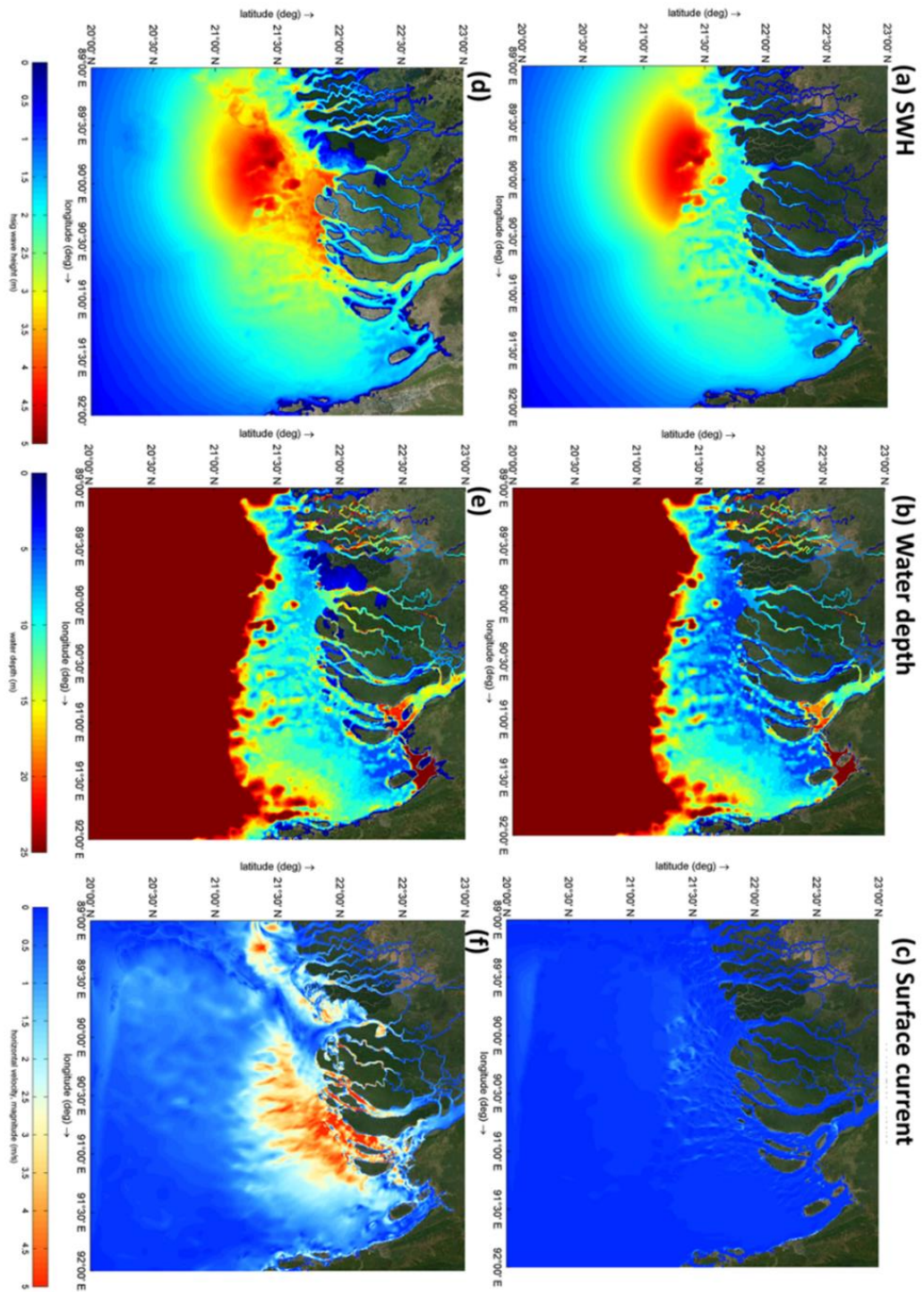


Figure B.6. SWH (a), (d), water depth (b), (e), and surface current magnitude (c), (f) for the only waves (Run1) and wave-current interaction (Run7) scenarios at 1400 UTC, 15 November 2007.

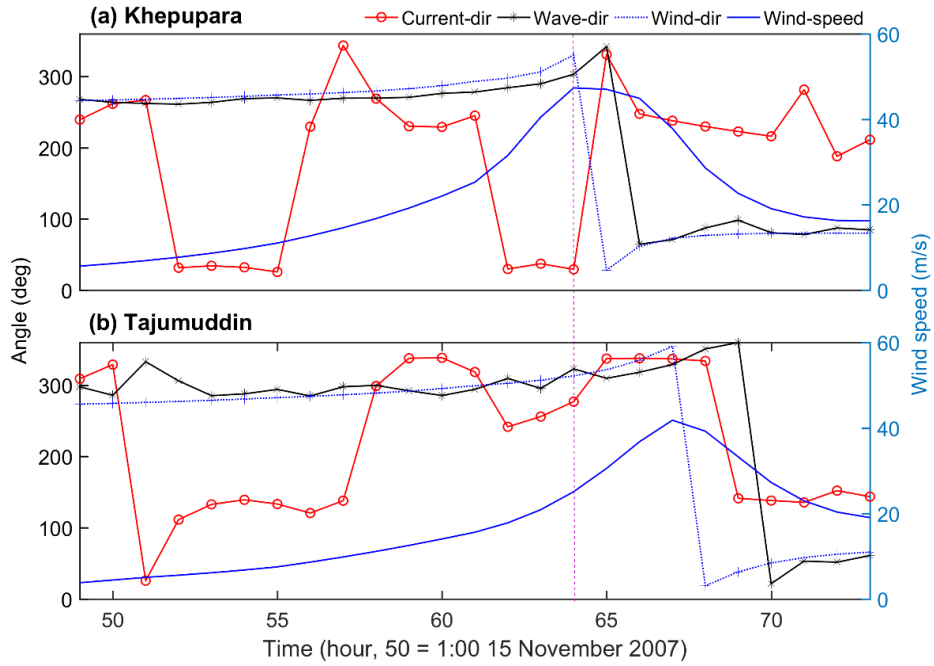


Figure B.7. Direction of current, wave and wind along with wind speed at: (a) Khepupara; and (b) Tajumuddin for the wave-current interaction scenario (Run7).

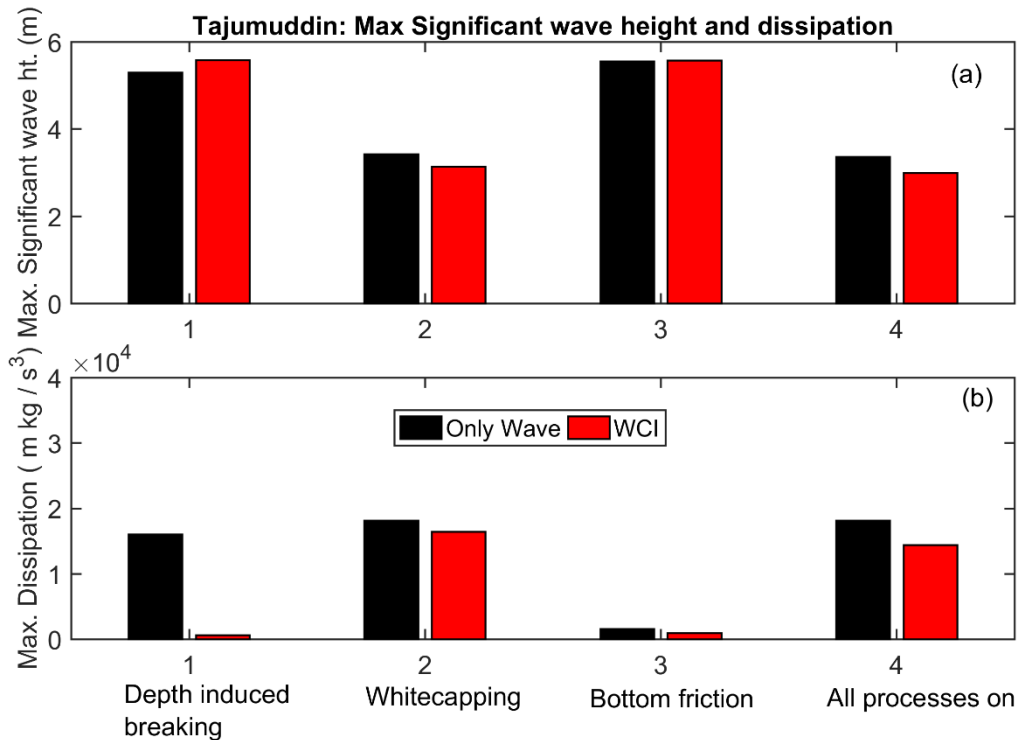


Figure B.8. Maximum: (a) significant wave height; and (b) wave energy variations with and without wave-current interaction at Tajumuddin during Cyclone Sidr for different wave dissipation processes.

Table B.3. Significant wave heights at different stations for the 'Only Wave' and 'WCI' scenarios.

SWH	Only Wave (m)	WCI (m)	Difference (m)	Change in %
Chittagong	1.32	1.72	0.40	30.17
Coxsazar	1.54	1.65	0.11	7.40
Galachipa	0.95	1.63	0.68	72.27
Hironpoint	2.60	3.16	0.57	21.93
Khepupara	1.80	2.87	1.07	59.35
Nilkamal	3.69	3.94	0.25	6.75
Sandwip	1.77	2.19	0.42	23.79
Tajumuddin	3.36	2.99	-0.36	-10.78
D1	2.43	3.62	1.19	49.20
D2	6.15	6.05	-0.10	-1.58
D3	8.74	8.95	0.21	2.42
D4	7.71	8.04	0.33	4.25

C. Cyclone-induced storm surge flooding (Chapter 4)

Table C.1. Flooded area in the GBMD for different mean sea level rise scenarios

MSL	Flooded area (sq. km)					
	Cyclone + Tide	Incr. by (Cyclone + Tide)	Only Tide	Incr. by Only tide	Flooded area by Cyclone = (Cyclone + Tide) – (Only tide)	Incr. by Cyclone
MSL = 0 m	4284		1918		2366	
MSL + 0.5 m	5493	1209	2720	802	2773	407
MSL + 1 m	7771	3487	4362	2444	3409	1043
MSL + 1.5 m	11848	7564	8433	6515	3415	1049

* Increased area = (MSL + xx) – (MSL = 0)